

Numerical Modeling of Annular Laminar Film Condensation in Circular and Non-Circular Micro-Channels under Normal and Micro-Gravity

THÈSE N° 4655 (2010)

PRÉSENTÉE LE 31 MARS 2010

À LA FACULTÉ SCIENCES ET TECHNIQUES DE L'INGÉNIEUR
LABORATOIRE DE TRANSFERT DE CHALEUR ET DE MASSE
PROGRAMME DOCTORAL EN ENERGIE

ÉCOLE POLYTECHNIQUE FÉDÉRALE DE LAUSANNE

POUR L'OBTENTION DU GRADE DE DOCTEUR ÈS SCIENCES

PAR

Stefano NEBULONI

acceptée sur proposition du jury:

Dr J. Van Herle, président du jury
Prof. J. R. Thome, directeur de thèse
Prof. F. Gallaire, rapporteur
Prof. O. Kabov, rapporteur
Prof. D. Poulidakos, rapporteur



ÉCOLE POLYTECHNIQUE
FÉDÉRALE DE LAUSANNE

Suisse
2010

To Erika

Acknowledgements

This study has been carried out at the Laboratory of Heat and Mass Transfer (LTCM), Swiss Federal Institute of Technology (EPFL), under the direction of Prof. John R. Thome. This work has been supported financially by the European Space Agency (ESA) which I gratefully acknowledge.

I would like to express my gratitude to Prof. John R. Thome for giving me the opportunity to undertake this work and for his constant guidance and fruitful discussions. I thank Prof. Oleg Kabov (Université libre de Bruxelles), Prof. Dimos Poulikakos (ETH Zurich), Dr. Jan Van Herle (EPFL) and Prof. François Gallaire (EPFL) for their valued comments and suggestions and for being the examiners of this thesis.

I wish to acknowledge all my friends and colleagues at LTCM for their cooperation and friendship. Thank you for the good time spent together, for the useful debates, the enjoyable coffee breaks, the exciting beach volley games and football matches.

I would like to thank my family for their constant support during all these years and above all I would like to thank my wife Erika, to whom this thesis is dedicated, for her affection and love.

Stefano

*Raffiniert ist der Herrgott,
aber boshaft ist er nicht*

Subtle is God,
but malicious He is not

Complesso è il Signore,
ma malizioso Egli non è

A. Einstein

Abstract

A theoretical and numerical model to predict film condensation heat transfer in mini, micro and ultra micro-channels of different internal shapes is presented in this thesis. The model is based on a finite volume formulation of the Navier-Stokes and energy equations and it includes the contributions of the unsteady terms, surface tension, axial shear stresses, gravitational forces and wall thermal conduction. Notably, interphase mass transfer and near-to-wall effects (disjoining pressure) are also included. This model has been validated versus various benchmark cases and versus published experimental results from three different laboratories, predicting micro-channel heat transfer data with an average error of 20 % or better.

The conjugate heat transfer problem arising from the coupling between the thin film fluid dynamics, the heat transfer in the condensing fluid and the heat conduction in the channel wall has been studied and analyzed. The work has focused on the effects of three external wall boundary conditions: a uniform wall temperature, a non uniform wall heat flux and single-phase convective cooling. The thermal axial and peripheral conduction occurring in the wall of the channel can affect the behavior of the condensate film, not only because it redistributes the heat, but also because the annular laminar film condensation process is dependent on the local saturation to wall temperature difference. When moving from mini to micro and ultra-micro channels, the results shows that the axial conduction effects can become very important in the prediction of the wall temperature profile and they can not be ignored. Under these conditions, the overall performances of the heat exchanger become dependent not only on the fluid properties and the operative conditions but also on the geometry and wall material. Results obtained for steady state conditions are presented for circular, elliptical and flattened shape cross sections for R-134a and ammonia, for hydraulic diameters between 10 μm and 3 mm.

Microscale condensation finds applications in heat pipes and compact heat exchangers for electronic equipment or spacecraft thermal control, in automotive condensers, in residential air conditioning and in refrigeration applications: the influence of the steady or unsteady gravitational field and of the inertia forces on the flow field and consequently on the heat transfer performances is investigated allowing the model to be applied as a design and optimization tool for enhanced heat exchangers.

Keywords: condensation, numerical model, annular flow, microchannel, dimensional analysis, conjugate heat transfer, micro-gravity

Sommario

In questa tesi viene presentato un modello teorico e numerico sviluppato per predire lo scambio termico in condensazione a film per mini, micro e ultra micro canali di diversa sezione interna.

Il modello è basato sulla formulazione a volumi finiti delle equazioni di Navier-Stokes e dell'energia e include i contributi dei termini non stazionari, della tensione superficiale, dello sforzo di taglio all'interfaccia in direzione assiale, dei termini gravitazionali e della conduzione termica nella parete del canale. In particolare sono oltresì inclusi gli effetti legati al trasferimento di massa all'interfaccia e gli effetti di prossimità di parete (*disjoining pressure*). Il modello è stato validato attraverso dei test di riferimento e comparato con risultati sperimentali di tre differenti laboratori, predicendo tali risultati con un errore medio del 20% o inferiore.

Il problema che nasce dall'accoppiamento tra la dinamica del sottile strato di liquido, lo scambio termico nel processo di condensazione e la conduzione termica attraverso le pareti del canale viene studiato e analizzato. Il lavoro è focalizzato sugli effetti di tre possibili condizioni al contorno imposte a parete: temperatura uniforme, flusso termico non uniforme e condizione al contorno di tipo convettivo. La conduzione termica che avviene lungo l'asse e il perimetro del canale influenza il comportamento del processo, non solo perchè il flusso termico viene ridistribuito, ma anche perchè il processo di condensazione a film è dipendente dal valore locale del salto termico tra la temperatura di saturazione e la temperatura di parete. Riducendo la scala da mini, a micro, fino agli ultra-micro canali, i risultati mostrano che la conduzione assiale può diventare molto importante nella predizione della distribuzione di temperatura e questo fenomeno non può essere ignorato. In tali circostanze, l'efficienza complessiva dello scambio termico viene a dipendere non solo dalle proprietà del fluido e dalle condizioni operative ma anche dalla geometria e dalle proprietà termiche del canale. Risultati ottenuti per condizioni in stato stazionario sono presentati per canali a sezioni circolari, ellittiche e *deformate* (a forma di stadio), per diametri idraulici compresi tra 10 μm e 3 mm.

Il processo di condensazione in micro-canali trova applicazione negli *heat pipes* e scambiatori di calore di dimensioni ridotte, nell'equipaggiamento elettronico oppure nel controllo termico di attrezzature spaziali, nei condensatori di autovetture, negli impianti di condizionamento e di refrigerazione: l'influenza sul campo di moto e conseguentemente sulle caratteristiche di scambio termico da parte di campi gravitazionali stazionari o non stazionari e delle forze di inerzia viene in questa sede analizzato, permettendo al modello numerico sviluppato di essere utilizzato come

strumento di progetto e ottimizzazione di scambiatori di calore di prossima generazione.

Parole chiave: condensazione, modello numerico, flusso anulare, micro-canale, analisi dimensionale, scambio termico, micro-gravità

Contents

| | |
|---|-----------|
| Acknowledgements | v |
| Abstract | vii |
| Sommario | ix |
| List of Figures | xv |
| Nomenclature | xxi |
| 1 Introduction | 1 |
| 2 State of The Art on Condensation Heat Transfer | 3 |
| 2.1 Condensation Inside Tubes | 3 |
| 2.2 Condensation Heat Transfer in Mini and Microchannels | 7 |
| 2.2.1 Experimental Studies and Empirical Methods | 7 |
| 2.2.2 Theoretical and Numerical Investigations | 18 |
| 2.3 Condensation Heat Transfer in Microgravity Environments | 23 |
| 2.4 Summary | 26 |
| 3 Mathematical Model | 29 |
| 3.1 Model General Description and Hypotheses | 29 |
| 3.2 General Form of Conservation Equations | 31 |
| 3.3 Coordinate, Basis Vector Systems and Numerical Grid | 32 |
| 3.4 Boundary and Internal Conditions | 36 |

| | | |
|----------|---|-----------|
| 3.5 | Energy Equation | 37 |
| 3.6 | Mass Conservation Equations | 42 |
| 3.6.1 | Liquid Domain | 42 |
| 3.6.2 | Vapor Domain | 42 |
| 3.7 | Momentum Conservation Equations | 43 |
| 3.7.1 | Liquid Domain | 44 |
| 3.7.2 | Vapor Domain | 46 |
| 3.8 | Limits of the Model | 47 |
| 3.9 | Summary | 48 |
| 4 | Dimensional Analysis and Theoretical Investigation | 49 |
| 4.1 | Order of Magnitude and Dimensional Analysis | 49 |
| 4.2 | Dimensional Parameters of the Physical Model | 51 |
| 4.2.1 | Imposed Wall Temperature | 51 |
| 4.2.2 | Imposed Heat Flux | 53 |
| 4.2.3 | External Heat Transfer Coefficient | 55 |
| 4.2.4 | Mini to Microscale Condensation Transition: Capillary and Gravity dominated regimes | 57 |
| 4.3 | Summary of the Dimensionless Numbers | 58 |
| 4.3.1 | Dimensionless Form of the Solution | 60 |
| 4.4 | Summary | 61 |
| 5 | Numerical and Experimental Validation of The Model | 63 |
| 5.1 | Solution Algorithm | 63 |
| 5.2 | Verification of the Numerical Scheme | 67 |
| 5.2.1 | Liquid-Vapor Interface Simple Advection | 67 |
| 5.2.2 | Steady State Analysis: Comparison with Analytical Solutions | 68 |
| 5.3 | Experimental Validation: Heat Transfer Coefficient | 74 |

| | | |
|----------|---|------------|
| 5.3.1 | Heat Transfer Coefficient: Circular Channel | 74 |
| 5.3.2 | Wall Temperature Distribution: Comparison with a Square Mini-Channel | 79 |
| 5.4 | Comparison with an existing model | 83 |
| 5.5 | Summary | 84 |
| 6 | Simulation Results | 85 |
| 6.1 | Dimensionless Results: Parametric Analysis | 86 |
| 6.1.1 | Elliptical Channel Shape | 86 |
| 6.1.2 | Flattened Channel Shape | 95 |
| 6.2 | Wall Conduction Effects in Microchannels | 103 |
| 6.2.1 | Non-Uniform Heat flux and Conjugate Heat Transfer Length | 103 |
| 6.2.2 | Analysis of the Entrance Region | 105 |
| 6.2.3 | Mini to Microchannel Transition | 111 |
| 6.3 | Single Phase Convective Cooling Boundary Condition | 114 |
| 6.4 | Stability of the Annular Flow | 118 |
| 6.5 | Parabolic Flights Simulations | 124 |
| 7 | Conclusions | 131 |
| A | Lubrication Model | 135 |
| B | Buckingham's II-theorem | 139 |
| C | Conjugate Heat Transfer: One Dimensional Model | 143 |
| D | Dimensional Groups for Different Refrigerants | 147 |
| E | Meshes Examples and Numerical Convergence | 153 |
| E.1 | Mesh Size Dependence Test | 157 |
| F | Publication List from Thesis | 159 |

| | |
|------------------|-----|
| G Bibliography | 161 |
| Curriculum Vitae | 167 |

List of Figures

| | | |
|------|---|----|
| 2.1 | Condensation modes: (a) Film-wise condensation. (b) Homogeneous condensation. (c) Dropwise condensation. (d) Direct contact condensation. Illustration from Thome [1]. | 4 |
| 2.2 | Geometries investigated by Garimella et al [2] | 8 |
| 2.3 | Description of two-phase flow regimes reported by Garimella [2] | 9 |
| 2.4 | Physical model and coordinates for the Honda and Nozu model [3]. (a) Un-flooded region and (b) flooded region | 17 |
| 2.5 | Coolant channels, test section subassembly tested by [4] | 18 |
| 2.6 | Illustration from Wang [5]: physical model and coordinates for horizontal microchannels. | 20 |
| 2.7 | Liquid vapor interface obtained for two density ratios: on the top, $\rho_v/\rho_l = 5 \cdot 10^{-4}$; on the bottom, $\rho_v/\rho_l = 5 \cdot 10^{-3}$. Illustration from Miscevic [6] | 22 |
| 2.8 | Schematic of a heat pipe | 25 |
| 2.9 | Schematic of a capillary pumped loop | 25 |
| 2.10 | Comparison of correlations and theory for ammonia. Illustration from Su [7] | 26 |
| 3.1 | a) conceptual subdomain division (liquid and vapor phases) in the x and y plane (cross-sectional view) at an axial location; b) axial view of the channel geometry and interface; c) view of the film control volumes and nomenclature in the x - y plane; d) details of liquid cell geometrical elements | 30 |
| 3.2 | 3D view of the liquid cell control volume and boundaries | 33 |
| 4.1 | Dimensionless film thickness X and dimensionless temperature Θ solution of Eq. (4.40) plotted as a function of Π_α | 56 |
| 5.1 | Schematics of the solution algorithm | 66 |

| | | |
|------|---|----|
| 5.2 | Snapshots at different times of the liquid-vapor interface for a simple test case of pure advection in a circular channel: the liquid phase is flowing from right to left and no forces are present | 68 |
| 5.3 | Definition of the polar coordinate system for a circular channel | 69 |
| 5.4 | Circular channel minimum energy configuration of the liquid-vapor interface for different void fractions with $Bo_R = 0.1$ | 71 |
| 5.5 | Circular channel minimum energy configuration of the liquid-vapor interface for different void fractions with $Bo_R = 1.0$ | 71 |
| 5.6 | Circular channel minimum energy configuration of the liquid-vapor interface for different void fractions with $Bo_R = 3.0$ | 72 |
| 5.7 | Flattened shape channel minimum energy configuration of the liquid-vapor interface for different void fractions with $Bo_P = 0.10$ | 72 |
| 5.8 | Flattened shape channel minimum energy configuration of the liquid-vapor interface for different void fractions with $Bo_P = 0.25$ | 73 |
| 5.9 | Flattened shape channel minimum energy configuration of the liquid-vapor interface for different void fractions with $Bo_P = 3.0$ | 73 |
| 5.10 | Condensation heat transfer coefficients obtained experimentally by Yan and Lin [8] | 76 |
| 5.11 | Cross section of the tested tubes analyzed by Shin and Kim [9] | 77 |
| 5.12 | Condensation heat transfer coefficients obtained experimentally by Shin and Kim [9]: $D_h = 0.691$ mm | 77 |
| 5.13 | Condensation heat transfer coefficients obtained experimentally by Shin and Kim [10]: $D_h = 0.493$ mm | 78 |
| 5.14 | Values predicted by the model h_M normalized by the experimental values h_e versus the average vapor quality for circular channels with three different diameters: 2, 0.691 and 0.493 mm | 78 |
| 5.15 | Test section schematics from Agarwal et al. [11] and cross sectional view of the multi-mini channels simulated and tested geometry | 79 |
| 5.16 | Wall temperature evolution along the axis of the channel: comparison between the prediction of the numerical model and the experimental mean value | 81 |
| 5.17 | Predicted square channel local heat transfer coefficient at different locations, average heat flux $q'' = 8.3$ W/m ² | 81 |
| 5.18 | Wall temperature evolution along the axis of the channel: comparison between the prediction of the numerical model and the experimental mean value | 82 |

| | | |
|------|--|----|
| 5.19 | Predicted square channel local heat transfer coefficient at different locations, average heat flux $q'' = 11.1 \text{ W/m}^2$ | 82 |
| 5.20 | Comparison with Wang and Rose model: heat transfer coefficient versus vapor quality | 83 |
| 6.1 | Cross sectional shape of the elliptical channel | 86 |
| 6.2 | Nusselt numbers plotted versus the dimensionless axial location for elliptical shape channels (E) for different capillary Nusselt numbers | 89 |
| 6.3 | Nusselt numbers plotted versus the dimensionless axial location for elliptical shape channels (E) for different Bond numbers | 89 |
| 6.4 | Nusselt numbers plotted versus the dimensionless axial location for elliptical shape channels (E) for different capillary Reynolds numbers | 90 |
| 6.5 | Nusselt numbers plotted versus the dimensionless axial location for elliptical shape channels (E) for different density ratios | 90 |
| 6.6 | Nusselt numbers plotted versus the dimensionless axial location for elliptical shape channels (E) for different vapor liquid Weber numbers | 91 |
| 6.7 | Nusselt numbers plotted versus the dimensionless axial location for elliptical shape channels (E) for different vapor Reynolds numbers | 91 |
| 6.8 | Elliptical channel solution: interfacial shapes at low specific Nusselt numbers | 92 |
| 6.9 | Elliptical channel solution: interfacial shapes at high specific Nusselt numbers | 93 |
| 6.10 | Elliptical channel solution: interfacial shapes and gravity orientation | 94 |
| 6.11 | Cross sectional shape of the flattened channel | 95 |
| 6.12 | Nusselt numbers plotted versus the dimensionless axial location for flattened shape channels (F) for different capillary Nusselt numbers | 97 |
| 6.13 | Nusselt numbers plotted versus the dimensionless axial location for flattened shape channels (F) for different Bond numbers | 97 |
| 6.14 | Nusselt numbers plotted versus the dimensionless axial location for flattened shape channels (F) for different capillary Reynolds numbers | 98 |
| 6.15 | Nusselt numbers plotted versus the dimensionless axial location for flattened shape channels (F) for different density ratios | 98 |
| 6.16 | Nusselt numbers plotted versus the dimensionless axial location for flattened shape channels (F) for different liquid Weber numbers | 99 |

| | | |
|------|---|-----|
| 6.17 | Nusselt numbers plotted versus the dimensionless axial location for flattened shape channels (F) for different vapor Reynolds numbers | 99 |
| 6.18 | Flattened channel solution: interfacial shapes at low specific Nusselt numbers . . | 100 |
| 6.19 | Flattened channel solution: interfacial shapes at high specific Nusselt numbers . | 101 |
| 6.20 | Flattened channel solution: interfacial shapes and gravity orientation | 102 |
| 6.21 | Effect of the conjugate heat transfer length for a microchannel: wall temperature distribution | 104 |
| 6.22 | Entrance region wall temperature distribution in a microchannel: the conjugate heat transfer effects | 106 |
| 6.23 | Saturation to wall temperature difference perimeter distributions: the conjugate heat transfer effects | 106 |
| 6.24 | 3D wall temperature distributions in microchannels | 107 |
| 6.25 | Dimensionless distributions of the effective local heat flux: effect of the conjugate heat transfer | 109 |
| 6.26 | Distributions of the minimum and maximum dimensionless film thicknesses in the entrance region: effect of the conjugate heat transfer | 109 |
| 6.27 | Distributions of the minimum and maximum dimensionless axial bulk liquid film velocities in the entrance region: effect of the conjugate heat transfer | 110 |
| 6.28 | Distributions of the dimensionless frictional pressure drop in the entrance region: effect of the conjugate heat transfer | 110 |
| 6.29 | R-134a simulated heat transfer coefficients over a wide range of hydraulic diameters: effects of wall materials | 112 |
| 6.30 | Ammonia simulated mean heat transfer coefficients over a wide range of hydraulic diameters for the following conditions: 10°C saturation temperature, mass flux of 500 kg/(m ² s), nominal heat flux of 38.3 kW/m ² , length to hydraulic diameter ratio of 200 and wall thickness to hydraulic diameter ratio of 0.2. At each point the dimensionless parameter, expressed in percent, obtained by the ratio of the difference of the maximum and minimum wall temperatures and the saturation to mean wall temperature difference, is reported. The flattened shape channel with an aspect ratio of 0.5 is the simulated geometry | 113 |
| 6.31 | Schematics of a) co-current heat exchanger and b) counter current heat exchangers for condensation processes | 114 |
| 6.32 | Co-current and counter-current heat transfer coefficients for R-134a at 40°C . . . | 116 |

| | | |
|------|--|-----|
| 6.33 | Total vapor quality variation as a function of the external coolant side heat transfer coefficient for the counter-current heat exchanger configuration | 117 |
| 6.34 | Total vapor quality variation as a function of the external coolant side heat transfer coefficient for the co-current heat exchanger configuration | 117 |
| 6.35 | Time evolution of the liquid-vapor interface obtained for a mass flux of $25 \text{ kg}/(\text{m}^2\text{s})$ | 120 |
| 6.36 | Film thickness distribution plotted in a colored scale as a function of time and space, obtained for a mass flux of $25 \text{ kg}/(\text{m}^2\text{s})$ | 120 |
| 6.37 | Time evolution of the liquid-vapor interface obtained for a mass flux of $30 \text{ kg}/(\text{m}^2\text{s})$ | 121 |
| 6.38 | Film thickness distribution plotted in a colored scale as a function of time and space, obtained for a mass flux of $30 \text{ kg}/(\text{m}^2\text{s})$ | 121 |
| 6.39 | Time evolution of the liquid-vapor interface obtained for a mass flux of $35 \text{ kg}/(\text{m}^2\text{s})$ in normal gravity for a channel having an internal diameter equal to 1 mm | 122 |
| 6.40 | Time evolution of the liquid-vapor interface obtained for a mass flux of $35 \text{ kg}/(\text{m}^2\text{s})$ in normal gravity for a channel having an internal diameter equal to $500 \mu\text{m}$ | 122 |
| 6.41 | Evolution in time of the average heat transfer coefficients for three different mass fluxes and 1 mm hydraulic diameter | 123 |
| 6.42 | Comparison between the global heat transfer coefficient time evolutions obtained for a $500 \mu\text{m}$ internal diameter channel with and without a gravitational field . . . | 123 |
| 6.43 | Picture of the 0-g airplane of the European Space Agency | 125 |
| 6.44 | Evolution of the three components of the gravitational field measured onboard the airplane during the parabolic flight | 126 |
| 6.45 | Evolution in time of the global heat transfer coefficients during the parabolic flight characterized by the gravitational field depicted in Fig. (6.44) | 127 |
| 6.46 | Evolution in time of the exit vapor qualities during the parabolic flight characterized by the gravitational field depicted in Fig. (6.44) | 127 |
| 6.47 | Comparison between the calculated mean heat transfer coefficients evaluated during two different simulated parabolic flights | 128 |
| 6.48 | Comparison between the calculated exit vapor qualities evaluated during two different simulated parabolic flights | 129 |
| 6.49 | Evolution in time of the instantaneous volumetric void fractions during two parabolic flights | 129 |

| | | |
|-----|--|-----|
| A.1 | Schematic of the thin film model: the steady velocity profile \vec{u} induced by the interfacial shear stress, the pressure gradient and the body forces is represented | 135 |
| A.2 | Dimensionless film velocity profiles as a function of the dimensionless film thickness plotted for different values of the dimensionless parameter r defined in Eq. (A.6) | 137 |
| C.1 | Schematic of the one-dimensional model of the conjugate heat transfer problem | 143 |
| C.2 | Solution of the one-dimensional conjugate heat transfer problem: the dimensionless temperature (on the left) and the dimensionless condensing heat flux (on the right) are plotted as a function of the dimensionless position x/l_t | 146 |
| D.1 | Evolution of the dimensional variable F_T defined in Eq. (D.2) with the saturation temperature T_{sat} for different refrigerants | 150 |
| D.2 | Evolution of the dimensional variable F_q defined in Eq. (D.4) with the saturation temperature T_{sat} for different refrigerants | 150 |
| D.3 | Evolution of the dimensional variable R_T defined in Eq. (D.7) with the saturation temperature T_{sat} for different refrigerants | 151 |
| D.4 | Evolution of the dimensional variable R_q defined in Eq. (D.8) with the saturation temperature T_{sat} for different refrigerants | 151 |
| D.5 | Evolution of the dimensional variable γ_T defined in Eq. (D.11) with the saturation temperature T_{sat} for different refrigerants | 152 |
| D.6 | Evolution of the dimensional variable γ_q defined in Eq. (D.12) with the saturation temperature T_{sat} for different refrigerants | 152 |
| E.1 | Example of a liquid-vapor interface (dashed line) in a flattened channel shape | 154 |
| E.2 | Liquid-vapor interface (dashed line) and definition of the film thickness directions $\vec{\delta}$ in a discretized geometry | 154 |
| E.3 | Example of distribution of the liquid film thickness | 155 |
| E.4 | Example of meshing for an elliptical channel | 155 |
| E.5 | Example of meshing for a flattened shape channel | 156 |
| E.6 | Evolution of the simulation error evaluated using the Richardson extrapolation technique described in Chapter 5 by varying the mesh size | 157 |

Nomenclature

Roman Letters

| | | |
|-------------|--|--|
| A | Hamaker constant | $[\text{kg m}^2 \text{s}^{-2}]$ |
| a | linear acceleration | $[\text{m s}^{-2}]$ |
| Bo | Bond number | $[-]$ |
| B | Boiling number | $[-]$ |
| c | constant | $[-]$ |
| C_f | friction coefficient | $[-]$ |
| C_p | specific heat capacity | $[\text{m}^2 \text{s}^{-2} \text{K}^{-1}]$ |
| Ca | Capillary number | $[-]$ |
| D_h | hydraulic diameter | $[\text{m}]$ |
| E | entrainment fraction | $[-]$ |
| f | roughness factor | $[-]$ |
| f_b | body force per unit mass | $[\text{m}^2 \text{s}^{-1}]$ |
| \vec{g} | gravity field | $[\text{m s}^{-2}]$ |
| G | mass flux | $[\text{kg s}^{-1} \text{m}^{-2}]$ |
| H | mean absolute curvature | $[\text{m}^{-1}]$ |
| h | perimeter-averaged heat transfer coefficient | $[\text{kg s}^{-3} \text{K}]$ |
| h_g | global heat transfer coefficient | $[\text{kg s}^{-3} \text{K}]$ |
| h_l | local heat transfer coefficient | $[\text{kg s}^{-3} \text{K}]$ |
| I_d | disjoining pressure number | $[-]$ |
| I_p | interface pressure number | $[-]$ |

| | | |
|-----------|--|---|
| I_r | interface resistance number | [-] |
| J | evaporative or condensing mass flux | [kg m ⁻² s ⁻¹] |
| Ja | Jacob number | [-] |
| K | local mean curvature | [m ⁻¹] |
| k | thermal conductivity | [kg m s ⁻³ K ⁻¹] |
| l_c | characteristic heat transfer length | [m] |
| L | characteristic length | [m] |
| L_{ht} | dimensionless conjugate heat transfer length | [-] |
| \dot{m} | mass flow rate | [kg m ⁻² s ⁻¹] |
| \hat{n} | normal unit vector | [-] |
| Nu | Nusselt number | [-] |
| Pr | Prandtl number | [-] |
| p | pressure | [kg m ⁻¹ s ⁻²] |
| \dot{q} | heat flux | [kg s ⁻³] |
| \Re | universal gas constant | [m ² s ⁻² K ⁻¹] |
| Re | Reynolds number | [-] |
| \vec{r} | position vector | [m] |
| R | radius | [m] |
| Sn | characteristic capillary Nusselt number | [-] |
| S | surface | [m ²] |
| Θ | dimensionless temperature | [-] |
| T | temperature | [K] |
| t | time | [s] |
| U | vapor axial velocity | [m s ⁻¹] |
| u | velocity, x-axis velocity component | [m s ⁻¹] |
| \vec{v} | velocity vector | [m s ⁻¹] |
| Γ | density ratio | [-] |

| | | |
|------|------------------------------|-----|
| We | Weber number | [-] |
| X | vapor quality | [-] |
| x | x coordinate | [m] |
| y | y coordinate | [m] |
| Z | dimensionless axial location | [-] |
| z | axial coordinate | [m] |

Greek Letters

| | | |
|------------------|---|--|
| α_c | heat transfer coefficient | $[\text{kg s}^{-3} \text{K}^{-1}]$ |
| α_e | external heat transfer coefficient | $[\text{kg s}^{-3} \text{K}]$ |
| β | geometrical variable | [-] |
| Δh_{l-v} | latent heat of vaporization | $[\text{m}^2 \text{s}^{-2}]$ |
| δ | film thickness | [m] |
| ε | void fraction | [-] |
| ϕ | liquid film equivalent thermal resistance | $[\text{kg m}^{-2} \text{s}^{-1} \text{K}^{-1}]$ |
| ψ | surface tension parameter | [-] |
| λ | thickness | [m] |
| μ | kinematic viscosity | $[\text{kg m}^{-1} \text{s}^{-1}]$ |
| ρ | density | $[\text{kg m}^{-3}]$ |
| σ | surface tension | $[\text{kg s}^{-2}]$ |
| τ | shear stress | $[\text{kg m}^{-1} \text{s}^{-2}]$ |
| ν | accommodation coefficient | [-] |
| $\vec{\omega}$ | angular velocity | $[\text{s}^{-1}]$ |
| χ | Martinelli parameter | [-] |
| χ_{tt} | Lockhart-Martinelli parameter | [-] |
| ξ | curvilinear coordinate | [m] |
| Ω | control volume | $[\text{m}^3]$ |

Subscripts

| | |
|----------------------|---|
| B | gravity controlled condensation |
| F | forced convection condensation |
| C | Coriolis |
| c | capillarity |
| Δ | variation |
| ∂ | partial derivative or boundary notation |
| $\vec{\nabla} \cdot$ | divergence operator |
| E,W,N,S | East, West, North, South |
| f | frictional |
| g | gravity dominated |
| h | homogeneous |
| i | interface |
| j, k | indexes |
| l | liquid |
| l-o | liquid only |
| l-v | liquid-vapor |
| m | mixture |
| max | maximum |
| O | non-inertial reference point |
| + | turbulent, dimensionless |
| p | pressure |
| r | reference |
| rel | relative |
| * | laminar, dimensionless |
| * | turbulent, dimensional |
| sat | saturation conditions |
| T | temperature |

| | |
|-----------------|------------------------------|
| t | total |
| T, B | Top, Bottom |
| \underline{x} | mathematical vector notation |
| v | vapor |
| w | wall |

Chapter 1

Introduction

Film condensation heat transfer in micro-channels has received increasing attention in recent years with particular emphasis on how to enhance heat transfer to enable even more compact heat exchangers. From the experimental campaigns undertaken until now, a two-phase flow in a micro-channel is expected to have better thermal performance compared to other methods for thermal control. Microscale condensation finds applications in heat pipes and compact heat exchangers for electronic equipment or spacecraft thermal control, in automotive condensers, in residential air conditioning and in refrigeration applications. Although microscale condensation is already largely used in many applications, improved fundamental understanding on this subject has still to come.

An important physical mechanism that enhances condensation heat transfer in micro-channels is the thinning of the condensate film as it is pulled towards the low pressure regions (that is, typically the corners of non circular channels), a flow generated by the pressure gradient induced by the surface tension. This phenomenon has been studied theoretically and numerically by a few authors in the literature for channels having a hydraulic diameters higher than $100\ \mu\text{m}$ but most obtained results are applicable only in the 1 mm range. One of the earliest numerical models developed in order to investigate film condensation in mini-channels is the one by Zhao and Liao [12] in 2002 and an improved model was developed by Wang and Rose [13] in 2005. Since most of the heat transfer occurs in the thin film regions, a fundamental understanding of the mechanisms occurring at micro and nanoscale is a paramount requirement, especially if the ultra micro-scale (less than $100\ \mu\text{m}$) class of heat exchangers has to be studied. In these conditions, some of the assumptions that have been commonly assumed may not be correct anymore and, without accounting for their possible consequences, misleading results might be obtained. When condensation problems are encountered, a uniform imposed temperature or, less frequently, a uniform heat flux boundary condition at the channel wall is commonly assumed. By doing so, the wall thermal conduction properties are completely ignored and this assumption may not be appropriate when considering micro and ultra micro-channel condensation processes. In particular, a coupling mechanism that involves the condensation process, the thermal conduction

in the wall and the actual distribution of the *external* heat load (uniform or non uniform heat flux, or other types of boundary conditions) may occur, and the resulting performances of the heat exchanger may be dependent on all these parameters.

A systematic theoretical analysis of the laminar annular film condensation process, possibly including all the mentioned case studies, does not exist yet, and the dimensionless groups that tend to dominate this physical process have not been clearly identified yet. Within these, the understanding of the importance of the buoyancy forces with respect to the surface tension forces finds application in the prediction of the performances of thermal devices for both ground and space applications as Capillary Pumped Loops and Heat Pipes. The presence of unsteady components in the gravitational field like vibrations or periodic components may also be responsible for fluctuations and instabilities in the flow field, and hence the heat transfer might be enhanced or reduced, compromising in this way the correct functioning of the thermal subsystem.

The present work aims to obtain a general method for predicting local and mean heat transfer coefficients for laminar annular flows, allowing arbitrary channel geometries (circular and non-circular) to be treated. In particular, in the numerical model developed in the presented study, a method based on a curvilinear coordinate system has been developed and implemented including the effects of surface tension, axial shear stresses due to the relative velocity of vapor and liquid phases, unsteady contributions in the momentum and mass conservation equations, three dimensional gravity field, disjoining pressure and the interfacial resistance phenomena, thus allowing the model to be scaled down to ultra micro-channel sizes (down to $10\mu\text{m}$). The thermal conduction in the wall can also be accounted for, and the effects of different wall boundary conditions are investigated. The objective is to provide a further insight in the physical understanding of these systems, allowing optimized solutions to be obtained and possibly providing a consistent engineering tool for the design of the next future generation of ultra-compact heat exchangers. Importantly, the new numerical model will be compared and validated versus published experimental results.

This thesis is organized in the following Chapters:

- Chapter 1: Introduction
- Chapter 2: State of the art on condensation heat transfer
- Chapter 3: Description of the mathematical model
- Chapter 4: Dimensional analysis of the problem and theoretical investigation
- Chapter 5: Numerical and experimental validation of the model
- Chapter 6: Steady state and unsteady simulation results
- Chapter 7: Conclusion

Chapter 2

State of The Art on Condensation Heat Transfer

Microscale condensation finds applications in compact heat exchangers, heat pipes for electronic equipment, potentially in spacecraft and aircraft avionics thermal control, in automotive condensers, in residential air conditioning and in refrigeration applications. In addition to these applications, two-phase flow in microchannels is becoming important in a wide variety of other fields, such as chemical, pharmaceutical and biomedical. Although microscale condensation is already used in some of these applications, a fundamental understanding on this subject has yet to be reached. An overview of the major experimental studies, prediction methods, numerical and theoretical studies is presented in this chapter.

2.1 Condensation Inside Tubes

Condensation is the change of the physical state of aggregation of matter from a vapor phase into a liquid phase. Intube condensation is the heat transfer process which occurs inside a channel: depending on the conditions, the fluid entering the channel might have a thermodynamic vapor quality which is higher than 1 (superheated condition), equal to 1 (saturated condition) or below 1. The condensation involves a heat transfer process which occurs from the condensing fluid to a cold element. Four basic types of condensation are usually identified: *drop-wise* condensation, *film-wise* condensation, *direct contact* condensation and *homogeneous* condensation.

A detailed description of each of them is presented by Thome [1]: in drop-wise condensation, the drops of liquid form from the vapor on a solid surface at nucleation sites and the drops remain separate while growing until they are carried away by an external force (for instance gravity or vapor shear); in film-wise condensation, the surface is completely wetted by the condensate and a continuous film covers the wall and thus the condensation process occurs at the liquid-vapor interface; in direct contact condensation, the vapor condenses directly on the (liquid) coolant

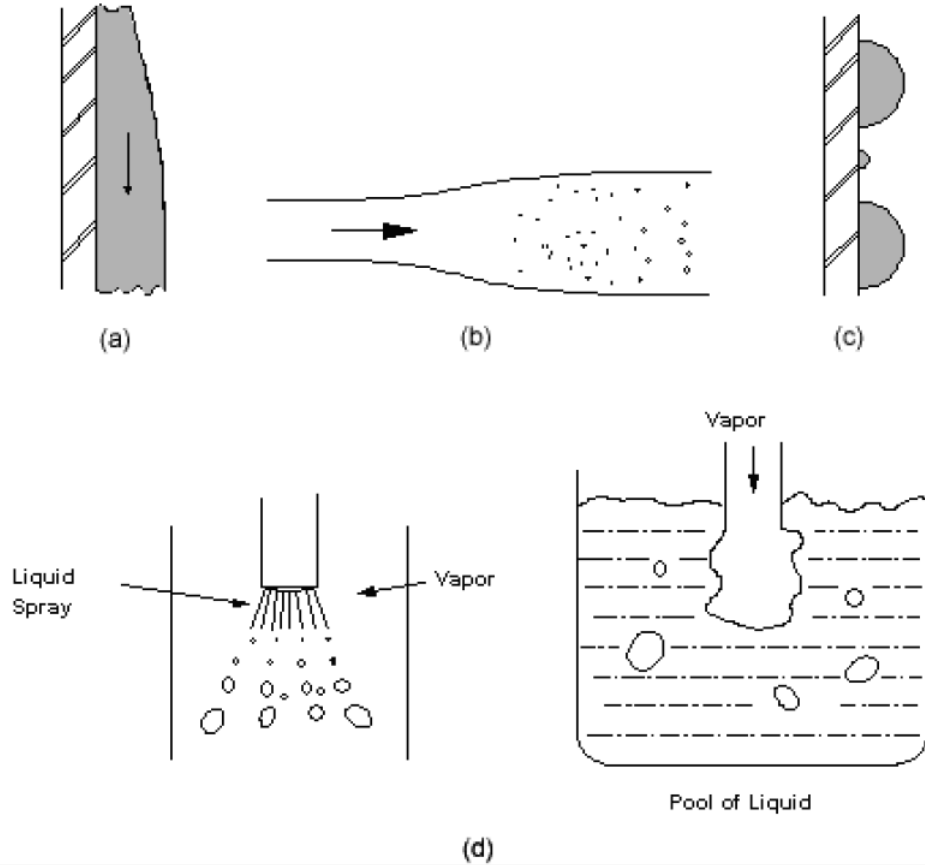


Figure 2.1: Condensation modes: (a) Film-wise condensation. (b) Homogeneous condensation. (c) Dropwise condensation. (d) Direct contact condensation. Illustration from Thome [1].

surface, which is injected directly into the vapor volume; finally, in homogeneous condensation, the liquid phase forms directly from supersaturated or saturated vapor, away from any surfaces.

A graphical description of these mechanisms is shown in Fig. (2.1). Among these condensation modes, film-wise condensation is the only process which is of industrial interest, except in particular occasions. Thus, the prediction of the *heat transfer performance* of intube condensation, which is dominated by the film-wise condensation process, is of paramount importance.

Heat transfer can be quantified by the *Nusselt* number, a dimensionless group which was identified by Wilhelm Nusselt who did the dimensional analysis of the heat convection problem before he had access to the Buckingham and Reyleight's work. He also proposed the first widely accepted model to predict convective heat transfer during film condensation [14]. The Nusselt number is defined by the following expression:

$$\text{Nu} = \frac{\alpha_c L}{k} \quad (2.1)$$

where α_c is the heat transfer coefficient, L is a characteristic length and k is the thermal conductivity. For intube condensation, the characteristic length L is commonly assumed equal to the hydraulic diameter D_h of the channel. However the more recent model of El Hajal et

al. [15] instead models film condensation as a film flow, and hence uses the local film thickness more correctly as the characteristic dimension. Several methods for predicting the Nusselt number have been developed in the last years in order to predict the condensation heat transfer inside convectional channels. The principal methods in literature are mentioned in the following paragraphs.

Akers' correlation

Within the several methods that have been proposed for gravity-controlled and shear-controlled condensation inside horizontal tubes, the approach of Akers et al. [16] for predicting intube condensation relies only on an equivalent tubular Reynolds number defined as:

$$\text{Re}_1 = \frac{G_e D_h}{\mu_l} \quad (2.2)$$

where the equivalent mass velocity G_e is given by the following expression in terms of the actual mass velocity G :

$$G_e = G \left[(1 - X) + X \left(\frac{\rho_l}{\rho_v} \right) \right] \quad (2.3)$$

The local heat transfer coefficient α_c is given by the following expression:

$$\frac{\alpha_c D_h}{k_l} = C \text{Re}_1^n \text{Pr}_1^{\frac{1}{3}} \quad (2.4)$$

where the values for the constants C and n are the following: if $\text{Re}_1 > 50000$ then $C = 0.0265$ and $n = 0.8$, otherwise $C = 5.03$ and $n = 1/3$. The prediction method, although very successful in the last decades, gives a discontinuity in the heat transfer coefficient at the switch in the methods when passing through the value of $\text{Re}_1 = 50000$, which is not observed experimentally.

Shah's correlation

Another widely quoted correlation has been presented by Shah [17]. Results from many refrigerants condensing in horizontal, vertical and inclined pipes with diameters from 7 mm to 40 mm have been included in the correlation. The fluids were condensed at reduced pressures p_r ranging from 0.002 to 0.44 for a wide range of mass fluxes and heat fluxes. The correlation for the heat transfer coefficient α_c is as follows:

$$\alpha_c = \alpha_l \left[(1 - X)^{0.8} + \frac{3.8 X^{0.76} (1 - X)^{0.04}}{p_r^{0.38}} \right] \quad (2.5)$$

where α_l is the heat transfer coefficient assuming all mass flowing as liquid and it is based on

the Dittus-Boelter equation [14, 18]:

$$\frac{\alpha_l D_h}{k_l} = 0.023 \text{Re}_{D_h}^{\frac{4}{5}} \text{Pr}_l^{0.3} \quad (2.6)$$

El Hajal, Thome and Cavallini's correlation

El Hajal et al. [15] and Thome et al. [19] developed a condensation prediction method for horizontal tubes, based on a physically based approach of heat transfer in different flow patterns (annular, intermittent, stratified and mist flow), where a new void fraction model was used to determine the flow pattern. The annular flow method contains only three empirical parameters which have been determined from a database of 15 different fluids at different vapor fractions, in tubes with diameters ranging from 3.1 to 21.4 mm, mass fluxes from 22 to 1022 kg/(m²s) and reduced pressures from 0.02 to 0.8. This new condensation model assumes that two types of heat transfer mechanisms occur within the tube: convective condensation and film condensation. For annular, intermittent and mist flow, the following correlation for the convective condensation heat transfer coefficient α_c was proposed:

$$\alpha_c = c \text{Re}_l^n \text{Pr}_l^m \frac{k_l}{\delta} f_i \quad (2.7)$$

where f_i is a roughness factor and c , m and n are the only three empirically determined coefficients which gave the best fit values: $c = 0.003$, $m = 0.5$ and $n = 0.74$. The roughness factor is given by:

$$f_i = 1 + \left(\frac{u_v}{u_l} \right)^{\frac{1}{2}} \left(\frac{(\rho_l - \rho_v) g \delta^2}{\sigma} \right)^{\frac{1}{4}} \quad (2.8)$$

where u_v and u_l are the phase velocities of the vapor and liquid respectively. These can be obtained from the following relationships:

$$u_v = \frac{GX}{\rho_v \varepsilon} \quad (2.9)$$

$$u_l = \frac{G(1-X)}{\rho_l(1-\varepsilon)} \quad (2.10)$$

where ε denotes the void fraction. The Reynolds number Re_l is based on the film thickness δ and it is defined as:

$$\text{Re}_l = \frac{4G(1-X)\delta}{\mu_l(1-\varepsilon)} \quad (2.11)$$

For annular, intermittent and mist flow, the film thickness can be calculated as follows:

$$\delta = \frac{D_h}{2} (1 - \sqrt{\varepsilon}) \quad (2.12)$$

The following expression was obtained in order to determine the void fractions:

$$\varepsilon = \frac{\varepsilon_h - \varepsilon_{ra}}{\ln(\varepsilon_h/\varepsilon_{ra})} \quad (2.13)$$

which was called the logarithmic mean void fraction. The homogeneous void fraction ε_h can be calculated via the following expression [1]:

$$\varepsilon_h = \left[1 + \left(\frac{1-X}{X} \right) \left(\frac{\rho_v}{\rho_l} \right) \right]^{-1} \quad (2.14)$$

For non-homogeneous flows, the following expression is assumed:

$$\varepsilon_{ra} = \frac{X}{\rho_v} \left([1 + 0.12(1-X)] \left[\frac{X}{\rho_v} + \frac{1-X}{\rho_l} \right] + \frac{1.18(1-X)[g\sigma(\rho_l - \rho_v)]^{0.25}}{G\rho_l^{0.5}} \right)^{-1} \quad (2.15)$$

A detailed description of the method is given in [1].

2.2 Condensation Heat Transfer in Mini and Microchannels

Numerous experimental studies on heat transfer and pressure drop for intube condensation exist nowadays for conventional channels. Nevertheless only a few experimental and theoretical studies have been carried out in the microchannel size range, due to the complexity of the problem and the stronger limitations existing in terms of accuracy and reliability of the experiments. In particular, the fundamental understanding of the mechanisms occurring at micro and nanoscale, such as capillary condensation, is not yet fully understood. It is believed that the surface tension force is the principal physical mechanism which is responsible for the *transition* from macro/mini to microchannel condensation. This transition refers to a boundary length scale (typically identified by the hydraulic diameter) below which the standard and commonly used macro channel methods for predicting pressure drop and heat transfer do not reproduce correctly the trends which are experimentally obtained. This transition, which may also be associated with a progressive extension of the laminar flow regime, is primarily identified by significant increases both in heat transfer coefficients and frictional pressure drop. Furthermore, different and new flow patterns and flow regimes which are not present in conventional channels have been found and analyzed in recent studies.

The major experimental studies, empirical models and theoretical investigations undertaken in the field of flow condensation in mini and microchannels are reported in the following paragraphs.

2.2.1 Experimental Studies and Empirical Methods

Condensation heat transfer in microchannels has received increasing attention only in recent years with particular emphasis on how to enhance heat transfer to enable even more compact

heat exchangers. Various definitions of the difference between micro, mini and convective channels exist in the literature, depending on which type of phenomenological aspect is analyzed, for instance the relative importance of different forces (gravity to inertia, gravity to surface tension, shear to inertia forces, etc.) or the progressively variation of some physical behavior. For many commonly used refrigerants like R-134a the transition to the *microchannel* region is identified for a hydraulic diameter of $\approx 200 \mu\text{m}$ but for different fluids like ammonia or water the transition can occur for larger length scales. The *transition region*, which can be identified for many refrigerants in approximately the hydraulic diameter range of 0.2 – 3 mm, has been investigated recently by several authors, while only few studies exist for the smaller channels.

Garimella [2] has presented an overview of the visualization studies for the development of pressure drop and heat transfer models for mini and microchannels during condensation of the commonly used refrigerant R-134a. Both circular and non-circular channels were investigated in this work. Part of the work is based on the previous research conducted by Garimella et al. [20]. A detailed explanation of the pressure drop calculation in circular minichannels is given in [21]. The range of hydraulic diameters investigated experimentally was between 0.5 mm and 4.91 mm for the circular channels and between 0.424 mm and 0.839 mm for non-circular channel shapes. The investigated geometries are shown in Fig. (2.2). The following main four flow patterns have been identified: *annular*, *wavy*, *intermittent* and *dispersed* flows. With the decrease of the hydraulic diameter, the wavy flow is increasingly replaced by the annular flow regime and wavy flow disappears in tubes of channels of approximately 1 mm and smaller. The description of the two-phase flow regimes reported by the author is presented in Fig. (2.3).

Mederic et al. [22] studied the convective condensation in tubes of various dimensions providing visual data on the condensation flow patterns for three tubes with inner diameters of 10, 1.1 and

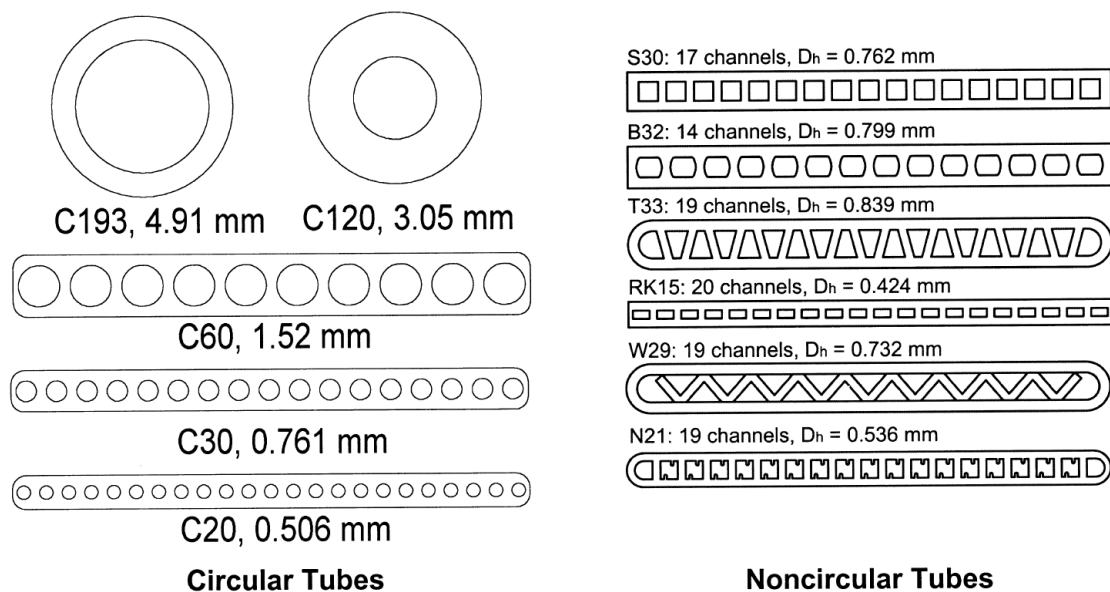


Figure 2.2: Geometries investigated by Garimella et al [2]

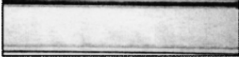
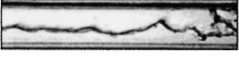

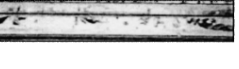


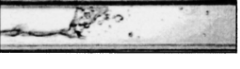




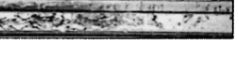


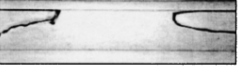

| | | FLOW REGIMES | | | |
|---|---|--|--|---|-----------|
| | | Annular | Wavy | Intermittent | Dispersed |
| Flow Patterns |  |  |  |  | |
| | Mist Flow | Discrete Wave (0) | Slug Flow | Bubbly Flow | |
| |  |  |  |  | |
| | Annular Ring | Discrete Wave (1) | Slug Flow | Bubbly Flow | |
| |  |  |  |  | |
| Wave Ring | Discrete Wave (2) | Plug Flow | Bubbly Flow | | |
|  |  |  | | | |
| Wave Packet | Disperse Wave (3) | Plug Flow | | | |
|  | | | | | |
| Annular Film | | | | | |

Figure 2.3: Description of two-phase flow regimes reported by Garimella [2]

0.56 mm. In order to characterize the capillary length scale, the following relation was proposed:

$$l_c = \left(\frac{\sigma}{g(\rho_l - \rho_v)} \right)^{\frac{1}{2}} \quad (2.16)$$

In the experiment, the capillary length scale is equal to 1.25 mm and thus three different cases have been analyzed: if the diameter of the channel is much smaller than l_c then the capillary force prevails; if $l_c \gg D_h$ then gravity is dominant; otherwise the two forces compete in determining the behavior of the flow. The instabilities occurring in the condensing flow have been analyzed with particular interest to the periodic formation of liquid slug at the end of the annular flow region.

Bandhauer's model

Experimental results of heat transfer coefficients for circular channels with hydraulic diameters of 1.52 mm, 0.761 mm and 0.506 mm have been presented by Bandhauer et al. [23] for the refrigerant R-134a. The detailed description of the data analysis procedure is reported by Garimella et al. [24]. Measurements have been conducted for a mass flux range between 150 and 750 kg/(m²s). Based on these results, the following empirical model for predicting heat transfer coefficients in circular mini-channels has been proposed. The Bandhauer model, which is based on the pressure drop model developed by Agarwal et al. [25], defines at first the following

turbulent parameters:

$$u^+ = \frac{u}{u^*} \quad (2.17)$$

$$R^+ = \frac{\rho_l R u^*}{\mu_l} \quad (2.18)$$

where:

$$u^* = \sqrt{\frac{\tau_i}{\rho_l}} \quad (2.19)$$

and R is the radius of the channel, thus $R = 0.5D_h$. The turbulent dimensionless temperature is defined as follows:

$$T^+ = \frac{\rho_l C_{p,l} u^*}{\dot{q}} \quad (2.20)$$

where \dot{q} is the heat flux. The heat transfer coefficient is given by the following expression:

$$h = \frac{\rho_l C_{p,l} u^*}{T^+} \quad (2.21)$$

The interfacial shear stress τ_i is calculated from the following expressions:

$$\tau_i = \left(\frac{\Delta p}{L} \right) \frac{D_h}{4} \quad (2.22)$$

$$\left(\frac{\Delta p}{L} \right) = \frac{1}{2} f_i \frac{G^2 X^2}{\rho_v \varepsilon^{2.5} D_h} \quad (2.23)$$

The void fraction ε is determined by:

$$\varepsilon = \left[1 + \left(\frac{1-X}{X} \right)^{0.74} \left(\frac{\rho_v}{\rho_l} \right)^{0.65} \left(\frac{\mu_l}{\mu_v} \right)^{0.13} \right]^{-1} \quad (2.24)$$

The interfacial friction factor f_i is obtained by the following expression:

$$f_i = f_l A \chi^a \text{Re}_l^b \psi^c \quad (2.25)$$

The Martinelli parameter χ is given by:

$$\chi = \left[\frac{(dp/dz)_l}{(dp/dz)_v} \right]^{\frac{1}{2}} \quad (2.26)$$

For this model the liquid-phase Reynolds is defined in terms of the annular flow area surrounding the vapor core that is occupied by the liquid phase and it is defined as follows:

$$\text{Re}_l = \frac{GD_h(1-X)}{\mu_l(1+\sqrt{\varepsilon})} \quad (2.27)$$

Similarly, the definition of the vapor-phase Reynolds number is:

$$\text{Re}_v = \frac{GD_h X}{\mu_v \sqrt{\varepsilon}} \quad (2.28)$$

The friction factor is calculated as follows: if $\text{Re}_1 < 2100$ then $A = 1.308 \cdot 10^{-3}$, $a = 0.427$, $b = 0.930$ and $c = -0.121$ and for $\text{Re}_1 > 3400$, $A = 25.64$, $a = 0.532$, $b = -0.327$ and $c = 0.021$. The friction factors required for the individual pressure drops in the Martinelli parameter are computed using $f = 64/\text{Re}$ for $\text{Re} < 2100$ and the Blasius expression $f = 0.316\text{Re}^{-0.25}$ for $\text{Re}_1 > 3400$. For the transition data, the friction factor is firstly calculated using the high and low values of the mass velocity corresponding to the laminar and turbulent boundaries and then a linear interpolation between these boundaries is then conducted. The surface tension parameter ψ is:

$$\psi = \frac{j_l \mu_l}{\sigma} \quad (2.29)$$

where:

$$j_l = \frac{G(1-X)}{\rho_l(1-\varepsilon)} \quad (2.30)$$

The turbulent dimensionless temperature T^+ is defined as follows:

- for $\text{Re}_1 < 2100$

$$T^+ = 5\text{Pr}_1 + 5\ln\left(1 + \text{Pr}_1\left(\frac{\delta^+}{5} - 1\right)\right) \quad (2.31)$$

- for $\text{Re}_1 \geq 2100$

$$T^+ = 5\text{Pr}_1 + 5\ln(5\text{Pr}_1 + 1) + \int_{30}^{\delta^+} \frac{dy^+}{\left(\frac{1}{\text{Pr}_1} - 1\right) + \frac{y^+}{5}\left(1 - \frac{y^+}{\text{R}^+}\right)} \quad (2.32)$$

The dimensionless film thickness is given by:

$$\delta^+ = \frac{\rho_l \delta u^*}{\mu_l} \quad (2.33)$$

$$\delta = (1 - \sqrt{\varepsilon}) \frac{D_h}{2} \quad (2.34)$$

The model has been optimized with the experimental data set and it is based on the turbulent analysis in the liquid film as most shear driven heat transfer models available in literature suggest [23]. The surface tension is not an important parameter in the model and therefore it is expected not to predict the heat transfer coefficient well for situations in which the capillary force becomes important.

Agarwal's model

Agarwal et al [11] evaluated the Bandhauer model for non-circular channels and found that

this model considerably underpredicted their experimental results. By the analysis of their experimental conditions, they assumed that the primary reason of this discrepancy comes from the effect of the corners which, by retaining the condensate, allow large regions of the inner perimeter of the channel to be covered by a thin layer of film, thus enhancing the heat transfer process. Although this phenomenon is due primarily to the surface tension forces, a mist-flow based empirical model was adopted by the authors, curiously without accounting for the surface tension property, assuming that the flow is dominated by the strong shear of the vapor phase which is able to entrain small droplets of liquid through the shear at the interface. The following mist flow correlation was then proposed:

$$\text{Nu} = 0.00345 \text{Re}_m^{0.9} \left(\frac{\mu_v \Delta h_{l-v}}{k_v (T_s - T_w)} \right)^{\frac{1}{3}} \quad (2.35)$$

where the mixture Reynolds number is defined as:

$$\text{Re}_m = \frac{GD_h}{\mu_m} \quad (2.36)$$

and the mixture viscosity μ_m is:

$$\mu_m = \left(\frac{X}{\mu_v} + \frac{1-X}{\mu_l} \right)^{-1} \quad (2.37)$$

The mist-flow based heat transfer coefficient is then given by:

$$\alpha = \text{Nu} \frac{k_l}{D_h} \quad (2.38)$$

Koyama's model

Koyama et al. [26] present experimental results of pressure drops and heat transfer coefficients for the condensation of refrigerant R-134a in two types of multi-port extruded tubes having eight channels of 1.11 mm hydraulic diameter and nineteen channels of 0.8 mm hydraulic diameter and rectangular shapes. By applying the pressure drop prediction method proposed by Mishima et al. [27] to the macroscale condensation model proposed by Haraguchi et al. [28], they obtained a new correlation which gave a good agreement with the experimental data. The Nusselt number is expressed as an asymptotic combination of the forced convection condensation and gravity controlled condensation terms:

$$\text{Nu} = (\text{Nu}_F^2 + \text{Nu}_B^2)^{\frac{1}{2}} \quad (2.39)$$

The forced convection term Nu_F is given by:

$$\text{Nu}_F = 0.0152 (1 + 0.6 \text{Pr}_1^{0.8}) \left(\frac{\Phi_v}{\chi_{tt}} \right) \text{Re}_1^{0.77} \quad (2.40)$$

where the liquid Reynolds number is defined as:

$$\text{Re}_l = \frac{G(1-X)D_h}{\mu_l} \quad (2.41)$$

The effect of the diameter D_h is considered as:

$$\Phi_v^2 = 1 + 21(1 - e^{-0.319D_h})\chi_{tt} + \chi_{tt}^2 \quad (2.42)$$

The Lockhart-Martinelli parameter χ_{tt} is defined as:

$$\chi_{tt} = \left(\frac{1-X}{X}\right)^{0.9} \left(\frac{\rho_v}{\rho_l}\right)^{0.5} \left(\frac{\mu_l}{\mu_v}\right)^{0.1} \quad (2.43)$$

The gravity controlled convection condensation term Nu_B is given by:

$$\text{Nu}_B = 0.725 H(\varepsilon) \left(\frac{\text{GaPr}_l}{\text{Ja}}\right)^{\frac{1}{4}} \quad (2.44)$$

where:

$$H(\varepsilon) = \varepsilon + \left[10(1-\varepsilon)^{0.1} - 1 + 1.7 \cdot \text{Re}_{l0}\right] \sqrt{\varepsilon} (1 - \sqrt{\varepsilon}) \quad (2.45)$$

$$\text{Ga} = \frac{g\rho_l^2 D_h^3}{\mu_l^2} \quad (2.46)$$

$$\text{Ja} = \frac{C_{p,l}(T_s - T_{w,i})}{\Delta h_{l-v}} \quad (2.47)$$

The liquid-only Reynolds number is $\text{Re}_{l0} = GD_h/\mu_l$. The void fraction ε is calculated as:

$$\varepsilon = \left[1 + \frac{\rho_v}{\rho_l} \left(\frac{1-X}{X}\right) \left(0.4 + 0.6 \sqrt{\frac{\frac{\rho_v}{\rho_l} + 0.4\frac{1-X}{X}}{1 + 0.4\frac{1-X}{X}}}\right)\right]^{-1} \quad (2.48)$$

Cavallini's model

Cavallini et al. [29] proposed a new heat transfer model considering the entrainment of the liquid phase in the vapor core. As in the Bandhauer's model, the local heat transfer coefficient is a function of the shear stress and the dimensionless temperature T^+ :

$$h = \frac{\rho_l C_{p,l}}{T^+} \sqrt{\frac{\tau}{\rho_l}} \quad (2.49)$$

The dimensionless temperature is calculated as follows:

- if $\delta^+ \leq 5$ then:

$$T^+ = \delta^+ \text{Pr}_l \quad (2.50)$$

- if $5 < \delta^+ < 30$ then:

$$T^+ = 5\{\text{Pr}_1 + \ln [1 + \text{Pr}_1 (\delta^+/5 - 1)]\} \quad (2.51)$$

- if $\delta^+ \geq 30$ then:

$$T^+ = 5\{\text{Pr}_1 + \ln(1 + 5\text{Pr}_1) + 0.495\ln(\delta^+/30)\} \quad (2.52)$$

The definition of the dimensionless film thickness is:

- for $\text{Re}_1 \leq 1145$ then:

$$\delta^+ = (\text{Re}_1/2)^{0.5} \quad (2.53)$$

- for $\text{Re}_1 > 1145$ then:

$$\delta^+ = 0.0504\text{Re}_1^{7/8} \quad (2.54)$$

where the liquid Reynolds number is defined as follows:

$$\text{Re}_1 = \frac{G(1-X)(1-E)D_h}{\mu_l} \quad (2.55)$$

The entrainment fraction E is calculated as follows:

$$E = \min \left[0.95, 0.015 + 0.44\log_{10} \left(10^4 \left(\frac{\rho_{gc}}{\rho_l} \right) \left(\frac{\mu_l j_v}{\sigma} \right)^2 \right) \right] \quad (2.56)$$

where

$$\rho_{gc} = \rho_v \left(1 + \frac{E(1-X)}{X} \right) \quad (2.57)$$

$$j_v = \frac{GX}{\rho_v} \quad (2.58)$$

The frictional pressure gradient, based on the previous work, and more recently reviewed and experimentally validated by Cavallini et al. [30], is calculated based on the following expression:

$$\left(\frac{dp}{dz} \right)_f = 2\Phi_{LO}^2 f_{LO} \frac{G^2}{\rho_l D_h} \quad (2.59)$$

where:

$$\Phi_{LO}^2 = Z + 3.595FH(1-E)^W W \quad (2.60)$$

$$Z = (1-X)^2 + X^2 \left(\frac{\rho_l}{\rho_v} \right) \left(\frac{\mu_v}{\mu_l} \right)^{0.2} \quad (2.61)$$

$$F = X^{0.9525} (1-X)^{0.414} \quad (2.62)$$

$$H = \frac{\rho_l}{\rho_v}^{1.132} \frac{\mu_v}{\mu_l}^{0.44} \left(1 - \frac{\mu_v}{\mu_l} \right)^{3.542} \quad (2.63)$$

The liquid-only friction coefficient f_{LO} is obtained for any Re_{LO} as follows:

$$f_{LO} = 0.046 \left(\frac{GD_h}{\mu_l} \right)^{-0.2} \quad (2.64)$$

Finally, the expression for the shear stress τ is obtained via the following expression:

$$\tau = \frac{D_h}{4} \left(\frac{dp}{dz} \right)_f \quad (2.65)$$

This annular and mist flow model is based on the analogy of heat and momentum transfer and it has been successfully applied to minichannels for the R-134a, R-410a and R-236ea. More recently, Matkovic et al. [31] investigated the condensation heat transfer coefficient inside a 0.96 mm diameter circular minichannel. The test results did not show discrepancies with the trends expected for macroscale tubes, except for a few data at low mass velocities and low vapor quality where the results were found to be slightly dependent on the saturation to wall temperature difference.

Other Recent Experimental Studies

Condensation heat transfer and pressure drop for methane and binary methane fluids in small circular channels have been recently published by Marak [32]. Both single and two-phase flow experiments have been investigated for a variety of mass fluxes, vapor qualities and heat fluxes for hydraulic diameters of 1 mm, 0.5 mm and 0.25 mm. Although too much experimental uncertainty exists for the results of the 0.5 mm and 0.25 mm diameters, it is nevertheless stated that for these two cases the measured heat transfer coefficients seems systematically higher than most of the existing models predict. The presented trends show that the heat transfer coefficient increases with increasing mass flux, higher vapor fraction and it generally decreases for increasing saturation pressure. Under these conditions it is found that the heat transfer coefficient is not significantly affected by the heat flux. Higher heat transfer coefficients are also obtained for smaller channels. The condensation heat transfer models from Thome [19], Akers [16] and Bandhauer [23] can be used to predict the results for the 1 mm tube reasonably well. The model from Shah [17] appears to be the most precise model for the 0.5 mm tube, however it completely fails to predict the 1 mm results. None of these models can predict the results from both the 1 mm and 0.5 mm tubes with reasonable accuracy. The model from Cavallini et al. [29] is the closest.

The characteristics of condensation heat transfer and pressure drop for R-134a in a horizontal small circular pipe ($D_h = 2$ mm) have been investigated experimentally by Yan et al. [8]. When compared with the data for a larger pipe ($D_h = 8$ mm), the measured heat transfer coefficients averaging over the entire quality range tested in this work for the small pipe is about 10 % higher. It was found that the condensation heat transfer coefficient is higher at a lower heat fluxes, at a lower saturation temperature, at a higher vapor qualities and at higher mass

fluxes.

A comparison between the heat transfer coefficients of circular and square minichannels is presented by Shin and Kim [9,10]. In their work, single circular channels (having a hydraulic diameter of 0.493, 0.691, and 1.067 mm) and square channels (with a hydraulic diameter of 0.494, 0.658, and 0.972 mm) were tested and compared for mass fluxes of 100, 200, 400, and 600 kg/(m²s) and for heat fluxes of 5 to 20 kW/m². Under the tested conditions, contrary to the results from Yan et al. [8], small effects of the heat flux have been found. The authors suggest that the effects of surface tension are evident at low mass fluxes, increasing the heat transfer performance of the square channel compared to the circular one, but they become less effective at higher mass fluxes as the shear becomes dominant in the condensation process. Clear enhancements of the heat transfer coefficient are obtained as the hydraulic diameter decreases. The condensation heat transfer coefficients have been compared with several empirical models: it is found that all the correlations under predicted their experimental results at low mass fluxes, while several of them predicted well for higher values.

Several authors have evaluated the condensation heat transfer characteristics in flattened or internally finned tubes. Chang et al [33] have determined the heat transfer performances for four flat tubes and one micro-fin tube with mass velocities up to 100 kg/(m²s) which is applicable to small window units and automobile air conditioning systems. It has been found that Shah's correlation can be used to predict the results only for plain aluminum flat tubes, although under predicting the test results in the high quality region. The heat transfer coefficient increases with increasing mass velocity and, for plain flat tubes, with smaller hydraulic diameters. For internally grooved tubes it is found that the heat transfer coefficient is always higher than for plain tubes. Webb et al. [34] analyzed the effects of the hydraulic diameter on condensation of R-134a in multi-port flat extruded aluminum tubes. Both the frictional pressure gradient and the heat transfer coefficients have been found to increase as the hydraulic diameter is decreased. Also in this case, the authors suggest that the surface tension may have a positive influence on the heat transfer coefficient, in particular for the micro-grooved tubes.

Recently, Yun et al. [35] investigated experimentally the condensation heat transfer characteristics of R-134a in two 13.27 mm integral fin-tubes made of stainless steel, having a fin height of 1.19 mm and two different fin densities. Enhancement factors of $\simeq 3$ or more were found. The interesting aspect of this work is that among the existing models, the Nozu and Honda [3] model, which considers the condensate retention angle, the geometry of the fin and its thermal conductivity, showed the smallest deviation between the predicted and experimental values. The schematic for the development of the model is represented in Fig. (2.4). The principle of the mechanism which allows higher heat transfer coefficients to be reached is the following: the condensate film thickness at the top of the groove (or fin) is reduced thanks to the net condensing flow that is pulled towards the region of low pressure, due to the surface tension and the local curvature in the meniscus flooded region. Although the accumulation of the condensate reduces the heat transfer in the flooded region, the net heat transfer results increased several

times, depending on the fluid properties and local saturation to wall temperature difference. This mechanism is thought to be the primary reason for which non-circular shaped channels (square, rectangular, triangular, flattened, etc ...) lead to significant increases in performances in particular at low mass fluxes, namely where the vapor shear is less effective compared to the capillarity effects.

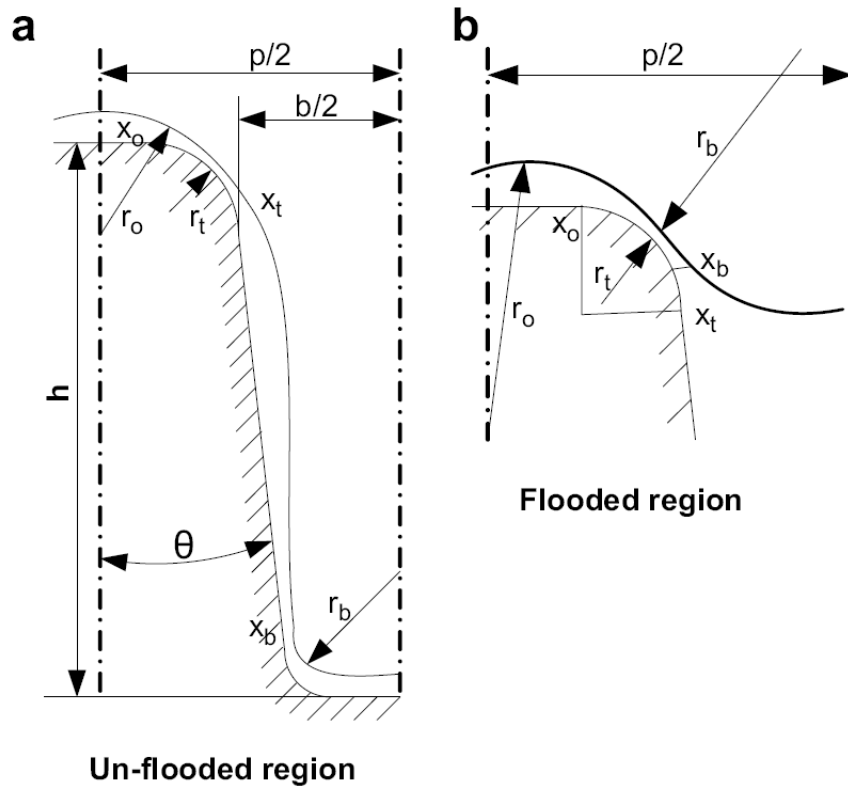


Figure 2.4: Physical model and coordinates for the Honda and Nozu model [3]. (a) Un-flooded region and (b) flooded region

Agarwal et al. [4] have analyzed condensation pressure drops and heat transfer coefficients in square and rectangular channels with $100 < D_h < 200 \mu\text{m}$. The channels were fabricated on a copper substrate by electroforming copper onto a mask patterned by X-ray lithography, and sealed by diffusion bonding. The test section assembly is shown in Fig. (2.5). Water at a high flow rate was used as the test section coolant to ensure that the condensation side was the governing thermal resistance. Heat transfer coefficients were measured for $200 < G < 800 \text{ kg}/(\text{m}^2\text{s})$ at several different saturation temperatures for R-134a. Conjugate heat transfer analyses were conducted in conjunction with local pressure drop profiles to obtain accurate driving temperature differences and heat transfer coefficients. Based on the existing flow transition criteria in the literature the authors surmised that the flow was either intermittent or annular under the tested conditions. Although affected by the experimental and post-processing modeling errors they described, the data show that both frictional pressure drop and heat transfer coefficients increase when decreasing the saturation temperature and increasing the mass flux. It is also

highlighted that all the existing models under predicted the heat transfer results obtained in this study.

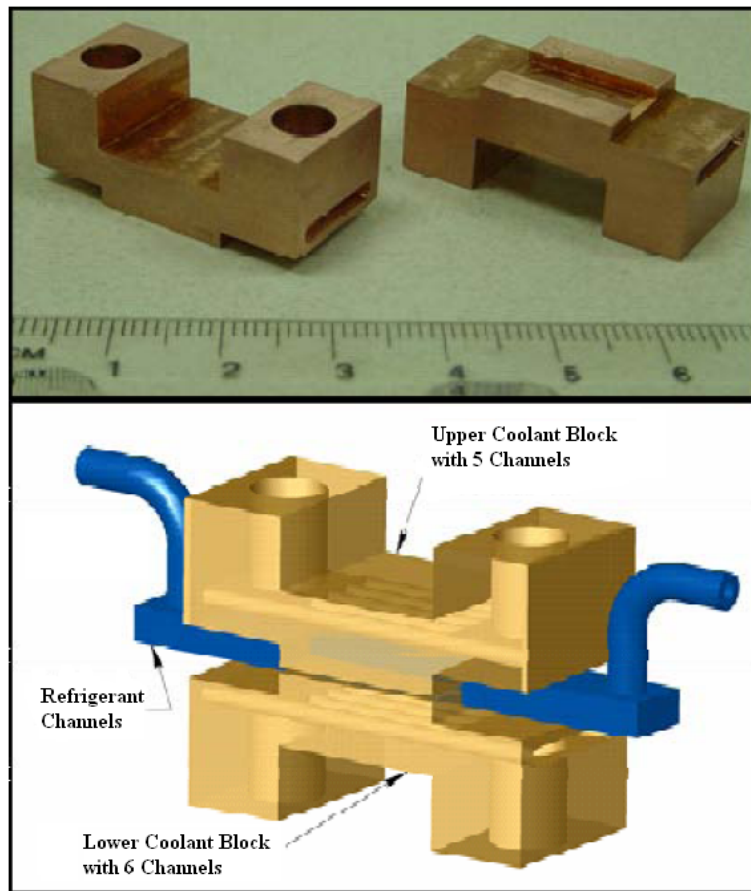


Figure 2.5: Coolant channels, test section subassembly tested by [4]

2.2.2 Theoretical and Numerical Investigations

Condensation in a two-dimensional capillary groove has been investigated by Zhang and Faghri [36] who developed a numerical model based on the Volume-Of-Fluid method. The effects of temperature drop, contact angle, surface tension and fin thickness on the condensation heat transfer have been investigated. The results show that the convection in the laminar liquid flow is not significant as the majority of the heat transfer is transferred through the condensation process in the fin's top surface. The fin was assumed to be isothermal and a uniform temperature boundary condition was adopted. It is found that the heat flux increases when increasing the saturation to wall temperature difference, but the heat transfer coefficient decreases since the liquid film thickens. An increase of surface tension leads to thinner films and higher heat fluxes, for the same conditions.

One of the earliest theoretical models developed in order to investigate film condensation in

mini-channels is the one by Zhao and Liao [12] in 2002. In this analytical model for the co-current vapor flow with the thin liquid film flow on the sidewall, the condensate flow in the corners and the vapor core flow in the center are modeled and the capillary forces are taken into account considering the two-dimensional liquid vapor curvature in the section of the vertical equilateral triangular channel. The axial variation of the average heat transfer coefficient of condensing steam was found to be substantially higher than that inside a round tube having the same hydraulic diameter, in particular in the entry region. Although several approximations were assumed in the model, the qualitative effects of the channel size, the wall subcooling, the saturation temperature and the mass flux could be analyzed. A similar analysis has been conducted by Chen et al. [37] who also included the effects of the contact angle, and thus the model is applicable for partially wetting fluids. It is found that the condensation length depends on the contact angle, the heat flux and the inlet steam pressure.

Wang and Rose [13] presented a theoretical model to predict film condensation heat transfer in horizontal microchannels. The model is based on a fundamental analysis assuming laminar condensate flow on the channel walls taking into account the effects of surface tension, vapor shear stress and gravity. Following the same theoretical approach as in Zhao and Liao's work, Wang and Rose [5, 38] presented simulations of film condensation heat transfer for R-134a, R-22 and R-410a vapor flow in horizontal square, circular, rectangular and equilateral triangular microchannels. Some of the assumptions used for their model were: (a) the flow in the condensate film is laminar, (b) the wall temperature is uniform and constant, (c) the gravity is constant in magnitude and orientation, (d) the thermal inertia of the condensate is negligible, (e) the fluid properties are constant in space and time and (f) the momentum equations have been simplified without including the momentum flux contributions. In the model, the two-dimensional curvature of the liquid-vapor interface was taken into account as in [36] and thus the axial contribution was neglected. The liquid domain was divided into different sectors at each location: a corner region where the condensates tends to accumulate due to the capillary effects and a thin film region. A schematic of the physical model and coordinate system is shown in figure Fig. (2.6). One important phenomenon that can be studied through their model is the drainage effect induced by the surface tension which tends to pull the liquid towards the corners, thus creating thinner films and more effective condensation surfaces in these regions: this phenomenon is know also as the 'Gregorig' effect, based on the first theoretical and analytical investigations done by Gregorig [39] in 1954. The model includes also the *interfacial resistance* phenomenon, that is, a finite temperature jump which occurs at the liquid-vapor interface when a net mass transfer is flowing from one phase to the other. Wang and Rose [40] analyze this effect showing that the interphase matter transfer has a significant effect on the heat transfer of steam on low-finned tubes with a reduction of the local heat transfer coefficient up to a factor of 2. Instead, the simulation results presented for different channel shapes for various refrigerants did not show any relevant dependency on the interface resistance, i.e. at the simulated conditions (1 mm hydraulic diameter range) it can be ignored. The results indicated a significant heat-transfer enhancement by surface tension towards the channel entrance. For

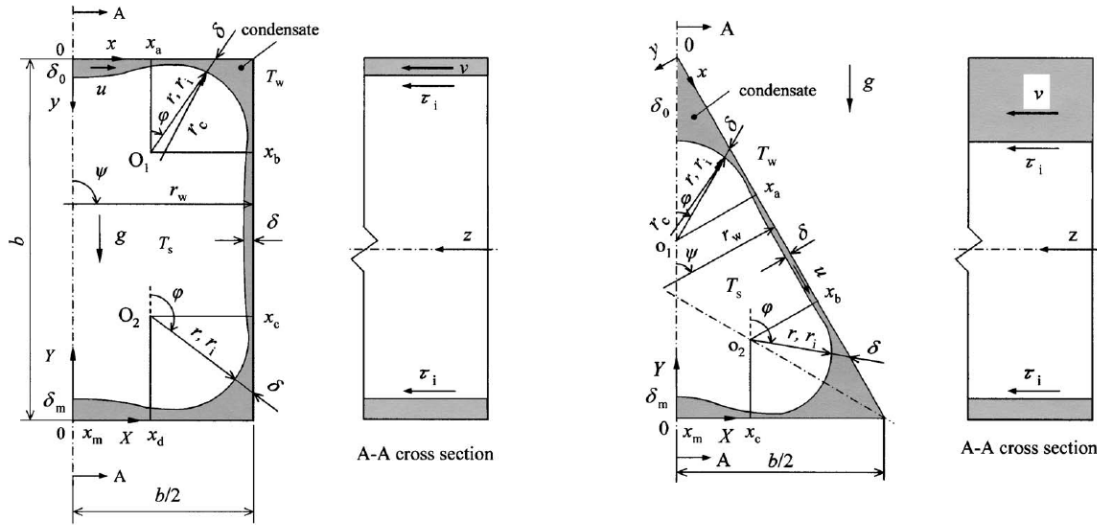


Figure 2.6: Illustration from Wang [5]: physical model and coordinates for horizontal microchannels.

smaller channels the initial enhancement is higher but falls off after a shorter distance along the channel; higher mass velocities result in an increased length of enhanced heat transfer, while no significant effect of the mass flux was found. This may be due to two main reasons: i) in the calculation of the liquid-vapor shear the absolute velocity of the liquid and not the relative velocity between the two phases at the interface is employed; ii) although the model is developed for laminar conditions, for the liquid phase most of the presented results fall in the turbulent region thus it can not capture the convective contribution which becomes more and more important as the liquid (local) Reynolds number increases.

More recently, Wu et al. [41] developed a numerical work to simulate steady state annular film condensation for steam in a rectangular microchannel, with hydraulic diameters of 300, 200 and 100 μm . An imposed uniform heat flux is assumed over the inner perimeter of the channel. The condensate flow, similar to Wang and Rose, is divided into two regions: the thin-film region and the meniscus region. The results indicate that, with the development of condensation, the condensate in the thin-film assumes a convex profile shape at the side wall. The average heat transfer coefficient and the wall temperature are obtained and it is found that the perimeter-averaged heat transfer coefficient decreases strongly as the vapor quality decreases. The disjoining pressure is not taken into account in the computation and the temperature profile is assumed linear along the thin film. Heat transfer coefficients on the order of 1 MW/(m²K) are obtained for the smaller simulated channels with saturated steam at $p_s = 2$ bar and a constant heat flux of 30 W/cm². Without accounting for the thermal conductivity of the channel wall, the simulation results give extremely high wall temperature gradients around the perimeter, leading even to a 6 K temperature difference over a distance of 40 μm , which would result in a quite significant wall conduction effects (neglected in their model) even considering a low thermal conductivity material like stainless steel.

The problem of vapor condensation on curvilinear isothermal fins has been studied by various authors. Already mentioned is the model by Nozu and Honda (1986) [3]; other theoretical models have been developed by Adamek (1981) [42] and Adamek and Webb (1990) [43]. Kabov et al. [44] have presented a theoretical work to predict the two-dimensional distribution of the thin condensate layer which deposits on a optimized non-isothermal fin made of copper. In particular, this work is focused on the effects of the capillary forces and it is aimed also to evaluate the effects of the *disjoining pressure*, an important physical phenomenon which is due to the mutual interaction between the liquid and wall molecules. Its effects become important when the characteristic film becomes very thin and it determines its dynamic stability and, consequently, the type of condensation (drop-wise or film wise). In their model, saturated steam and a perfectly wetting condition are assumed: the expression of the disjoining pressure is: $\Delta p_d = A/\delta^3$ with $A < 0$ thus reproducing the attractive nature of the liquid-to-wall forces. Local condensation heat transfer coefficients are shown as a function of the curvilinear coordinate that covers the entire perimeter of the fin. It is shown that very high heat transfer coefficients on the order of $50 \text{ kW}/(\text{m}^2\text{K})$ may be achieved by exploiting the capillarity effect and it is argued that even higher heat transfer coefficients may be reached primarily by reducing the size of the fin (the calculations refer to a fin height of approximately 2 mm). The theoretical investigation is aimed at understanding the basic mechanism of capillary-driven condensation which is of high importance in the design and optimization of Capillary Pumped Loops and Heat Pipes (see Section 2.3).

Condensation in capillary-driven two-phase flow loops has been investigated by Miscevic et al. [45] who studied the behavior of a prototype of a small capillary pumped loop (CPL). In this study, a channel having a hydraulic diameter of $560 \mu\text{m}$ and n-pentane fluid have been tested. The mass flux was very low, in the range of $3 - 15 \text{ kg}/(\text{m}^2\text{s})$, and the results showed the existence of two main flow regimes in the condenser: at low flow rates, the condensate takes the shape of an extended meniscus (an elongated stationary bubble); at higher flow rates, the meniscus brakes up producing a train of bubbles and strongly reducing by a factor of 4 the mean heat transfer coefficient, compared to the previous flow pattern. Since the condenser in the capillary loop plays an important role, it is important to understand the basic mechanism that leads to transition from one flow pattern to the other, especially because the process may become intrinsically unstable leading to fluctuations in the pressure which may also affect dramatically the evaporator performances. A one-dimensional model of convective condensation in the absence of gravity was developed by the authors and, more recently, an extensive explanation of the numerical model has been given by Miscevic et al. [6]. The model is based on a separated flow approach and it allowed then to obtain a stationary two-phase flow solution of the liquid-vapor interface for different operative conditions. Five dimensionless independent groups were identified by the authors; in particular, the effects of the capillary and the boiling numbers on the mean Nusselt number were analyzed. The liquid phase Reynolds number, the density ratio and the viscosity ratio complete the set of dimensionless groups. It is interesting to notice that, although the channel has a circular shape, since the condensation process occurs at very low mass fluxes and

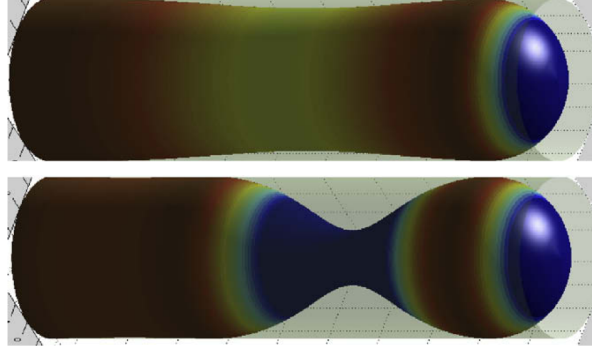


Figure 2.7: Liquid vapor interface obtained for two density ratios: on the top, $\rho_v/\rho_l = 5 \cdot 10^{-4}$; on the bottom, $\rho_v/\rho_l = 5 \cdot 10^{-3}$. Illustration from Miscevic [6]

in a very short channel length (the typical simulated total length to radius ratio is $\simeq 10$ – 15), the meniscus that is formed at the end of the condensation region is responsible for a large increase of the heat transfer as the condensing liquid phase is pulled towards the end of the channel where the liquid pressure is very low, due to the curvature of the interface. A typical simulation result is presented in Fig. (2.7) where the liquid-vapor interface is shown in the three-dimensional domain. In the model, a linear profile of the liquid phase is assumed and the vapor shear stress at the interface is calculated based on the relative velocity of the two phases. By analyzing the results, it is found that the pressure drop due to friction in the liquid mainly occurs at the junction between the thin layer region and the main meniscus region. The capillary number Ca has been found to have a strong influence on the mean Nusselt number. It is defined as:

$$Ca \equiv \frac{\mu_l u_l}{\sigma} \quad (2.66)$$

where u_l is the characteristic liquid axial liquid film velocity and, as the mass flux is imposed, it can be assumed equal to G/ρ_l . An increase of the capillary number leads to a reduction of the mean Nusselt number. The boiling number is defined as:

$$B \equiv \frac{\Delta h_{lv} (T_s - T_{out})}{Gl_v} \quad (2.67)$$

It is also found to have an influence of the overall performance and typically an increase in B leads to a reduction of the heat transfer coefficient.

Chen et al [46] recently presented a review of experimental and theoretical analyses of condensation in microchannels. They reported that the dominant flow pattern in these small channels is injection/slug/bubbly flow in contrast to the stratified and annular, for the same vapor quality and mass flux. It is reported that by carefully considering the resulting forces and their relative magnitudes, condensation in microchannels in one-g environments can reasonably simulate an 'equivalent system' in microgravity environments. Furthermore, the thermocapillary effects have been found to be considerably important if significant saturation temperature differences are encountered in the considered system.

2.3 Condensation Heat Transfer in Microgravity Environments

The role of surface tension for two-phase heat and mass transfer processes in the absence of gravity has been analyzed by Straub [47]. This work reports a summary of experimental results available at that time (1994) and the theoretical analysis of the surface tension physical phenomenon when the buoyancy is strongly reduced and transport processes are determined by the properties at the interface alone. Capillary and thermocapillary (due to the dependency of surface tension on the saturation temperature or the concentration of substances), pressure gradients, evaporation and condensation and coalescence mechanisms are discussed showing the growing importance of the surface tension related phenomena on the microgravity heat transfer processes. On the other end, the complexity of the experiments, especially conducted in microgravity environments, makes it difficult to discern the relative importance of many other phenomena which happen in these processes.

One of the earliest numerical studies on condensation has been proposed by Faghri et al. [48]: the film condensation process is analyzed for an annulus condenser configuration by applying the Nusselt theory for laminar film condensation for co-current vapor flows. Since both the inner and the outer wall cross sectional shapes are circular, under microgravity conditions the vapor shear is the only mechanism for the condensate removal and it is shown that this can effectively thin the condensate layer to ensure the continuous condenser operation.

The influence of microgravity, shear stress, surface tension, and/or capillary and centrifugal forces on condensation phenomena is discussed in this section. Chen et al. [49] presents a review of the recent investigations concerning the condensation process in the absence of body forces. With the development of more advanced applications, a spacecraft thermal control system must be able to transport and dissipate large quantities of heat over moderate distances. Standard mechanically pumped single-phase loops, widely used in the past, are being abandoned due to the large amount of pumping power required to overcome the pressure drops and meet the high heat removal demands of advanced spacecraft thermal control. The combination of high heat flux capacity, low weight-to-dissipated-power ratio and high degree of temperature uniformity provided by phase-change condensing radiators offers an effective alternative. The condensation heat transfer is used in these applications to transfer heat from the source to the radiators, where, through phase change, the desired heat transfer can be achieved and ultimately dissipated from the radiator surface to space. Effective condensing radiators are capable of dissipating high heat fluxes with small temperature differences and have a high heat-rejected to radiating-mass ratio. In this work it is stated that the mechanism of condensation in the absence of body forces is much different from that experienced in the presence of a gravitational body force. Furthermore, because of the difficulties of conducting experiments in reduced gravity environments (for instance space environment, 0-g flights and drop towers) only limited information is available. In presence of a wetting fluid, three major phenomena are listed as important in a microgravity environment: the vapor shear force, the 'wall suction' and the

centrifugal forces. Each of them or a combination of them could be used to enhance the performances of the film condensation process by removing in an efficient way the condensate from the cold surface. The use of microgrooves to enhance phase change has increased dramatically with the development of advanced machining methods. In this case the capillary force becomes the dominant factor in the two-phase flow and the heat transfer process becomes dominated by the meniscus region where the capillary induced pressure gradient allows the condensate film to be maintained very thin as described by Kabov et al. [44]. It is also mentioned that vapor shear, capillary and centrifugal forces are strongly size dependent and the proper combination of them in a micro heat pipe is required for an optimal functioning of the heat transfer device.

As mentioned earlier, another important element in a spacecraft thermal control system is the radiator itself. Naumann [50] presents a recent procedure for optimizing the configuration of a heat pipe/fin radiating element. The problem is stated as follows: given the mass per unit length of the heat pipe that feeds the fins and its operating temperature, the optimal fin width and thickness are obtained as a function of the thermal properties. The optimal solution maximizes the heat radiated per overall radiating mass. Although the optimization procedure does not account for any constraints on the geometry of the heat pipes (i.e. a minimum allowed fin thickness and/or a limited length of the heat exchanger) the presented results give an important insight to the physical problem.

A more generic approach to the satellite thermal control problem is presented by Gilmore [51], going from the satellite system overview, the thermal design process and analysis, the thermal control hardware (including the analysis of the thermal radiators) and a detailed overview of the heat pipes and capillary pumped loops. These two mentioned systems are becoming more and more used for their effectiveness and capability of working without any pump or driving device. Although the functioning process differs, the principle is similar. A schematic of the working principle of a heat pipe is given in Fig. (2.8) while that of a capillary pumped loop is shown in Fig. (2.9).

The heat pipe exploits the heat applied to the evaporator which raises the temperature of the vapor and depresses the meniscus since less liquid is present there. This process raises the local vapor pressure, since it remains in saturation with the heated liquid in the wick. The difference between the increased curvature of the meniscus in the evaporator wick causes a difference in capillary pressure sufficient to pull liquid from the condenser wick towards the evaporator, and thus the liquid replenishes the evaporator wick. At the same time, heated vapor flows from the evaporator to the condenser which is at lower pressure and when the vapor comes in contact with the cooler condenser surface and it condenses. Since the latent heat of vaporization of most heat-pipe working fluids is high, only small amounts of fluid need to flow to transport significant quantities of heat.

The capillary pumped loop in Fig. (2.9) is a two-phase heat transfer loop that uses a capillary structure to return liquid to the evaporator. This device is essentially a heat pipe with the return flow of condensate to the evaporator in a separate unwicked tube. This passive device is

able to drive larger flow rates of fluids and hence increases the working range of a normal heat pipe.

Mechanically assisted systems are an extension of heat pipes or capillary pumped loops by adding a small pump to force the liquid flow. Several of these systems, whose basic concept is still under development, have been proposed for use on the International Space Station and a number of prototypes have been built and tested.

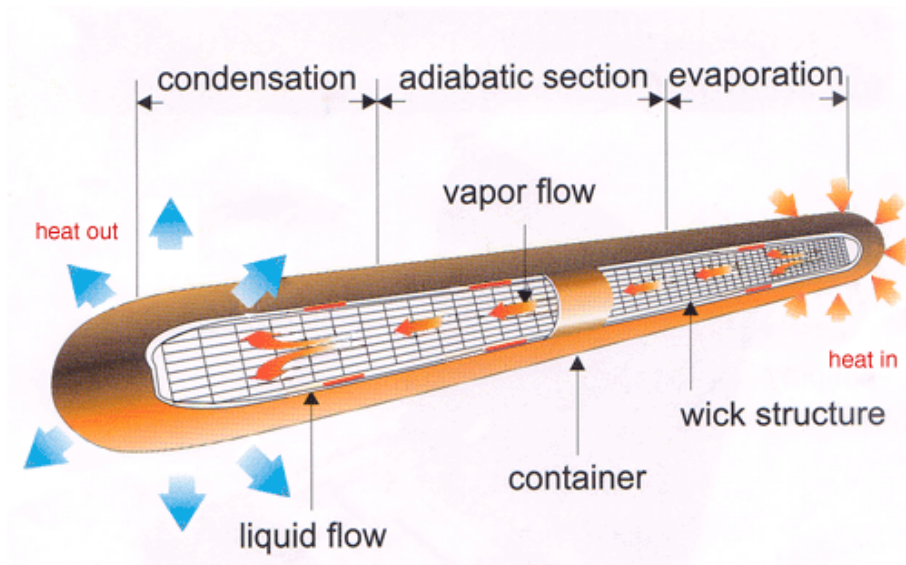


Figure 2.8: Schematic of a heat pipe

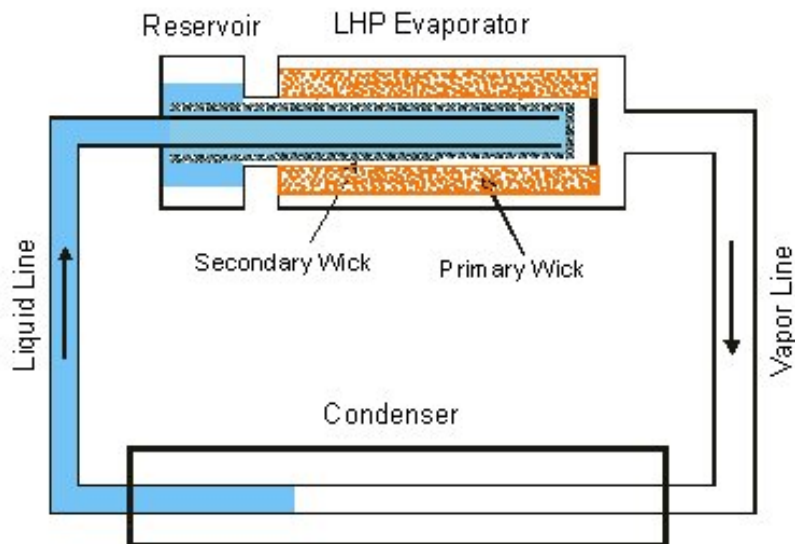


Figure 2.9: Schematic of a capillary pumped loop

2.4 Summary

Based on the experimental and theoretical work available in literature, several aspects still need to be clarified concerning the condensation phenomenon in microchannels and in microgravity conditions. Although some authors report that a parallelism exists between the two cases due to the fact that the surface tension tends to dominate on the gravity, this is only a "loosely" true.

Several models for predicting condensation heat transfer in minichannels exist but, although they can predict some trends for some fluids in a specific channel size range, most of the times they are not applicable either in smaller channels for the same fluid, either for the same channel but a different fluid. Su et al. [7] drew the attention to the fact that while four leading correlations are in fair agreement for predicting condensation in a 1 mm hydraulic diameter channel with the refrigerant R-134a, their predictions differ considerably when applied to other fluids, like ammonia. As an example, the comparison of heat transfer coefficients predicted for a square mini channel are shown in Fig. (2.10) where the numerical result obtained by the numerical model of Wang and Rose [5] is also plotted. Agarwal [4] has also shown that these methods do not work well when considering R-134a in a 100 μm channel.

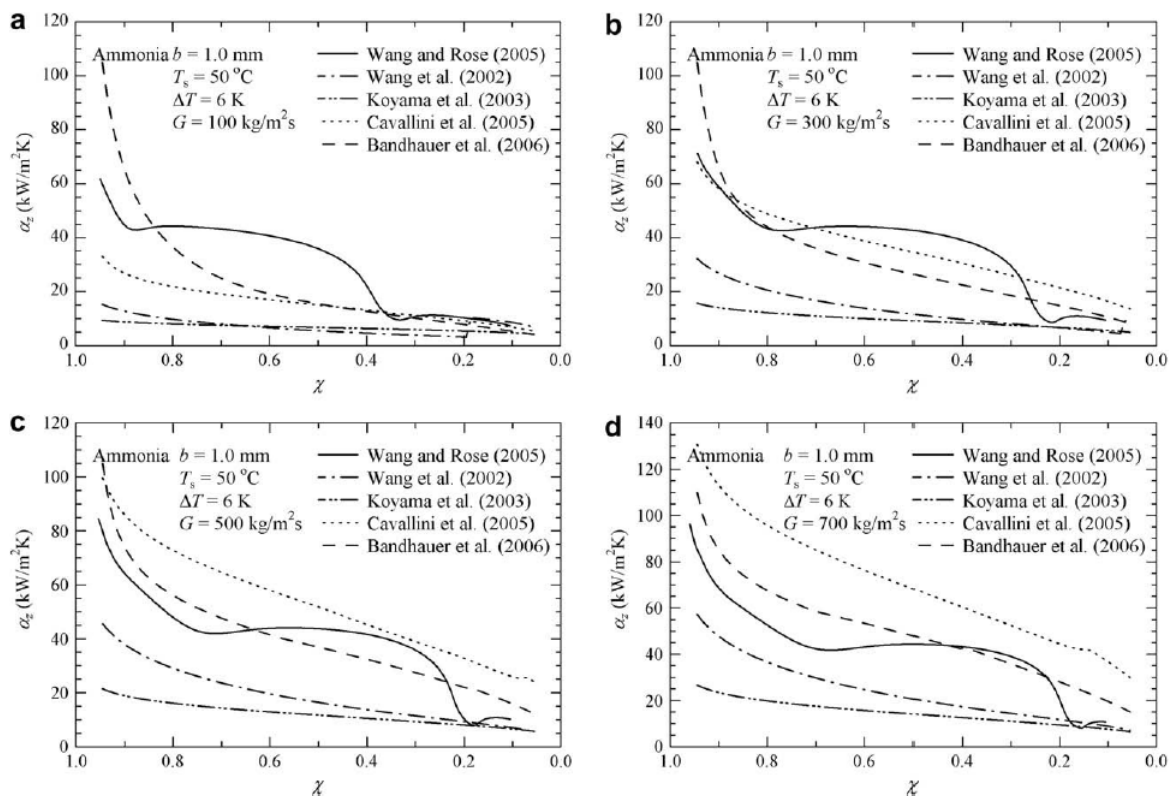


Figure 2.10: Comparison of correlations and theory for ammonia. Illustration from Su [7]

According to the literature reviewed here, various important issues still need to be treated,

proven or explained in order to better understand the physics of condensation in microchannels:

- the capillary forces seem to play an important role in mini and microchannel condensation. At lower Reynolds numbers (lower mass fluxes or hydraulic diameters for instance) this phenomenon becomes more evident, while at higher Reynolds numbers the flow tends to be shear dominated. Furthermore, as existing correlations have been developed for a specific geometry, usually they do not extrapolate well to other channel shapes;
- the existing empirical methods are primarily based on turbulent flow regime data; by progressively reducing the mass flux or the diameter, the liquid phase at first and secondly the vapor phase go through a transition from turbulent to laminar flow. Many experimental conditions and those of application, when considering an annular or wavy annular flow pattern, fall in the regime where the liquid film will be laminar, while the vapor core is still turbulent and hence this needs to be modeled;
- existing theoretical models are usually developed for steady state solutions, and thus they do not allow the study of the stability of the flow or the effects of variable (in time) boundary or operating conditions, such as the mass flux, the heat flux or the gravity field, which is of particular interest when analyzing the effects of vibrations (in automotive systems for instance) or residual gravitational forces (in aerospace systems);
- the conjugate heat transfer problem, that is, the coupling between the condensation process and thermal conduction in the wall is usually neglected by assuming either a uniform wall temperature or heat flux as a boundary condition at the inner perimeter of the channel. Moving to microscale, the coupling effects tend to become more and more important and thus a better understanding of the link between these physical phenomena in microchannel condensation needs to be studied;
- finally, when dealing with ultra-thin liquid layers, the effects of temperature and pressure jump occurring at the interface start to become very important. These effects are due to the interfacial resistance (which is commonly included in numerical calculations) and to the pressure jump due to liquid-vapor interface curvature, momentum transfer and disjoining pressure effects: these latter aspects are usually not included so far in the existing models.

The understanding of these effects may lead to a better comprehension of the two-phase heat transfer and a better exploitation of its potentials, particularly in terms of energy efficiency and performances. Thus the above issues will be addressed in this thesis. Furthermore, it is important to prove that numerical solutions can predict experimental observations and that will be done in detail here for the first time.

Chapter 3

Mathematical Model

In this chapter the description of the physical problem, the mathematical modeling and the hypothesis are described. The developed model allows the process of annular laminar film condensation to be studied and analyzed for different channel shapes and operative conditions. In this work, the finite volume method is applied in order to solve the Navier-Stokes equations of the liquid phase while a hybrid method based on the finite volume and finite difference approach is used to obtain the temperature field distribution. A special emphasis is put in describing the interfacial mass transfer mechanism and its modeling, accounting for the temperature jump at the liquid-vapor interface as well as the wall effect which may become important for very thin liquid films.

3.1 Model General Description and Hypotheses

The following hypotheses have been assumed in order to simplify the model:

- the computational domain is conceptually divided into two well defined regions: a vapor domain and a liquid domain as it is represented in Fig. (3.1); since the objective of this work is to study annular flow regimes, the surface that describes the interface between the two phases is unique and it is open at the two extremes (inlet and outlet). This surface exclusively defines the boundary between the liquid film subdomain and the vapor core subdomain;
- the flow in the vapor core can be either turbulent, laminar or in the transition regime while the flow in the liquid film is always treated as laminar; the interfacial shear of the vapor on the interface is not computed numerically but instead is calculated using well-known friction factor expressions, thus greatly reducing the complexity of the model and computational time;
- in the liquid subdomain it is assumed that the behavior of the film is primarily described

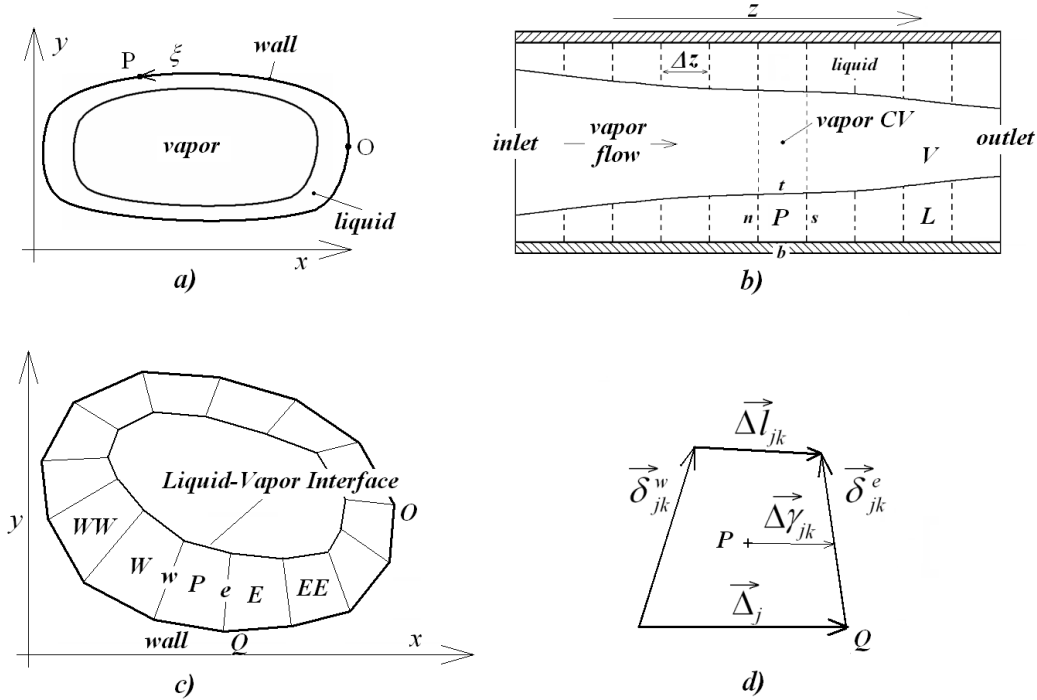


Figure 3.1: a) conceptual subdomain division (liquid and vapor phases) in the x and y plane (cross-sectional view) at an axial location; b) axial view of the channel geometry and interface; c) view of the film control volumes and nomenclature in the x - y plane; d) details of liquid cell geometrical elements

by the locally tangential and the axial film bulk velocities (ξ and z direction respectively). The local velocity component perpendicular to the wall is assumed negligible with respect to the other two components. All the details about the way the momentum fluxes and the wall shear stresses are calculated are given in Appendix A;

- the sensible heat contribution in the energy equation of the liquid film is neglected with respect to the latent heat; this assumption can be formulated in terms of the Jakob number: $Ja = C_{p,l}\Delta T/\Delta h_{l-v} \ll 1$, where $C_{p,l}$ is the specific heat at constant pressure of the liquid phase, Δh_{l-v} is the enthalpy of vaporization and ΔT is the reference temperature difference across the film. A similar hypothesis is used in the development of Nusselt laminar film condensation theory which is described in details in Lienhard [14] and Incropera et al. [18]; the thermal conduction across the film is considered as the fundamental mechanism of heat transfer while axial and peripheral thermal conduction in the wall may or may not be activated in the model; the axial conduction in the liquid film is neglected compared to the axial conduction contribution due to the wall (i.e. $k_l\delta \ll k_w\lambda_w$, with k_l the liquid thermal conductivity, δ the characteristic liquid film thickness, k_w the wall thermal conductivity and λ_w the the equivalent conductive wall thickness);
- the vapor phase mass and momentum balance are treated as one-dimensional and the vapor is assumed to be saturated at each axial location;

- only pure substances are considered; all the thermodynamic properties are assumed constant in time and space and are evaluated at the inlet saturation condition using REFPROP 2007 of NIST [52];
- the interphase mass transfer effects are taken into account in the formulation of the mass and energy conservation equations; the disjoining pressure effects (i.e. the near to the wall effects) are taken into account as well as, since the aim of this work is to investigate the behavior of laminar film condensation down to the micro-scale where the effects of these mentioned phenomena are expected to become important;
- three different wall boundary conditions are investigated: 1) constant and uniform wall temperature, 2) imposed heat flux (time and space dependent) and 3) single phase external heat transfer coefficient. Through a proposed theoretical analysis of the conjugate heat transfer problem, the characteristic dimensionless numbers will be identified and transition criteria where conjugate effects become significant will be proposed;
- the body forces acting on the fluid are written for a generic non inertial reference system, including the transport acceleration, the relative acceleration and the Coriolis acceleration: the effects of variable gravity (which are present for instance on the International Space Station) and generic disturbances can also be investigated.

3.2 General Form of Conservation Equations

For a generic intensive property ϕ the conservation equation in integral form for a control volume Ω is written as [53]:

$$\frac{d}{dt} \int_{\Omega} \rho \phi d\Omega = \oint_{\partial\Omega} \rho \phi (\vec{v}_{\partial} - \vec{v}) \cdot d\vec{S} + \dot{Q}_{\Omega} + \dot{Q}_{\partial\Omega} \quad (3.1)$$

with \vec{v}_{∂} the velocity of the boundary $\partial\Omega$, ρ the density, \vec{v} the velocity field, $d\vec{S}$ the surface element and \dot{Q}_{Ω} and $\dot{Q}_{\partial\Omega}$ the body and surface source terms. The mass conservation equation can be obtained by formal substitution of $\phi = 1$ into Eq. (3.1) and setting to zero the volumetric and boundary source terms:

$$\frac{d}{dt} \int_{\Omega} \rho d\Omega = \oint_{\partial\Omega} \rho (\vec{v}_{\partial} - \vec{v}) \cdot d\vec{S} \quad (3.2)$$

The momentum equation can be obtained by substituting $\phi = \vec{v}$ into Eq. (3.1) where the body source term \vec{f}_b and stress tensor \vec{F} are included as source terms:

$$\frac{d}{dt} \int_{\Omega} \rho \vec{v} d\Omega = \oint_{\partial\Omega} \rho \vec{v} (\vec{v}_{\partial} - \vec{v}) \cdot d\vec{S} + \int_{\Omega} \rho \vec{f}_b d\Omega + \oint_{\partial\Omega} \vec{F} \cdot d\vec{S} \quad (3.3)$$

For Newtonian fluids, the stress tensor \vec{F} can be written as:

$$\vec{F} = - \left(p + \frac{2}{3} \mu \vec{\nabla} \cdot \vec{v} \right) \vec{I} + \mu \left(\vec{\nabla} \vec{v} + \vec{\nabla} \vec{v}^T \right) \quad (3.4)$$

where μ is the dynamic viscosity, \vec{I} is the unit tensor and p is the pressure. The set of integral conservation Eq. (3.2) and Eq. (3.3) have been integrated over the discretized domain under the hypothesis that are detailed in the following paragraphs.

3.3 Coordinate, Basis Vector Systems and Numerical Grid

A Finite Volume (FV) method has been implemented to solve the set of Eq. (3.1) and Eq. (3.3). The domain is depicted in Fig. (3.1). The liquid film subdomain which is referred with the superscript 'L' wets the wall of the channel and surrounds the vapor core subdomain (superscript 'V'). From the geometry of the wall and the liquid-vapor interface reconstruction based on a curvilinear coordinate system, all the control volume geometrical variables (lengths, surfaces, volume), L-V interface velocities, fluxes and film thickness time derivatives can be calculated. The liquid cell boundary follows continuously the interface thus allowing the curvature to be calculated with accuracy without loss of mass that other grid schemes may create when representing the curved interface. The diffusive fluxes are calculated based on the second order truncation error Central Differencing Scheme [53], [54], while the convective fluxes have been implemented both using both the First Order Upwind Scheme and the QUICK Scheme [54].

The first step in the discretization process is the definition of the inner wall geometry. For a fixed size and shape of geometrical section along the axis, the geometry \vec{r}_w can be entirely described in the x - y plane (see Fig. (3.1)):

$$\vec{r}_w = \vec{r}_w(x, y) = x(\xi) \hat{x} + y(\xi) \hat{y} = \vec{r}_w(\xi) \quad (3.5)$$

where ξ is the curvilinear coordinate defined with respect to an arbitrary origin point O :

$$\xi_Q \equiv \int_O^Q \sqrt{(\vec{r}_{w,x} \cdot \vec{r}_{w,x}) dx^2 + (\vec{r}_{w,y} \cdot \vec{r}_{w,y}) dy^2} \quad (3.6)$$

The cross section area S_0 can be computed through the following integral evaluated over the entire internal perimeter P with the following expression:

$$S_0 = \frac{1}{2} \left| \int_P \vec{r}_w \times d\vec{r}_w \right| \quad (3.7)$$

At each point Q is then associated a film thickness unit vector $\hat{\delta}(\xi)$. The L-V interface can then

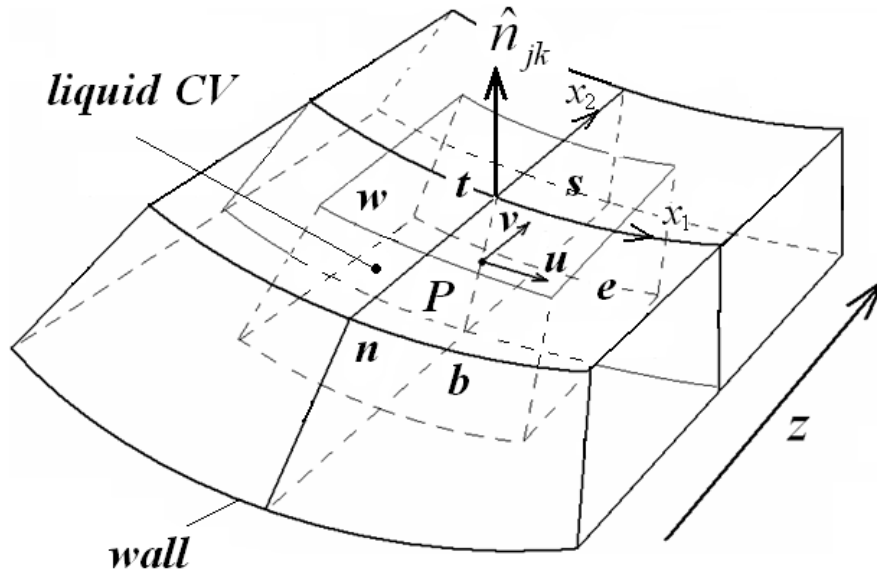


Figure 3.2: 3D view of the liquid cell control volume and boundaries

be described as a function of the two free coordinates ξ and z :

$$\vec{r}_i(z, \xi) = \vec{r}_w(\xi, z) + \hat{\delta}(\xi) \delta(z, \xi) \quad (3.8)$$

In this way the reconstruction of the L-V interface is based only on the function $\delta(\xi, z)$ since wall geometry and unit vector field are known. The same two free coordinates are used to solve for the velocity field and pressure in the whole domain.

In order to make the representation of the surface unique, it has to be guaranteed that [55]:

$$\frac{\partial}{\partial z} \vec{r}_i(z, \xi) = \frac{\partial}{\partial z} \vec{r}_w(\xi, z) + \hat{\delta}(\xi) \frac{\partial}{\partial z} \delta(z, \xi) \neq \vec{0} \quad (3.9)$$

$$\frac{\partial}{\partial \xi} \vec{r}_i(z, \xi) = \frac{\partial}{\partial \xi} \vec{r}_w(\xi, z) + \delta(z, \xi) \frac{\partial}{\partial \xi} \hat{\delta}(\xi) + \hat{\delta}(\xi) \frac{\partial}{\partial \xi} \delta(z, \xi) \neq \vec{0} \quad (3.10)$$

The first constraint is always satisfied as the axial unit vector and the thickness unit vector are orthogonal by construction. The second equation instead can be replaced by a more restrictive and simpler constraint:

$$\delta(z, \xi) < \delta_{\max}(\xi) \quad (3.11)$$

which is taken into account both in the meshing generation process and in the solution of the problem. By differentiating Eq. (3.8) with respect to time and indicating with the superscript ‘.’ the time derivative, the L-V interface velocity can be obtained:

$$\vec{v}_{\partial,i} = \frac{d}{dt} \vec{r}_i(z, \xi) = \hat{\delta}(\xi) \frac{d}{dt} \delta(z, \xi) = \hat{\delta}(\xi) \dot{\delta}(z, \xi) \quad (3.12)$$

The discretized domain is represented in Fig. (3.1) and Fig. (3.2). The inner perimeter of

the channel is divided into N segments j ($j = 1, \dots, N$); since the wall geometry is assumed constant along the channel axis, this discretized set of elements is repeated for M sections along the z direction, with a constant spacing equal to Δz so that the total length of the channel L_t is:

$$L_t = M \cdot \Delta z \quad (3.13)$$

The following nomenclature is introduced for convenience: the index j and k refer to the ξ and z directions respectively; the six boundary surfaces of the film cell control volume (CV) depicted in Fig. (3.2) are indicated with n, s, e, w, t and b , namely north, south, east, west, top and bottom respectively; cell centers are indicated with a capital letter P while neighbor cells are named with the capital letters E, W, N, S . Inlet and outlet boundaries are set in correspondence of n and s boundaries of the first set of CV ($k = 1$) and the last set of CV ($k = M$). The vapor subdomain is discretized by M control volumes identified only by the index k . Based on this, the axial location of a CV corresponding to the k index is:

$$z_{jk} = \frac{\Delta z}{2} + (k - 1) \Delta z \quad (3.14)$$

Following Eq. (3.6), the curvilinear coordinate of the boundary points Q_j is:

$$\xi_{Q_j} = \sum_{i=1}^{i=j} \left| \vec{\Delta}_i \right| \quad (3.15)$$

By construction, referring to Fig. (3.1), all the geometrical elements of the generic CV can be computed

$$\Delta \vec{l}_{jk} = \vec{\Delta}_j + \vec{\delta}_{j,k}^e - \vec{\delta}_{j,k}^w \Rightarrow \quad (3.16)$$

$$\Delta \vec{l}_{jk} \cdot \Delta \vec{l}_{jk} = \vec{\Delta}_j \cdot \vec{\Delta}_j + 2\vec{\delta}_{j,k}^e \cdot \vec{\Delta}_j - 2\vec{\delta}_{j,k}^w \cdot \vec{\Delta}_j - 2\vec{\delta}_{j,k}^e \cdot \vec{\delta}_{j,k}^w + \vec{\delta}_{j,k}^e \cdot \vec{\delta}_{j,k}^e + \vec{\delta}_{j,k}^w \cdot \vec{\delta}_{j,k}^w \quad (3.17)$$

Applying the same approach to other cell elements and defining the following sets of constants:

$$s_{1,j} = \frac{1}{2} \left(\vec{\Delta}_j \times \hat{\delta}_j^w \right) \cdot \hat{z} \quad (3.18)$$

$$s_{2,j} = \frac{1}{2} \left(\vec{\Delta}_j \times \hat{\delta}_j^e \right) \cdot \hat{z} \quad (3.19)$$

$$s_{3,j} = \frac{1}{2} \left(\hat{\delta}_j^w \times \hat{\delta}_j^e \right) \cdot \hat{z} \quad (3.20)$$

$$c_{1,j} = \hat{\delta}_j^w \cdot \hat{\delta}_j^e \quad (3.21)$$

$$c_{2,j} = \vec{\Delta}_j \cdot \hat{\delta}_j^w \quad (3.22)$$

$$c_{3,j} = \vec{\Delta}_j \cdot \hat{\delta}_j^e \quad (3.23)$$

$$c_{4,j} = \vec{\Delta}_j \cdot \vec{\Delta}_j \quad (3.24)$$

Readjusting Eq. (3.17) it is possible to write:

$$\Delta \vec{l}_{jk} \cdot \Delta \vec{l}_{jk} = \delta_{j,k}^w \delta_{j,k}^w + \delta_{j,k}^e \delta_{j,k}^e - 2c_{1,j} \delta_{j,k}^w \delta_{j,k}^e - 2c_{2,j} \delta_{j,k}^w + 2c_{3,j} \delta_{j,k}^e + c_{4,j} \quad (3.25)$$

$$\Delta \vec{\gamma}_{jk} \cdot \Delta \vec{\gamma}_{jk} = \frac{1}{16} \delta_{j,k}^w \delta_{j,k}^w + \frac{1}{16} \delta_{j,k}^e \delta_{j,k}^e - \frac{1}{8} c_{1,j} \delta_{j,k}^w \delta_{j,k}^e - \frac{1}{4} c_{2,j} \delta_{j,k}^w + \frac{1}{4} c_{3,j} \delta_{j,k}^e + \frac{c_{4,j}}{4} \quad (3.26)$$

The projected area of each cell in the x - y plane can be easily obtained by:

$$\Delta S_{jk} = s_{1,j} \delta_{j,k}^w + s_{2,j} \delta_{j,k}^e + s_{3,j} \delta_{j,k}^w \delta_{j,k}^e \quad (3.27)$$

Referring to Fig. (3.1), the approximate value (second order truncation error in Δz) of the liquid film cell volume Ω_{jk} is:

$$\Delta \Omega_{jk} = (s_{1,j} \delta_{j,k}^w + s_{2,j} \delta_{j,k}^e + s_{3,j} \delta_{j,k}^w \delta_{j,k}^e) \Delta z \quad (3.28)$$

The time derivative of the control volume can be written in terms of the time derivatives of the local film thickness:

$$\frac{d}{dt} \Delta \Omega_{jk} = \Delta z (s_{1,j} + s_{3,j} \delta_{j,k}^e) \dot{\delta}_{j,k}^w + \Delta z (s_{2,j} + s_{3,j} \delta_{j,k}^w) \dot{\delta}_{j,k}^e \quad (3.29)$$

The distance between two consecutive cell centers can be computed as:

$$\Delta \xi_{jk}^e = \Delta \gamma_{jk} + \Delta \gamma_{j+1,k} \quad (3.30)$$

For each CV the two unit vectors $\hat{\xi}_{jk}$ and \hat{z}_{jk} are also defined. The first one is obtained as the local tangent to the wall direction. Based on the presented assumptions, the local liquid film velocity and the axial vapor velocity can be represented as:

$$\vec{v}_{jk} = u_{jk} \hat{\xi}_{jk} + v_{jk} \hat{z} \quad (3.31)$$

$$\vec{U}_k^V = U_k^V \hat{z} \quad (3.32)$$

The boundary surfaces ΔS_{jk}^i ($i = 'n', 's', 'e', 'w', 't', 'b'$) of the CV's are calculated as follows:

$$\Delta S_{jk}^e = \Delta z \delta_{j,k}^e \quad (3.33)$$

$$\Delta S_{jk}^w = \Delta z \delta_{j,k}^w \quad (3.34)$$

$$\Delta S_{jk}^t = \Delta z \cdot \Delta l_{jk} \quad (3.35)$$

$$\Delta S_{jk}^b = \Delta z \cdot \Delta \xi_{jk} \quad (3.36)$$

$$\Delta S_{jk}^n = (\Delta S_{jk} + \Delta S_{j,k-1})/2 \quad (3.37)$$

$$\Delta S_{jk}^s = (\Delta S_{jk} + \Delta S_{j,k+1})/2 \quad (3.38)$$

while vapor cell control volume and cross section area are respectively:

$$\Delta\Omega_k^V = \Delta z \cdot S_0 - \sum_j \Delta\Omega_{jk} \quad (3.39)$$

$$\Delta S_k^V = S_0 - \sum_j \Delta S_{jk} \quad (3.40)$$

The normal unit vectors are indicated with the same notation used for surfaces: vector \hat{n}_{jk}^i is orthogonal to face the 'i' of CV jk .

3.4 Boundary and Internal Conditions

At the inlet $z = z_0$, the following boundary conditions are imposed: film velocities, vapor velocity, vapor pressure and film distribution. This model allows the inlet vapor mass flux G_v to be varied in time:

$$G_v = \rho_v U_0^v = G_v(t) \quad (3.41)$$

In order to define the outflow and inflow local curvatures, the liquid-vapor (L-V) interface needs to be extrapolated outside the domain by interpolating from internal sections. Only for specific cases, as benchmark tests, periodic boundary (inlet - outlet) conditions have been applied; the no slip condition is imposed at the wall and this condition is embedded in the calculation of the diffusive flux in the momentum equation. The vapor temperature is assumed constant along the axis and therefore it is treated as boundary condition for the conduction problem at each section; at the liquid-vapor interface, continuity of the stress tensor is applied. The L-V interface, having \hat{n} as the normal unit vector pointing from the liquid to the vapor phase, can be described as a function \vec{r}_i dependent on two local coordinates x_1 and x_2 (see Fig. (3.2)):

$$\vec{r}_i = \vec{r}(x_1, x_2) \quad (3.42)$$

The normal unit vector can be calculated from the following expression [55]:

$$\hat{n} = \frac{\vec{r}_{x_1} \times \vec{r}_{x_2}}{|\vec{r}_{x_1} \times \vec{r}_{x_2}|} \quad (3.43)$$

where \vec{r}_{x_i} indicates the partial derivative of \vec{r} with respect to x_i and ' \times ' indicates the cross product operation. The first and the second fundamental forms of the surface can be written as [55]:

$$\mathfrak{S}_1 = (\vec{r}_{x_1} \cdot \vec{r}_{x_1}) dx_1^2 + 2(\vec{r}_{x_1} \cdot \vec{r}_{x_2}) dx_1 dx_2 + (\vec{r}_{x_2} \cdot \vec{r}_{x_2}) dx_2^2 \quad (3.44)$$

$$\mathfrak{S}_2 = (\vec{r}_{x_1 x_1} \cdot \hat{n}) dx_1^2 + 2(\vec{r}_{x_1 x_2} \cdot \hat{n}) dx_1 dx_2 + (\vec{r}_{x_2 x_2} \cdot \hat{n}) dx_2^2 \quad (3.45)$$

The local mean curvature K can finally be computed with the following expression:

$$K(x_1, x_2) = \frac{(\vec{r}_{x_1} \cdot \vec{r}_{x_1})(\vec{r}_{x_2 x_2} \cdot \hat{n}) - 2(\vec{r}_{x_1} \cdot \vec{r}_{x_2})(\vec{r}_{x_1 x_2} \cdot \hat{n}) + (\vec{r}_{x_2} \cdot \vec{r}_{x_2})(\vec{r}_{x_1 x_1} \cdot \hat{n})}{(\vec{r}_{x_1} \cdot \vec{r}_{x_1})(\vec{r}_{x_2} \cdot \vec{r}_{x_2}) - (\vec{r}_{x_1} \cdot \vec{r}_{x_2})^2} \quad (3.46)$$

In order to describe the motion of the fluid in non-inertial reference systems, the theorem of composition of the accelerations has to be taken into account in order to evaluate the body source term in Eq. (3.3). The actual acceleration \vec{a} of a generic point can be written as:

$$\vec{a} = \vec{a}_{\text{rel}} + \vec{a}_{\text{T}} + \vec{a}_{\text{C}} \quad (3.47)$$

being \vec{a}_{rel} the acceleration relative to a reference point \vec{x}_0 , \vec{a}_{T} is the transport acceleration and \vec{a}_{C} is the Coriolis acceleration. The non-inertial reference system has a proper velocity $\frac{d\vec{x}_O}{dt}$, acceleration $\frac{d^2\vec{x}_O}{dt^2}$, angular velocity $\vec{\Omega}$ and angular acceleration $\frac{d\vec{\Omega}}{dt}$. Following the definitions, the transport and Coriolis accelerations of a point \vec{x} can be written in the following way:

$$\vec{a}_{\text{T}} = \vec{a}_O + \vec{\Omega} \times (\vec{\Omega} \times \vec{x}) + \frac{d\vec{\Omega}}{dt} \times (\vec{x} - \vec{x}_O) \quad (3.48)$$

$$\vec{a}_{\text{C}} = 2\vec{\Omega} \times \vec{v} \quad (3.49)$$

where the velocity vector \vec{v} is relative to the non-inertial reference point O. The body source term can be finally written as:

$$\vec{f}_b = (\vec{g} - \vec{a}_t) - \vec{\Omega} \times (\vec{\Omega} \times \vec{x}) - \frac{d\vec{\Omega}}{dt} \times (\vec{x} - \vec{x}_0) - 2\vec{\Omega} \times \vec{v} \quad (3.50)$$

where \vec{g} is the gravity field.

3.5 Energy Equation

As the scale of the problem is reduced (i.e. moving from small scale to micro scale sizes), interphase resistance and disjoining pressure effects may become important as the liquid film becomes very thin. Wang and Rose [40] showed that the interphase mass transfer effect for condensing steam on a low-finned tube can reduce locally the heat flux of a factor of 2, when the liquid film is very thin. Similar considerations are presented in a previous work by Madejski [56]. At the interface between two distinct phases, the resulting net mass transfer from phase 1 to phase 2 can be calculated as the difference between two fluxes, one going from 1 to 2, the other going from 2 to 1. Different expressions, based on the application of kinetic theory, have been adopted by various authors. Wayner et al. [57] adopted an expression that takes into account the pressure and temperature of each phase and an evaporation coefficient or accommodation coefficient which reflects the intrinsic characteristic of the molecular interaction during the transfer process, leading to a complex phenomenon of reflection, replacements and effective

transfer of each molecule across the interface:

$$J = \frac{\nu}{2 - \nu} \sqrt{\frac{M}{2\pi\Re}} \left(\frac{p_{lv}}{\sqrt{T_{lv}}} - \frac{p_v}{\sqrt{T_v}} \right) \quad (3.51)$$

where J is the net mass flux per unit surface evaporating from the l - v region (liquid-vapor interface) to the v region (vapor), M is the molar mass, \Re is the universal gas constant, p and T are respectively the pressure and the temperature of each phase and ν is the accommodation coefficient, which can be different for evaporation and condensation processes. A detailed analysis of Eq. (3.51) including the limits of applicability is presented by Harvie [58]. Authors [59–61] adopt the value 1 for both of these two coefficients and Wang et al. [61] shows that non polar-liquids (such as benzene or hexadecane) have an experimentally determined accommodation coefficient of unity, while there is much debate about the value of this constant for polar fluids, like water and methanol. Ajaev [60] and Hristov et al. [62] adopt a linearized version of the interface mass transfer expression, assuming that the interface is not far away from saturation conditions and a similar approach is adopted by [40, 63], expressing the temperature jump across the interface as a linear function of the local heat flux. A comparison between the linearized expression and the complete expression is proposed by [61], who concluded that the linearized version is a good approximation as long as the temperature difference between the liquid-vapor interface and saturation temperature is below $5K$, while the complete formulation has to be adopted for higher superheated conditions. The following expression for low superheat conditions as per [59], [61] and [62] is adopted here:

$$J = \frac{2\rho_v \Delta h_{lv}}{T_s \sqrt{2\pi\Re T_s}} \Delta T + \frac{2\rho_v}{\rho_l \sqrt{2\pi\Re T_s}} \Delta p = J_T \Delta T + J_p \Delta p \quad (3.52)$$

where ρ_v and ρ_l are the vapor and liquid densities, Δh_{lv} is the latent heat of vaporization evaluated at the saturation temperature T_s , T and p are the temperature jump and pressure jump across the interface while J_T and J_p are functions of saturation temperature. In Eq. (3.52) the second term is usually neglected compared to the first one which can be responsible for a significant reduction of the heat transfer coefficient when the local mass flux becomes high. Nevertheless, when the pressure jump becomes very strong, the second term can have a locally important effect on the liquid film distribution. The pressure jump can be caused by liquid-vapor interface curvature or by the near to wall induced effect. When the film becomes very thin, the molecules at the interface start to feel the presence of the wall molecules. Molecules near to the wall always feel this influence (as liquid-solid surface tension) but, as long as the interface is far from this region, no macroscopic effect is found. An extensive explanation and some examples are given by Stephan [64]. The interaction is very complex (electromagnetic far range Van der Waals forces) and it has been studied by several authors. Liquid molecules can feel a higher attraction (toward the wall) or repulsion. It has been shown that this effect can be reconducted to a pressure variation (occurring at the interface), positive or negative, that has a certain dependency on the film thickness. This phenomenon is generally referred to as the disjoining or adhesive pressure. For wetting fluids, namely fluids where the molecules are

attracted towards the wall, authors [57, 59, 60] adopted the following expression:

$$\Delta p_d = \frac{A}{\delta^3} \quad (3.53)$$

where δ is the film thickness and A is the Hamaker constant. The order of magnitude of this constant is $10^{-20} - 10^{-21} \text{ kg m}^2 \text{ s}^{-2}$ and is negative, reflecting the attractive nature of the forces. The modified Laplace equation can be obtained by a momentum balance across the interface [62]:

$$\Delta p^i = p^i - p^v = \sigma K + \frac{A}{\delta^3} + \left(\frac{1}{\rho_v} - \frac{1}{\rho_l} \right) J^2 \quad (3.54)$$

where p^i and p^v are respectively the liquid film pressure at the interface, σ is the liquid-vapor surface tension and K is the curvature of the liquid-vapor interface.

Neglecting the thermal inertia of the liquid phase ($C_p \Delta T / \Delta h_{lv} \simeq 0$) and assuming the vapor temperature at the interface equal to the saturation temperature, then the problem is reduced to solving the thermal conduction problem across the liquid film with the following boundary conditions:

$$\begin{aligned} T|_{wall} &= T^w \\ k_l \frac{\partial T}{\partial n}|_i &= J^c \Delta h_{lv} \end{aligned} \quad (3.55)$$

where k_l is the liquid thermal conductivity, T the film temperature, T_w the wall temperature, \hat{n} the direction normal to the interface i , J^c the condensing mass flux and Δh_{lv} the specific enthalpy of vaporization. The condensing mass flux is given by Eq. (3.52):

$$J_{jk}^c = J_T (T^s - T_{jk}^i) + J_p (p_k^v - p_{jk}^i) \quad (3.56)$$

where T_s is the saturation temperature, p^v is the vapor pressure and T_{jk}^i and p_{jk}^i are respectively the temperature and pressure evaluated at the interface. Neglecting the minor axial gradient of liquid temperature and approximating with the central difference scheme the temperature gradient at the interface and at the wall, the bulk temperature T_{jk} can be obtained by the following relationships:

$$\Delta \xi_{jk} k_l \frac{\partial T}{\partial \delta} \Big|_{w,jk} - \Delta l_{jk} k_l \frac{\partial T}{\partial \delta} \Big|_{i,jk} = 0 \quad (3.57)$$

Applying the central difference scheme, the temperature gradients at the two interfaces can be computed with the following expressions:

$$\frac{\partial T}{\partial \delta} \Big|_{w,jk} \approx \frac{T_{jk} - T^w}{\delta_{jk}/2} \quad (3.58)$$

$$\frac{\partial T}{\partial \delta} \Big|_{i,jk} \approx \frac{T_{jk}^i - T_{jk}}{\delta_{jk}/2} \quad (3.59)$$

Substituting in Eq. (3.57) and solving with respect to T_{jk} , it is found that:

$$T_{jk} = \frac{T^w + \beta_{jk} T_{jk}^i}{1 + \beta_{jk}} \quad (3.60)$$

where the coefficient β_{jk} is defined as:

$$\beta_{jk} \equiv \frac{\Delta l_{jk}}{\Delta_j} \quad (3.61)$$

The temperature gradient at the interface is then:

$$\left. \frac{\partial T}{\partial \delta} \right|_{i,jk} \approx \frac{2}{1 + \beta_{jk}} \frac{T_{jk}^i - T^w}{\delta_{jk}} \quad (3.62)$$

If the surface is locally flat, then $\beta_{jk} = 1$ and the temperature gradient becomes simply $(T_{jk}^i - T^w)/\delta_{jk}$. Substituting Eq. (3.56) and Eq. (3.62) into Eq. (3.55) leads to:

$$\frac{k_l}{\delta_{jk} \Delta h_{lv}} \frac{2}{1 + \beta_{jk}} (T_{jk}^i - T^w) = J_T (T^s - T_{jk}^i) + J_P (p_k^v - p_{jk}^i) \quad (3.63)$$

which can be solved for $T_{i,jk}$ as a function of the saturation temperature and the local wall temperature. Defining:

$$\phi_{jk} = \frac{k_l}{\delta_{jk} \Delta h_{lv}} \frac{2}{1 + \beta_{jk}} \quad (3.64)$$

from Eq. (3.63) the interfacial temperature is:

$$T_{jk}^i = \frac{\phi_{jk} T^w + J_T T^s + J_P (p_k^v - p_{jk}^i)}{\phi_{jk} + J_T} \quad (3.65)$$

The net condensing mass flux is then obtained by substituting Eq. (3.65) into Eq. (3.56):

$$J_{jk}^c = \frac{\phi_{jk} J_T}{\phi_{jk} + J_T} (T^s - T^w) + \frac{\phi_{jk} J_P}{\phi_{jk} + J_T} (p_k^v - p_{jk}^i) \quad (3.66)$$

This expression is an expanded version of equation Eq. (3.52) that now includes the film thermodynamic properties and geometry. It contains the interfacial pressure jump $p_k^v - p_{jk}^i$ which is function of J_{jk}^c through Eq. (3.54):

$$J_{jk}^c = \frac{\phi_{jk} J_T}{\phi_{jk} + J_T} (T^s - T^w) + \frac{\phi_{jk} J_P}{\phi_{jk} + J_T} \left[-\sigma K_{jk} - \frac{A}{\delta_{jk}^3} - \left(\frac{1}{\rho_v} - \frac{1}{\rho_l} \right) (J_{jk}^c)^2 \right] \quad (3.67)$$

Finally, solving the previous equation, the net condensing mass flux can be written in the following form:

$$J_{jk}^c = \frac{\sqrt{1 + 4a_{jk} b_{jk}} - 1}{2a_{jk}} \quad (3.68)$$

where a_{jk} and b_{jk} are defined as:

$$a_{jk} \equiv \left(\frac{1}{\rho_v} - \frac{1}{\rho_l} \right) \left(\frac{\phi_{jk} J_P}{\phi_{jk} + J_T} \right) \quad (3.69)$$

$$b_{jk} \equiv \frac{\phi_{jk} J_T}{\phi_{jk} + J_T} (T^s - T^w) - \frac{\phi_{jk} J_P}{\phi_{jk} + J_T} \left(\sigma K_{jk} + \frac{A}{\delta_{jk}^3} \right) \quad (3.70)$$

In the limiting case as J_T becomes very large and J_P is neglected, $\alpha_{jk} \rightarrow 0^+$ and consequently $J_{jk}^c \rightarrow \phi_{jk} (T^s - T^w)$, which is consistent with the standard Nusselt theory case when interface resistance and pressure difference effects can be neglected. If the wall temperature is imposed (boundary condition of the first type) then the calculation of the local condensing mass flux can be directly implemented and the following symbolic relationship can be written:

$$\underline{J}^c = \underline{f}_J(\underline{\delta}, \Delta T) \quad (3.71)$$

where \underline{J}^c is the vector of mass fluxes, $\underline{\delta}$ is the vector of liquid film thicknesses and $\Delta T = T^s - T^w$. The functional relationship \underline{f}_J includes the fluid thermal properties and the geometry as well.

If the wall temperature is not assigned, the wall energy balance has to be taken into account as wall. The wall energy balance with a shell approximation (i.e. conduction may occur in the axial and the peripheral directions), neglecting the heat capacity contribution, becomes the following:

$$\beta_{jk} \Delta h_{lv} J_{jk}^c + q_k'' + k_w \lambda_w \nabla_{\xi z}^2 T^w = 0 \quad (3.72)$$

where q_k'' is the local imposed heat flux (negative for condensation) at the wall and it is function only of the axial coordinate z_k , $\nabla_{\xi z}$ is the Laplacian operator restricted to the two directions, k_w is the thermal conductivity of the wall and λ_w is the equivalent conductive wall thickness that is defined as the ratio between the axial conductive wall channel area and the internal perimeter. Adiabatic conditions are assumed at the inlet and the outlet sections of the channel. The formal implicit relationship can be now written in terms of the unknown T^w :

$$\underline{f}_q(\underline{T}^w, \underline{\delta}, \underline{q}) = \underline{0} \quad (3.73)$$

where \underline{q} is heat flux vector and \underline{T}^w is the vector of the unknown wall temperatures.

If a boundary condition of the third type is considered (i.e. external single phase heat transfer coefficient α_e), Eq. (3.72) becomes:

$$\beta_{jk} \Delta h_{lv} J_{jk}^c + \alpha_e (T_k^c - T_{jk}) + k_w \lambda_w \nabla_{\xi z}^2 T^w = 0 \quad (3.74)$$

being T_k^c the local cold fluid temperature, function only of the axial coordinate z_k . The formal relationship can now be written as:

$$\underline{f}_\alpha(\underline{T}^w, \underline{\delta}, \underline{\alpha}, \underline{T}^c) = \underline{0} \quad (3.75)$$

3.6 Mass Conservation Equations

3.6.1 Liquid Domain

The mass conservation equation for a generic cell $\Delta\Omega$ is:

$$\frac{d}{dt} \int_{\Delta\Omega} d\Omega = \oint_{\partial\Delta\Omega} (\vec{v}_\partial - \vec{v}) \cdot d\vec{S} \quad (3.76)$$

The boundary velocity vector at the interface is obtained by Eq. (3.12), while it is equal to zero at the wall and it is perpendicular to $d\vec{S}$ everywhere else. As the L-V boundary of the control volume is following the interface, through an interface mass balance equation it is possible to verify that the contribution in Eq. (3.76) is equivalent to the local condensing volumetric flow rate:

$$\oint_{\partial\Omega_{jk,t}} (\vec{v}_\partial - \vec{v}) \cdot d\vec{S} = \frac{1}{\rho_l} J_{jk}^c \Delta S_{jk}^t \quad (3.77)$$

Substituting the previous expression into Eq. (3.76) and introducing the discrete control volumes:

$$\frac{d}{dt} (\Delta\Omega_{jk}) = \frac{1}{\rho_l} J_{jk}^c \Delta S_{jk}^t + \sum_{\substack{i=e',t,w', \\ n',s'}} v_{jk}^i \Delta S_{jk}^i \quad (3.78)$$

Indicating with $\underline{\delta}$ the vector of unknown liquid film thicknesses, with \underline{u} and \underline{v} the unknown vectors of the liquid film velocities and with \underline{T}^w the wall temperature vector, the liquid film mass balance can be written in the following compact form:

$$\dot{\underline{\delta}} = \underline{f}_\delta(\underline{\delta}, \underline{u}, \underline{v}, \underline{T}^w) \quad (3.79)$$

3.6.2 Vapor Domain

In a similar way, it is possible to obtain the mass conservation equation of the vapor phase. For each vapor control volume $\Delta\Omega_k^v$ delimited by $z - \Delta z/2$ and $z + \Delta z/2$ it is possible to write:

$$\Delta\Omega_k^V + \sum_j \Delta\Omega_{jk} = A_0 \Delta z \quad (3.80)$$

where A_0 is the cross sectional area of the channel. By differentiating the previous expression with respect to time, it is possible to obtain the time derivative of the vapor control volume:

$$\frac{d}{dt} \Delta\Omega_k^V = -\frac{d}{dt} \sum_j \Delta\Omega_{jk} \quad (3.81)$$

The mass conservation Eq. (3.2) can be written explicitly in terms of the vapor axial velocity U^v as:

$$(U^v S^v)_{k+1} = (U^v S^v)_k + \sum_j \frac{d}{dt} \Delta \Omega_{jk} - \frac{1}{\rho_v} \sum_j J_{jk}^c \Delta S_{jk}^t \quad (3.82)$$

where the expressions $(U^v S^v)_k$ and $(U^v S^v)_{k+1}$ indicate the momentum flux per unit density calculated at the *north* and *south* faces respectively. Substituting Eq. (3.78) into the previous equation, the following equation is obtained:

$$(U^v S^v)_{k+1} = (U^v S^v)_k + \sum_j \left(\frac{1}{\rho_l} - \frac{1}{\rho_v} \right) J_{jk}^c \Delta S_{jk}^t + \sum_j \sum_{\substack{i=e',w', \\ 'n', 's'}} v_{jk}^i \Delta S_{jk}^i \quad (3.83)$$

In a compact form, indicating with \underline{U} the vector of axial vapor velocities, the mass conservation equations for the vapor phase can be written as:

$$\underline{U} = \underline{f}_U(\underline{\delta}, \underline{u}, v, \underline{T}^w) \quad (3.84)$$

3.7 Momentum Conservation Equations

The momentum conservation equation in integral form, for constant density fluids, is as follows:

$$\frac{d}{dt} \int_{\Delta \Omega} \vec{v} d\Omega = \oint_{\partial \Delta \Omega} \vec{v} (\vec{v}_\partial - \vec{v}) \cdot d\vec{S} + \int_{\Delta \Omega} \vec{f}_b d\Omega + \oint_{\partial \Delta \Omega} \left(-\frac{p}{\rho} \vec{I} + \frac{\mu}{\rho} (\vec{\nabla} \vec{v} + \vec{\nabla} \vec{v}^T) \right) \cdot d\vec{S} \quad (3.85)$$

Consistent with the hypothesis of annular flow, the axial shear stress at the L-V interface is calculated with a modified version of the single phase correlation adopted by [38], in order to account for the relative velocity between the two phases. The modified version is detailed in the following lines. when vapor velocity is much greater than the interfacial liquid velocity then the axial shear stress reduces to the original expression. Indicating with U^v the mean axial vapor velocity, with U_r^v and Re_r^v the mean vapor velocity and vapor Reynolds number relative to the interface defined as:

$$U_r^v = U^v - v_\partial^l \quad (3.86)$$

$$Re_r^v = \frac{\rho_v D_{h,v} U_r^v}{\mu_v} \quad (3.87)$$

where $D_{h,v}$ is the vapor hydraulic diameter and v_∂^l is the axial superficial film velocity, the interface axial shear stress τ^i can be obtained with the following expression:

$$\tau^i = \frac{1}{2} C_f \rho_v (U_r^v)^2 \quad (3.88)$$

where C_f is the friction coefficient that can be calculated as follows:

$$C_f = \frac{\varphi}{e^\varphi - 1} C_{f,v} \quad (3.89)$$

$$\varphi = -\frac{2J^c}{C_{f,v}\rho_v U_r^v} \quad (3.90)$$

$$C_{f,v} = 2 \left[\left(\frac{8}{\text{Re}_r^v} \right)^{12} + \frac{1}{(A+B)^{3/2}} \right]^{\frac{1}{12}} \quad (3.91)$$

$$A = \left[-4\sqrt{2} \log_{10} \left(\frac{6.9}{\text{Re}_r^v} \right)^{0.9} \right]^{16} \quad (3.92)$$

$$B = \left(\frac{37530}{\text{Re}_r^v} \right)^{16} \quad (3.93)$$

where $C_{f,v}$ is the zero transpiration friction coefficient whereas ρ_v and μ_v are the vapor density and the dynamic viscosity. This correlation covers a wide range of vapor Reynolds numbers, in particular it is valid for $\text{Re}_r^v < 50000$. The correction term φ includes the momentum transfer effect induced by the condensation process (this phenomenon is often referred to as the "suction" effect). It results always in an increase of equivalent interfacial shear ($C_f \geq C_{f,v}$) but when the local condensing mass flow rate is negligible then $\varphi \rightarrow 0$ and consequently $C_f \rightarrow C_{f,v}$.

3.7.1 Liquid Domain

Referring to Eq. (3.85), the first term can be simply written based on the assumption that the liquid film velocity can be projected into two orthogonal directions, $\hat{\xi}_{jk}$ and \hat{z} :

$$\frac{d}{dt} \int_{\Delta\Omega} \vec{v} d\Omega = \frac{d}{dt} \left(u_{jk} \hat{\xi}_{jk} \Delta\Omega_{jk} \right) + \frac{d}{dt} \left(v_{jk} \hat{z} \Delta\Omega_{jk} \right) \quad (3.94)$$

By integrating over the surfaces of the cell control volume, the first term on the right hand side of Eq. (3.85), indicated with the symbol $\Delta\vec{Q}_{m,jk}$, can be written as:

$$\Delta\vec{Q}_{m,jk} = \sum_i \vec{v}_{jk} (\vec{v}_{\partial,jk} - \vec{v}_{jk}) \cdot \hat{n}_{jk}^i \Delta S_{jk}^i \quad (3.95)$$

The last term on the right hand side of Eq. (3.85) is composed by two different terms, being the first one related to the pressure and the second one to the momentum diffusive contribution. The pressure term $\Delta\vec{Q}_{p,jk}$ can be written in the following compact form:

$$\Delta\vec{Q}_{p,jk} = \frac{1}{\rho_l} \sum_i \hat{n}_{jk}^i p_{jk}^i \Delta S_{jk}^i \quad (3.96)$$

The momentum diffusive term is:

$$\Delta \vec{Q}_{\mu,jk} = \frac{1}{\rho_l} \sum_{i \neq t'} \hat{n}_{jk}^i \cdot \vec{F}_{jk}^i \Delta S_{jk}^i \quad (3.97)$$

The terms in the sums Eq. (3.95) and Eq. (3.97) corresponding to the index $i = 't'$ require a particular attention: as the equivalent interfacial shear Eq. (3.88) takes into account both the shear and the momentum transfer contribution due to the mass transfer process, it is then possible to write:

$$\vec{v}_{jk} (\vec{v}_{\partial,jk} - \vec{v}_{jk}) \cdot \hat{n}_{jk}^t \Delta S_{jk}^t + \hat{n}_{jk}^t \cdot \vec{F}_{jk}^t \Delta S_{jk}^t = \frac{1}{\rho_l} \hat{z} \tau_{jk}^t \Delta S_{jk}^t \quad (3.98)$$

The sum of the momentum diffusive term $\Delta \vec{Q}_{\mu,jk}$ and the momentum flux term $\Delta \vec{Q}_{m,jk}$, indicated with $\Delta \vec{Q}_{f,jk}$ is finally:

$$\Delta \vec{Q}_{f,jk} = - \sum_{i \neq t'} \vec{v}_{jk} (\vec{v}_{jk} \cdot \hat{n}_{jk}^i) \Delta S_{jk}^i + \frac{1}{\rho_l} \sum_{i \neq t'} \hat{n}_{jk}^i \cdot \vec{F}_{jk}^i \Delta S_{jk}^i + \frac{1}{\rho_l} \hat{z} \tau_{jk}^t \Delta S_{jk}^t \quad (3.99)$$

Each term of the momentum fluxes appearing in the first sum of the previous equation can be written in function of the bulk velocities $\vec{u}_{jk} = u_{jk} \hat{u}_{jk}$ and $\vec{v}_{jk} = v_{jk} \hat{v}_{jk}$ as it is detailed in Appendix A:

$$\vec{v}_{jk} (\vec{v}_{jk} \cdot \hat{n}_{jk}^i) \Delta S_{jk}^i = \kappa_{uv,jk} u_{jk} v_{jk} \hat{u}_{jk} (\hat{v}_{jk} \cdot \hat{n}_{jk}^i) \Delta S_{jk}^i \quad (3.100)$$

where:

$$\kappa_{uv,jk} = \frac{\frac{1}{3} - \frac{5}{24} (r_{u,jk} + r_{v,jk}) + \frac{2}{15} r_{u,jk} r_{v,jk}}{\frac{1}{4} - \frac{1}{6} (r_{u,jk} + r_{v,jk}) + \frac{1}{9} r_{u,jk} r_{v,jk}} \quad (3.101)$$

and the parameter $r_{u,jk}$ is defined by the following equation:

$$r_{u,jk} = - \left| \frac{1}{\tau_{jk}^{i,u}} \left(\frac{\partial p}{\partial z} \Big|_k - \rho_l \vec{f}_{b,jk} \cdot \hat{z} \right) \frac{\Delta S_{jk}}{\Delta l_{jk}} \right| \quad (3.102)$$

where the superficial shear stress $\tau_{jk}^{i,u}$ is the component in the direction of u_{jk} . Based on the assumptions and the hypothesis done, since the film velocity profile in the ξ direction is pressure gradient dominated (i.e. the interfacial shear stress is neglected with respect with the pressure gradient), then $r_{u,jk} \rightarrow -\infty$. Consequently, substituting into Eq. (3.101), it is possible to obtain:

$$\kappa_{uu,jk} = \frac{6}{5} \quad (3.103)$$

$$\kappa_{uv,jk} = \kappa_{vu,jk} = \frac{\frac{5}{8} - \frac{2}{5} r_{v,jk}}{\frac{1}{2} - \frac{1}{3} r_{v,jk}} \quad (3.104)$$

$$\kappa_{vv,jk} = \frac{\frac{1}{3} - \frac{5}{12} r_{v,jk} + \frac{2}{15} r_{v,jk}^2}{\frac{1}{4} - \frac{1}{3} r_{v,jk} + \frac{1}{9} r_{v,jk}^2} \quad (3.105)$$

The wall shear stress components can be written in the following forms:

$$\left(\hat{n}_{jk}^{(b)} \cdot \overleftarrow{F}_{jk}^{(b)} \right) \cdot \hat{\xi}_{jk} = -3\mu_l \frac{u_{jk}}{\delta_{jk}} \quad (3.106)$$

$$\left(\hat{n}_{jk}^{(b)} \cdot \overleftarrow{F}_{jk}^{(b)} \right) \cdot \hat{z} = -\frac{6 - 6r_{v,jk}}{3 - 2r_{v,jk}} \mu_l \frac{v_{jk}}{\delta_{jk}} \quad (3.107)$$

The body source term contribution $\Delta \vec{Q}_{b,jk}$ is simply written as:

$$\Delta \vec{Q}_{b,jk} = \vec{f}_{b,jk} \Delta \Omega_{jk} \quad (3.108)$$

By substituting Eq. (3.96), Eq. (3.99), Eq. (3.108) and Eq. (3.94) into Eq. (3.85) and projecting the obtained vector equation into the two directions $\hat{\xi}_{jk}$ and \hat{z}_{jk} , two sets of differential equations are obtained:

$$u_{jk} \frac{d}{dt} \Delta \Omega_{jk} + \Delta \Omega_{jk} \frac{d}{dt} u_{jk} = \Delta \vec{Q}_{f,jk} \cdot \hat{\xi}_{jk} + \Delta \vec{Q}_{fb,jk} \cdot \hat{\xi}_{jk} + \Delta \vec{Q}_{p,jk} \cdot \hat{\xi}_{jk} \quad (3.109)$$

$$v_{jk} \frac{d}{dt} \Delta \Omega_{jk} + \Delta \Omega_{jk} \frac{d}{dt} v_{jk} = \Delta \vec{Q}_{f,jk} \cdot \hat{z} + \Delta \vec{Q}_{fb,jk} \cdot \hat{z} + \Delta \vec{Q}_{p,jk} \cdot \hat{z} \quad (3.110)$$

The interfacial pressure p_{jk}^i in Eq. (3.96) is calculated with Eq. (3.54) and therefore it accounts for the surface tension and disjoining pressure contributions:

$$p_{jk}^i = p_k^v + \sigma K_{jk} + \frac{A}{\delta_{jk}^3} + \left(\frac{1}{\rho_v} - \frac{1}{\rho_l} \right) (J_{jk}^c)^2 \quad (3.111)$$

where the vapor pressure p_k^v is function only of the axial coordinate z_k . The axial L-V shear stress is calculated with Eq. (3.88), Eq. (3.89), Eq. (3.90), Eq. (3.91), Eq. (3.92) and Eq. (3.93). The liquid pressure across the film (in a direction perpendicular to the film) is assumed to be a linear function of local depth due to the local gravitational contribution which can be obtained by scalar multiplication of the body source vector with the local normal to the wall unit vector. By indicating with \underline{p} the vector of the vapor phase pressures, the liquid film momentum equations can be written in the following compact form:

$$\begin{aligned} \underline{\dot{u}} &= \underline{f}_u(\underline{\delta}, \underline{u}, \underline{v}, \underline{T}^w) \\ \underline{\dot{v}} &= \underline{f}_v(\underline{\delta}, \underline{u}, \underline{v}, \underline{T}^w, \underline{U}, \underline{p}) \end{aligned} \quad (3.112)$$

3.7.2 Vapor Domain

The time derivative of the vapor axial momentum per unit mass can be computed as:

$$\frac{d}{dt} (\Delta \Omega_k^v U_k^v) = U_k^v \frac{d}{dt} \Delta \Omega_k^v = -U_k^v \sum_j \frac{d}{dt} \Delta \Omega_{jk} + \Delta \Omega_k^v \frac{d}{dt} U_k^v \quad (3.113)$$

The control volume $\Delta\Omega_k^v$ is calculated through Eq. (3.81). The sum of the momentum diffusive term and the momentum flux term per unit density, indicated with $\Delta Q_{f,k}^v$, is calculated in the following way:

$$\Delta Q_{f,k}^v = U_k^v (U^v S^v)_k^{(n)} - U_k^v (U^v S^v)_k^{(s)} - \frac{1}{\rho_v} \sum_j \tau_{jk}^i \Delta S_{jk}^t \quad (3.114)$$

The body force contribution and the pressure term contribution are:

$$\Delta \vec{Q}_{b,k}^v = \vec{f}_{b,k}^v \Delta \Omega_k^v \quad (3.115)$$

$$\Delta Q_{p,k}^v = \frac{1}{\rho_v} \left(p_k^{v,(n)} - p_k^{v,(s)} \right) S_k^v \quad (3.116)$$

$$\Delta Q_{\mu,k}^V = -\frac{1}{\rho_v} \sum_j \tau_{jk}^i \Delta S_{jk}^t \quad (3.117)$$

Solving for the vapor pressure, the momentum equation of the vapor phase can be written in the following compact form:

$$\underline{p} = \underline{f}_p \left(\underline{\delta}, \underline{u}, \underline{v}, \underline{U}, \underline{\dot{U}} \right) \quad (3.118)$$

3.8 Limits of the Model

The model has been developed on the basic assumption that the film flow is laminar. Based on the work presented by Cioncolini et al. [65], the criterion that can be used to determine if the flow is laminar is based on the definition of the following turbulent parameter δ^+ :

$$\delta^+ = \sqrt{\frac{\tau_w}{\rho_l} \frac{\rho_l \delta}{\mu_l}} \quad (3.119)$$

where τ_w is the shear stress calculated at the wall. If $\delta^+ < 50$, then it is possible to say that the turbulent viscosity and turbulent conductivity are negligible. For some of the simulated cases, the maximum calculated values of δ^+ are reported in the simulations in Chapter 6. This turbulent parameter is proportional to the square root of the liquid Reynolds number, therefore moving to the microchannel range while keeping constant the mass flux allows the model to be applied to a wider range of conditions, as the Reynolds number is reduced. On the other hand, an increase of the hydraulic diameter facilitates a earlier transition from laminar to turbulent flow, thus limiting the applicability of the present model (particularly to low vapor qualities).

An other important assumption concerns the flow pattern: the model is developed for annular flow only; that is, it is only applicable when a unique liquid-vapor interface is present in the domain in such a way that can be described by a function $\vec{\delta}$. Intermittent flows or two-phase flows having a non negligible amount of entrainment cannot be simulated; consequently, the complete condensation process (from a vapor quality of 1 to 0) cannot be simulated but only partial condensation can be investigated (having an exit vapor quality greater than 0).

3.9 Summary

The structure of the numerical model and the hypothesis that have been assumed are presented in this chapter. The two fluids modeling approach has been chosen and the finite volume method has been adopted to solve for Navier-Stokes and energy equations. The resulting set of ordinary differential equations can be solved with the specified initial conditions and boundary conditions. The evolution in time of the liquid-vapor interface, liquid and vapor velocity and pressure, temperature distribution and condensation mass flux can be obtained and analyzed for different geometries and conditions.

Chapter 4

Dimensional Analysis and Theoretical Investigation

The dimensional analysis of the physical problem is addressed in this chapter. The appropriate selection of the reference parameters is obtained thus allowing the dimensionless set of equations and boundary conditions to be identified. The Order of Magnitude Analysis (O.M.A.) method is used in order to set the group of independent dimensionless numbers.

4.1 Order of Magnitude and Dimensional Analysis

The equations that have been developed in the previous chapter contain sets of dimensional groups and the solution is a function of those parameters. It is useful to derive from those the independent dimensionless groups in order to characterize in a unique way the system of equations and to provide scalable solutions. The following advantages make this approach well suited for the considered physical problem:

- a deeper physical understanding of the phenomena can be achieved allowing similarity solutions to be obtained;
- the leading equations can be simplified by removing the terms containing the dimensionless groups which under certain circumstances do not influence the result;
- the solution procedure of the set of equations in dimensionless form is much better conditioned in terms of numerical stability of the code and this becomes necessary when a large scale parametric study is undertaken (i.e. ranging from 2 *mm* down to 10 μ *m* hydraulic diameters)

An important reference parameter is the characteristic length of the problem. This length is assumed to be proportional to H^{-1} where H is the mean absolute curvature of the section (in

the x - y plane), it has the dimensions of m^{-1} and it is defined as follows:

$$H \equiv \frac{1}{P} \int_P |K|_{xy} dl \quad (4.1)$$

This parameter is always positive and accounts for concave and convex geometries as well while for a circular channel it becomes simply the inverse of its radius. Indicating with D_h the hydraulic diameter of the channel, it is interesting to note that the product $D_h H = r = \text{const.}$ for a given geometry. This first dimensionless group r depends on the actual shape of the inner perimeter and not on its size.

The distribution of the film thickness, the liquid and vapor velocities, liquid and vapor pressure are the outputs of the solution. From the heat transfer point of view, the most important are the following: the local heat transfer coefficient, the perimeter-averaged heat transfer coefficient and the global heat transfer coefficient; furthermore the wall temperature distribution, the frictional pressure drop and the vapor quality distribution are also relevant. The local heat transfer coefficient h_l is defined as:

$$h_l \equiv \frac{k_l}{T^w - T^s} \left. \frac{\partial T}{\partial n} \right|_w \quad (4.2)$$

Following this definition, the local perimeter-averaged heat transfer coefficient $h(z)$ is:

$$h(z) \equiv \frac{k_l}{T^w(z) - T^s} \frac{1}{P} \int_P \left. \frac{\partial T}{\partial n} \right|_w(z) dl \quad (4.3)$$

The global heat transfer coefficient h_g is then:

$$h_g \equiv \frac{1}{L_t} \int_0^{L_t} h(z) dz \quad (4.4)$$

The local vapor quality X is defined as:

$$X \equiv \frac{\dot{m}_v}{\dot{m}_v + \dot{m}_l} = \frac{\dot{m}_v}{GS_0} \quad (4.5)$$

where \dot{m}_v and \dot{m}_l are the vapor and liquid mass flow rates. Each of these parameters, which can be obtained by solving the set of equations, depends exclusively on the sets of dimensional groups in the equations. The Buckingham II theorem, which is reported in Appendix B, guarantees that a proper relationship can be written in dimensionless form including these groups and maximal set of independent dimensionless numbers. The Order of Magnitude Analysis (O.M.A.) is applied here to identify the characteristic dimensional groups. Some of these can be obtained through a straightforward definition, while a detailed analysis is conducted to characterize the capillary heat transfer process when different boundary conditions are applied at the energy equation .

4.2 Dimensional Parameters of the Physical Model

The order of magnitude of the interfacial shear stress τ_r^i is estimated by the single phase friction factor correlation Eq. (3.88):

$$\tau_r^i = \frac{1}{2} C_f (Re_v) \frac{G^2}{\rho_v} \quad (4.6)$$

where Re^v is the single phase vapor Reynolds number. The corresponding reference pressure drop is defined based on the single phase expression:

$$\Delta p_r = -4\tau_r^i \frac{L_t}{D_h} \quad (4.7)$$

The axial single phase liquid and vapor mean velocities are set as the reference axial velocities:

$$v_{r,l} = \frac{G}{\rho_l} \quad (4.8)$$

$$U_{r,v} = \frac{G}{\rho_v} \quad (4.9)$$

In case that the wall temperature and the gravity field g_{x_i} ($i = 1, 2, 3$) are assigned, the following dimensional matrix can be identified from the equations:

| | | | | | | | | | | | |
|-----|-----|------------------------|--------------------|-------------------------|---|-----|----------------------|-------------------------------------|---------------------------------|-----------|--------|
| | H | $\frac{\mu_l}{\rho_l}$ | $\frac{G}{\rho_l}$ | $\frac{\sigma}{\rho_l}$ | $\frac{k_l \Delta T}{\rho_l \Delta h_{lv}}$ | z | $\frac{A}{\sigma H}$ | $\frac{J_P \sigma H}{J_T \Delta T}$ | $\frac{k_l}{J_T \Delta h_{lv}}$ | g_{x_i} | |
| [m] | -1 | 2 | 1 | 3 | 2 | 1 | 3 | 0 | 1 | 1 | (4.10) |
| [s] | 0 | -1 | -1 | -2 | -1 | 0 | 0 | 0 | 0 | -2 | |

If the steady state condition is assumed and imposed wall temperature boundary condition is applied, the Buckingham II theorem shows that there are 13 independent dimensionless numbers including the geometrical relationship existing between H and the hydraulic diameter. If the imposed heat flux condition is assumed a further dimensionless group is necessary accounting for the effects of the axial conduction; finally, if an external single phase heat transfer coefficient is assumed then another independent dimensionless group appears, accounting for the relative importance of internal and external heat transfer coefficients. The detailed derivations of these groups are shown in the following subsections.

4.2.1 Imposed Wall Temperature

The following reasoning is proposed, in order to identify the characteristic film thickness and peripheral liquid film bulk velocity when the wall temperature is imposed. It is assumed that the capillary and liquid viscosity forces (acting at the channel surface) are dominant in the physical problem being considered. The axial contributions are neglected and the corresponding terms are set to zero in the O.M.A. The curvilinear coordinate, consistently with the choice of the dimensional scale, is supposed to be proportional to H^{-1} . From the momentum equation,

indicating the characteristic film velocity with u_σ and the film thickness with δ_σ , assuming that the order of magnitude of the groups in the Navier-Stokes equations corresponding to capillary forces and viscous forces are the same, we have:

$$\delta_\sigma \frac{\sigma}{\rho_l} \frac{\partial}{\partial \xi} \left(\frac{\partial^2 \delta_\sigma}{\partial \xi^2} \right) \approx \frac{\mu_l u_\sigma}{\rho_l \delta_\sigma} \Rightarrow \delta_\sigma \frac{\sigma}{\rho_l} H \cdot H^2 \delta_\sigma \approx \frac{\mu_l u_\sigma}{\rho_l \delta_\sigma} \Rightarrow u_\sigma = \frac{\sigma}{\mu_l} H^3 \delta_\sigma^3 \quad (4.11)$$

From the mass balance equation, equalizing the terms corresponding to convective contribution and condensing contribution and substituting the expression of u_σ from the previous equation we obtain:

$$\frac{\partial}{\partial \xi} (u_\sigma \delta_\sigma) \approx \frac{k_l \Delta T}{\rho_l \Delta h_{l-v}} \frac{1}{\delta_\sigma} \Rightarrow H \cdot \frac{\sigma}{\mu_l} H^3 \delta_\sigma^3 \cdot \delta_\sigma = \frac{k_l \Delta T}{\rho_l \Delta h_{l-v}} \frac{1}{\delta_\sigma} \quad (4.12)$$

Solving for the characteristic film thickness and velocity, we finally obtain:

$$\delta_\sigma = \left(\frac{k_l \mu_l \Delta T}{\sigma \rho_l \Delta h_{l-v} H^4} \right)^{\frac{1}{5}} \quad (4.13)$$

$$u_\sigma = \left(\frac{\sigma^2 k_l^3 \Delta T^3 H^3}{\mu_l^2 \rho_l^3 \Delta h_{l-v}^3} \right)^{\frac{1}{5}} \quad (4.14)$$

The characteristic Nusselt number, identified by the symbol Sn_T , can be obtained by the parameters defined above:

$$\text{Sn}_T \equiv H^{-1} \delta_c^{-1} = \left(\frac{\sigma \rho_l \Delta h_{l-v}}{k_l \mu_l \Delta T H} \right)^{\frac{1}{5}} \quad (4.15)$$

This dimensionless number is sought to represent how the local Nusselt number scales for difference sizes, different subcoolings and different fluids. In fact, from the definition of Sn_T , it is possible to verify that:

$$\text{Sn}_T = \left(\frac{\sigma \rho_l \Delta h_{l-v}}{k_l \mu_l \Delta T H} \right)^{\frac{1}{5}} = H^{-1} \delta_c^{-1} = \frac{1}{H} \frac{k_l}{\delta_c} \frac{1}{k_l} = \frac{h_c}{H k_l} \propto \frac{h D_h}{k_l} = \text{Nu} \quad (4.16)$$

The capillary Reynolds number Re_T definition is straightforward:

$$\text{Re}_T \equiv \frac{\rho_l u_\sigma \delta_\sigma}{\mu_l} = \left(\frac{\sigma \rho_l k_l^4 \Delta T^4}{\mu_l^6 \Delta h_{l-v}^4 H} \right)^{\frac{1}{5}} \quad (4.17)$$

The dimensionless axial location $Z \equiv \frac{z}{D_h}$, the liquid Weber number, the vapor Reynolds number, the Bond numbers (related to the three directions of the gravity field) and the density ratio follow the standard definitions (see 4.3).

By the analysis of Eq. (3.69) and Eq. (3.70) and the characteristic capillary film thickness definition, the interface mass transfer can be characterized by three dimensionless numbers: the interface resistance number, the interface pressure number and the disjoining pressure number. The interface mass transfer number represents the ratio between the interfacial resistance and

the liquid film thermal resistance; for the imposed wall temperature case it is defined as:

$$\mathbf{I}_{r,T} \equiv \frac{\phi_r}{J_T} = \frac{k_l}{J_T \Delta h_{l-v} \delta_\sigma} = \frac{1}{J_T} \left(\frac{\sigma k_l^4 \rho_l H^4}{\mu_l \Delta h_{l-v}^4 \Delta T} \right)^{\frac{1}{5}} \quad (4.18)$$

The interface pressure number represents the ratio between the mass flux contribution due to the pressure jump across the interface and the mass flux due to temperature difference; consistently with the choice of the dimensional scale, the characteristic curvature is assumed to be equal to H :

$$\mathbf{I}_{p,T} \equiv \frac{J_p \sigma H}{J_T \Delta T} \quad (4.19)$$

Finally, referring to Eq. (3.70), the disjoining pressure number is conveniently defined as the ratio between the characteristic pressure jump occurring at the L-V interface due to the disjoining pressure (evaluated at $\delta = \delta_\sigma$) and the pressure jump due only to the curvature:

$$\mathbf{I}_{d,T} \equiv \frac{A}{\sigma H \delta_\sigma^3} = A \left(\frac{\rho_l^3 \Delta h_{l-v}^3 H^7}{\sigma^2 \mu_l^3 k_l^3 \Delta T^3} \right)^{\frac{1}{5}} \quad (4.20)$$

It is interesting to see how these numbers scale with the characteristic length H^{-1} : the exponent of the mean absolute curvature is respectively $-4/5$, -1 and $-7/5$, thus suggesting that the importance of these terms becomes relevant as the scale of the problem is reduced (micro-channel).

The expression of the characteristic interface mass transfer value, referring to Eq. (3.68) Eq. (3.69) and Eq. (3.70) can be finally written as:

$$J_r^c = J_{r,0}^c \frac{\sqrt{1+4\varrho} - 1}{2\varrho} \quad (4.21)$$

where:

$$J_{r,0}^c = \frac{\phi_r \Delta T}{1 + \mathbf{I}_{r,T}} [1 - \mathbf{I}_{p,T} (1 + \mathbf{I}_{d,T})] \quad (4.22)$$

and

$$\varrho = \left(\frac{1}{\Gamma} - 1 \right) \frac{\mathbf{I}_{p,T}}{(1 + \mathbf{I}_{r,T})^2} [1 - \mathbf{I}_{p,T} (1 + \mathbf{I}_{d,T})] \frac{\text{Re}_T}{\text{Sn}_T^4} \quad (4.23)$$

4.2.2 Imposed Heat Flux

If the steady state condition is assumed (i.e. the heat flux is assumed constant) the Buckingham Π theorem shows that in this case there are 14 independent dimensionless numbers, namely one more than in the previous case. This number is related to the conduction problem in the wall which now is coupled with the inner condensation process. A theoretical approach, which is

described in Appendix C, shows that this number can be conveniently defined as:

$$L_{\text{ht}} \equiv \frac{l_c}{L_t} \quad (4.24)$$

where l_c is the characteristic heat transfer length defined as:

$$l_c = \sqrt{\frac{k_w \lambda_w}{h_i}} \quad (4.25)$$

being h_i the characteristic heat transfer coefficient on the condensing side.

An approach similar to the one proposed in the previous section can be applied in order to estimate the characteristic film thickness, liquid film bulk velocity and temperature difference when an imposed heat flux condition is considered. In the limit of neglecting the thermal conductivity of the channel wall and making use of Eq. (4.11), the mass balance equation leads to:

$$H \cdot \frac{\sigma}{\mu_l} H^3 \delta_q^3 \cdot \delta_q = \frac{|\dot{q}|}{\rho_l \Delta h_{l-v}} \quad (4.26)$$

being $|\dot{q}|$ the absolute value of the heat flux. Solving for the characteristic film thickness δ_q we obtain:

$$\delta_q = \left(\frac{\mu_l |\dot{q}|}{\sigma \rho_l \Delta h_{l-v} H^4} \right)^{\frac{1}{4}} \quad (4.27)$$

Substituting back this expression into Eq. (4.11):

$$u_q = \left(\frac{\sigma |\dot{q}|^3}{\mu_l \rho_l^3 \Delta h_{l-v}^3} \right)^{\frac{1}{4}} \quad (4.28)$$

The characteristic Nusselt number Sn_q results in:

$$\text{Sn}_q \equiv \left(\frac{\sigma \rho_l \Delta h_{l-v}}{\mu_l |\dot{q}|} \right)^{\frac{1}{4}} \quad (4.29)$$

The characteristic film Reynolds number Re_q is:

$$\text{Re}_q = \frac{|\dot{q}|}{\mu_l \Delta h_{l-v} H} \quad (4.30)$$

The characteristic film temperature difference ΔT_q is:

$$\Delta T_q = \left(\frac{\mu_l |\dot{q}|^5}{\sigma k_l^4 \rho_l \Delta h_{l-v} H^4} \right)^{\frac{1}{4}} \quad (4.31)$$

The interface resistance, interfacial pressure and disjoining pressure numbers follow the formal

definitions given above:

$$I_{r,q} \equiv \frac{1}{J_T} \left(\frac{\sigma k_l^4 \rho_l H^4}{\mu_l \Delta h_{l-v}^3 |\dot{q}|} \right)^{\frac{1}{4}} \quad (4.32)$$

$$I_{p,q} \equiv \frac{J_p}{J_T} \left(\frac{\sigma^5 \rho_l k_l^4 \Delta h_{l-v} H^8}{\mu_l |\dot{q}|^5} \right)^{\frac{1}{4}} \quad (4.33)$$

$$I_{d,q} \equiv A \left(\frac{\rho_l^3 \Delta h_{l-v}^3 H^8}{\sigma \mu_l^3 |\dot{q}|^3} \right)^{\frac{1}{4}} \quad (4.34)$$

4.2.3 External Heat Transfer Coefficient

If it is assumed that the condensation process is induced by a cold fluid flowing outside the refrigerant channel and the external heat transfer coefficient α_e is fixed, the O.M.A. of the mass balance equation has to be corrected to account for the external-internal coupling for the heat transfer. Setting δ_α the characteristic film thickness and maintaining the assumptions previously done, the energy balance equation of the wall can be formally written as:

$$\frac{k_l (T^s - T^w)}{\delta_\alpha} = \alpha_e (T^w - T^c) \quad (4.35)$$

where T^c is the cold fluid temperature. The saturation to local wall temperature difference becomes then:

$$T^s - T^w = \frac{1}{1 + \frac{k_l}{\alpha_e \delta_\alpha}} (T^s - T^c) \quad (4.36)$$

Substituting this expression in the mass conservation equation Eq. (4.12):

$$\frac{\sigma}{\mu_l} H^4 \delta_\alpha^4 = \frac{k_l (T^s - T^c)}{\rho_l \Delta h_{l-v}} \frac{1}{\delta_\alpha} \frac{1}{1 + \frac{k_l}{\alpha_e \delta_\alpha}} \quad (4.37)$$

In the limit of very high external heat transfer coefficient ($\alpha_e \rightarrow +\infty$), the film characteristic thickness $\delta_{\alpha,\infty}$ is:

$$\delta_{\alpha,\infty} = \left(\frac{k_l \mu_l (T^s - T^c)}{\sigma \rho_l \Delta h_{l-v} H^4} \right)^{\frac{1}{5}} \quad (4.38)$$

which is formally equivalent to the expression of δ_T in Eq. (4.13), where the actual temperature difference ΔT is substituted by $T^s - T^c$. The mass conservation equation Eq. (4.37) can now be written in the following form:

$$\rho_l \Delta h_{l-v} \frac{\sigma}{\mu_l} H^4 \delta_\alpha^4 (\alpha_e \delta_\alpha + k_l) = \alpha_e k_l (T^s - T^c) \quad (4.39)$$

Defining $X \equiv \frac{\delta_\alpha}{\delta_{\alpha,\infty}}$, the previous equation can be finally written in this non dimensional form:

$$X^5 + \Pi_\alpha X^4 - 1 = 0 \quad (4.40)$$

where $\Pi_\alpha \equiv \frac{k_l}{\alpha_e \delta_{\alpha, \infty}}$ represents the ratio between the characteristic internal and the external heat transfer coefficients. This equation defines the implicit relationship $X = X(\Pi_\alpha)$. The dimensionless temperature difference Θ can be conveniently defined as:

$$\Theta \equiv \frac{T^s - T^w}{T^s - T^c} = \frac{X(\Pi_\alpha)}{X(\Pi_\alpha) + \Pi_\alpha} \quad (4.41)$$

The condition by which the internal and the external heat transfer coefficients are equal (the wall temperature is in this case the mean value between the cold fluid and the saturation temperatures which corresponds to a value of $\Theta = 0.5$), leads to a value of $X = \Pi_\alpha = 2^{-\frac{1}{5}} \simeq 0.8706$. The solution $X = X(\Pi_\alpha)$ of Eq. (4.40) and the function $\Theta = \Theta(\Pi_\alpha)$ are represented in Fig. (4.1). The definitions of the interface dimensionless numbers follow the ones given in 4.2.1 where the characteristic film thickness is set arbitrary to $\delta_{\alpha, \infty}$. It is clear from Fig. (4.1) then when

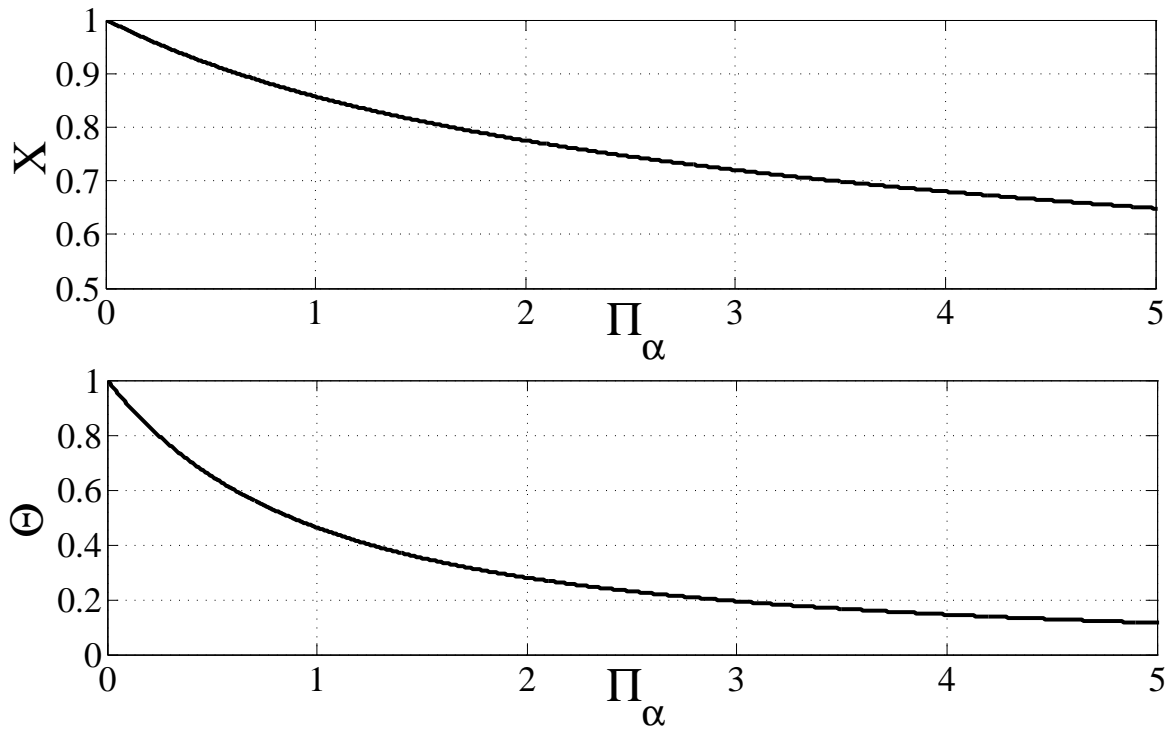


Figure 4.1: Dimensionless film thickness X and dimensionless temperature Θ solution of Eq. (4.40) plotted as a function of Π_α

the external heat transfer coefficient is sufficiently large then the characteristic dimensionless film thickness X tends to 1, namely the wall temperature becomes constant and equal to the cold fluid temperature T^c ; on the other hand, if the internal heat transfer coefficient becomes predominant then the wall temperature tends to the saturation temperature. For a sufficiently large saturation to wall temperature difference, this case corresponds to the uniform imposed heat flux limit.

4.2.4 Mini to Microscale Condensation Transition: Capillary and Gravity dominated regimes

The O.M.A. method can be applied in the same way as in 4.2.1 and 4.2.2 in order to identify the proper length scale (condensate film thickness) when a gravity field (belonging to the $x - y$ plane) is assumed to be the leading term in the Navier-Stokes equations and laminar conditions are assumed. From the momentum equation, indicating the characteristic film velocity with $u_{g,T}$ and the film thickness with $\delta_{g,T}$, assuming that the order of magnitude of the groups in the Navier-Stokes equations corresponding to gravity forces and viscous forces are the same, we have:

$$\mu_l \frac{u_g}{\delta_{g,T}} \approx \delta_{g,T} (\rho_l - \rho_v) g \Rightarrow u_{g,T} = \frac{\delta_{g,T}^2}{\mu_l} (\rho_l - \rho_v) g \quad (4.42)$$

From the mass balance equation, equalizing the terms corresponding to convective contribution and condensing contribution and substituting the expression of $u_{g,T}$ from the previous equation we obtain:

$$\frac{\partial(u\delta)}{\partial w} \approx \frac{k_l \Delta T}{\rho_l \Delta h_{l-v}} \frac{1}{\delta_g} \Rightarrow H \cdot \frac{\delta_g^2}{\mu_l} (\rho_l - \rho_v) g \cdot \delta_g = \frac{k_l \Delta T}{\rho_l \Delta h_{l-v}} \frac{1}{\delta_g} \quad (4.43)$$

Solving for the characteristic film thickness, we finally obtain:

$$\delta_g = \left(\frac{\mu_l k_l \Delta T}{\rho_l (\rho_l - \rho_v) \Delta h_{l-v} g H} \right)^{\frac{1}{4}} \quad (4.44)$$

$$u_g = \left(\frac{k_l \Delta T (\rho_l - \rho_v) g}{\mu_l \rho_l \Delta h_{l-v} H} \right)^{\frac{1}{2}} \quad (4.45)$$

The corresponding characteristic Nusselt number Sn_g is then:

$$Sn_g = H^{-1} \delta_g^{-1} = \left(\frac{\rho_l \Delta h_{l-v} (\rho_l - \rho_v) g}{k_l \Delta T \mu_l H^3} \right)^{\frac{1}{4}} \quad (4.46)$$

Solving the same problem for the imposed heat flux case leads to the following characteristic film thickness $\delta_{g,q}$ and velocity $u_{g,q}$:

$$\delta_{g,q} = \left(\frac{\mu_l |\dot{q}|}{\rho_l \Delta h_{l-v} (\rho_l - \rho_v) g H} \right)^{\frac{1}{3}} \quad (4.47)$$

$$u_{g,q} = \left(\frac{g (\rho_l - \rho_v) |\dot{q}|^2}{\mu_l \rho_l^2 \Delta h_{l-v}^2 H^2} \right)^{\frac{1}{3}} \quad (4.48)$$

The ratio between δ_σ and δ_g or δ_q and $\delta_{g,q}$ may be considered as an indication of the relative importance of capillary and gravitational forces:

$$\frac{\delta_\sigma}{\delta_g} = \frac{g^{\frac{1}{4}} (\rho_l - \rho_v)^{\frac{1}{4}} \rho_l^{\frac{1}{20}} \Delta h_{l-v}^{\frac{1}{20}} H^{-\frac{11}{20}} \Delta T^{-\frac{1}{20}}}{\sigma^{\frac{1}{5}} k_l^{\frac{1}{20}} \mu_l^{\frac{1}{20}}} \quad (4.49)$$

$$\frac{\delta_q}{\delta_{g,q}} = g^{\frac{1}{3}} H^{-\frac{2}{3}} |\dot{q}|^{-\frac{1}{12}} \frac{(\rho_l - \rho_v)^{\frac{1}{3}} \rho_l^{\frac{1}{12}} \Delta h_{l-v}^{\frac{1}{12}}}{\mu_l^{\frac{1}{12}} \sigma^{\frac{1}{4}}} \quad (4.50)$$

If $\delta_\sigma \simeq \delta_g$ it is expected that the condensation process is affected by the combined effect of gravity and capillary forces ($\text{Sn}_T \simeq \text{Sn}_g$); this condition may be identified as a threshold between capillary dominated laminar condensation ($\text{Sn}_T \gg \text{Sn}_g$) and gravity driven dominated laminar condensation ($\text{Sn}_T \ll \text{Sn}_g$).

4.3 Summary of the Dimensionless Numbers

The following non-dimensional numbers represent the selected independent dimensionless groups of the problem:

- Capillary Nusselt Number (Sn): it represents the characteristic Nusselt number for annular laminar film condensation when the physical process is dominated by the viscous and surface tension forces in the liquid phase. Its definitions are given in Eq. (4.15) and Eq. (4.29) for imposed temperature difference and heat flux respectively;
- Capillary Reynolds Number (Re): it represents the characteristic ratio between the inertia forces and viscous forces in the capillary and viscous dominated regime in the liquid film. Its definitions are given in Eq. (4.17) and Eq. (4.30);
- Single Phase Weber Number (We_l): it represents the relative importance of the inertia forces and surface tension forces in the liquid phase:

$$\text{We}_l \equiv \frac{D_h G^2}{\sigma \rho_l} \quad (4.51)$$

- Single Phase Vapor Reynolds Number (Re_v): it is a measure of the ratio of the inertia forces to viscous forces in the vapor phase:

$$\text{Re}_l \equiv \frac{G D_h}{\mu_v} \quad (4.52)$$

- Density Ratio Number (Γ): it is the ratio between the vapor and the liquid densities:

$$\Gamma \equiv \frac{\rho_v}{\rho_l} \quad (4.53)$$

- Interfacial Resistance Number (I_r): it represents the ratio of the temperature jump at the liquid-vapor interface and the liquid film temperature jump. Its definition is given in Eq. (4.18);

- Interfacial Pressure Number (I_p): this number represents the relative importance of pressure jump and temperature jump in the mass transfer process at the L-V interface and the definition is given in Eq. (4.19);
- Interfacial Disjoining Pressure Number (I_d): this number represents the relative importance of the pressure gradient in the capillary film between adhesion forces and surface tension forces. Eq. (4.20) gives its formal definition;
- Bond numbers (Bo_{x_i}): this number is a measure of the importance of body forces compared to surface tension forces. For a given gravitational field having components g_{x_i} the definition is:

$$Bo_{x_i} \equiv \frac{(\rho_l - \rho_v) g_{x_i} D_h^2}{\sigma} \quad (4.54)$$

- Axial position (Z): the dimensionless ratio between the axial position z and the hydraulic diameter D_h ;
- Dimensionless Time (Π_t): it is defined as the ratio of time t and the characteristic time t_c which is defined as:

$$t_c \equiv \frac{\delta_\sigma}{u_\sigma} \quad (4.55)$$

Within the dimensionless groups that can be obtained from the solution of the problem, the most relevant for the heat transfer point of view are the following:

- Nusselt number (Nu): it represents the ratio of the heat transfer due to the condensation process and the heat transfer due to the pure conduction of the liquid phase. It is defined as:

$$Nu \equiv \frac{h D_h}{k_l} \quad (4.56)$$

where h is the heat transfer coefficient. Following the definitions of local, perimeter-averaged and global heat transfer coefficients given in Eq. (4.2), Eq. (4.3) and Eq. (4.4), the corresponding definitions of Nusselt numbers are straightforward;

- vapor quality (X): it is the ratio of vapor mass flow rate over the sum of vapor and liquid mass flow rates. Its definition is given in Eq. (4.5)
- dimensionless film thickness (δ^*): it is the ratio of the local film thickness δ over the characteristic film thickness defined by Eq. (4.13) or Eq. (4.27) depending on the case:

$$\delta^* \equiv \frac{\delta}{\delta_{\sigma,(q)}} \quad (4.57)$$

- dimensionless axial velocity (v^*): the dimensionless ratio between the local axial liquid film bulk velocity v and the characteristic liquid film velocity defined in Eq. (4.8);

- dimensionless temperature (Θ):

$$\Theta \equiv \frac{T_{ref} - T}{\Delta T_{ref}} \quad (4.58)$$

where T_{ref} and ΔT_{ref} are a reference temperature and a reference temperature difference respectively. The definition is applicable to either the interfacial temperature $T = T^i$, the film bulk temperature $T = T_f$ or the wall temperature $T = T^w$;

- dimensionless frictional pressure drop $\left(\frac{\partial P}{\partial Z}\right)_f^*$: it is defined as the ratio of the local frictional pressure drop and the frictional pressure drop that is due to the vapor phase only having the same total mass flow rate:

$$\left(\frac{\partial P}{\partial Z}\right)_f^* \equiv -\frac{D_h}{4\tau_r^i} \frac{\partial p_f}{\partial z} = -\frac{\rho_v D_h}{2C_f (Re_v) G^2} \frac{\partial p_f}{\partial z} \quad (4.59)$$

4.3.1 Dimensionless Form of the Solution

Following the Buckingham Theorem, each of the dependent dimensionless number Φ presented in the previous section that can be obtained from the solution of the problem can be expressed as a unique function of the free dimensionless groups in the form:

$$\Phi = \Psi(\Pi_1, \Pi_2, \dots, \Pi_n) \quad (4.60)$$

where n is the number of free independent dimensionless numbers Π_i .

Applying this theorem to the perimeter-averaged Nusselt number and the vapor quality, when imposed wall temperature is considered, the steady state solution (i.e. all the boundary and subdomain conditions are constant in time) for a specific geometry can be written as:

$$\text{Nu} = \text{Nu}(Z, \text{Sn}_T, \text{Re}_T, \text{We}_l, \text{Re}_v, \Gamma, \text{Bo}_{x_i}, \text{I}_{r,T}, \text{I}_{p,T}, \text{I}_{d,T}) \quad (4.61)$$

$$X = X(Z, \text{Sn}_T, \text{Re}_T, \text{We}_l, \text{Re}_v, \Gamma, \text{Bo}_{x_i}, \text{I}_{r,T}, \text{I}_{p,T}, \text{I}_{d,T}) \quad (4.62)$$

Assuming that it is possible to invert the previous equation solving with respect to Z and substituting back into Eq. (4.61), the Nusselt number can be expressed as a function of the local vapor quality:

$$\text{Nu} = \text{Nu}(X, \text{Sn}_T, \text{Re}_T, \text{We}_l, \text{Re}_v, \Gamma, \text{Bo}_{x_i}, \text{I}_{r,T}, \text{I}_{p,T}, \text{I}_{d,T}) \quad (4.63)$$

If the imposed heat flux is considered, then Eq. (4.63) becomes:

$$\text{Nu} = \text{Nu}(X, \text{Sn}_q, \text{Re}_q, \text{We}_l, \text{Re}_v, \Gamma, \text{Bo}_{x_i}, \text{I}_{r,q}, \text{I}_{p,q}, \text{I}_{d,q}, \text{L}_{ht}) \quad (4.64)$$

which includes also the conjugate heat transfer dimensionless length L_{ht} . Finally, if the single phase external cooling is imposed, then the relative importance of internal and external heat

transfer coefficients have to be taken into account as well through Π_α :

$$\text{Nu} = \text{Nu}(X, \text{Sn}_T, \text{Re}_T, \text{We}_l, \text{Re}_v, \Gamma, \text{Bo}_{x_i}, I_{r,T}, I_{p,T}, I_{d,T}, L_{ht}, \Pi_\alpha) \quad (4.65)$$

Similar kind of representations can be obtained for all the dimensionless numbers thus allowing a systematic approach to be selected in order to analyze the separate effects of each of the groups appearing in the equations. Nevertheless, due to the large amount of free variable, it is not possible to study extensively Eq. (4.63), Eq. (4.64) and Eq. (4.65) in all the domain. Instead, few projections of these equations will be discussed and analyzed in order to give quantitative results in specific regions of applicability of the model. Furthermore the effect of different parametrized geometries will be investigated. The qualitative importance of each dimensionless group will be highlighted focusing in particular on the capillary Nusselt and Reynolds number importance in the annular laminar film condensation process.

Based on the theoretical considerations presented so far, the order of magnitude of the heat transfer coefficient of different fluids in the capillary dominated regime can be obtained: results and details are represented in Appendix D.

4.4 Summary

In this chapter, the dimensional analysis of the considered physical problem has been done. The Order of Magnitude Analysis allows to characterize from a theoretical point of view the annular laminar film condensation process when it is dominated by capillary and viscous forces. A characteristic dimensionless number, indicated with Sn , represents how the local Nusselt number scales for different characteristic lengths, fluid properties and wall subcoolings. The conjugate heat transfer problem occurring when considering the thermal conduction in the wall has been assessed and a characteristic heat transfer length which is related to the wall geometrical and thermal properties has been identified. Furthermore, when considering the condensation process being induced by an external cold fluid, the characteristic internal to external heat transfer ratio becomes a very important dimensionless number which is governing the coupled physical problem. The interfacial mass transfer process is characterized by 3 different numbers related to the temperature jump occurring across the interface and the pressure jump due to the local curvature and the short range Van der Waals forces (disjoining pressure). An asymptotic comparison between capillary-viscous dominated regimes and gravity-viscous dominated regimes has also been obtained and a quantitative scaling law has been obtained which describes the relative importance of capillary and gravitational forces with respect to the heat transfer process. All the remaining dimensionless numbers have been identified thus allowing scalable solutions to be obtained.

Chapter 5

Numerical and Experimental Validation of The Model

The first part of this chapter is focused on the method used for solving the equations and on the numerical validation of the developed code, including, where it is possible, comparisons with exact solutions. In the second part of this chapter the experimental validation is given by comparing the experimental results from the literature with those predicted by the numerical model. A comparison with an existing numerical model is also proposed in the last part of this chapter, showing a good agreement when the new implemented features are suppressed.

5.1 Solution Algorithm

If an imposed heat flux or an imposed external heat transfer coefficient is given, it has been shown in Chapter 3 that the following set of non linear algebraic and ordinary differential equations have to be integrated in time:

$$\begin{aligned} \underline{f}_q(\underline{T}, \underline{\delta}, q) &= \underline{0} && \text{Energy Equation} \\ \dot{\underline{\delta}} - \underline{f}_\delta(\underline{\delta}, \underline{u}, \underline{v}, \underline{T}) &= \underline{0} && \text{Mass - Liquid Phase} \\ \underline{U} - \underline{f}_U(\underline{\delta}, \underline{u}, \underline{v}, \underline{T}) &= \underline{0} && \text{Mass - Vapor Phase} \\ \dot{\underline{u}} - \underline{f}_u(\underline{\delta}, \underline{u}, \underline{v}, \underline{T}) &= \underline{0} && \text{Momentum - Liquid Phase} \\ \dot{\underline{v}} - \underline{f}_v(\underline{\delta}, \underline{u}, \underline{v}, \underline{T}, \underline{U}, \underline{p}) &= \underline{0} && \text{Momentum - Liquid Phase} \\ \underline{p} - \underline{f}_p(\underline{\delta}, \underline{u}, \underline{v}, \underline{U}, \underline{\dot{U}}) &= \underline{0} && \text{Momentum - Vapor Phase} \end{aligned} \tag{5.1}$$

where it has been assumed for simplicity $\underline{T} = \underline{T}^w$. The initial condition at $t = t_0$ is assigned to $\underline{\delta}$, \underline{u} and \underline{v} :

$$\begin{aligned} \underline{\delta}(t_0) &= \underline{\delta}_0 \\ \underline{u}(t_0) &= \underline{u}_0 \\ \underline{v}(t_0) &= \underline{v}_0 \end{aligned} \tag{5.2}$$

The inlet boundary condition for the liquid film is assigned in a similar way:

$$\begin{aligned}\underline{\delta}(\xi, z = 0) &= \underline{\delta}_i(\xi) \\ \underline{u}(\xi, z = 0) &= \underline{u}_i(\xi) \\ \underline{v}(\xi, z = 0) &= \underline{v}_i(\xi)\end{aligned}\quad (5.3)$$

If the wall temperature is given, the first equation in the previous system formally disappears and the number of unknowns is reduced. The problem has a wide range of time scales, ranging from the long characteristic time related to the condensation process itself to the very fast dynamics induced by surface tension. This kind of problem is called *stiff* and it can be extremely difficult to solve with accuracy and stability [53], [66]. If an explicit method were to be used, numerical stability would force the time step to be of the same order as the smallest characteristic time, making it difficult, if not impossible, to find the solution with a very fine mesh and small diameters.

One way of overcoming this problem is to use an implicit method. This choice suits the problem well as it is already formulated in an implicit way (pressure and mass conservation equations). Furthermore, by approximating the time derivative with the backward-difference method [66], Eq. (5.1) can be written in the following way:

$$\begin{aligned}\underline{f}_q(\underline{T}^{t+\Delta t}, \underline{\delta}^{t+\Delta t}, \underline{q}^{t+\Delta t}) &= \underline{0} \\ \underline{\delta}^{t+\Delta t} - \underline{\delta}^t - \Delta t \underline{f}_\delta(\underline{\delta}^{t+\Delta t}, \underline{u}^{t+\Delta t}, \underline{v}^{t+\Delta t}, \underline{T}^{t+\Delta t}) &= \underline{0} \\ \underline{U}^{t+\Delta t} - \underline{f}_U(\underline{\delta}^{t+\Delta t}, \underline{u}^{t+\Delta t}, \underline{v}^{t+\Delta t}, \underline{T}^{t+\Delta t}) &= \underline{0} \\ \underline{u}^{t+\Delta t} - \underline{u}^t - \Delta t \underline{f}_u(\underline{\delta}^{t+\Delta t}, \underline{u}^{t+\Delta t}, \underline{v}^{t+\Delta t}, \underline{T}^{t+\Delta t}) &= \underline{0} \\ \underline{v}^{t+\Delta t} - \underline{v}^t - \Delta t \underline{f}_v(\underline{\delta}^{t+\Delta t}, \underline{u}^{t+\Delta t}, \underline{v}^{t+\Delta t}, \underline{T}^{t+\Delta t}, \underline{U}^{t+\Delta t}, \underline{p}^{t+\Delta t}) &= \underline{0} \\ \underline{p}^{t+\Delta t} - \underline{f}_p(\underline{\delta}^{t+\Delta t}, \underline{u}^{t+\Delta t}, \underline{v}^{t+\Delta t}, \underline{U}^{t+\Delta t}, \frac{1}{\Delta t}(\underline{U}^{t+\Delta t} - \underline{U}^t)) &= \underline{0}\end{aligned}\quad (5.4)$$

One possible approach of solving the system of equations Eq. (5.4) is simply by iteration. Nevertheless, the limit of convergence of this method is very slow as a very small time step may be required. The method that has been implemented in order to overcome the limitation induced by the numerical stability is based on Newton's method [66]. Given a generic function $\underline{F} = \underline{F}(\underline{X})$, the solution of the equation $\underline{F}(\underline{X}) = \underline{0}$ can be obtained by the following iterative method:

$$\underline{X}^{k+1} = \underline{X}^k - \left(\frac{\partial \underline{F}}{\partial \underline{X}} \right)^{-1} \underline{F}(\underline{X}^k) \quad (5.5)$$

where $\frac{\partial \underline{F}}{\partial \underline{X}}$ is the Jacobian of the function \underline{F} . The iteration proceeds until the error $|\underline{X}^{k+1} - \underline{X}^k|$ is below a certain tolerance. In order to guarantee a good convergence, the method should be initialized by setting an initial guess \underline{X}^0 'sufficiently close' to the solution. Since the system of equations Eq. (5.4) can be written in the compact form:

$$\underline{X}^{t+\Delta t} - \underline{X}^t - \Delta t \underline{F}(t + \Delta t, \underline{X}^{t+\Delta t}) = \underline{0} \quad (5.6)$$

having defined with \underline{X} the vector of unknown, then Newton's method can be directly applied.

Even so the calculation of the Jacobian matrix which is done numerically can result in a significant computational effort and the continuous update is equivalent or even worse (in terms of required computational time) than the explicit method. Furthermore, the origin of the numerical instability is primarily due to the surface tension and momentum diffusive contributions and therefore it is important to model properly these terms.

The following modified Newton's method is proposed and applied here:

- a 'reduced' Jacobian (which includes only the contribution of surface tension and momentum diffusive contributions) is calculated;
- the iterative method Eq. (5.6) is applied for m time steps keeping the same Jacobian matrix;
- when the iteration convergence is deteriorated or the convergence is impossible then the Jacobian matrix is calculated again.

At each time step, the iterations, indicated by the counter n , are interrupted when the following convergence criteria are both satisfied:

$$\max \left(\frac{\delta_{jk}^{t+\Delta t, n+1} - \delta_{jk}^{t+\Delta t, n}}{\delta_{jk}^{t+\Delta t, n+1}} \right) < \varepsilon_\delta \quad (5.7)$$

$$\frac{1}{\Delta p_r} \max \left(p_k^{t+\Delta t, n+1} - p_k^{t+\Delta t, n} \right) < \varepsilon_p \quad (5.8)$$

where Δp_r is defined through Eq. (4.7). The values adopted for the tolerances ε_δ and ε_p are typically of the order of 10^{-4} - $5 \cdot 10^{-4}$. A control on the liquid film and vapor velocity is also done in order to guarantee the convergence of the method.

When the steady state solution has to be obtained, a pseudo-transient method is applied: the system Eq. (5.4) loses the explicit dependency on time and it is then solved until the convergence is obtained.

In Fig. (5.1), the scheme of the solver sequence is sketched. The graph shows the most general case, including transient mass flux $G(t)$, body forces $a_T(t)$, angular velocity $\Omega(t)$ and heat flux $q(t)$ which may all vary with time. At each time step the iteration requires also the vector of unknown r_v to be updated since this variable can be obtained only knowing both the film thickness distribution and the vapor to liquid relative velocity values.

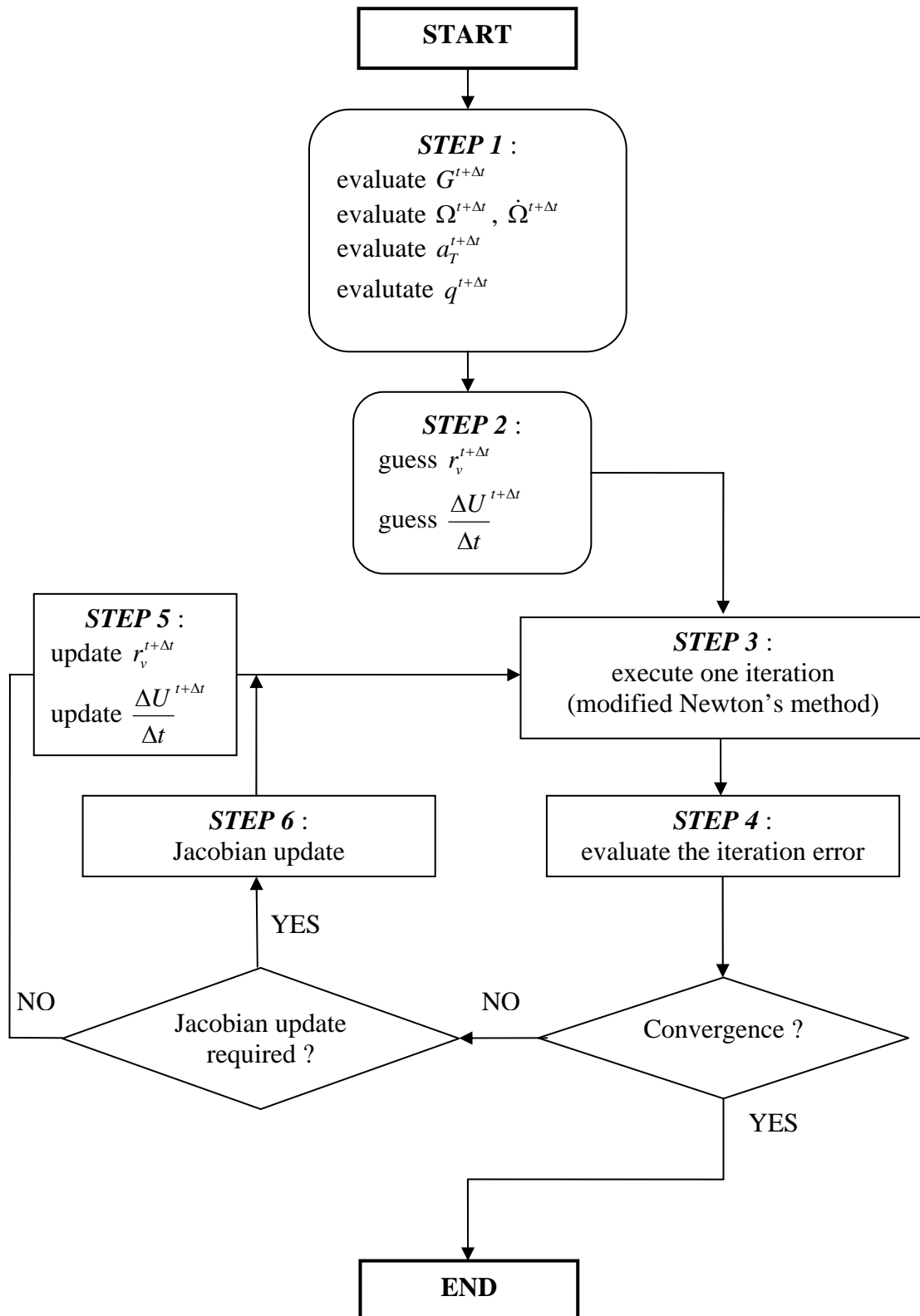


Figure 5.1: Schematics of the solution algorithm

5.2 Verification of the Numerical Scheme

Grid size independence tests have been performed to verify the numerical scheme. Norms of relative errors of local and mean heat transfer coefficient (or Nusselt number) are indicative of the accuracy when the time step or the grid size changes. The following expression has been used to assess the convergence rate ν of the numerical model [53]:

$$\nu = \frac{\ln\left(\frac{\phi_{\Delta} - \phi_{2\Delta}}{\phi_{2\Delta} - \phi_{4\Delta}}\right)}{\ln(2)} \quad (5.9)$$

where ϕ_{Δ} is the solution (temperature, Nusselt number, etc.) obtained with a reference spacing Δ . The Richardson extrapolation technique allows one to obtain a solution that is more accurate than the solution ϕ_{Δ} on the finest grid:

$$\varphi_R = \varphi_{2\Delta} + \frac{\varphi_{2\Delta} - \varphi_{\Delta}}{2^q - 1} \quad (5.10)$$

On this basis it is possible to define the mesh relative error ε_{Δ} as:

$$\varepsilon_{\Delta} = \frac{\varphi_{\Delta} - \varphi_R}{\varphi_R} \quad (5.11)$$

Second order accuracy in space and first order in time have been verified. More details, examples of meshes and numerical convergence tests are reported in Appendix E.

5.2.1 Liquid-Vapor Interface Simple Advection

The special case of L-V interface advection, without any force acting on the system and in adiabatic conditions, has been analyzed in order to assess the consistency and the accuracy of the model. If the initial condition is set such that the liquid film velocity has only one axial component v_0 in the entire liquid subdomain and if the surface tension and viscous forces are neglected, then the film thickness function is simply convected in time as stated by the following expression:

$$\delta(z, t) = \delta_0(z - v_0 t) \quad (5.12)$$

where δ_0 is the initial film thickness distribution. This test is especially addressed to study the effect of numerical diffusion in the calculation of convective terms (both momentum and mass). The First order upwind scheme, although very robust and easy to implement, has shown not to be suitable for the present problem because it gives a very low convergence rate and too large discretization errors, thus the second order upwind QUICK Scheme ([53, 54]) has been adopted. As an example, Fig. (5.2) shows the result obtained for a circular channel of 1 mm diameter, 25 mm length, arbitrary mean axial liquid velocity and initial film distribution. Different tests were conducted by varying the axial mesh spacing Δz and calculating the error based on the exact Eq. (5.12), thus allowing the model convergence to be assessed.

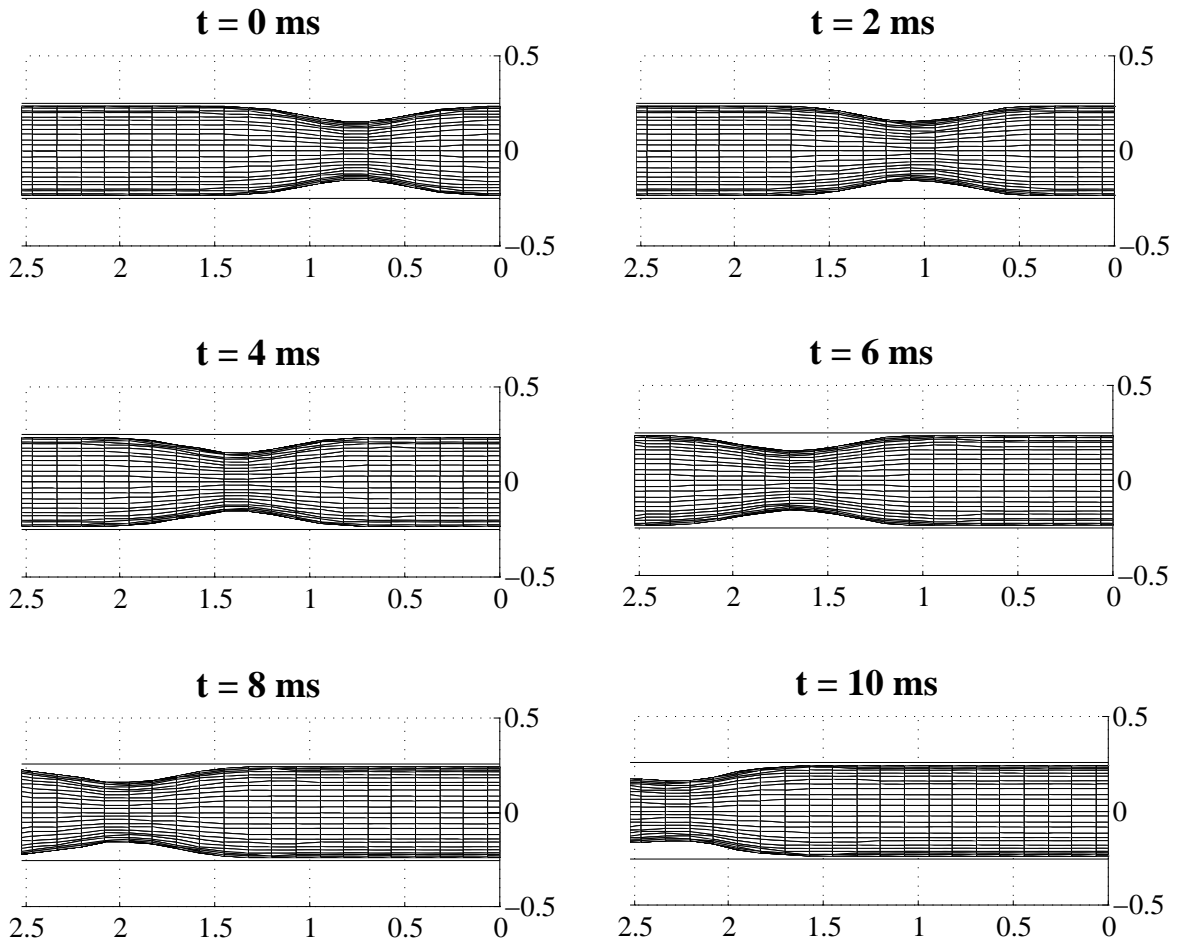


Figure 5.2: Snapshots at different times of the liquid-vapor interface for a simple test case of pure advection in a circular channel: the liquid phase is flowing from right to left and no forces are present

5.2.2 Steady State Analysis: Comparison with Analytical Solutions

An interesting limit case that can be used for comparison is a particular set of solutions that correspond to the equilibrium configurations of the liquid-vapor interface when the system is subjected only to a steady and uniform gravitational field and the surface tension forces, and adiabatic conditions are considered (namely the condensing mass flux is zero everywhere). If there is no vapor flow then the velocity field is zero and the shape of the interface is independent of the axial location. Consistent with the hypothesis of totally wettable fluid, the wall can never be dry and the steady state solution can be described by a unique function \vec{r}_i which represents the interface at each position. Under the described conditions, the L-V interface will assume the shape that minimizes the mechanical energy per unit depth of the system. This is given by the sum of potential energy E_g and surface tension energy E_σ ; if the gravity vector is assumed

parallel to a reference y axis, it is possible to write the two contributions in the following way:

$$E_g = \int_{A_0} g\rho(y - y_{ref}) d\Omega \quad (5.13)$$

$$E_\sigma = \int_{\partial A_0} \sigma dl \quad (5.14)$$

where y_{ref} is an arbitrary reference location. Fig. (5.3) shows an example of the definition of the system coordinates for a circular channel. The equilibrium solution is given by the minimum of

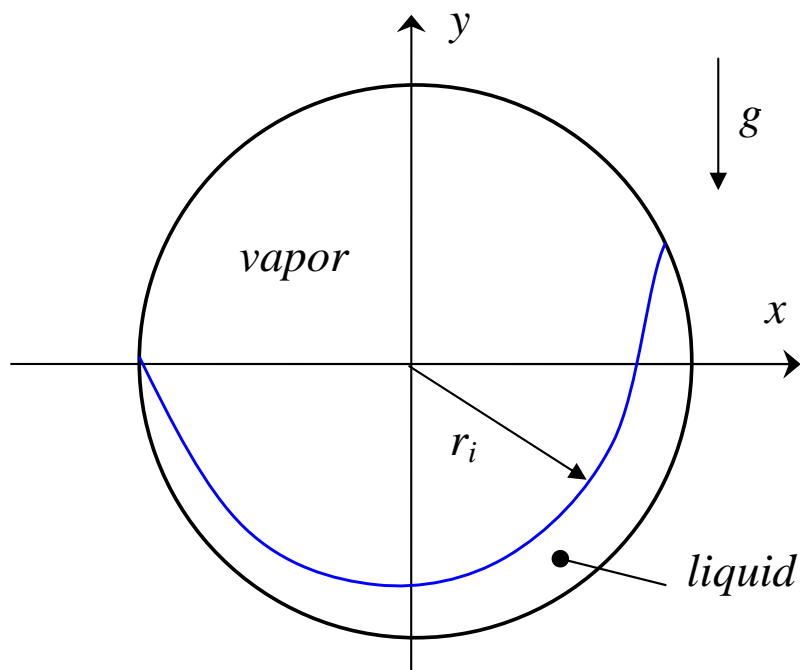


Figure 5.3: Definition of the polar coordinate system for a circular channel

the function $E_g + E_\sigma$; the total amount of liquid (or vapor) per unit depth is imposed and this constraint can be formulated in terms of the cross sectional void fraction e , defined as the ratio of vapor area and total section area: $e = S_v/S_0$. The problem of minimizing the functional sum of $E_g + E_\sigma$ has been solved for different geometries in a polar coordinate system for the unknown \vec{r}_i which can be made dimensionless with respect to a characteristic length L :

$$\vec{r}_i(\theta) = L\eta(\theta)\hat{r}(\theta) \quad (5.15)$$

where:

$$\hat{r}(\theta) = \cos(\theta)\hat{x} + \sin(\theta)\hat{y} \quad (5.16)$$

is the radial unit vector and θ the anomaly. In polar geometry the element length and the element area can be obtained immediately:

$$d\vec{l} = r d\theta \hat{\theta} \Rightarrow dl^2 = L^2 (\eta^2 + \eta'^2) \quad (5.17)$$

$$d\Omega = r dr d\theta = L^2 \eta d\eta d\theta \quad (5.18)$$

Introducing the Bond number Bo_L :

$$\text{Bo}_L = \frac{g(\rho_l - \rho_v) L^2}{\sigma} \quad (5.19)$$

The total energy E_t^* per unit depth can be written in dimensionless form as:

$$E_t^* = E_0^* + \oint_{\partial\Omega^*} \sqrt{\eta^2 + \eta'^2} d\theta - \text{Bo}_L \int_{\Omega_v^*} \eta^2 \sin(\theta) d\eta d\theta \quad (5.20)$$

where E_0^* is a constant independent of the function η . The first line integral is the dimensionless length of the interface, while the second integral is the scaled gravitational potential. The minimum of the function E_t depends only on two dimensionless numbers: Bo_L and e . In order to compare the exact solution of the stated problem with the model's prediction, proper initial conditions (initial liquid to vapor volume ratio) need first to be set and then Eq. (5.1) to be solved until the steady state is obtained. The correct solution should fulfill two criteria: the solution has to be independent of axial position z and the difference between the exact and the calculated solutions should be below a certain tolerance.

Fig. (5.4), Fig. (5.5) and Fig. (5.6) show the resulting calculated L-V interfaces for different void fractions and Bond numbers for the circular channel case. In this case the reference length L has been set equal to the channel radius. Fig. (5.7), Fig. (5.8) and Fig. (5.9) show instead the solutions obtained for a flattened shape channel having an aspect ratio (defined as the ratio of the flat segment length connecting the two curved ends over the diameter of the rounded ends) of 0.5 where the characteristic length has been set equal to $P/(2\pi)$, where P is the perimeter.

The relative errors between the calculated solutions from the model and the equilibrium solutions were found to be below 10^{-3} for all these cases.

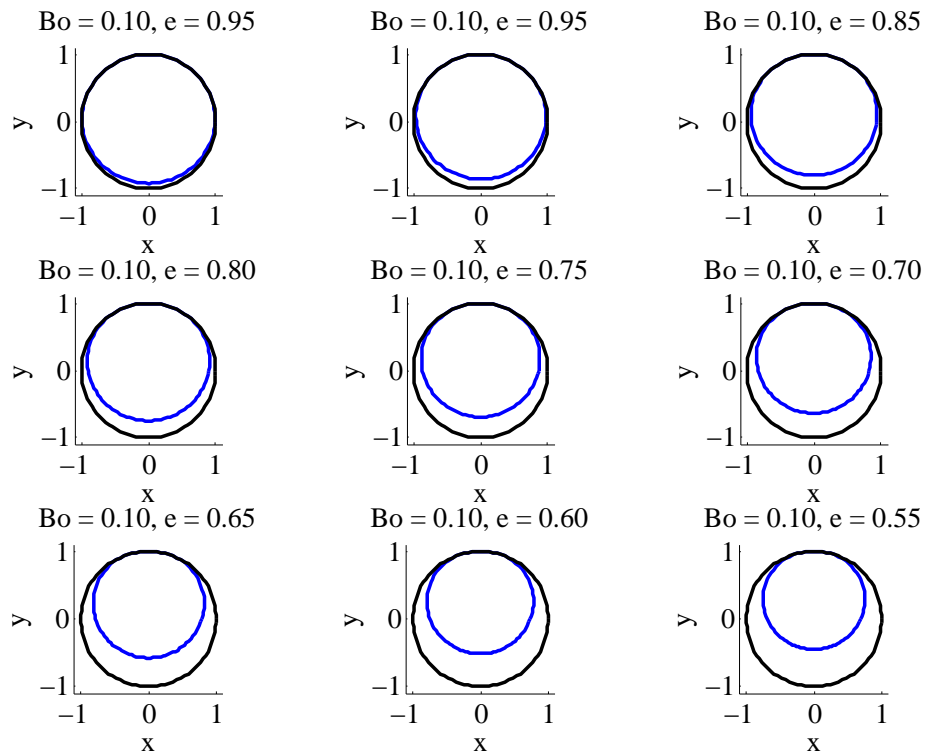


Figure 5.4: Circular channel minimum energy configuration of the liquid-vapor interface for different void fractions with $Bo_R = 0.1$

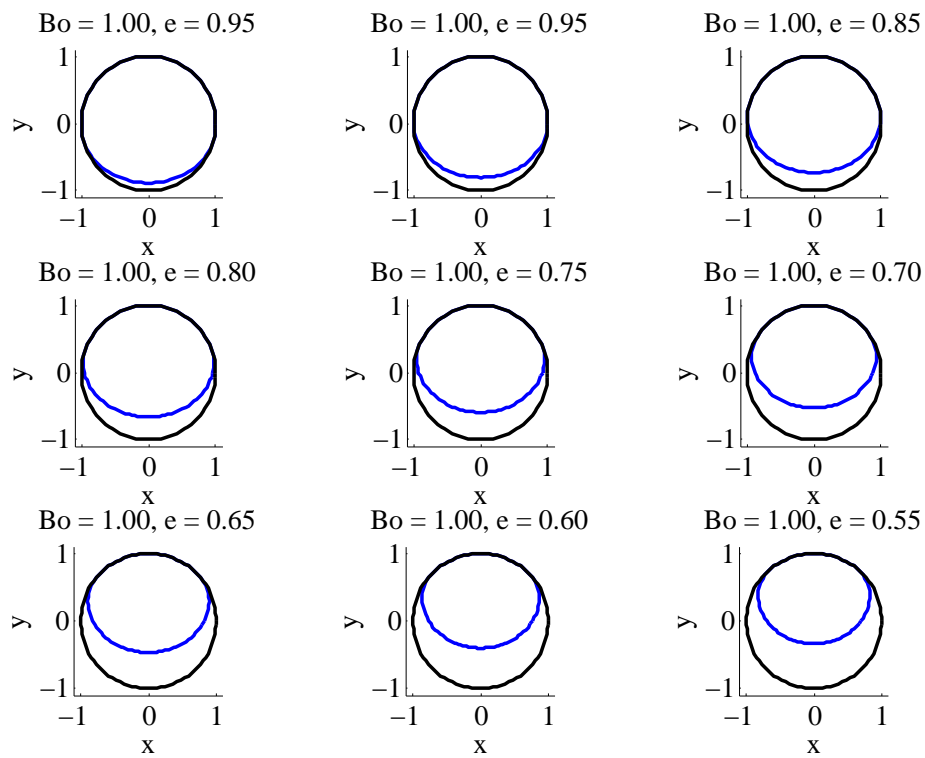


Figure 5.5: Circular channel minimum energy configuration of the liquid-vapor interface for different void fractions with $Bo_R = 1.0$

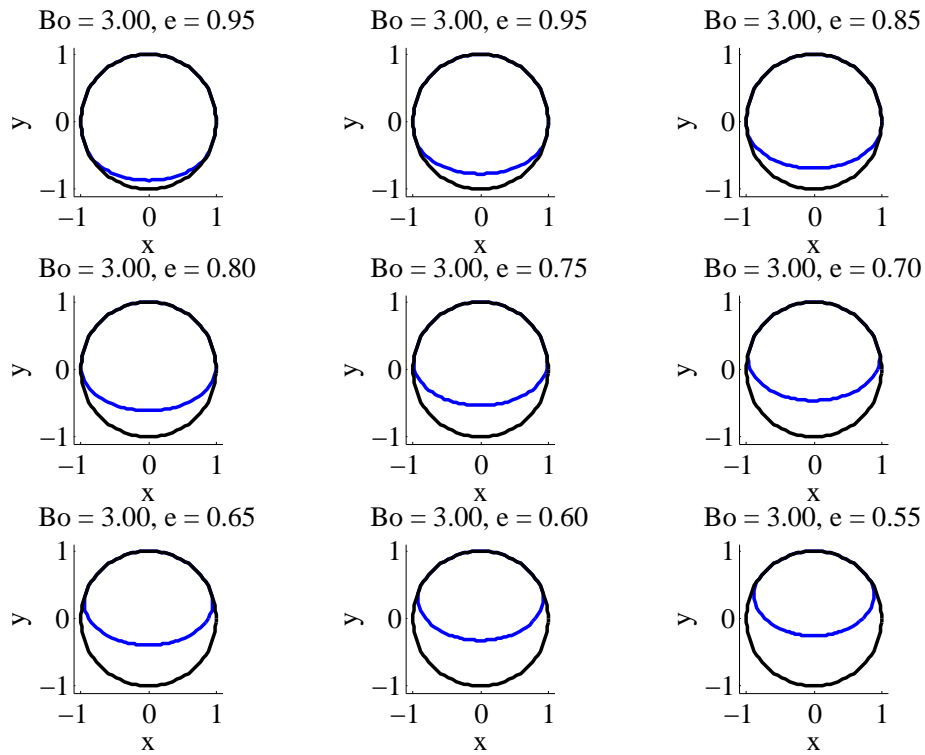


Figure 5.6: Circular channel minimum energy configuration of the liquid-vapor interface for different void fractions with $Bo_R = 3.0$

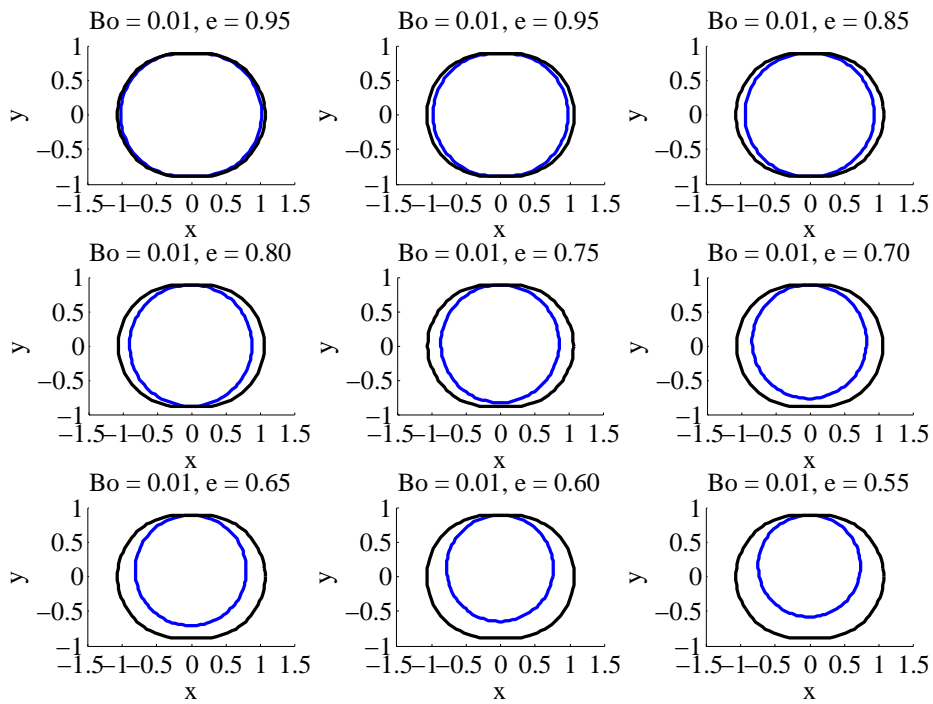


Figure 5.7: Flattened shape channel minimum energy configuration of the liquid-vapor interface for different void fractions with $Bo_P = 0.10$

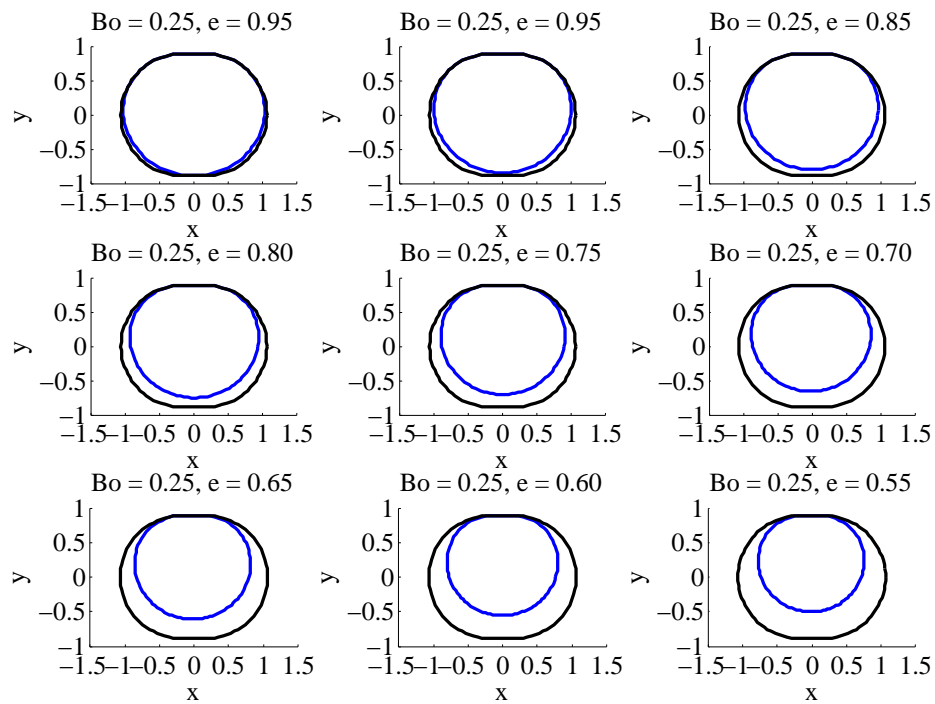


Figure 5.8: Flattened shape channel minimum energy configuration of the liquid-vapor interface for different void fractions with $Bo_P = 0.25$

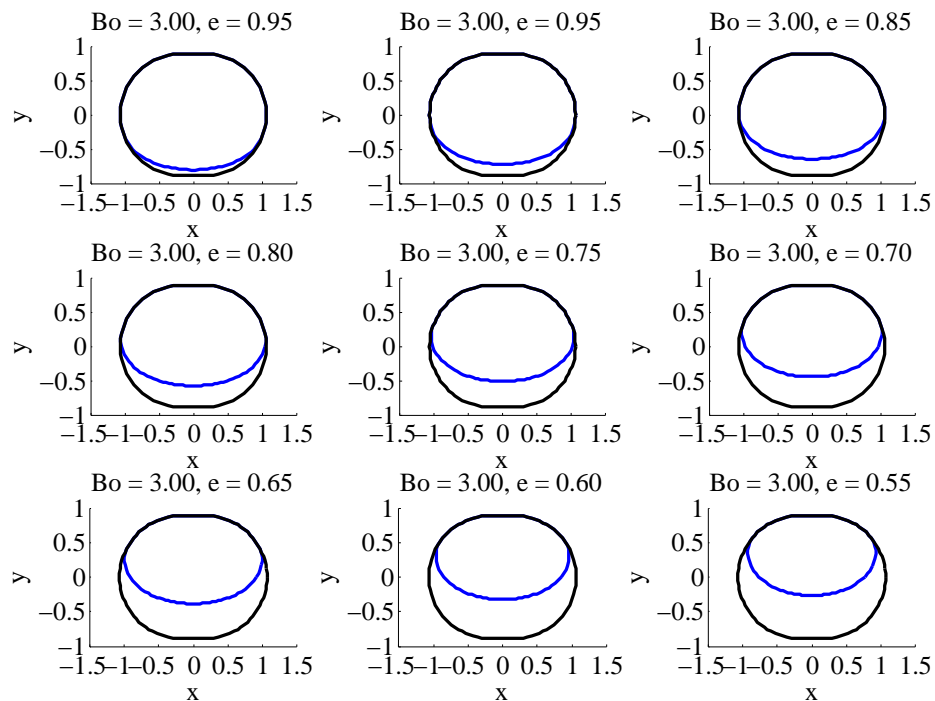


Figure 5.9: Flattened shape channel minimum energy configuration of the liquid-vapor interface for different void fractions with $Bo_P = 3.0$

5.3 Experimental Validation: Heat Transfer Coefficient

A growing number of condensation heat transfer data are available in the literature from different authors and labs; nevertheless the majority are classified as 'macroscale' cases and capillarity forces have a minimal effect compared to inertia and gravity. Furthermore the region in which the liquid film can be thought to be laminar is limited to medium and high vapor qualities, where the film is very thin. In recent works the characteristics of condensation heat transfer of pure refrigerants in small channels have been explored. In this section, the results obtained by different authors are compared with the predicted values obtained applying the presented numerical model.

5.3.1 Heat Transfer Coefficient: Circular Channel

In this section the results obtained by Yan and Lin [8] and Shin and Kim [9, 10], who present data of heat transfer coefficients plotted against mean vapor qualities for circular channels with three different diameters (0.493, 0.691 and 2.0 mm), are compared to the proposed numerical model. The experimental results are shown in Fig. (5.10), Fig. (5.12) and Fig. (5.13). In both studies, a commonly used refrigerant R-134a was tested for different values of mass flux, mean heat flux and saturation temperature. In order to proceed with this evaluation, the actual flow pattern has to be assessed: annular or semi-annular flow conditions have to be identified before the comparison with the experimental data since only these regimes can be compared to the model. Within the existing flow pattern maps for microchannel condensation flow, the one proposed by Garimella et al. [20] has been adopted in the present study: the transition criteria between intermittent (I) and non-intermittent (NI) flows was developed for R-134a and for horizontal circular channels with hydraulic diameters between 0.5 and 4.1 mm. The dimensional relationship they proposed to identify the transition value of vapor quality X_{I-NI} is the following:

$$X_{I-NI} = \frac{a(D_h)}{b(D_h) + G} \quad (5.21)$$

where the constants a and b are calculated as follows:

$$a(D_h) = 69.57 + 22.60 \exp(0.259D_h) \quad (5.22)$$

$$b(D_h) = -59.99 + 176.8 \exp(0.383D_h) \quad (5.23)$$

G is the mass flux expressed in $\text{kg}/(\text{m}^2\text{s})$ and D_h the hydraulic diameter in millimeters. The minimal condition that has to be satisfied in order to have a non intermittent flow structure (that is, an annular type of flow) is that the actual vapor quality is higher than the transition vapor quality X_{I-NI} . The first step is then to identify the set of data points which belong to the applicable region of the numerical model. The flow in the channel is strongly dependent on

the boundary conditions applied; in particular, inlet conditions can influence the development of the flow along the channel. From an experimental point of view, the data reduction process of the mean heat transfer coefficient (axial average value over the interval of vapor quality in the test section) is possible once the geometry, the heat duty, the flow rate, the wall and the fluid temperature and the inlet vapor quality are known; the calculated heat transfer coefficient can be considered as a mean value, both in space (referred to a specific region of the test section) and in time (the flow field can be intrinsically unsteady, from the presence of waves for instance, but the mean variation of certain parameters within a specified time scale can be zero since the data are reported for steady state conditions). The complete set of inlet flow conditions (liquid film distribution and velocity) is not available for each experiment, while the following time-averaged parameters are measured (directly or indirectly): the mass flux G_e , the inlet saturation temperature $T_{s,e}$, the inlet vapor quality $X_{i,e}$, the mean or quasi-local heat flux q_e and the wall temperature $T_{w,e}$. The mean heat transfer coefficient can be obtained as a function of the mean vapor quality X_e , which is defined as follows:

$$x_e = x_{i,e} + \frac{1}{2}\Delta x_e \quad (5.24)$$

$$\Delta x_e = \frac{4q_e}{G_e \Delta h_{v,e}} \frac{L}{D_h} \quad (5.25)$$

$$h_e \equiv \frac{q_e}{T_{s,e} - T_{w,e}} \quad (5.26)$$

In order to set the correct inlet vapor quality $X_{i,e}$ (of the considered experimental data point), a pre-condensing simulation is run at first so that the outlet vapor quality is coincident with the desired value.

Secondly, the simulation of the real test section (having the specified length, diameter and equivalent wall thickness) is run, applying the previously calculated boundary conditions (film thickness and film velocities) that guarantees the proper inlet vapor quality. The steady state solution is calculated, assuming that the unsteady contributions due to vibrations, non-constant mass flux, etc. have a negligible influence in this case on the mean distribution of the wall temperature. Wall heat flux imposed boundary conditions, equivalent to the measured values, have been run, setting the geometry and the wall properties of each specific experiment. Highly conductive copper tubes ($k_w = 400W/(mK)$) have been tested in the experiments considered here. The average heat transfer coefficient h_M based on the mean temperature difference has been calculated for each steady state solution and then compared with the measured experimental values. The error ε_j , for $j = 1, \dots, N_T$ number of experimental data points, is:

$$\varepsilon_j = \frac{h_{M,j} - h_{e,j}}{h_{e,j}} \quad (5.27)$$

The mean quadratic error is defined as:

$$\varepsilon_{\sigma} = \sqrt{\frac{1}{N_T} \sum_j \varepsilon_j^2} = \sqrt{\frac{1}{N_T} \sum_j \frac{(h_{M,j} - h_{e,j})^2}{h_{e,j}^2}} \quad (5.28)$$

The results of the simulations are shown in Fig. (5.14), which represents the ratio of the predicted heat transfer coefficients normalized by the experimental heat transfer coefficients plotted versus vapor quality for all the data points that have been tested. Based on these results, it is possible to say that the model accurately predicts values the trends of the heat transfer coefficient with respect to diameter, mass flux, vapor quality and saturation temperature. The mean quadratic errors for the three separate sets of data are: 11.1% for the 2 mm channel, 10.3% for the 0.691 mm channel and 8.4% for the 0.493 mm channel; 94.1 % of the analyzed experimental data are within a 20% error band, which is similar to the actual experimental errors encountered in such tests.

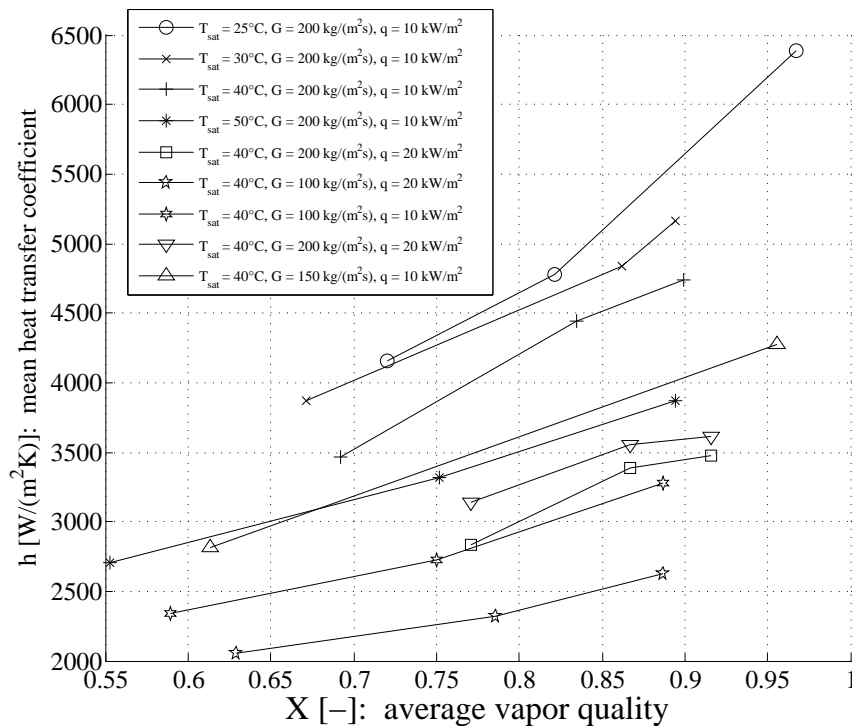


Figure 5.10: Condensation heat transfer coefficients obtained experimentally by Yan and Lin [8] for a circular mini channel with hydraulic diameter of 2 mm for the R-134a

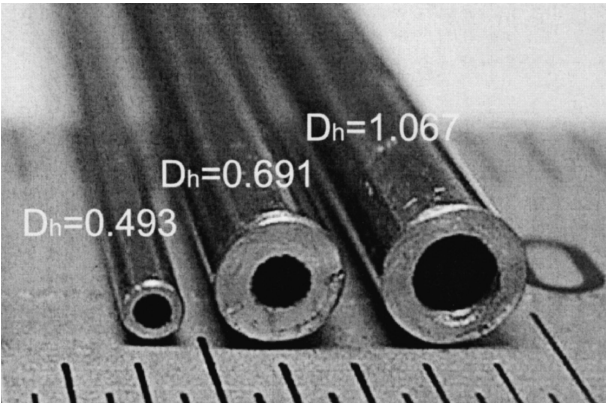


Figure 5.11: Cross section of the tested tubes analyzed by Shin and Kim [9]

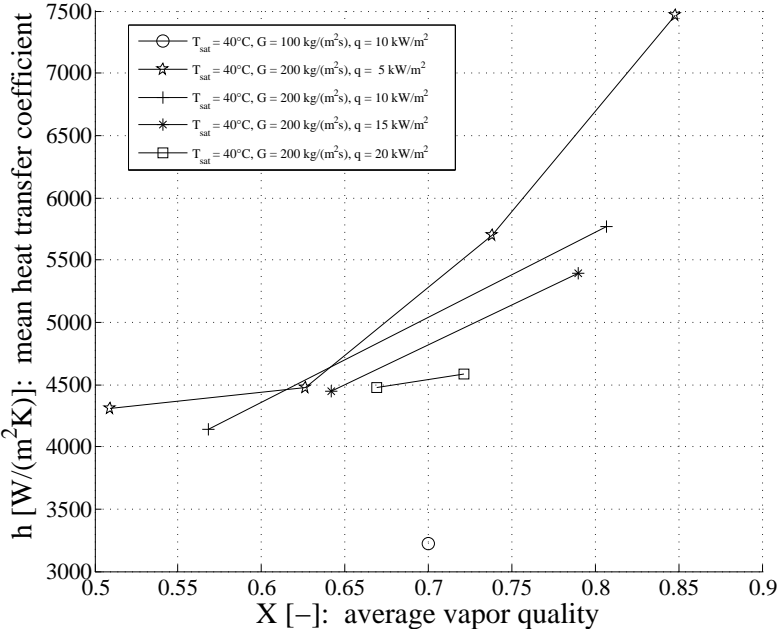


Figure 5.12: Condensation heat transfer coefficients obtained experimentally by Shin and Kim [9] for a circular mini channel with hydraulic diameter of 0.691 mm for R-134a

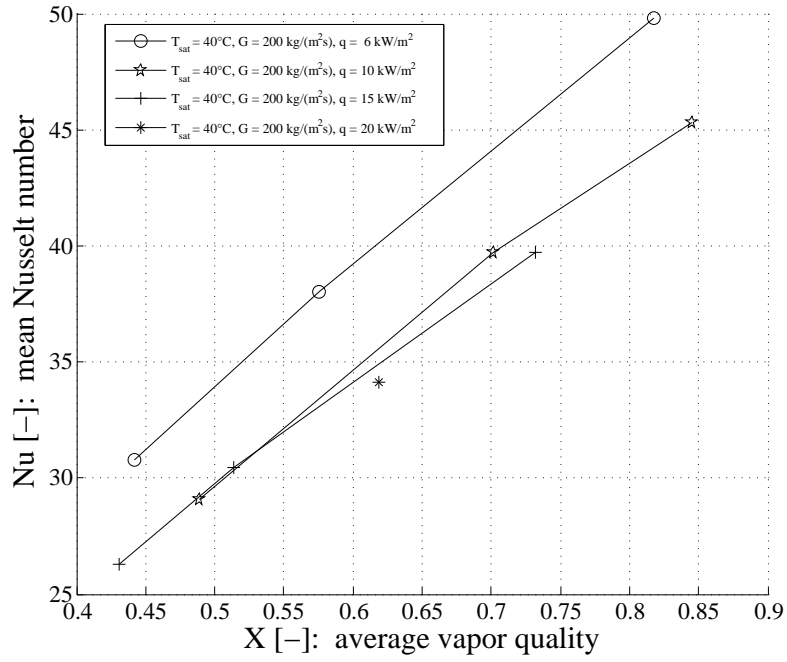


Figure 5.13: Condensation heat transfer coefficients obtained experimentally by Shin and Kim [10] for a circular mini channel with hydraulic diameter of 0.493 mm for R-134a

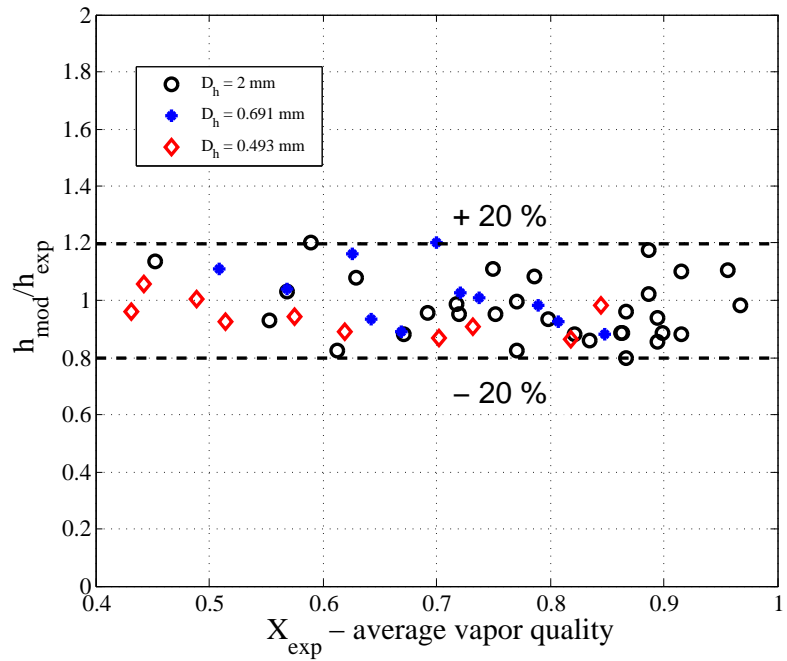


Figure 5.14: Values predicted by the model h_M normalized by the experimental values h_e versus the average vapor quality for circular channels with three different diameters: 2, 0.691 and 0.493 mm

5.3.2 Wall Temperature Distribution: Comparison with a Square Mini-Channel

A comparison between the numerical model and experimental data available in literature obtained for a square mini-channel ($D_h = 0.762$ mm) is presented in this section. Two experimental test cases taken by Agarwal et al. [11] have been selected. Fig. (5.15) shows the test section geometry: it consists of a multi microchannel element made of copper. Condensation is obtained by flowing cold water on the external side of the element while the hot condensing refrigerant flows inside. A cross sectional view of the selected case is shown in Fig. (5.15). The following two conditions have been simulated:

- R-134a, 57.18 °C saturation temperature, mass flux $G = 293.9$ kg/(m²s), average heat flux $q = -8360$ W/m², average vapor quality $X_{av} = 0.610$;
- R-134a, 57.52 °C saturation temperature, mass flux $G = 450.8$ kg/(m²s), average heat flux $q = -11130$ W/m², average vapor quality $X_{av} = 0.794$.

The procedure that has been followed in order to make the comparison is the same as presented in the previous section. In particular, a pre-condensing simulation is run at first so that the outlet condition can be used as the inlet boundary condition having the required vapor quality. The equivalent wall thickness, based on the real geometry, has been calculated to be $\lambda_w = 1.2$ mm; the wall material is copper, therefore the thermal conductivity is set to a reference value of $k_w = 400$ W/(mK). The distribution of the local heat flux can deviate from the nominal mean value for two primary reasons:

1. the coolant side temperature and heat transfer coefficient may not be uniform, both in axial and peripheral directions;
2. as the experiment is done in a multi micro-channel configuration, possible maldistributions of the local heat flux and mass fluxes may occur, thus influencing the condensation process.

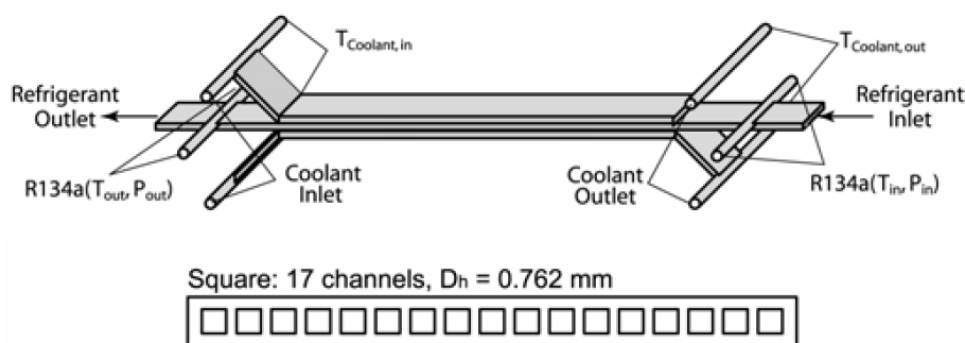


Figure 5.15: Test section schematics from Agarwal et al. [11] and cross sectional view of the multi-mini channels simulated and tested geometry

Despite the fact that these phenomena may be present to some extent, as it is not possible to assess the importance of them from the experiments, a uniform heat flux equivalent to the average one has been set as boundary condition to the simulated cases. Fig. (5.16) and Fig. (5.18) show the predicted results compared with the average experimental value. In the figures, two different values of mean heat transfer coefficients are indicated. Experimentally, in order to determine the mean heat transfer coefficient $h_{av,e}$ over the section, the following averaging procedure may be applied:

$$h_{av,e} = \frac{1}{N} \sum_{i=1}^{i=N} \frac{q_{e,i}}{T_{s,i} - T_{w,i}} \quad (5.29)$$

where N is the number of sections where the wall temperature and the heat flux are measured. A mean wall temperature can also be calculated and, based on this value, a mean *effective* heat transfer coefficient can be obtained.

$$h_{av,e,\Delta T} = \frac{\dot{q}}{\frac{1}{N} \sum_{i=1}^{i=N} (T_{s,i} - T_{w,i})} \quad (5.30)$$

In a similar way, the result of the integration of the local heat transfer coefficient over the entire inner channel surface S_T leads to the $h_{av,mod}$:

$$h_{av,mod} = \frac{1}{S_T} \int_{S_T} h dS_T \quad (5.31)$$

while the mean channel wall temperature value leads to the calculated mean *effective* heat transfer coefficient as follows:

$$h_{av,mod,\Delta T} = \frac{\dot{q}}{\frac{1}{S_T} \int_{S_T} (T_s - T_w) dS_T} \quad (5.32)$$

Since not all the details of the calculation of the heat transfer coefficient are reported in the article, both calculated values have been reported for comparison. The graphs show the saturation to wall temperature difference plotted as a function axial position (the variation of temperature around the perimeter has been found negligible under these conditions). The simulation results were found to be very sensitive to the inlet vapor quality and to the total vapor quality variation as well. Based on these results, the error on the prediction of the saturation to wall temperature difference, and consequently on the global heat flux, was found to be below 16% (which is within the experimental uncertainty of 25 % as indicated in [11]). The heat transfer predictions in Fig. (5.16) agree to their measured values within 4.10% and 6.22%, while in Fig. (5.18) the agreement is within 15.7% and 3.7%

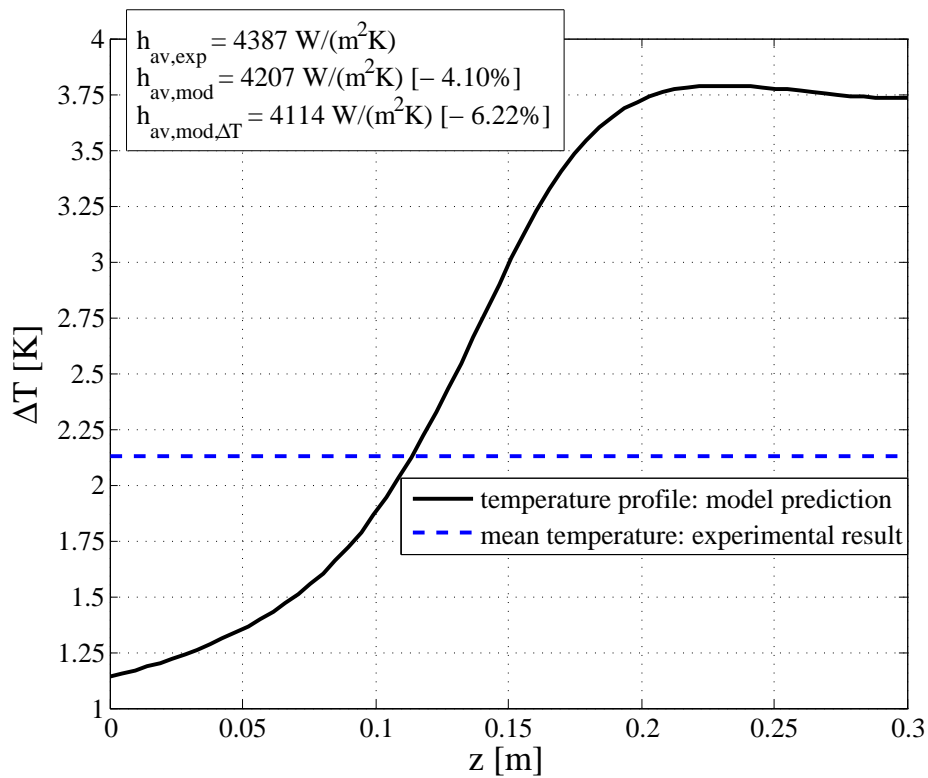


Figure 5.16: Wall temperature evolution along the axis of the channel: comparison between the prediction of the numerical model and the experimental mean value

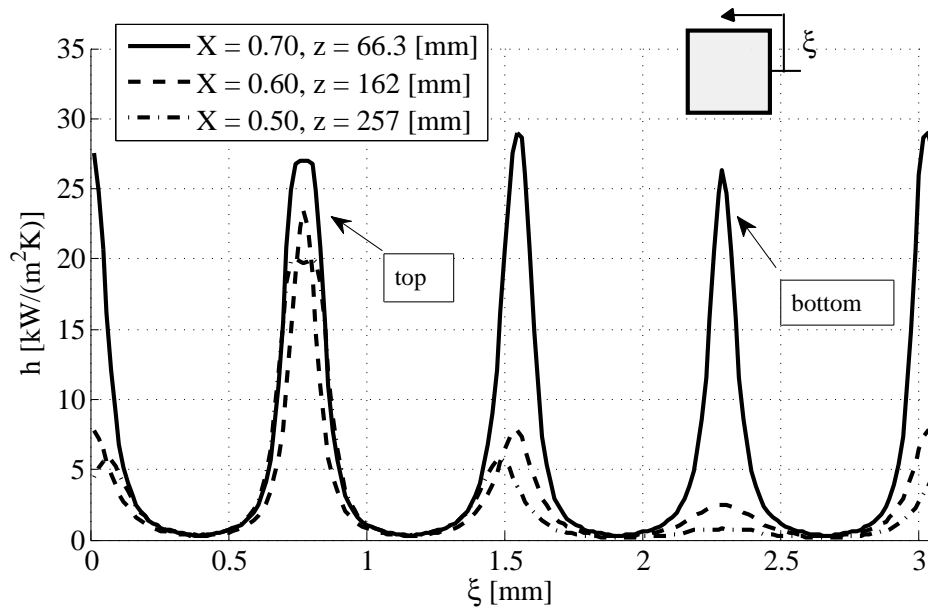


Figure 5.17: Predicted square channel local heat transfer coefficients plotted as a function of the peripheral coordinate at different axial locations and vapor qualities. The average heat flux is $q'' = 8.3 \text{ kW/m}^2$

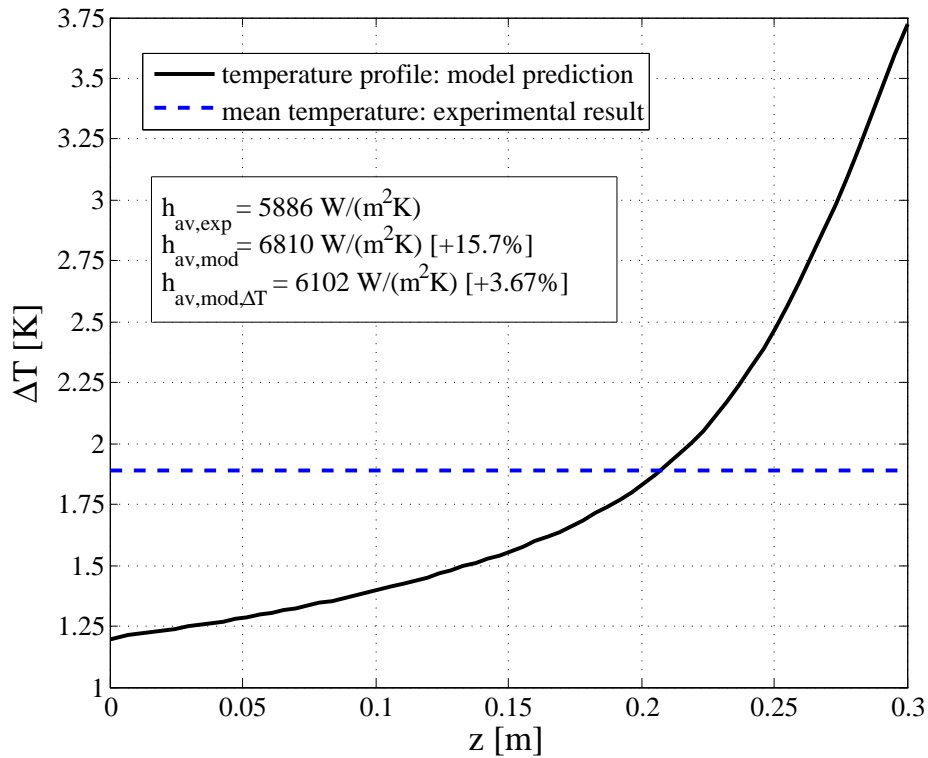


Figure 5.18: Wall temperature evolution along the axis of the channel: comparison between the prediction of the numerical model and the experimental mean value

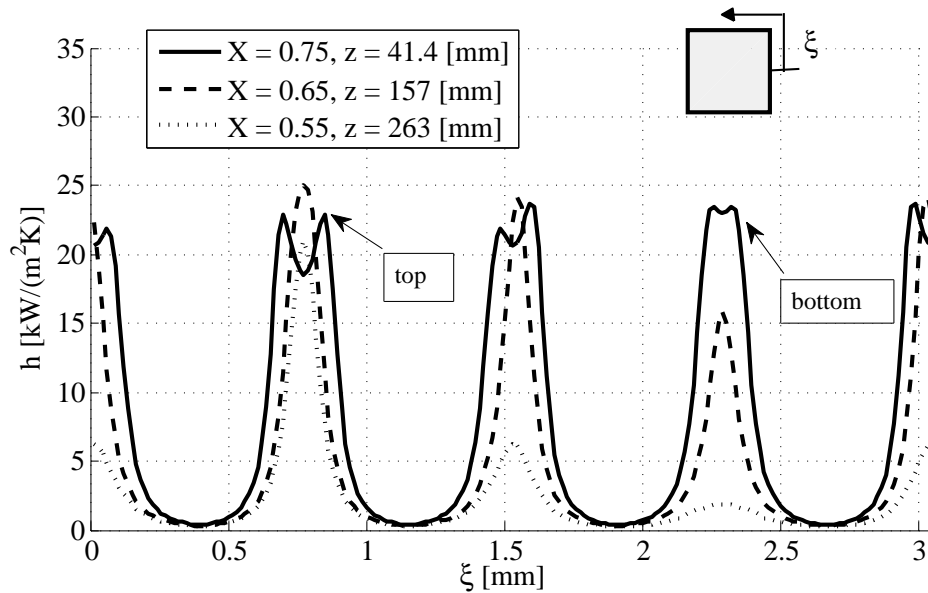


Figure 5.19: Predicted square channel local heat transfer coefficients plotted as a function of the peripheral coordinate at different axial locations and vapor qualities. The average heat flux is $q'' = 11.1 \text{ kW/m}^2$

5.4 Comparison with an existing model

As mentioned above, only a few models have been developed in order to predict heat transfer coefficients of micro-channels for condensing flows; within these, the one presented in 2005 by Wang and Rose [38] is up to now the most complete model developed for predicting steady state annular laminar condensing flow heat transfer coefficients for circular, square, triangular, rectangular and square channels. In their model, based on the finite difference method, the wall temperature is assumed constant, the axial curvature is neglected, the non linear terms coming from the momentum fluxes in the liquid film are considered negligible and the vapor to axial liquid film relative velocity is approximated by the absolute vapor velocity. All of these hypotheses have been implemented in the current model by adjusting it in order to have these simplifying features (i.e. by "turning off" their effects). Nevertheless some of the fundamental differences cannot be set to zero, due to the basic differences of the two models. In particular, the thermal conduction in the film far from the corners is always calculated in Wang's model as $\approx \frac{1}{3}$ without taking into account the fact that the liquid-vapor surface may be locally curved (the L-V surface, when the interfacial mass transfer effects are negligible, is a constant temperature surface thus the local temperature gradient can be directed only in the normal direction which is not, in general, $\hat{\delta}$).

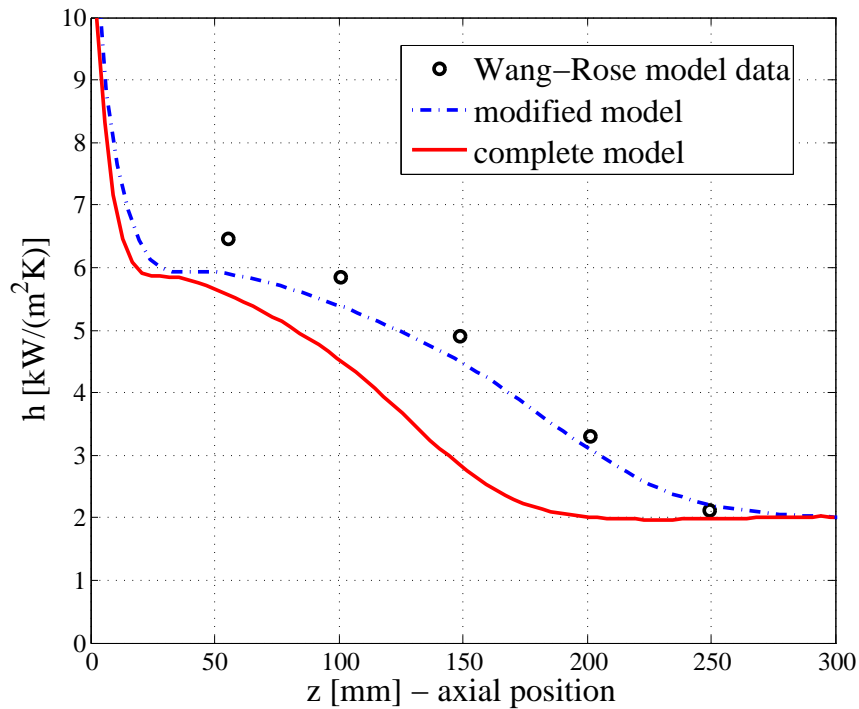


Figure 5.20: Comparison of simulated mean (around the perimeter of the channel) heat transfer coefficients of R-134a obtained with the model by Wang and Rose (circles in black), by the reduced actual model (dashed line, in blue) and the complete model (continuous line, in red); these simulations have been obtained for a square channel having a 1 mm hydraulic diameter for the following parameters: $G = 300 \text{ kg}/(\text{m}^2\text{s})$, $\Delta T = 6 \text{ K}$, $T_s = 50 \text{ }^\circ\text{C}$ and normal gravity

The comparison in Fig. (5.20) gives a good agreement in terms of trends (dependency of wall subcooling, mass flux, channel size and fluid properties). The results obtained with the current modified model and the values obtained by Wang and Rose for the following test case have been compared: 1 mm square channel, $G = 300\text{kg}/(\text{m}^2\text{s})$, $\Delta T = 6\text{K}$, $T_s = 50^\circ\text{C}$, normal gravity and R-134a. For this case, as reported in their paper, the interfacial mass transfer phenomena have been found to have negligible effects. The same graph shows the trend obtained for the same conditions with the present complete model, including all the terms presented before: this results is a similar trend (in terms of shape) but with a net change in values and local distribution. It has been found that the neglected terms listed before would lead to an overestimation of approximately 23% if compare with the values obtained experimentally and reported in [8–10].

5.5 Summary

The description of the solution algorithm, the numerical validation based on benchmark tests and the experimental validation are presented in this chapter. The verification of the numerical model is obtained by comparing some of the obtained steady state adiabatic solutions with the exact solutions obtained by minimization of the total potential energy due to the surface tension forces and the gravitational forces. Comparisons between the experimental results of heat transfer coefficients which are available in literature by different authors with the model simulations are also presented showing that the model is capable of accurately predict the trends in terms of vapor qualities, saturation temperatures, mass fluxes, heat fluxes, refrigerant properties, and channel size. The mean prediction error has been found to be around 10% for the simulated circular channels and 16% for the square mini channels: these values are very close to the actual experimental errors encountered in such test. These considerable and meaningful results allow the model to be validated and thus its application under different conditions may be undertaken.

Chapter 6

Simulation Results

In this chapter the annular laminar film condensation results obtained by simulating different test cases are shown. The results obtained with the dimensionless formulation of the problem are shown in the first section, while in the second part of the chapter the dimensional results are discussed. The following simulated cases are analyzed in this chapter:

- the effects of the channel shape on the local and global performances of the heat transfer coefficient are detailed by comparing the results obtained for flattened and elliptical inner channel shapes, with different aspect ratios;
- a parametric analysis on the effects of the axial conduction is shown, with particular attention on the distributions of the local heat flux and the saturation to wall temperature difference ΔT ;
- a detailed analysis of the conjugate heat transfer length effects are then discussed in presence of the entrance region with a sharp change of the externally imposed nominal heat flux;
- the condensation process induced by a single phase cooling boundary condition is analyzed with particular emphasis on the effects of the coolant side temperature distribution (co-current or counter-current configurations) and of the coolant side heat transfer coefficient;
- the combined effects of wall heat transfer and the dynamics of the thin condensing film are discussed in a large scale analysis set of simulations, indicating a possible criterium for the mini to micro and ultra-micro channel transition condition;
- the single phase convective cooling boundary condition is analyzed and its effects on the heat transfer coefficient distribution are presented;
- the stability of the annular flow is then discussed showing the formation of instabilities for different non stationary problems: the time dependent formations of waves and perturbations that tends to bring to a flow pattern transition are shown and analyzed;

- the effects of an unsteady gravitational field on the heat transfer performance of a small intube condenser are analyzed, showing the effects of the micro-gravity conditions that can be reproduced onboard of a dedicated aircraft.

6.1 Dimensionless Results: Parametric Analysis

For the simulations presented in this section, it has been assumed that the interface resistance and disjoining pressure effects are negligible, namely the interfacial pressure, disjoining pressure and interface resistance numbers have been set to zero. Furthermore, for all the cases presented, the inlet condition is set to a uniform thin film distribution and a constant axial liquid phase velocity such that the inlet vapor quality is equal to 0.998, while the wall temperature is set constant. Since the number of free dimensionless parameters is significative (including the geometry that in some cases can be parameterized) and since the necessary time for computation of unsteady solutions can be much longer compared to the steady state analysis, focus on the latter has been adopted here, thus permitting coverage of more geometries and dimensionless numbers. In order to explore the effects of a particular dimensionless group, each set of simulations that is being presented here is obtained maintaining fixed all the parameters except the specific ones whose effects are analyzed and discussed. In all the results presented, the reference solution corresponds to the following set of dimensionless groups: $Sn_q = 25$, $Re_q = 0.3$, $\Gamma = 0.05$, $Re_v = 15000$, $We_l = 3.0$, $Bo_y = -1.5$, $L_{ht} = 0.05$ and the total dimensionless channel length $Z_t = 200$.

6.1.1 Elliptical Channel Shape

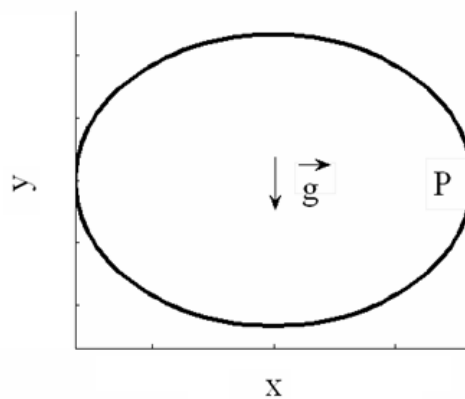


Figure 6.1: Cross sectional shape of the elliptical channel

Elliptical shape channels are an interesting class of geometries to study since this also includes the circular channel shape. As will be seen, elliptical shapes can have a very beneficial effect on heat transfer. The geometrical shape and the selected gravity orientation are shown in Fig. (6.1). Fig. (6.2) shows the calculated perimeter averaged Nusselt number as a function of

the dimensionless axial location Z for elliptical sections having different aspect ratios r_E (x semi-axis length over y semi-axis length). A comparison with the circular channel ($r_E = 1.0$) is also presented in the graph: the legend shows (i) the mean Nusselt number obtained by integration over the entire inner surface, (ii) the calculated vapor quality variation, (iii) the dimensionless frictional pressure drop and (iv) the *performance* parameter $\Delta P_f^*/\Delta X$: this parameter quantifies the efficiency of the condensing process and it is proportional to the required input mechanical power that is necessary to release a thermal power proportional to ΔX . Near to the inlet, where the void fraction is close to 1, the tendency of the condensate to flow towards the region of higher curvature (and lower pressure) results in a strong enhancing effect of the value of the local Nusselt number especially for non-uniform channel shapes. It is evident from the results that, as suggested by the dimensional analysis of the problem, higher values of Sn lead to nearly proportionally higher local and mean Nusselt numbers.

In general it is possible to see that the heat transfer process loses its efficacy moving along the channel axis, that is, at lower vapor qualities. The highest average Nusselt number is achieved with the elliptical channel with the highest aspect ratio, which exploits the capillary effects in an optimal way. Considering the results obtained for $Sn = 23$: the average Nusselt numbers for the three different aspect ratios $r_E = 1.0, 1.2$ and 1.4 are respectively $Nu_{av} = 38.0, 35.7$ and 43.5 over nearly the same vapor quality range ($\simeq 0.430\text{--}0.998$). Thus, in this particular range, an increase of the eccentricity of the channel does not produce in general a monotonic increment of the heat transfer performance as a minimum can be found for $r_E = 1.2$. In order to identify the reason of this phenomenon, the coupled effects of the capillary forces and the gravitational forces have to be considered: the accumulation of the condensate towards the local convex regions tends to gradually reduce the effective heat transfer area where the condensate film is thin; gravity tends to pull down the liquid thus allowing the removal of the liquid from the accumulation regions, but, under certain circumstances, this flow is significantly reduced by the capillary force itself which counteracts this flow, trying to keep the condensate at the top of the channel. In particular, when the gravity is oriented as the longer axis of the ellipse, the thinning of the condensate on the right and left sides of the channel tends to partially prevent the natural gravity driven downward flow. When the higher local values of heat transfer coefficients at the two sides do not compensate the reduction of highly performing heat transfer area, this results in a globally lower performance. It is interesting to note the existence of a *minimum* of the heat transfer performance which is gradually weakened as the capillary number increases and completely disappears for the highest value of $Sn = 30$. Within all the reported simulations, the best performances are achieved by the circular channel for all the Nusselt numbers.

Up to now, only the case where the gravity is oriented with the longer axis of the ellipse has been analyzed. Fig. (6.3) shows instead the effects of different gravity intensities when it is oriented with the shorter axis direction(x). For all these simulations the value of $Sn = 25$ has been set constant. Also in these cases it is possible to note that an increase of the Bond number (in terms of absolute value) does not necessarily lead to higher performance (as it would be expected if only the gravity is dominating the condensation process, thus favoring the stratification and

the consequently increase of highly performing heat transfer areas): this is true for the circular channel shape and for the elliptical shape having $r_E = 1.2$ but it is not the case for the highest aspect ratio case.

Fig. (6.4), Fig. (6.5), Fig. (6.6) and Fig. (6.7) show instead the effects of the capillary Reynolds number Re_q , the density ratio Γ , the Weber number We and the single phase vapor Reynolds number Re_v . Although the capillary Nusselt number is very important in determining the heat transfer characteristics for annular laminar film condensation, the other dimensionless groups have been found to have in certain cases a significant effect. The capillary Reynolds number Re has been found to have a small effect on heat transfer, but a much stronger effect on the frictional pressure drop. Smaller values of Re , as it is possible to see in Fig. (6.4) lead to higher Nusselt numbers but also to smaller vapor quality variations. It has been highlighted the fact that higher values of Sn leads to lower characteristic film thicknesses thus it can be considered a *local* effect. The capillary Reynolds number instead has an *integral* effect, influencing mainly the shape of the distribution of the condensate film and not its minimum values. Lower Reynolds numbers tend to retard the accumulation of the condensate in the low pressure regions thus increasing the highly effective heat transfer area but also the average frictional pressure drop.

The effects of the vapor to liquid density ratio is also very important as it can be seen in Fig. (6.5) which shows the simulation results for $\Gamma = 0.01, 0.02, 0.05$: lower values of Γ lead to much higher Nusselt numbers (local or global) over the same vapor quality range. In this case the explanation is mainly related to the increase of the vapor phase axial velocity which leads to stronger interfacial shear stresses, and thus to a more efficient way of removing the condensate in the section of the channel. Following the same reasoning, the effects of the liquid Weber and the vapor phase Reynolds numbers can be seen in Fig. (6.6) and Fig. (6.7): higher interfacial shear leads to higher Nusselt numbers, as expected. It can be noted that, within this range of independent numbers, the effect of the vapor phase Reynolds number is much less significant than that of the liquid Weber number.

The calculate liquid-vapor interfacial shapes for some of these simulations are depicted in Fig. (6.8), Fig. (6.9) and Fig. (6.10). In particular, in Fig. (6.8) and Fig. (6.9), the simulations corresponding to $Sn = 23$ and $Sn = 30$ are compared for three geometries, indicated with the letters a), b) and c). As previously commented, the stratification due to the gravitational forces is evident, especially at lower vapor qualities and it is favored in the circular channel, while the capillary forces tend to retard it in the non-circular channels. Instead, when the gravity is oriented on the shorter axis, pointing to the right in Fig. (6.10), the gravity and the capillary forces together pull the condensate towards the concave regions and this results in an earlier and more extensive stratification from which the heat transfer benefits.

For the presented simulation case, the range of values of the turbulent parameter δ^+ as defined in Chapter 3 is 1.5 – 34.

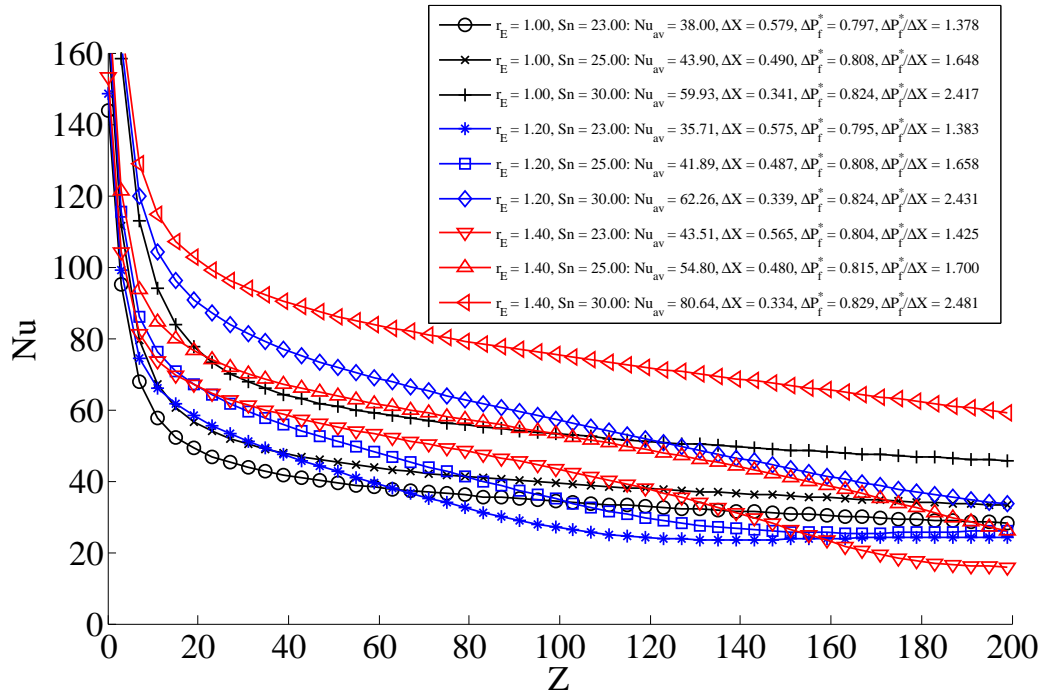


Figure 6.2: Nusselt numbers plotted versus the dimensionless axial location for elliptical shape channels (E) with different aspect ratios and capillary Nusselt numbers for the following conditions: $Re_q = 0.3$, $\Gamma = 0.05$, $Re_v = 15000$, $We = 3.0$, $Bo_y = -1.5$ and $L_{ht} = 0.05$

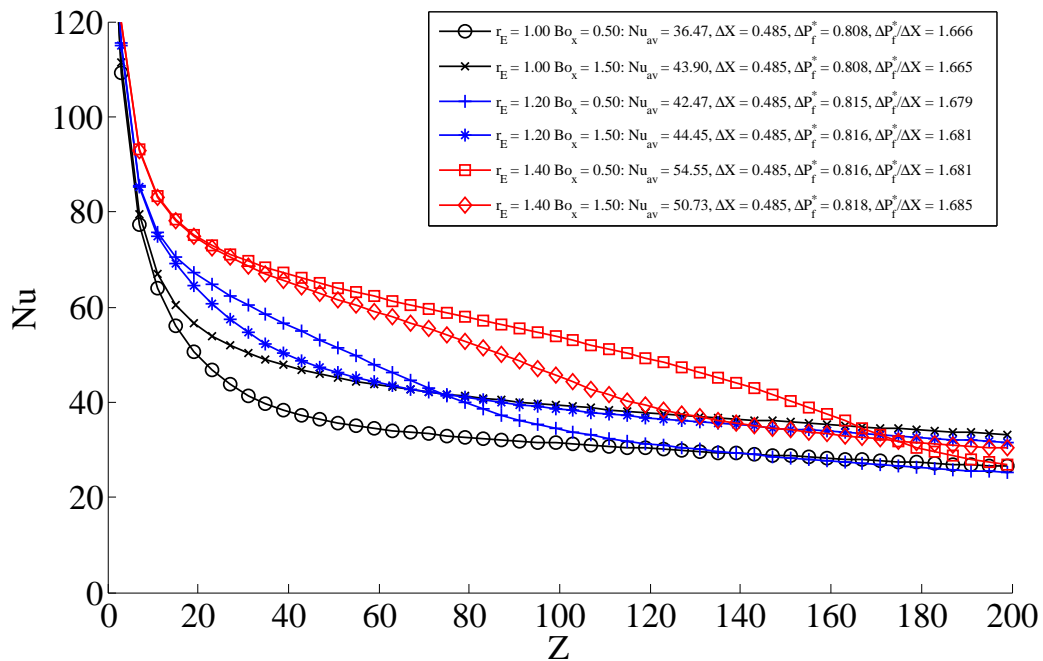


Figure 6.3: Nusselt numbers plotted versus the dimensionless axial location for elliptical shape channels (E) with different aspect ratios and Bo numbers for the following conditions: $Sn_q = 25$, $Re_q = 0.3$, $\Gamma = 0.05$, $Re_v = 15000$, $We = 3.0$ and $L_{ht} = 0.05$

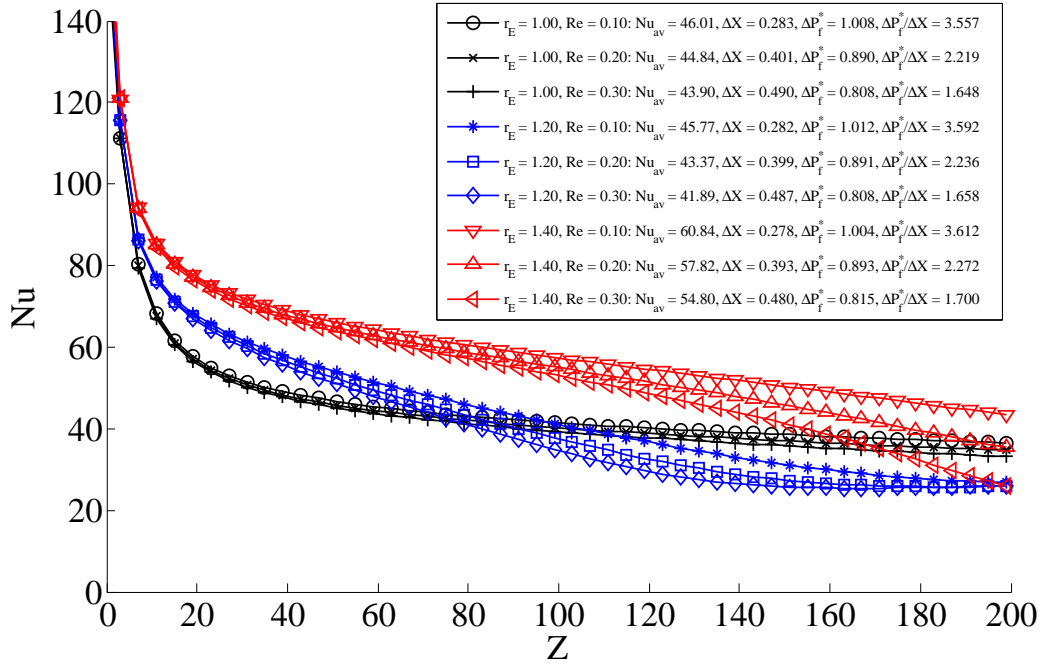


Figure 6.4: Nusselt numbers plotted versus the dimensionless axial location for elliptical shape channels (E) with different aspect ratios and capillary Reynolds numbers for the following conditions: $Sn_q = 25$, $\Gamma = 0.05$, $Re_v = 15000$, $We = 3.0$, $Bo_y = -1.5$ and $L_{ht} = 0.05$

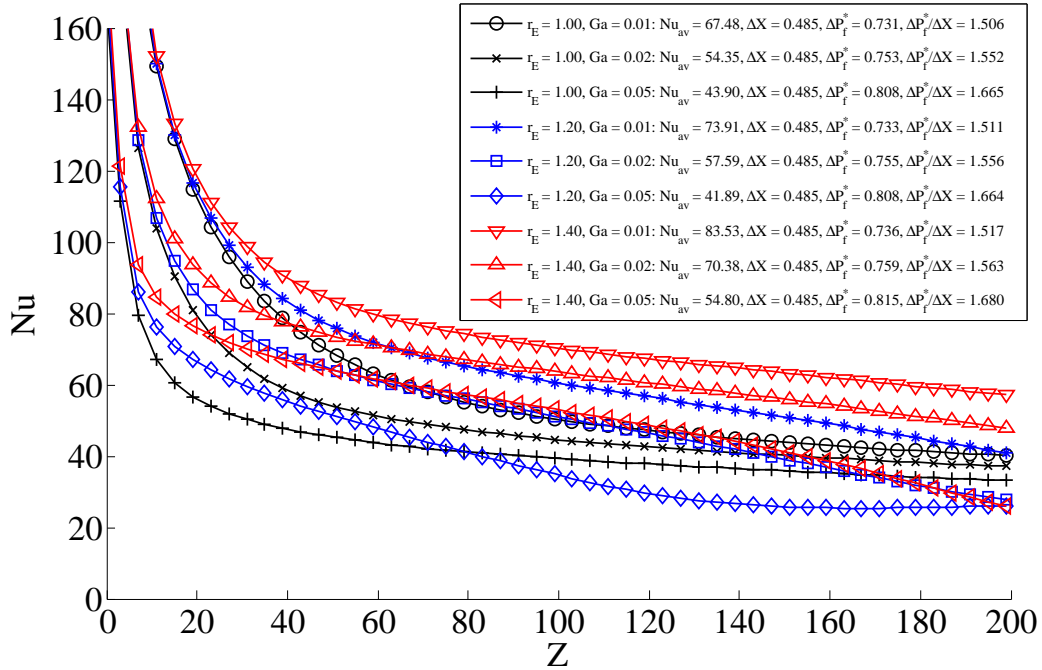


Figure 6.5: Nusselt numbers plotted versus the dimensionless axial location for elliptical shape channels (E) with different aspect ratios and density ratios for the following conditions: $Sn_q = 25$, $Re_q = 0.3$, $Re_v = 15000$, $We = 3.0$, $Bo_y = -1.5$ and $L_{ht} = 0.05$

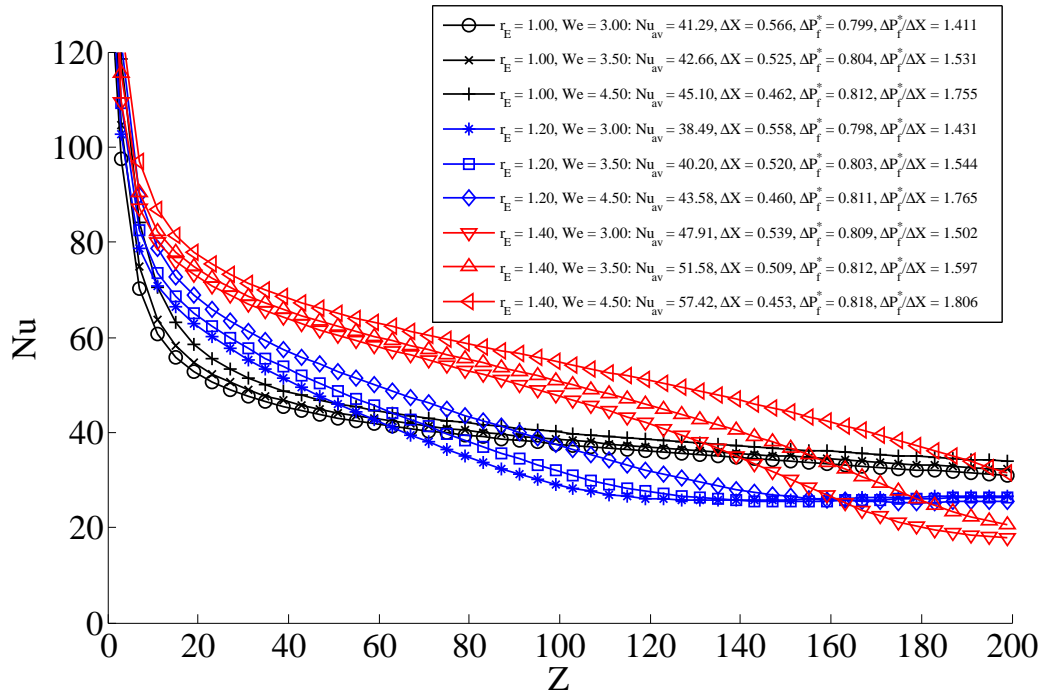


Figure 6.6: Nusselt numbers plotted versus the dimensionless axial location for elliptical shape channels (E) with different aspect ratios and liquid Weber numbers for the following conditions: $Sn_q = 25$, $Re_q = 0.3$, $\Gamma = 0.05$, $Re_v = 15000$, $Bo_y = -1.5$ and $L_{ht} = 0.05$

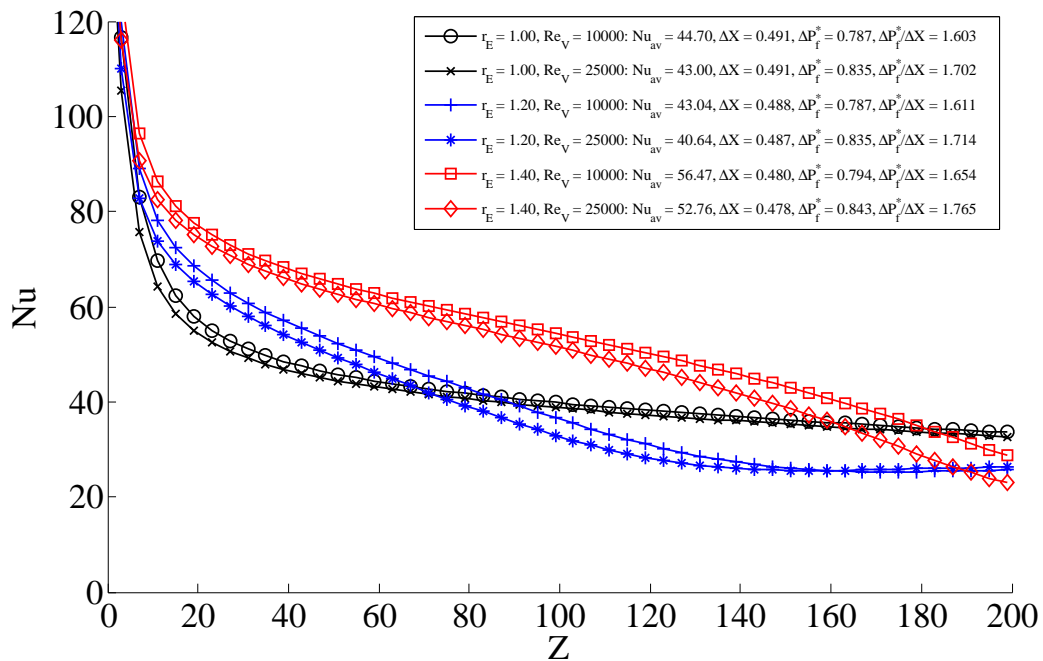


Figure 6.7: Nusselt numbers plotted versus the dimensionless axial location for elliptical shape channels (E) with different aspect ratios and vapor Reynolds numbers for the following conditions: $Sn_q = 25$, $Re_q = 0.3$, $\Gamma = 0.05$, $We = 3.0$, $Bo_y = -1.5$ and $L_{ht} = 0.05$

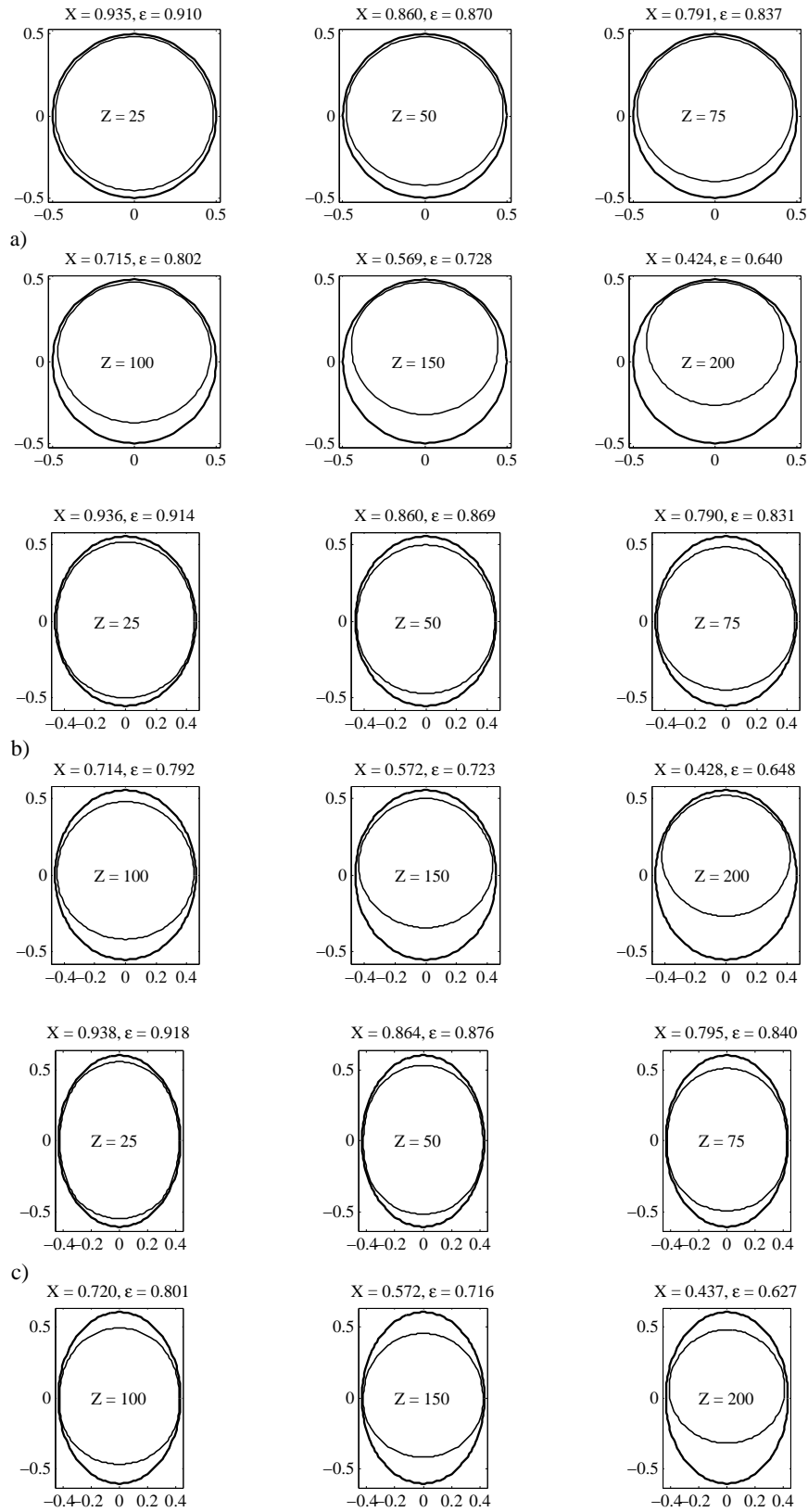


Figure 6.8: Steady state calculated liquid-vapor interfacial shapes for the following conditions: $Sn = 23$, $Re_d = 0.3$, $\Gamma = 0.05$, $Re_v = 15000$, $L_{ht} = 0.05$, $Bo_y = -1.5$ and three different aspect ratios: a) $r_E = 1.0$ (circular case), b) $r_E = 1.2$ and c) $r_E = 1.4$

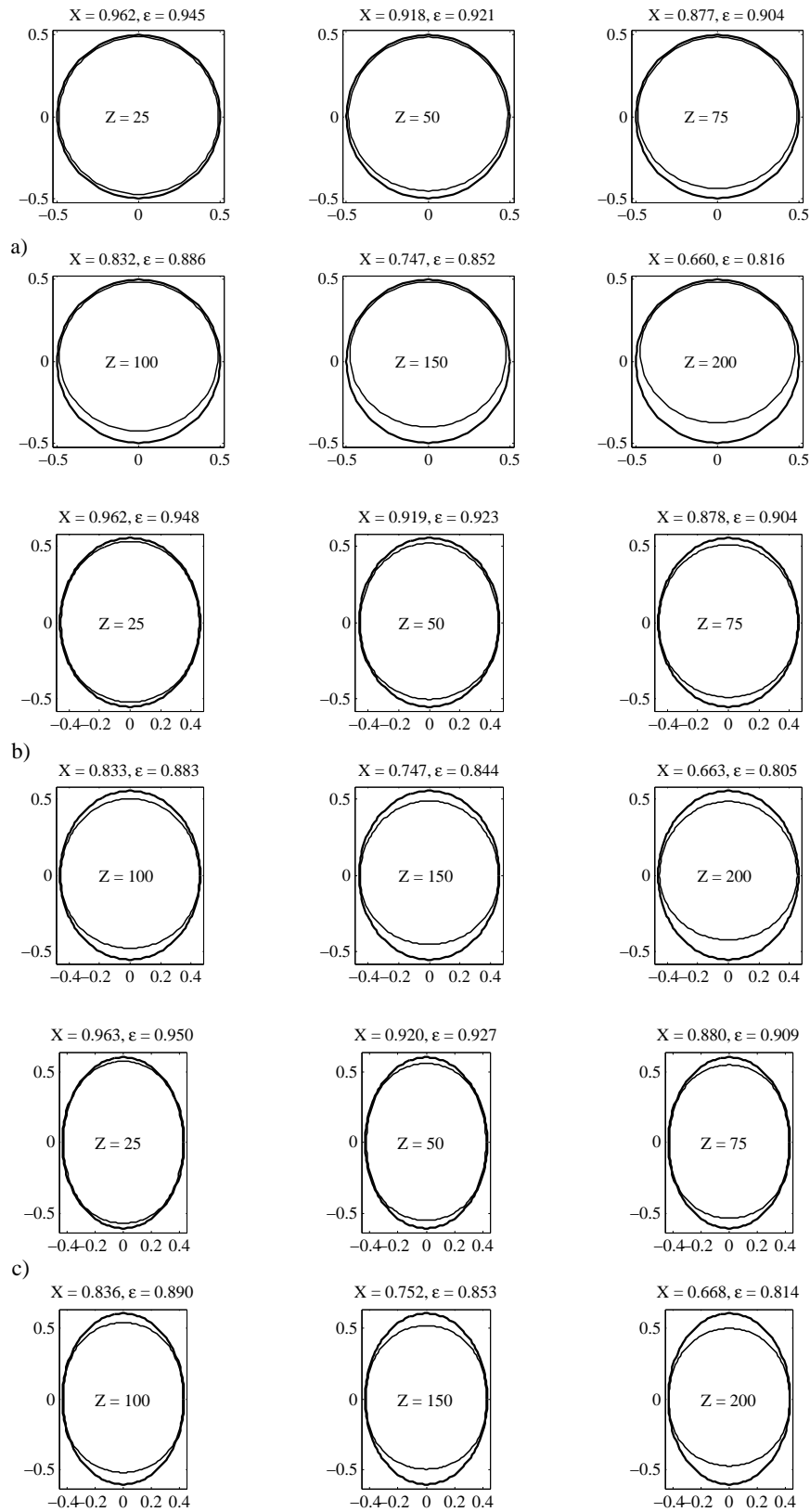


Figure 6.9: Steady state calculated liquid-vapor interfacial shapes for the following conditions: $Sn = 30$, $Re_q = 0.3$, $\Gamma = 0.05$, $Re_v = 15000$, $L_{ht} = 0.05$, $Bo_y = -1.5$ and three different aspect ratios: a) $r_E = 1.0$ (circular case), b) $r_E = 1.2$; c) $r_E = 1.4$

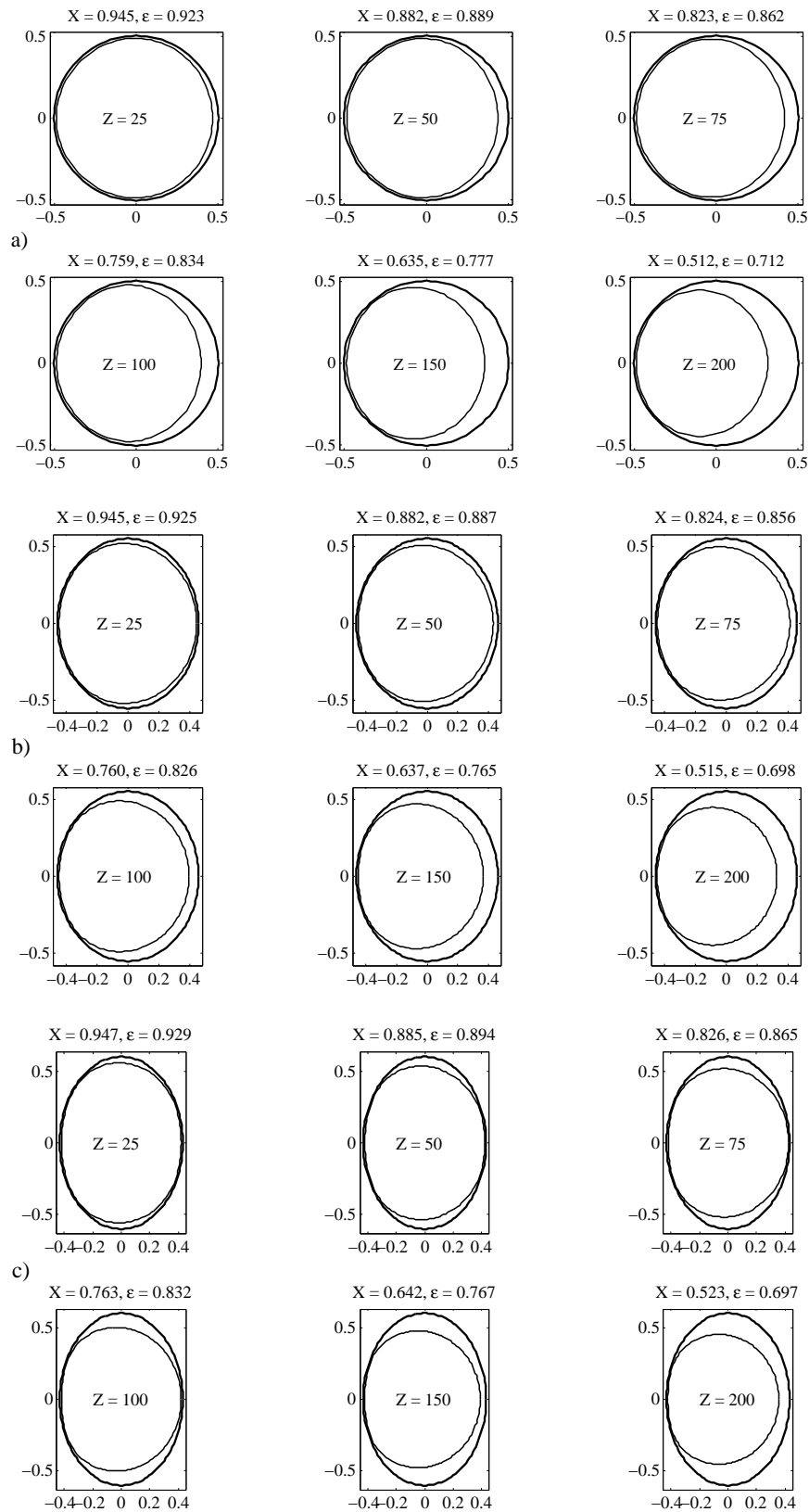


Figure 6.10: Steady state calculated liquid-vapor interfacial shapes for the following conditions: $Sn = 25$, $Re_q = 0.3$, $\Gamma = 0.05$, $Re_v = 15000$, $L_{ht} = 0.05$, $Bo_x = 1.5$ (the gravity points to the right) and three different aspect ratios: a) $r_E = 1.0$ (circular case), b) $r_E = 1.2$ and c) $r_E = 1.4$

6.1.2 Flattened Channel Shape

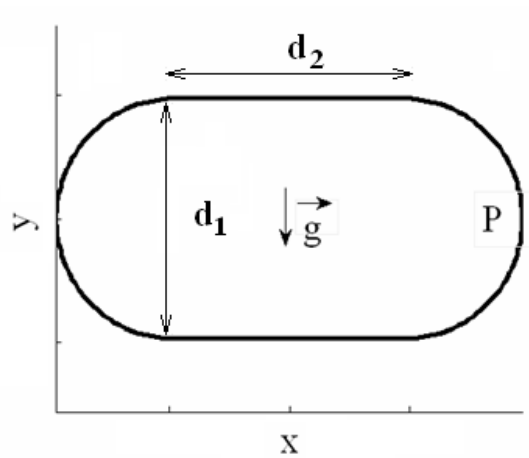


Figure 6.11: Cross sectional shape of the flattened channel

Flattened channel shapes can be found in various application, such as tubes that have been flattened to fix to cold plated for satellite radiation (cooling) panels. This shape is also interesting since in the limit, as it can be seen in Fig. (6.11), this shape reverts to a circular channel. Qualitative similar results have hence been obtained for the flattened shape channels, for the same range of dimensionless numbers. The aspect ratio r_F in this case is defined as the ratio of the flat segment length connecting the two curved ends (d_2) over the diameter of the rounded ends (d_1).

The effects of the capillary Nusselt number are shown in Fig. (6.12): as in the case of the elliptical channel, higher values of Sn lead to higher Nusselt numbers and smaller vapor quality variations (as the channel dimensionless length is kept constant). The heat transfer efficiency $\Delta P_f^*/\Delta X$ declines as the capillary Nusselt number is increased and this occurs for all the flattening ratios r_F . The mean Nusselt numbers for $r_F = 0.5$ are equal to 48.4, 58.9 and 87.0 for $Sn_q = 23, 25$ and 30 respectively: if compared with the results obtained for the circular channel shape ($r_E = 1.0$ in Fig. (6.2)) the enhancement factors are respectively equal to 27%, 34% and 45%. The most interesting point can be highlighted when considering the solutions obtained for different aspect ratios: for $Sn_q = 23$ and $Sn_q = 25$, the geometry which gives the highest average Nusselt numbers corresponds in both cases to a flattening ratio of $r_F = 1.0$, while for the highest capillary Nusselt number $Sn_q = 30$, the best geometrical configuration is obtained for $r_F = 0.5$.

The effects of the orientation of the gravity field with respect to the geometrical axis (in the x - y plane) are shown in Fig. (6.13): in this case, for $r_F = 0.5$ and $r_F = 1.5$ a gravitational field oriented parallel to the flat side of the channel has a positive effect on the Nusselt number and it also leads to a more uniform distribution of the heat transfer; for $r_F = 1.0$ the differences are barely noticeable.

The effects of the capillary Reynolds number, the density ratio, the liquid Weber number and the Reynolds number are shown in Fig. (6.14), Fig. (6.15), Fig. (6.16) and Fig. (6.17): although they show the same qualitative trends discussed in the previous section for the elliptical channel, it can be seen that the sensitivities to these parameters are quite different and a modification of one (or more) of these groups has a direct impact on the heat transfer performances which can be higher or lower depending on the particular operative range and on the geometry. Consider for instance Fig. (6.16): incrementing the Weber number from $We_1 = 3.0$ to $We_1 = 4.5$ gives only a 1.7 % increase in heat transfer for the flattening ratio $r_F = 0.5$ while it gives an increase of 7.9 % for $r_F = 1$. Similarly, referring to Fig. (6.14), a reduction of the capillary Reynolds number from the value $Re = 0.3$ to $Re = 0.1$ leads to a 10 % increase in the average Nusselt number for $r_F = 0.5$ while this enhancement is limited to 3 % for the same conditions for $r_F = 1.5$.

This behavior, which is characteristic of complex non-linear systems, is due to complex interactions between the two-phase flow, the geometry and the gravitational forces: while a certain variation of a specific parameter is not able to trigger a significant change in the solution for a specific set of parameters, the same variation may be enough in other circumstances to lead to strong differences.

The calculated liquid-vapor interfacial shapes for some of the simulations are depicted in Fig. (6.18) Fig. (6.19) and Fig. (6.20). In particular, the solutions corresponding to $Sn = 23$ and $Sn = 30$ are compared in Fig. (6.18) and Fig. (6.19) to three geometries, indicated with the letters a), b) and c), corresponding to three different aspect ratios. In all these cases, stratification is barely noticeable as the capillary forces are capable of maintaining the condensate in the rounded corner regions and, in doing so, a high heat transfer area is continuously maintained in the central region at the top and bottom. The effects on the liquid-vapor interface of a gravity field oriented in the x axis direction are depicted in Fig. (6.20): it is interesting to note that the effect of the very thin film in the center of the channel prevents the natural gravity driven flow (in the figure, from left to right); thus at each location, the amount of accumulated liquid at the two rounded sides is approximately the same.

For the presented simulation case, the range of values of the turbulent parameter δ^+ as defined in Chapter 3 is 1 – 26.

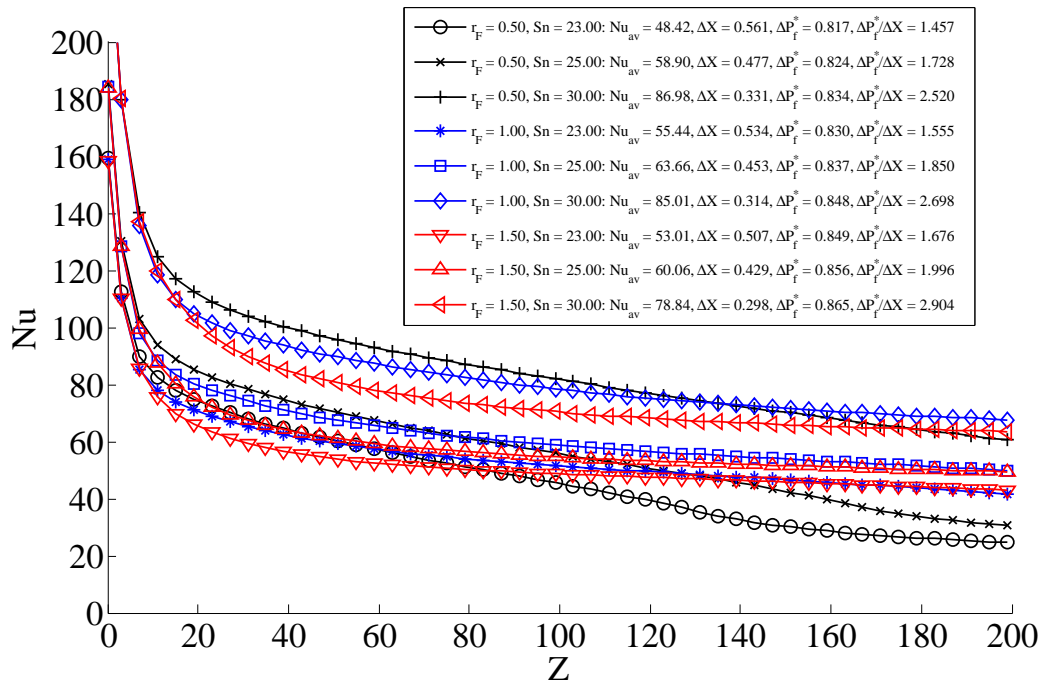


Figure 6.12: Nusselt numbers plotted versus the dimensionless axial location for flattened shape channels (F) with different aspect ratios and capillary Nusselt numbers for the following conditions: $Re_q = 0.3$, $\Gamma = 0.05$, $Re_v = 15000$, $We = 3.0$, $Bo_y = -1.5$ and $L_{ht} = 0.05$

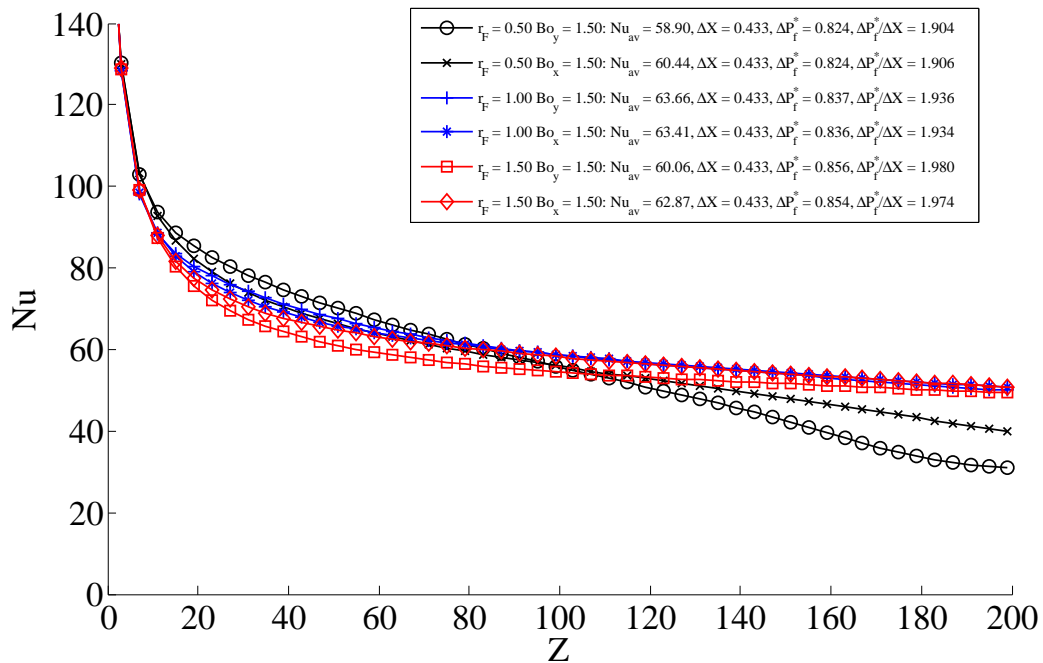


Figure 6.13: Nusselt numbers plotted versus the dimensionless axial location for flattened shape channels (F) with different aspect ratios and Bond numbers for the following conditions: $Sn_q = 25$, $Re_q = 0.3$, $\Gamma = 0.05$, $Re_v = 15000$, $We = 3.0$ and $L_{ht} = 0.05$

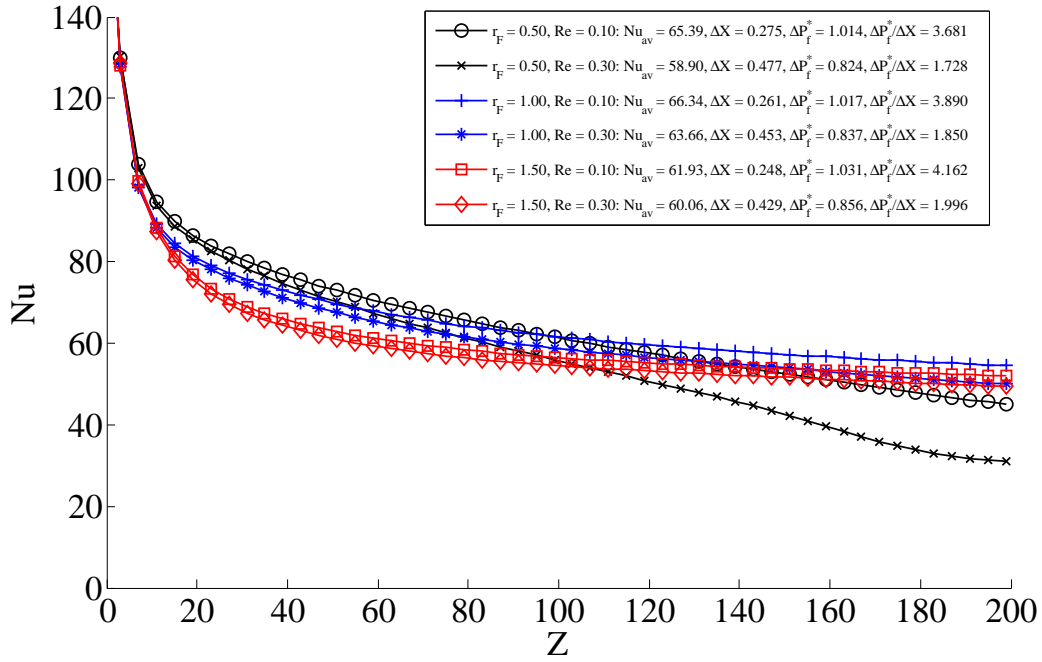


Figure 6.14: Nusselt numbers plotted versus the dimensionless axial location for flattened shape channels (F) with different aspect ratios and capillary Reynolds numbers for the following conditions: $\text{Sn}_q = 25$, $\Gamma = 0.05$, $\text{Re}_v = 15000$, $\text{We} = 3.0$, $\text{Bo}_y = -1.5$ and $L_{\text{ht}} = 0.05$

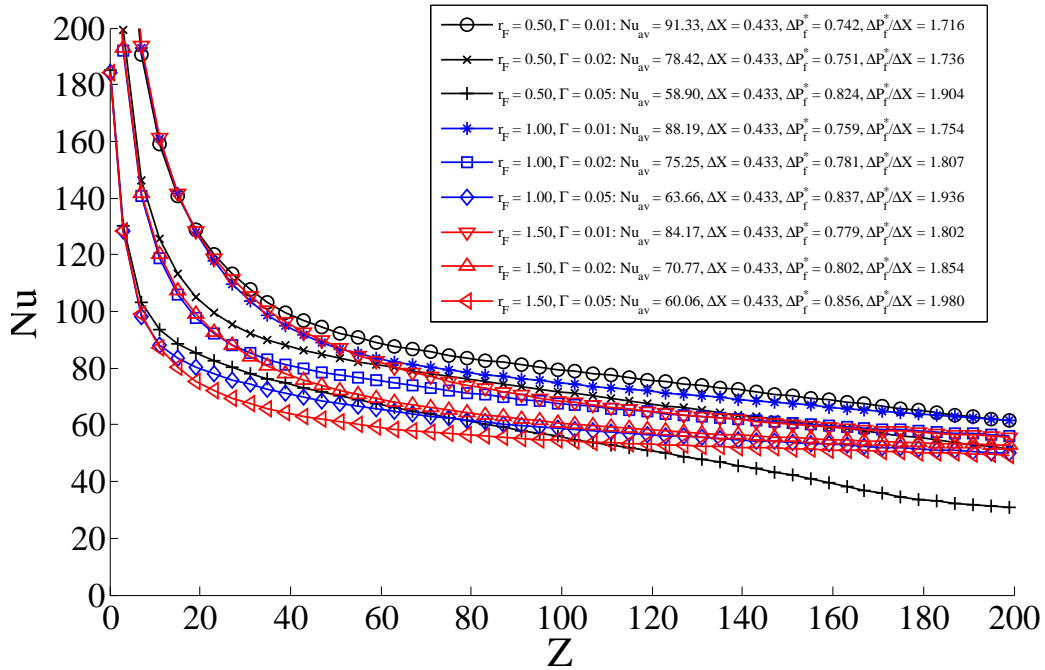


Figure 6.15: Nusselt numbers plotted versus the dimensionless axial location for flattened shape channels (E) with different aspect ratios and density ratios for the following conditions: $\text{Sn}_q = 25$, $\text{Re}_q = 0.3$, $\text{We} = 3.0$, $\text{Re}_v = 15000$, $\text{Bo}_y = -1.5$ and $L_{\text{ht}} = 0.05$

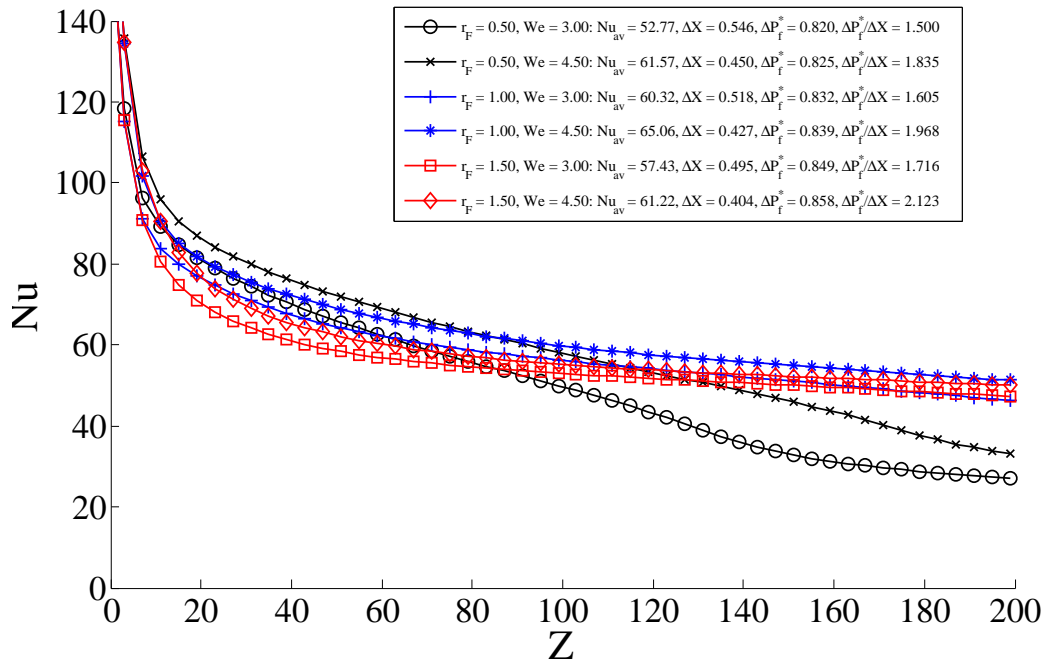


Figure 6.16: Nusselt numbers plotted versus the dimensionless axial location for flattened shape channels (F) with different aspect ratios and liquid Weber numbers for the following conditions: $Sn_q = 25$, $Re_q = 0.3$, $\Gamma = 0.05$, $Re_v = 15000$, $Bo_y = -1.5$ and $L_{ht} = 0.05$

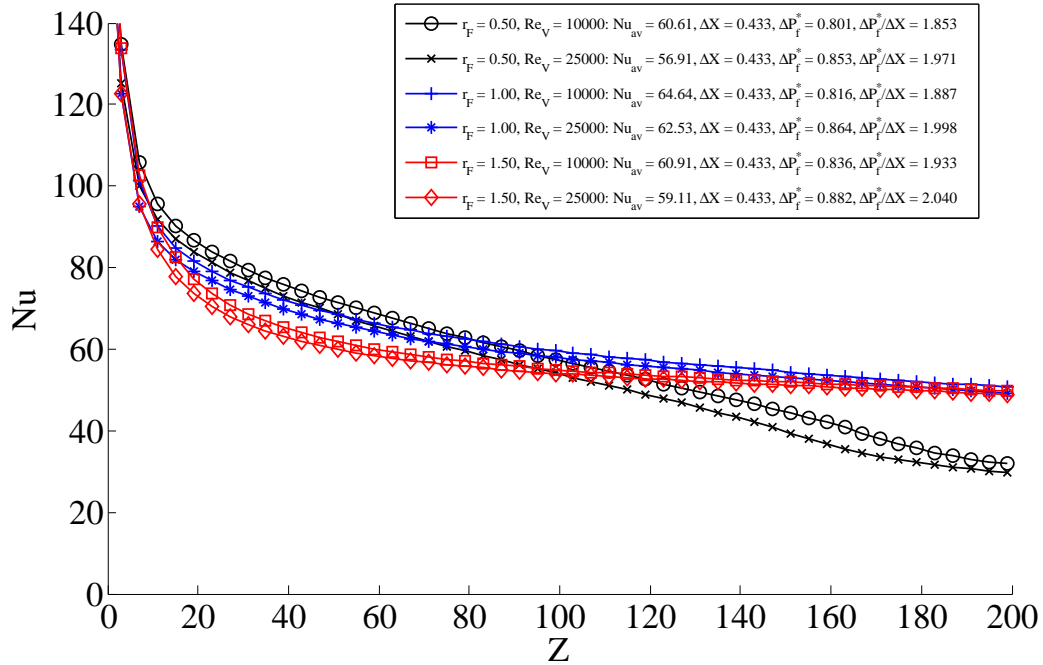


Figure 6.17: Nusselt numbers plotted versus the dimensionless axial location for flattened shape channels (F) with different aspect ratios and vapor Reynolds numbers for the following conditions: $Sn_q = 25$, $Re_q = 0.3$, $\Gamma = 0.05$, $We = 3.0$, $Bo_y = -1.5$ and $L_{ht} = 0.05$

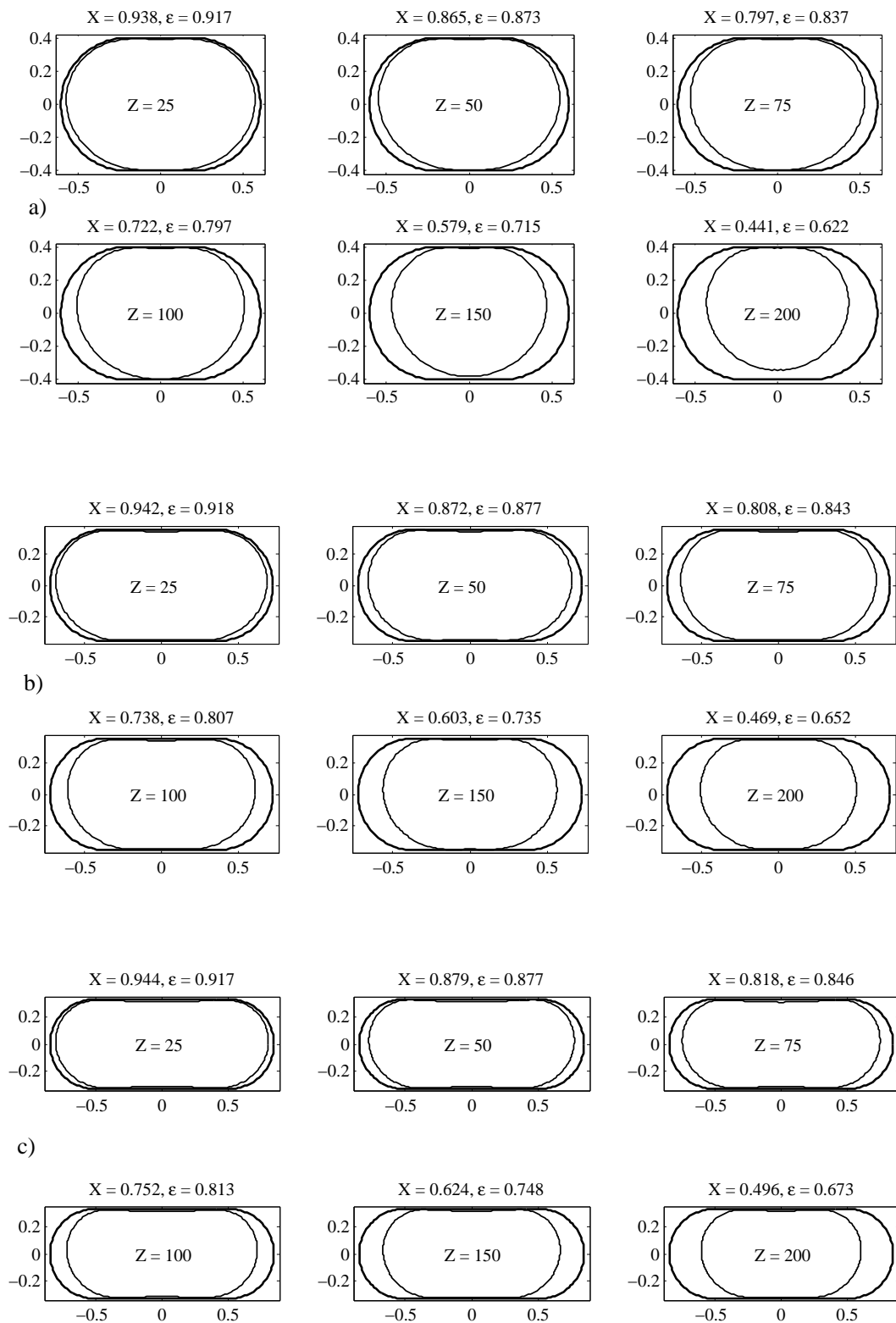


Figure 6.18: Steady state calculated liquid-vapor interfacial shapes for the following conditions: $Sn = 23$, $Re_q = 0.3$, $\Gamma = 0.05$, $Re_v = 15000$, $L_{ht} = 0.05$, $Bo_y = -1.5$ for three different aspect ratios: a) $r_F = 0.5$, b) $r_F = 1.0$ and c) $r_F = 1.5$

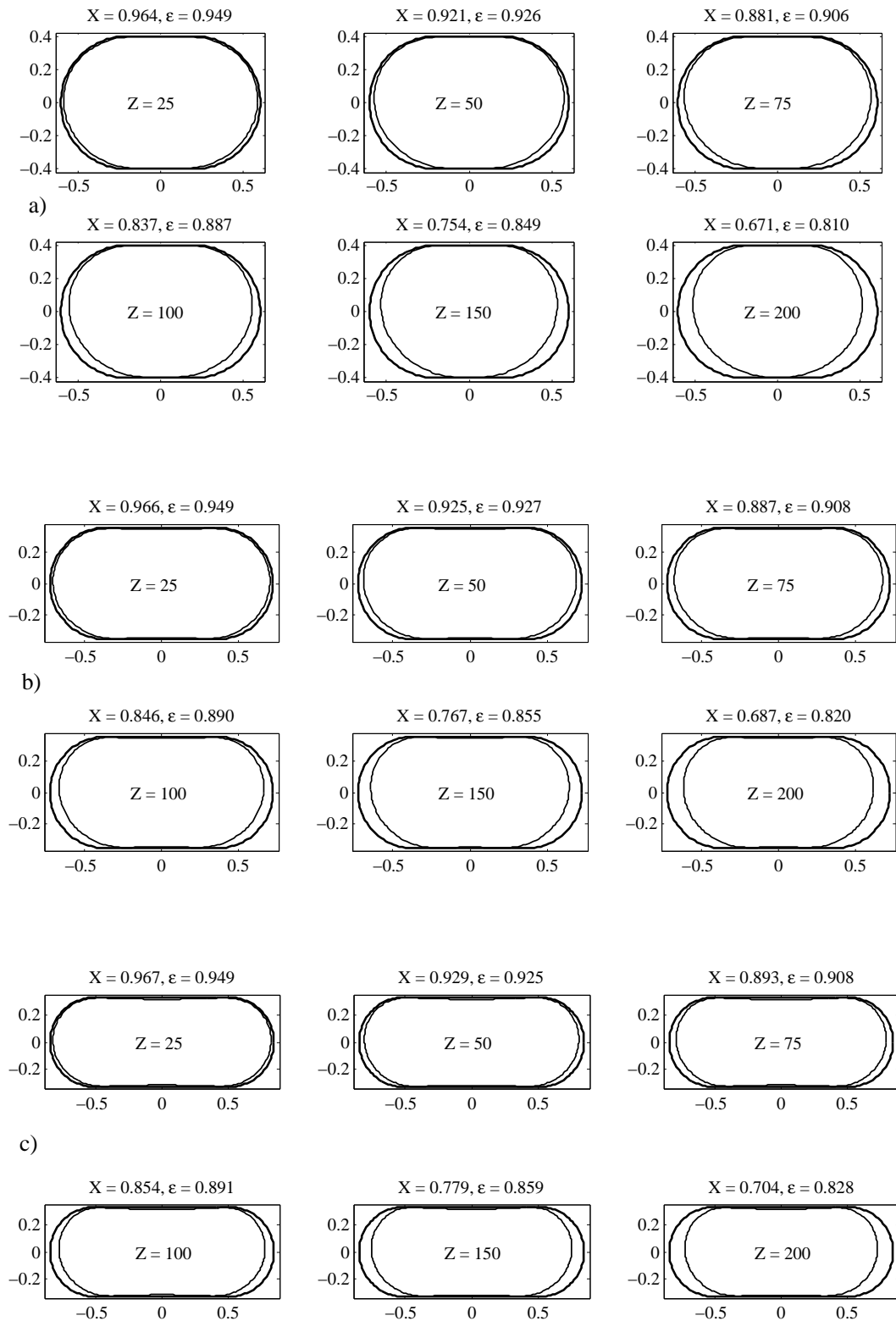


Figure 6.19: Steady state calculated liquid-vapor interfacial shapes for the following conditions: $Sn = 30$, $Re_q = 0.3$, $\Gamma = 0.05$, $Re_v = 15000$, $L_{ht} = 0.05$, $Bo_y = -1.5$ for three different aspect ratios: a) $r_F = 0.5$, b) $r_F = 1.0$ and c) $r_F = 1.5$

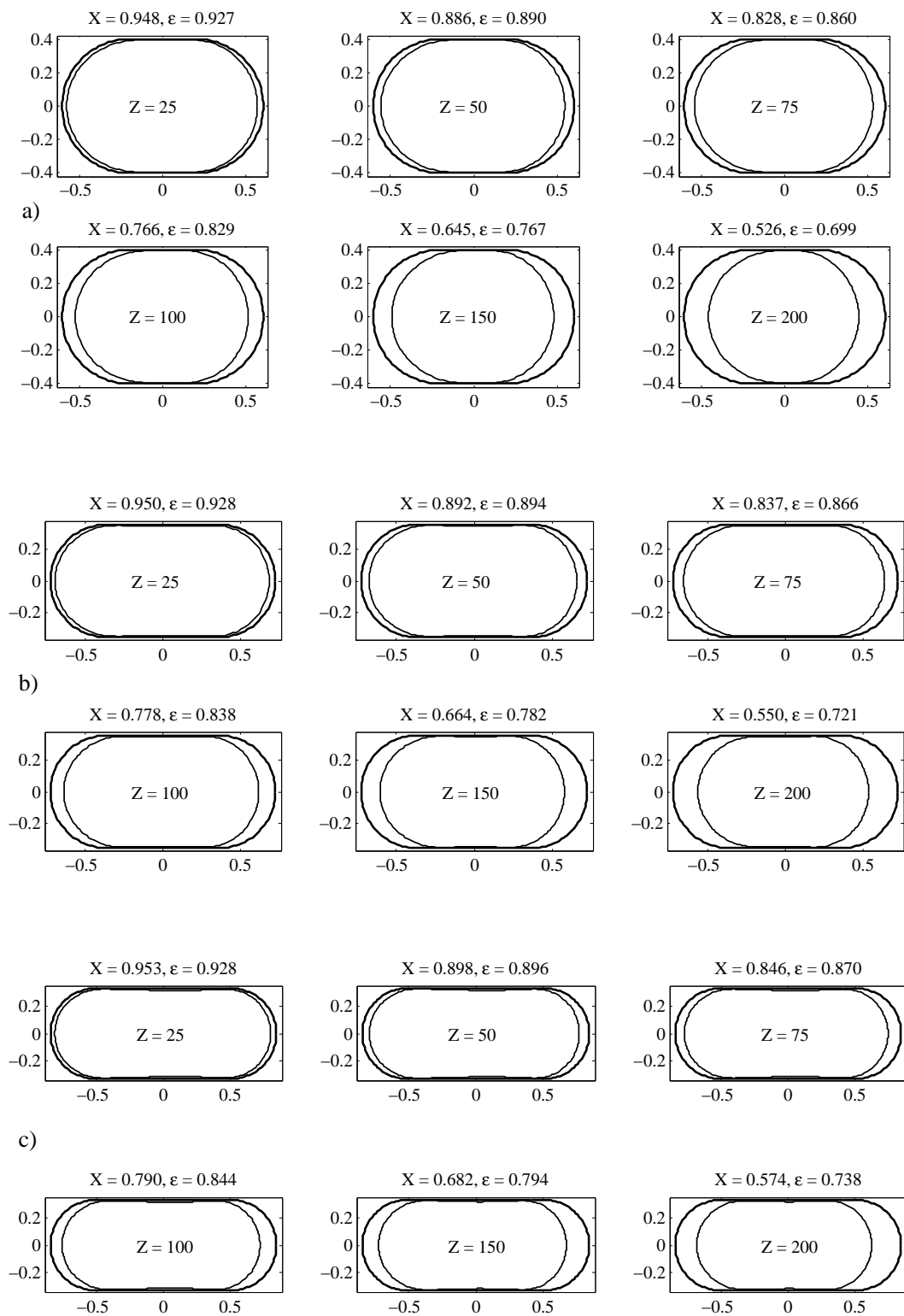


Figure 6.20: Steady state calculated liquid-vapor interfacial shapes for the following conditions: $Sn = 30$, $Re_q = 0.3$, $\Gamma = 0.05$, $Re_v = 15000$, $L_{ht} = 0.05$, $Bo_x = 1.5$ (gravity in the direction of the flat side, pointing to the right) for three different aspect ratios: a) $r_F = 0.5$, b) $r_F = 1.0$ and c) $r_F = 1.5$

6.2 Wall Conduction Effects in Microchannels

Axial and peripheral conduction occurring in the wall of the channel can affect the behavior of the condensate film inside, not only because it redistributes the heat, but also because the annular laminar film condensation process is dependent on the local saturation to wall temperature difference. The effects can be important for the uniform heat flux condition and for non-uniform heat flux conditions as well. In order to evaluate the effects of wall conduction, two different simulated cases are presented in the following sub-sections, focusing in particular on (i) actual heat flux and wall temperature distributions (i.e. typical experimental conditions for measuring the heat transfer coefficient) and (ii) on entrance region effects.

6.2.1 Non-Uniform Heat flux and Conjugate Heat Transfer Length

One way of investigating the effects of the wall conduction is to compare different simulated solutions obtained by varying the dimensionless *conjugate heat transfer length* that is derived in Appendix C, through Eq. (C.25), and maintaining the following reference conditions constant:

- flattened channel shape with $r_F = 0.5$ is assumed, with a hydraulic diameter of $100\ \mu\text{m}$ and a length to diameter ratio of 200;
- fluid is R-134a at $20\ ^\circ\text{C}$ saturation temperature;
- total mass flux is $G = 500\ \text{kg}/(\text{m}^2\text{s})$;
- inlet vapor quality is $X_{in} = 0.999$;
- mean heat flux is equal to $50\ \text{kW}/\text{m}^2$ and its distribution is an imposed function of the axial location: for $z/L_t < 0.05$ and $z/L_t > 0.95$ the heat flux is equal to 5% of the mean value, while in the remaining part it is equal to the 110% of the mean value;

The conjugate heat transfer length is defined as:

$$l_{ch} = \sqrt{\frac{\lambda_w k_w}{h_{i,0}}} \quad (6.1)$$

The dimensionless conjugate heat transfer length L_{ch} is simply defined as the ratio of l_{ch} and the total length of the channel. The results of the simulations have been obtained for four different values of L_{ch} and the distributions of the saturation to mean wall temperature difference are shown in Fig. (6.21). The calculated total frictional pressure drop is nearly constant (32 kPa) for all the cases which corresponds to an average frictional pressure gradient of 1.6 MPa/m and the mean heat transfer coefficient (based on the wall mean temperature) is $37.3\ \text{kW}/(\text{m}^2\text{K})$. The local distribution of the perimeter-averaged heat transfer coefficient depends on the actual difference between the saturation temperature and the perimeter-averaged wall temperature.

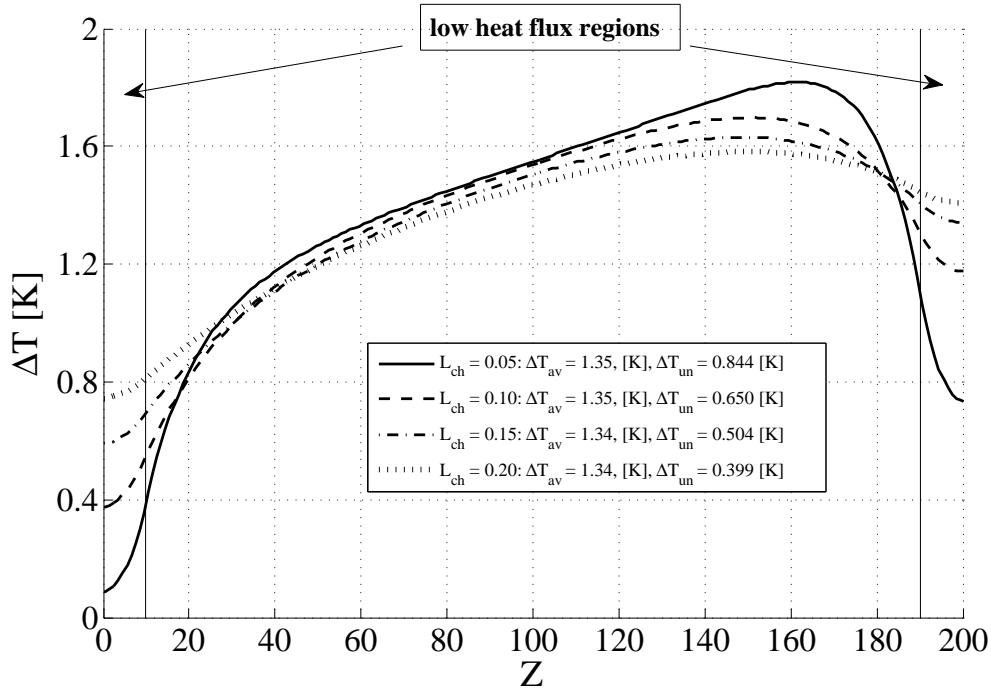


Figure 6.21: Wall temperature distributions obtained for R-134a condensing in a $100\ \mu\text{m}$ hydraulic diameter flattened shape microchannel with aspect ratio $r_F = 0.5$ for $G = 500\ \text{kg}/(\text{m}^2\text{s})$, 20°C saturation temperature and mean heat flux equal to $50\ \text{kW}/\text{m}^2$ for different dimensionless conjugate heat transfer lengths L_{ch}

The simulations show that there can be quite a strong influence of the wall heat conduction. Low values of L_{ch} , which can be due to a low wall thermal conductivity or a thin channel wall, lead to sharper variations of the wall temperature profile and therefore of the heat transfer coefficient. On the other hand, a highly conductive wall leads as expected to a much more uniform temperature distribution. In particular, it can be noted that for low values of L_{ch} , the ΔT tends to drop in the region of low heat flux ($Z < 10$ and $Z > 190$), and the condensation process is gradually reduced in these regions. This reduction in heat transfer is more evident at the entrance than at the exit: this is due to non-symmetric conditions that occurs at these sections: at the inlet, the film covering the inner channel perimeter is very thin and thus extremely high heat transfer coefficients bring the local wall temperature very close to the saturation temperature; on the other hand, at the exit, where the vapor quality reaches a value of 0.54, the heat transfer coefficient is much lower, thus it takes longer distances for the wall temperature distribution to *adapt* itself to the new condition, consistent with the theoretical result obtained in Appendix C. In fact, the required length which is necessary in order to end the condensation process is proportional to l_{ch} (and therefore to L_{ch}). Thus, higher wall thermal conductivities and higher wall thicknesses, in conjunction with lower internal characteristic heat transfer coefficients $h_{i,0}$, lead to a longer extension of the condensing region.

In the legend, the parameter ΔT_{un} is also reported: this variable is defined as the maximum deviation along the channel from the mean wall temperature: for $L_{ch} = 0.05$ this value reaches

more than twice that of $L_{ch} = 0.20$ and consequently, as the heat flux is constant in the central region of the channel, the variations of local heat transfer coefficient are much higher in the first case than in the second.

In order to analyze more in the detail the flow and heat transfer characteristics in the proximity of a sharp variation of imposed heat flux, a detailed study of this entrance region is presented in the following section. The entrance and exit effects become much more significant as the condenser becomes more compact.

6.2.2 Analysis of the Entrance Region

The analysis of the entrance region in the presence of a sharp variation of the imposed heat flux is presented in this section: the channel length is 20 times the hydraulic diameter of $250 \mu\text{m}$ and the same channel geometry as in the previous section is considered here (flattened shape with an aspect ratio of 0.5). The imposed heat flux is equal to 2.5 kW/m^2 for the first half of the channel (that is, close to adiabatic conditions are applied), while it is fixed to 50 kW/m^2 in the second half ($Z > 10$). The inlet vapor quality is $X = 0.999$ which, for a total mass flux of $G = 250 \text{ kg/(m}^2\text{s)}$, corresponds to a mean vapor velocity of $\simeq 9 \text{ m/s}$. The mean absolute curvature H of the channel, as defined by Eq. (4.1), is equivalent to 6790 m^{-1} . The characteristic film thickness δ_q (based on the highest heat flux value) is equal to $7.09 \mu\text{m}$ while the characteristic capillary film velocity and the axial liquid single phase velocities are $u_q = 4.65 \text{ mm/s}$ and $v_{r,l} = 204 \text{ mm/s}$ respectively. For these calculations the interfacial resistance and disjoining pressure effects are included, assuming a value of the Hamaker constant $A = -10^{-21} \text{ kg m}^2 \text{ s}^{-2}$. For these conditions, the dimensionless numbers are the following: $\text{Sn}_q = 20.8$, $\text{Re}_q = 0.192$, $\Gamma = 0.0227$, $\text{Re}_v = 5400$, $\text{Bo}_y = -0.0837$, $\text{I}_{r,q} = 7.22 \cdot 10^{-4}$, $\text{I}_{p,q} = 1.83 \cdot 10^{-5}$ and $\text{I}_{d,q} = -4.09 \cdot 10^{-7}$.

Fig. (6.22) depicts the calculated saturation to mean wall temperature difference profiles for different dimensionless conjugate heat transfer lengths, from $L_{ch} = 0.5$ to $L_{ch} = 10$, covering a wide range of wall thermal conductivities. The maximum deviation of temperature over the perimeter of the channel with respect to the local perimeter-averaged wall temperature is also indicated by the parameter $\Delta T_{un,\xi}$: under these conditions, the temperature distribution in the channel wall becomes a strong function of both axial and peripheral directions.

The local saturation to wall temperature difference is plotted in Fig. (6.23) as a function of the normalized curvilinear coordinate W (the origin $W = 0$ corresponds to the point P in Fig. (6.11)) at different axial locations, when the lowest thermal conductivity case is considered. The local wall temperature distributions obtained for the lowest and the highest conjugate heat transfer lengths are shown in the 3-dimensional plots in Fig. (6.24): the highest value of wall thermal conductivity not only leads to a more uniform temperature distribution along the axis of the channel but also the temperature is more uniform over the perimeter. In correspondence to the thin film regions the wall temperature is much closer to the saturation temperature while it is lower elsewhere: this is evident in Fig. (6.24)a, in particular for $Z > 10$.

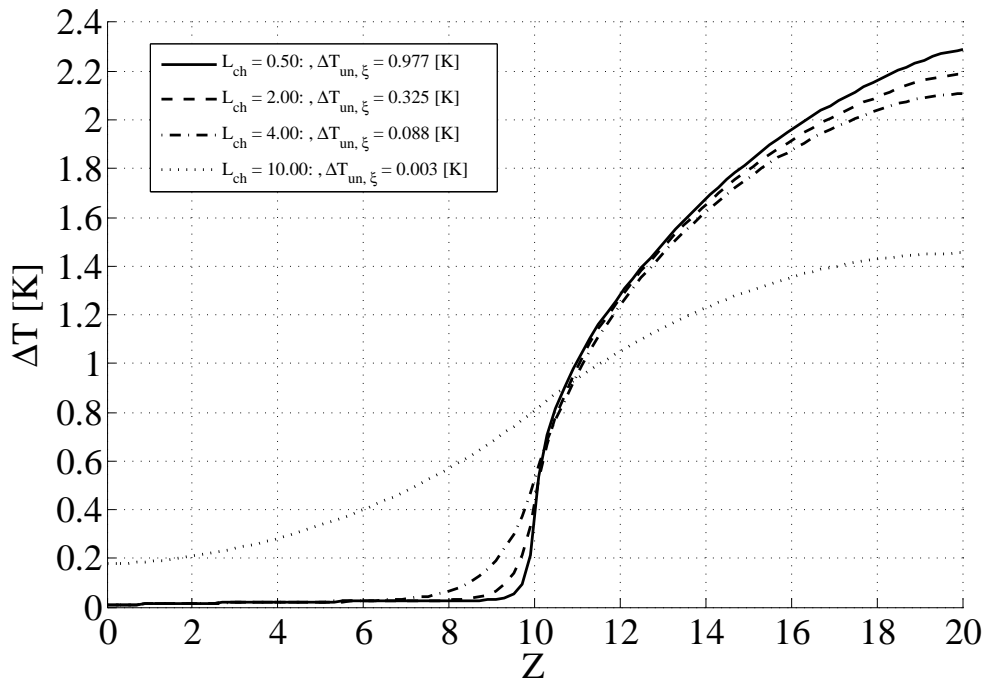


Figure 6.22: Saturation to perimeter averaged wall temperature difference distributions along the channel axis obtained for R-134a condensing in the entrance region of a $250\ \mu\text{m}$ hydraulic diameter flattened shape microchannel with aspect ratio $r_F = 0.5$ for $G = 250\ \text{kg}/(\text{m}^2\text{s})$, $20\ ^\circ\text{C}$ saturation temperature for different dimensionless conjugate heat transfer lengths L_{ch}

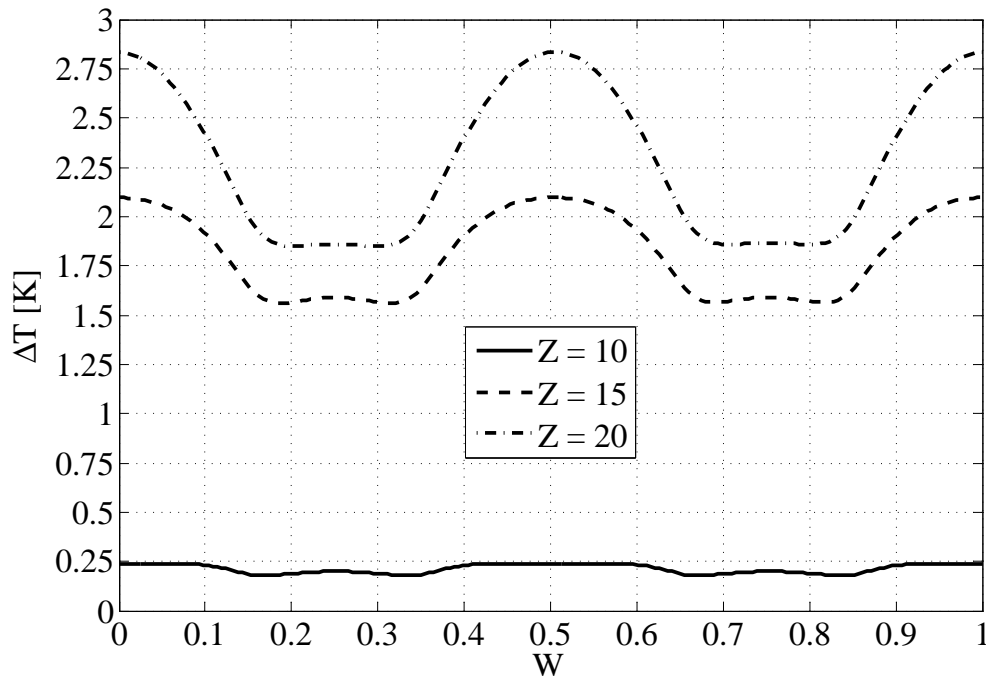


Figure 6.23: Distributions of the local saturation to wall temperature differences around the perimeter plotted at different axial locations, in correspondence to a low wall thermal conductivity condition ($L_{\text{ch}} = 0.5$)

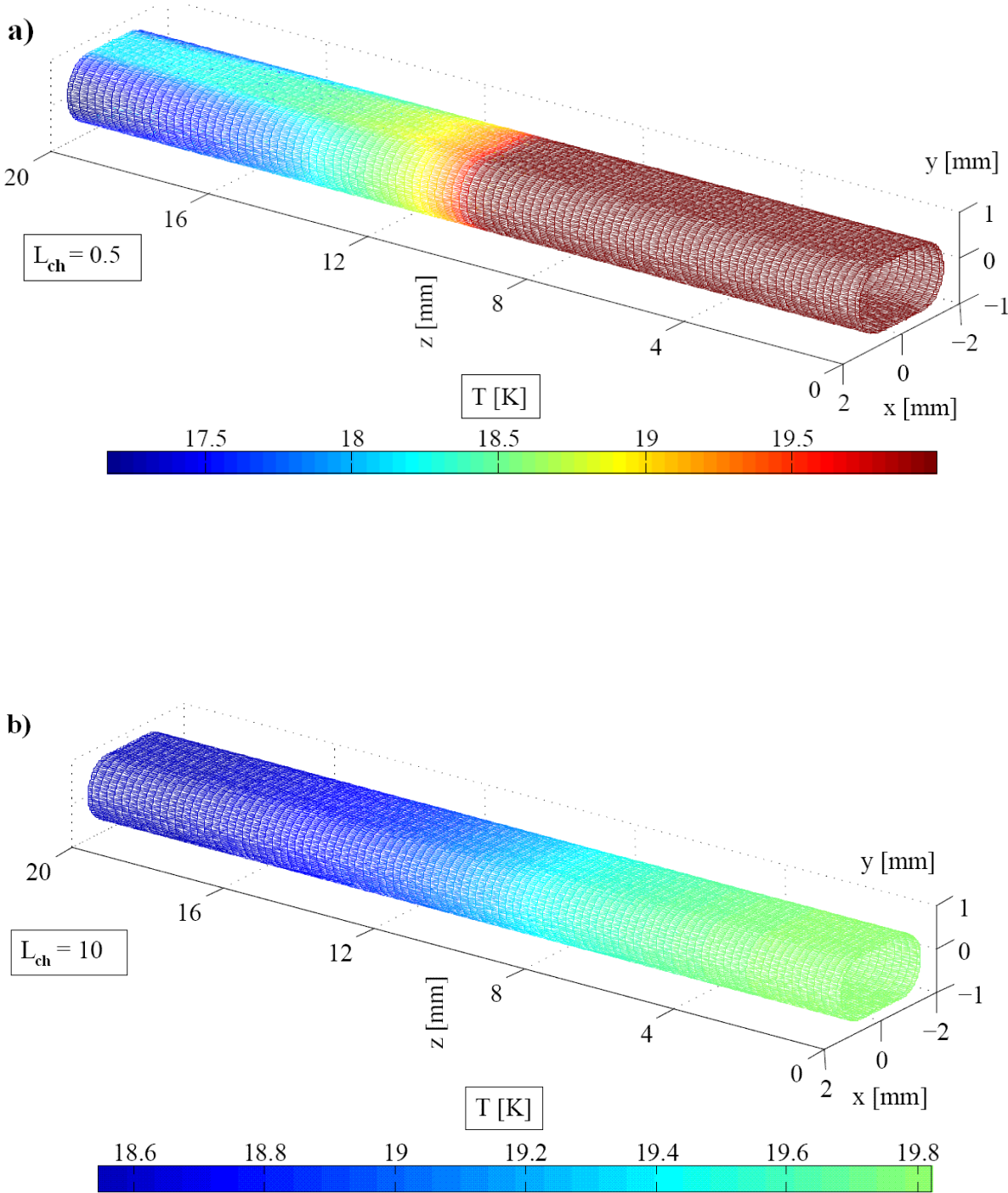


Figure 6.24: 3D plot of the wall temperature distribution for two different wall thermal conductivities corresponding to $L_{ch} = 0.5$ and $L_{ch} = 10$. The saturation temperature of the refrigerant is $T_s = 20^\circ\text{C}$

The local distribution of the perimeter-averaged effective heat flux, normalized by the peak value of $50 \text{ kW}/(\text{m}^2\text{K})$, is presented in Fig. (6.25). As expected, as the conductivity of the wall becomes lower and lower, the profile of the dimensionless heat flux Q approaches a *step function* between the values of 0.01 and 1. The axial conduction extends the entrance region by 4 to 8 hydraulic diameters in axial direction for $L_{\text{ch}} \leq 4$ while the highest value of L_{ch} leads to a condensation process which extends over the entire channel. The rise in the local heat flux which is shown in the graph for $L_{\text{ch}} = 10$ and $Z < 2$ is the result of the influence of the inlet condition (film and velocity distributions), which are not yet *adapted* to the geometry as these conditions have been arbitrarily imposed at the inlet. The average heat transfer coefficients evaluated over the entire length of the channel (which is half a centimeter) based on the mean wall temperature are shown in the legend in Fig. (6.25): a difference of 7.5% exists between the highest and the lowest values, which occur for the highest and lowest dimensionless conjugate lengths respectively. The reason of this difference is primarily attributable to the combined effect of the interfacial resistance and wall thermal conduction: if the wall thermal conduction is not capable of sustaining the high local heat transfer coefficient (where the film becomes extremely thin), as the wall temperature approaches the saturation temperature, the actual local contribution of the heat flux is thus reduced and, since the interfacial resistance reduces locally the heat transfer process, the overall performances are thus affected and reduced (the heat duty is then redistributed elsewhere). This *crisis* phenomenon occurring in microchannels represents an important aspect and its effects on large scale solutions are discussed in Section 6.2.3.

The dimensionless distributions of maximum and minimum (over the perimeter at a given section) film thicknesses and axial bulk liquid film velocities are shown in Fig. (6.26) and Fig. (6.27). Similar to the heat transfer coefficient profiles, the film and velocity profiles along the channel are influenced by the wall thermal conductivity and these effects are more evident in the transition region (around $Z = 10$), especially for the minimum values. It is interesting to note that at the exit of the channel, where the vapor quality is equal to $X = 0.9538$, the maximum bulk axial condensate velocity is nearly equivalent to the single phase bulk velocity calculated considering only the liquid phase flowing in the channel (0.204 m/s).

The calculated frictional pressure drop is shown in Fig. (6.28) in dimensionless form, where the reference frictional pressure drop value, calculated based on the single phase flow of saturated vapor only, is $-165 \text{ kPa}/\text{m}$. The local added momentum transfer from the vapor flow towards the channel walls due to the condensation process is mainly responsible for the increase of frictional pressure drop. At around $Z = 10$ this phenomenon is clearly evident as it is associated with a local peak of the pressure gradient. The location and the intensity of this peak is affected by the conjugate effects since a higher spreading of the condensation process leads to a more extended condensation area and a local reduction of added momentum transfer.

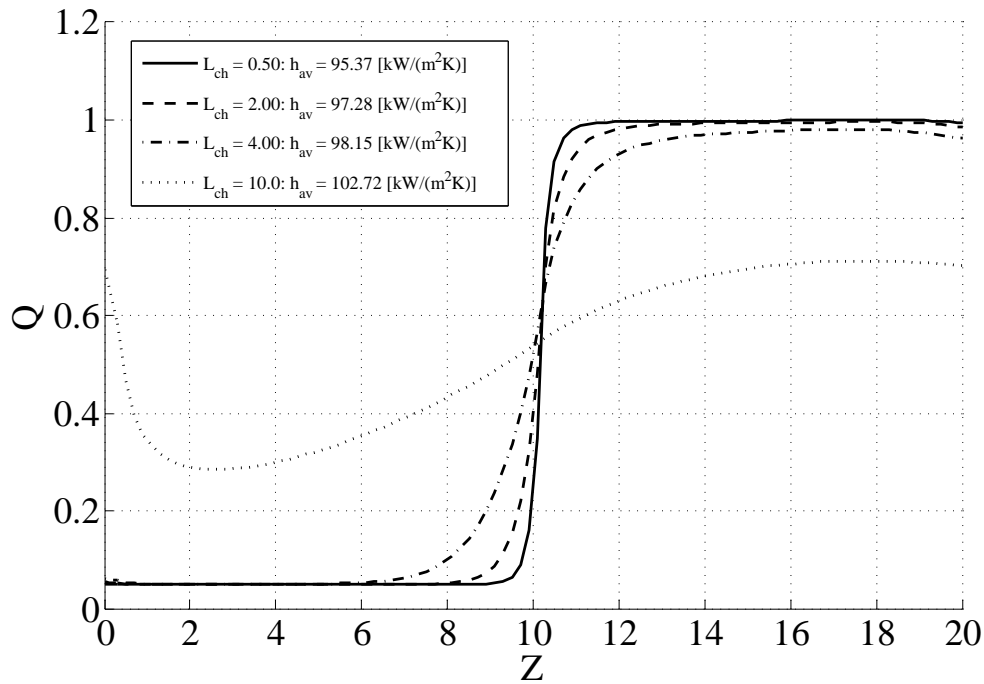


Figure 6.25: Distributions of the effective local heat flux, normalized by the reference value of 50 kW/(m²K) in the entrance region of a 250 μ m hydraulic diameter microchannel for different conjugate heat transfer lengths L_{ch}

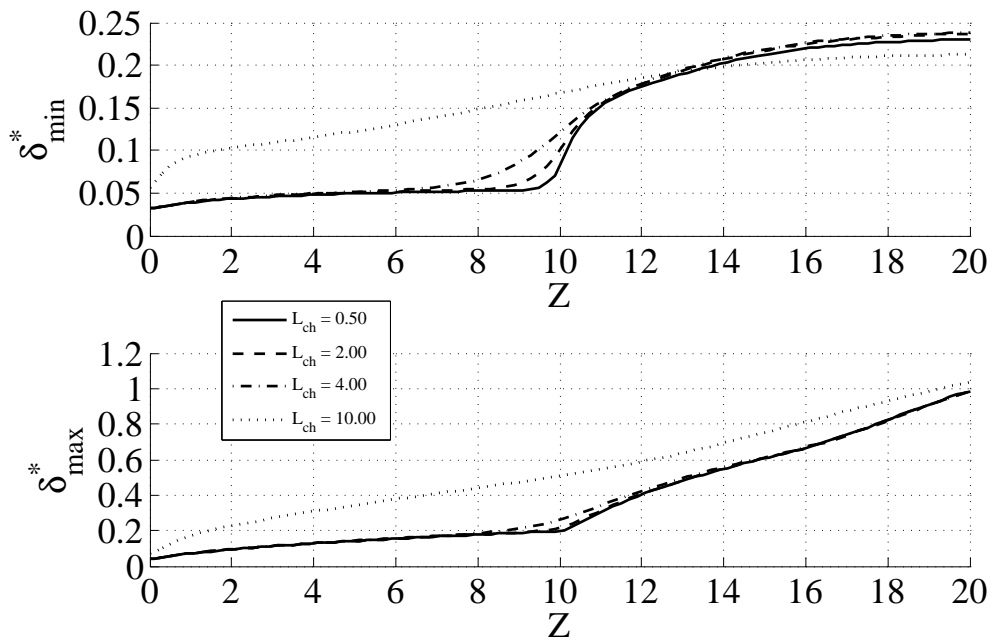


Figure 6.26: Distributions of the minimum and maximum dimensionless film thicknesses in the entrance region of a 250 μ m hydraulic diameter microchannel for different conjugate heat transfer lengths L_{ch}

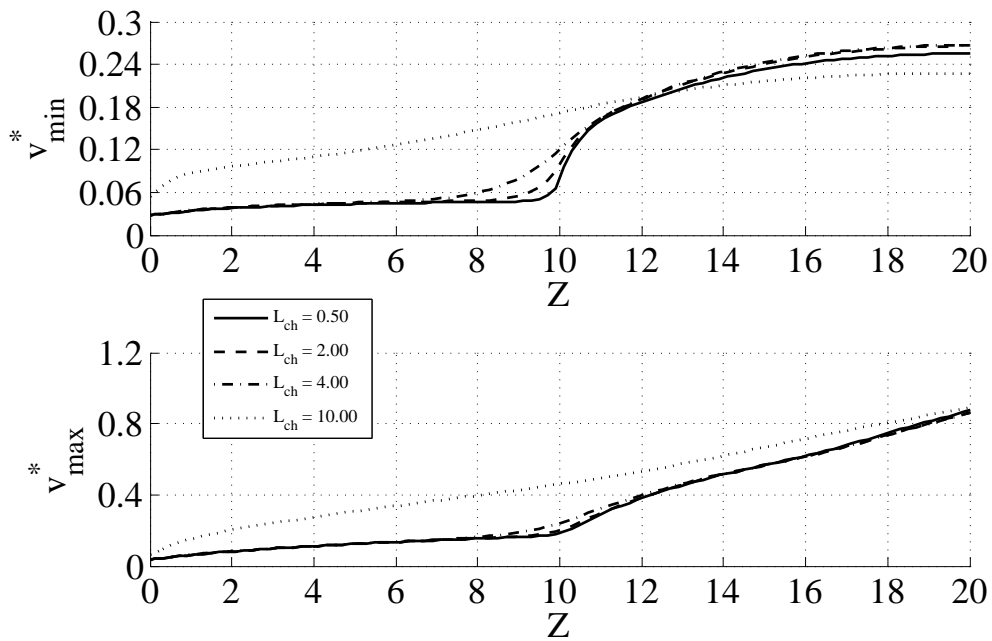


Figure 6.27: Distributions of the minimum and maximum dimensionless axial bulk liquid film velocities in the entrance region of a $250\ \mu\text{m}$ hydraulic diameter microchannel for different conjugate heat transfer lengths L_{ch}

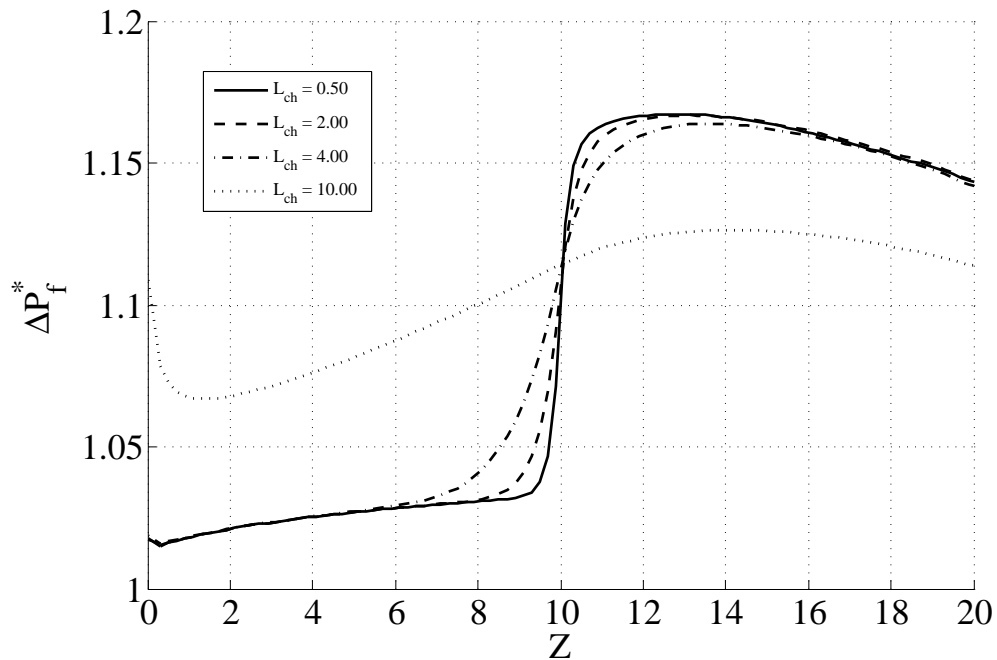


Figure 6.28: Distributions of the dimensionless frictional pressure drop profile calculated in the entrance region of a $250\ \mu\text{m}$ hydraulic diameter microchannel for different conjugate heat transfer lengths L_{ch}

6.2.3 Mini to Microchannel Transition

As it has been mentioned in the previous section, a very important phenomenon occurring in microchannel condensation is the strong coupling between the wall temperature distribution and the laminar film condensation process: as the film gets thinner and thinner, that is, when moving to microscale conditions, the local heat transfer coefficient increases strongly, but becomes limited by the growing importance of the interfacial resistance. The heat flux which is applied at the external surface of the channel is distributed over the inner surface by the conduction in the wall. In the presence of peaks of condensing side heat transfer coefficient, which occurs especially in non-circular channels when the capillary forces tends to dominate the process, the local wall temperature approaches the saturation temperature and, in doing so, the efficiency of the heat transfer deteriorates. A more uniform wall temperature, which results when the wall thermal conduction is high, leads to better performance.

From the analysis presented in Chapter 4 it is expected that, as the size of the channel decreases, the conjugate heat transfer length gradually reduces and, by doing so, it tends to approach the order of magnitude of the channel perimeter length: this means that, in the presence of highly non uniform heat transfer coefficient distributions within the section (which is the case especially for non circular channel shapes), the inner wall temperature can be highly non uniform in the cross section as well. In Fig. (6.24), subfigure a), this can be seen only in the transition area where the heat transfer coefficient is very large. A direct consequence is that the performance tends to increasingly depend on the channel geometry and material even more, as a higher non-uniform temperature distribution tends to trigger the *crisis* phenomenon previously discussed: in the regions where the film is very thin and becomes absorbed on the channel wall, the *local* interfacial resistance compromises and reduces the local heat transfer coefficient and the heat flux is redistributed; when these regions tend to interest larger portions of the inner channel surface then the global heat transfer coefficient is penalized.

The graphs in Fig. (6.29) and Fig. (6.30) show two examples where the effects of the wall conduction on the global condensation process are not negligible. In Fig. (6.29) the calculated global Nusselt number based on the average wall temperature value is plotted as a function of the hydraulic diameter: for this particular set of simulations, the mass flux is fixed at $500 \text{ kg}/(\text{m}^2\text{s})$, the uniform condensing heat flux (externally imposed) is $59.6 \text{ kW}/\text{m}^2$ (the total vapor quality variation is 0.5), the length to hydraulic diameter ratio is 200 and the refrigerant is R-134a at 10°C saturation temperature; the channel has a flattened shape with an aspect ratio of 0.5 and the wall thickness to hydraulic diameter ratio is 0.2. In the figure, two graphs are reported: the first one shows the results obtained when the wall material is aluminum (the thermal conductivity is $k_w = 200 \text{ W}/(\text{mK})$) and the second one is stainless steel ($k_w = 15 \text{ W}/(\text{mK})$). As expected, the aluminum heat transfer coefficients are always higher and the relative difference becomes more and more important as the size of the channel reduces. In correspondence of each point, the dimensionless parameter, expressed in percent, obtained by the ratio of the maximum saturation to wall temperature difference and the saturation to mean temperature difference is also

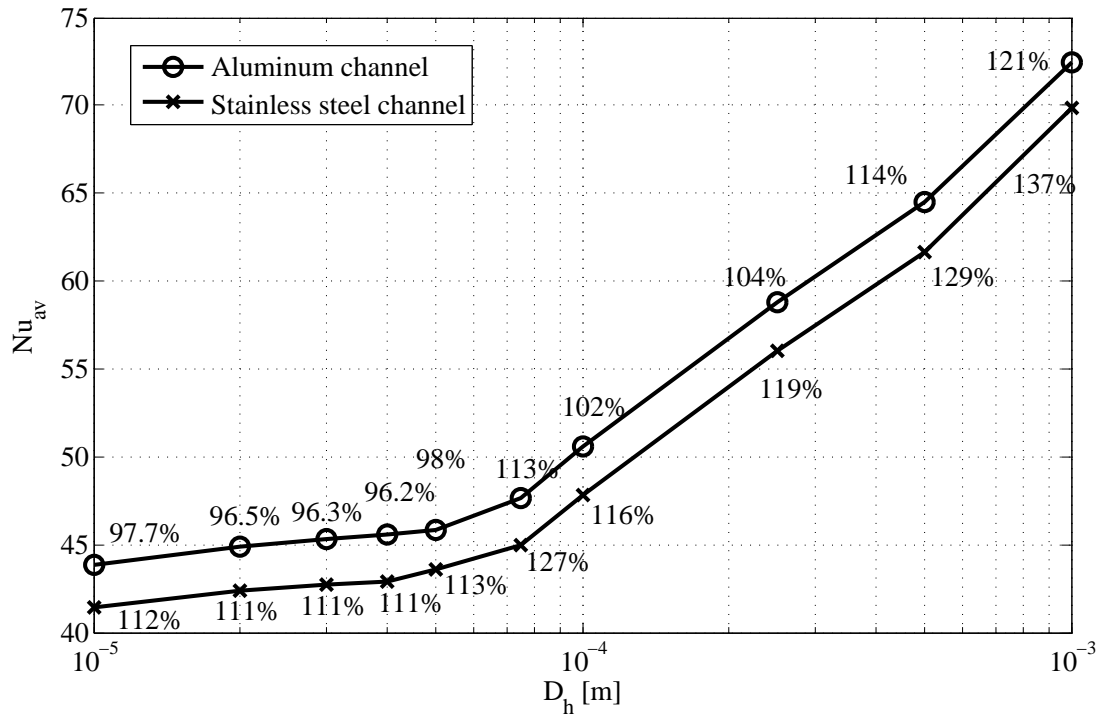


Figure 6.29: R-134a simulated mean heat transfer coefficients over a wide range of hydraulic diameters for the following conditions: 10°C saturation temperature, mass flux of 500 kg/(m²s), nominal heat flux of 59.6 kW/m², length to hydraulic diameter ratio of 200 and wall thickness to hydraulic diameter ratio of 0.2. At each point the dimensionless parameter, expressed in percent, obtained by the ratio of the difference of the maximum and minimum wall temperatures and the saturation to mean wall temperature difference, is reported. The flattened shape channel with an aspect ratio of 0.5 is the simulated geometry

reported: it can be noted that it tends to gradually reduce as the size of the channel decreases (due to the effects of the axial conduction) but this reduction is not always monotonic.

In Fig. (6.30) the calculated global Nusselt number based on saturation to average wall temperature difference is plotted as a function of the hydraulic diameter for ammonia at 10°C saturation temperature: for this particular set of simulations, the mass flux is fixed at 500 kg/(m²s), the uniform condensing heat flux (externally imposed) is 38.3 kW/m² (also in these cases the total vapor quality variation is 0.5), and the same geometry as in the case of R-134a is set. Compared to R-134a, higher Nusselt numbers and much higher heat transfer coefficients are obtained and the differences between the two materials (aluminum and stainless steel) in terms of global performance are much more evident, up to nearly 30% for the smallest simulated hydraulic diameter. The resulting wall temperature distributions are always less uniform (with relative variations of even 200%) compared to R-134a. The results obtained for the stainless steel wall show a typical example where, due to the coupling between the capillary condensation process and the wall conduction, the global performance of the heat exchanger deteriorates due to the strong non uniformity of the wall temperature field and, consequently, of the local heat transfer coefficient distribution.

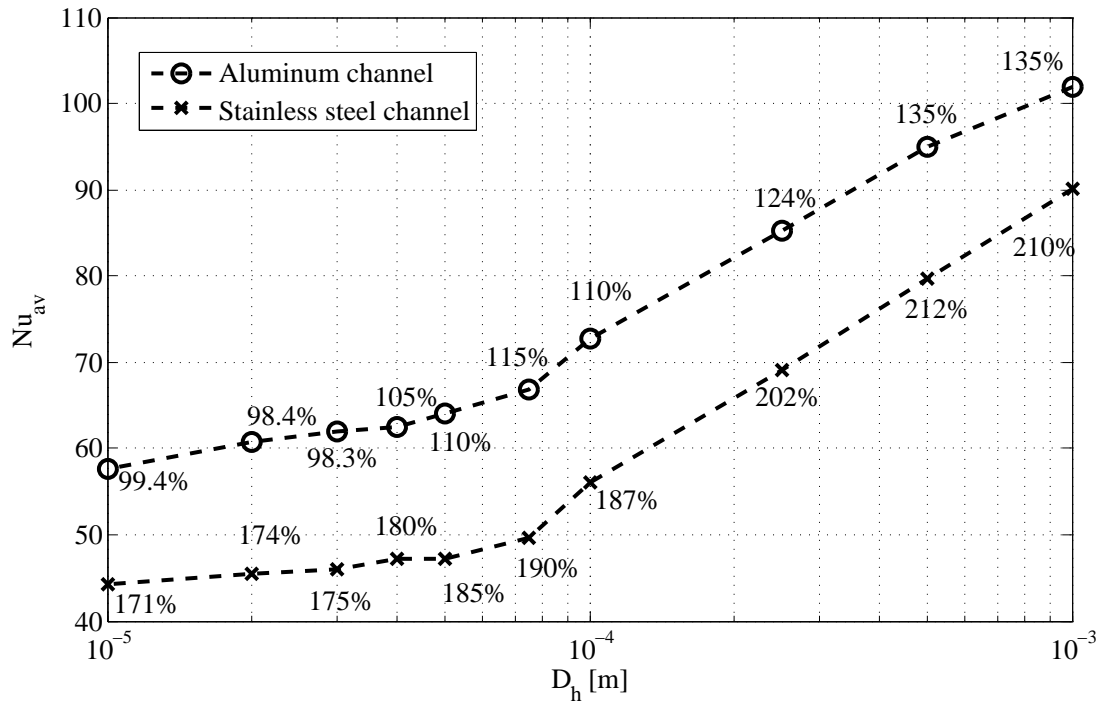


Figure 6.30: Ammonia simulated mean heat transfer coefficients over a wide range of hydraulic diameters for the following conditions: 10°C saturation temperature, mass flux of $500 \text{ kg}/(\text{m}^2\text{s})$, nominal heat flux of $38.3 \text{ kW}/\text{m}^2$, length to hydraulic diameter ratio of 200 and wall thickness to hydraulic diameter ratio of 0.2. At each point the dimensionless parameter, expressed in percent, obtained by the ratio of the difference of the maximum and minimum wall temperatures and the saturation to mean wall temperature difference, is reported. The flattened shape channel with an aspect ratio of 0.5 is the simulated geometry

The onset of global effects on the heat transfer process due to the local micro scale physical phenomena, which control the mass transfer process, could denote a possible transition *criterion* from mini to micro scale annular film condensation.

6.3 Single Phase Convective Cooling Boundary Condition

Based on the theoretical analysis proposed in Chapter 4, the heat transfer wall boundary condition is expected to have an important effect on the characteristics of the annular laminar film condensation. The two cases of imposed uniform and non-uniform heat flux and imposed wall temperature have been investigated in the previous sections. A commonly type of heat exchanger is obtained by means of two or more fluids flowing inside a more or less complex geometry that allows the heat to be transported efficiently from one fluid to the other. One of the simplest configurations of condensers is obtained by flowing the hot fluid inside a channel and a cold fluid flow outside the channel. If the direction of the cold fluid is the same as the hot fluid, then this type of device is called a co-current heat exchanger, otherwise if the cold fluid flows in the opposite direction then it is called a counter-current heat exchanger. Schematically this is shown in Fig. (6.31). Since focusing on the condensation process is the main goal of this work, attention is placed here on the effects of different subcoolings (saturation to mean cold fluid temperature difference) and on different cold fluid temperature variations on the local perimeter-averaged heat transfer coefficient distribution.

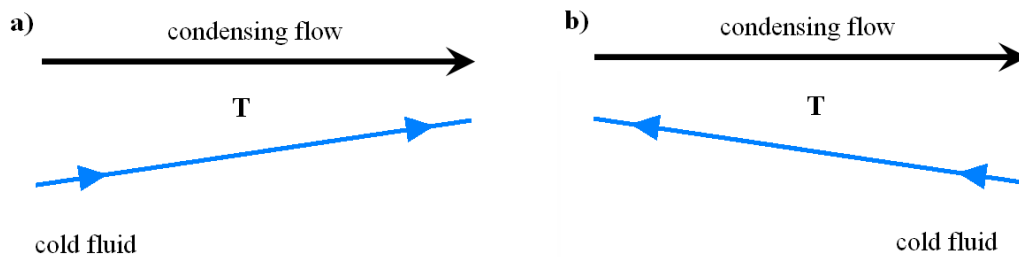


Figure 6.31: Schematics of a) co-current heat exchanger and b) counter current heat exchangers for condensation processes

In the following pages, the effects of a single phase convective cooling boundary condition are presented. The following set of parameters are kept constant as reference conditions within the present steady state calculated solutions:

- flattened shape channel with $r_F = 1.0$ is assumed, with a hydraulic diameter of $250 \mu\text{m}$ and a length to diameter ratio of 240;
- refrigerant is R-134a at 40°C saturation temperature;
- mass flux is set to $G = 500 \text{ kg}/(\text{m}^2\text{s})$;
- inlet vapor quality is $X_{in} = 0.98$;
- test section material is aluminum and the equivalent wall thickness is $500 \mu\text{m}$.

Parametric solutions obtained by varying the temperature difference $\Delta T_c = T_s - T_{c,m}$ (saturation to mean cold fluid temperature difference) and the external single phase heat transfer coefficient α_{ext} are shown in Fig. (6.32), where the local heat transfer coefficient is plotted as a function of the vapor quality. In each sub figure, three different cases are presented, assuming an external profile of the coolant side temperature which varies linearly along the axis of the channel with the following relationship:

$$T_c(Z) = T_{c,m} \left[1 + \left(Z - \frac{1}{2} \right) \frac{\Delta T_c}{T_{c,m}} \right] \quad (6.2)$$

ΔT_c is the variation of the coolant temperature between $Z = 0$ and $Z = 240$, therefore a negative value corresponds to a counter-current configuration heat exchanger type (the cold fluid is warmer towards the entrance of the channel), while a positive value corresponds to the co-current configuration (the cold fluids is warmer at the exit of the channel). The reference values of $\Delta T_c = \pm 1$ K have been set for the two cases shown in Fig. (6.32), while $\Delta T_c = 0$ K corresponds to the limiting case of uniform coolant temperature. As expected, higher subcoolings lead to larger vapor quality variations (going from a ΔX of 10% for $\Delta T = 2$ K and $\alpha_{ext} = 2$ kW/(m²K) to a ΔX of 50% for $\Delta T = 5$ K and $\alpha_{ext} = 10$ kW/(m²K)) and, in general, the perimeter averaged heat transfer coefficient decreases for lower vapor qualities. Nevertheless, when considering the co-current configuration, as the vapor quality diminishes, it is possible to note that for all the presented cases the heat transfer coefficient reaches a minimum value and then it starts rising again. This particular behavior is due to the coupling between the condensation process and the coolant side temperature distribution and this connection is handled by the thermal conduction through the wall. In particular, the ratio between the characteristic internal and the external heat transfer coefficients and the conjugate heat transfer effects, as it is shown in Section 4.2.3, are responsible for the significant different behaviors. The results of the simulations show that, even for the same conditions of the refrigerant (vapor quality, mass flux, saturation temperature), the heat transfer coefficient is strongly affected by the type of boundary condition or, in other words, by the particular configuration of the heat exchanger.

The total vapor quality variation expressed as a function of the external heat transfer coefficient α_{ext} is presented in Fig. (6.33) and Fig. (6.34) for all the different simulated conditions; at each point the global (based on the mean value of the wall temperature) heat transfer coefficient is reported in kW/(m²K). An increase of α_{ext} favors the condensation process (larger ΔX) but, on the other hand, it leads to lower values of the condensation side mean heat transfer coefficient. Similarly, an increase of the wall subcooling strongly enhances the condensation process and deteriorates the performances. Although the local values can differ significantly, the global heat transfer coefficients of the co-current and counter-current configurations have been found to be very close to each other.

When considering these types of heat exchangers, the limiting cases of uniform imposed heat flux and uniform wall temperature can be obtained respectively with large subcoolings and low external heat transfer coefficient for the first case, and with a very high external heat transfer

coefficient (much higher than the condensing side) for the second case.

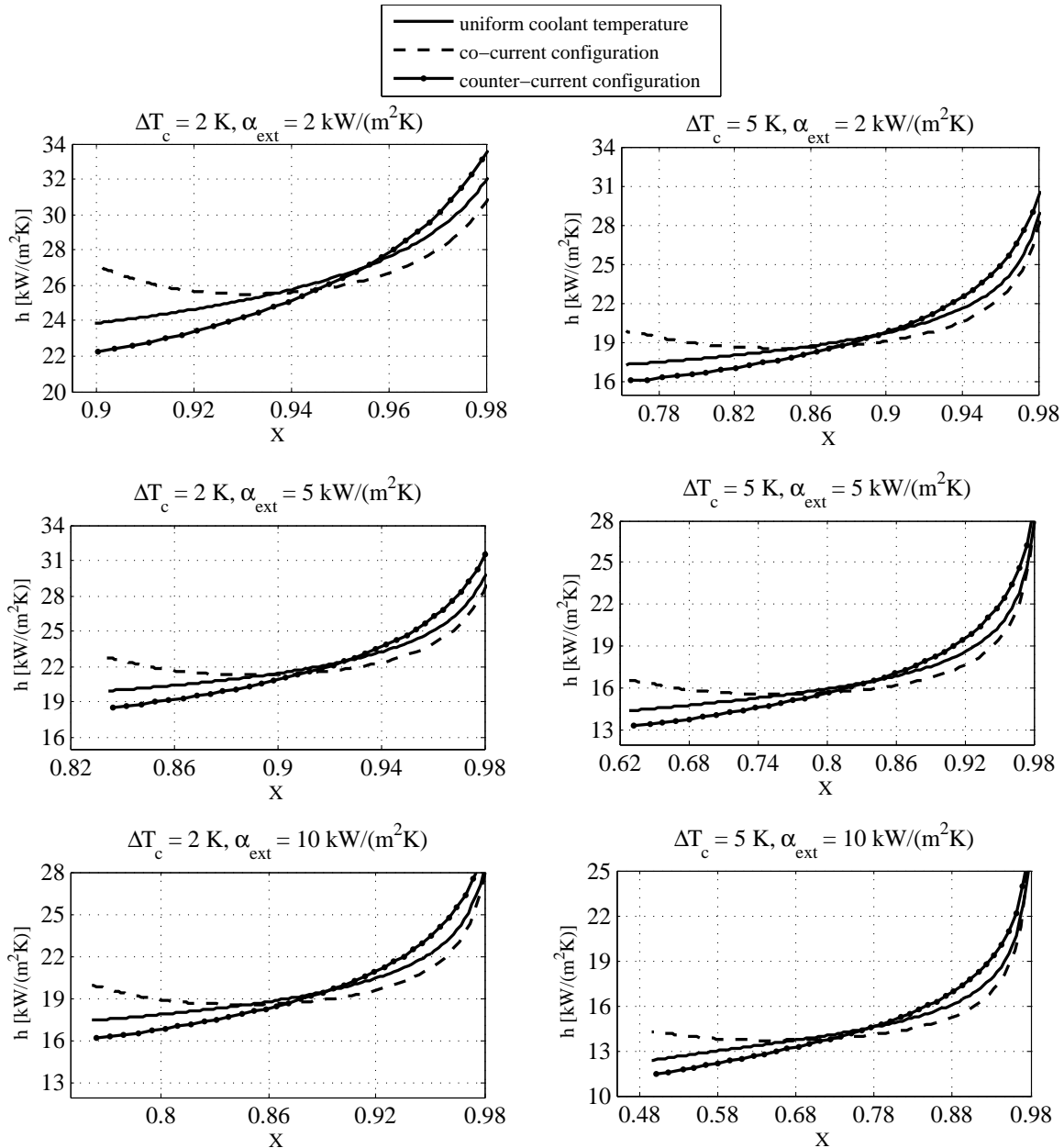


Figure 6.32: Heat transfer coefficients plotted as a function of vapor quality for different sub-coolings ΔT_c and coolant side heat transfer coefficients α_{ext} for R-134a at 40°C for the following conditions: $G = 500 \text{ kg}/(\text{m}^2\text{s})$, $X_{in} = 0.98$, the simulated geometry is the flattened shape channel with $r_F = 1.0$, with a hydraulic diameter of $250 \mu\text{m}$ and a length to diameter ratio of 240

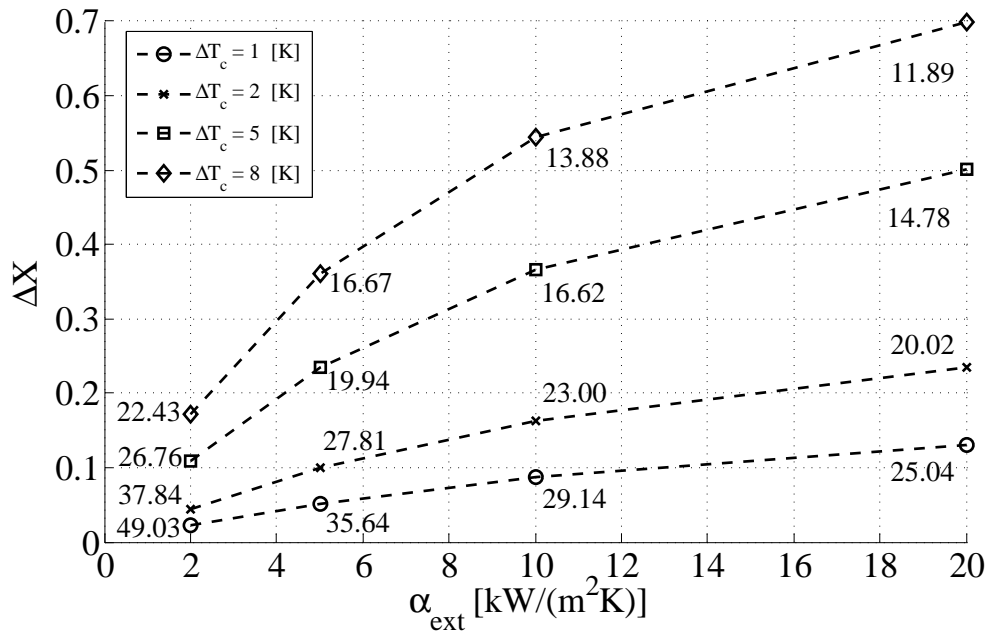


Figure 6.33: Total vapor quality variation as a function of the external coolant side heat transfer coefficient for the counter-current heat exchanger configuration. For each point, the average heat transfer coefficient is reported, expressed in kW/(m²K)

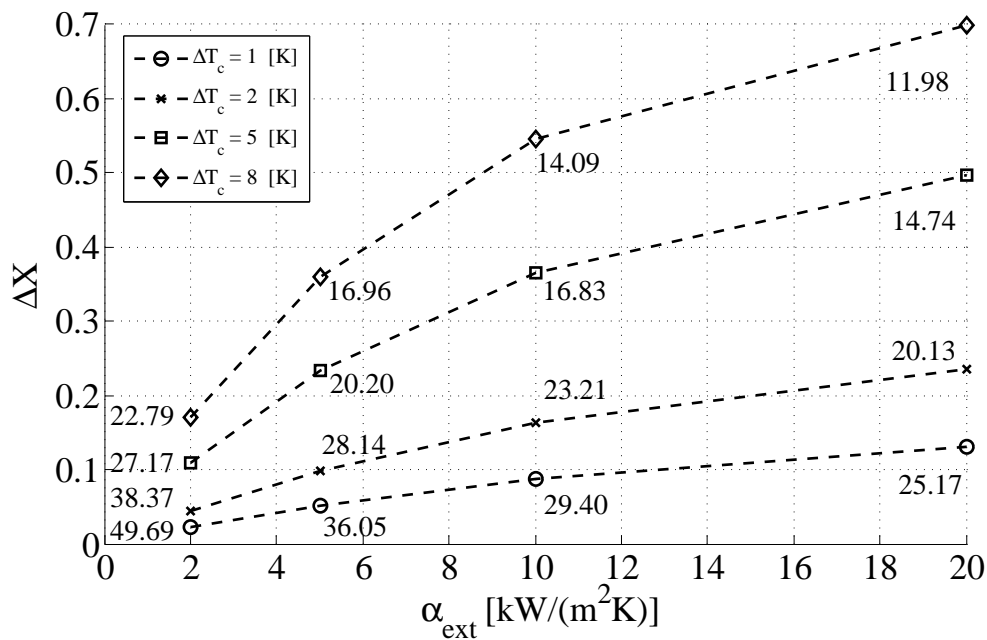


Figure 6.34: Total vapor quality variation as a function of the external coolant side heat transfer coefficient for the co-current heat exchanger configuration. For each point, the average heat transfer coefficient is reported, expressed in kW/(m²K)

6.4 Stability of the Annular Flow

So far, only steady state solutions have been investigated, notwithstanding the analysis of their *stability*. In fact, several actions might induce instabilities in the flow, leading to periodical fluctuations around a meta-stable condition or, in other cases, to the end of the annular flow and the appearance of other flow patterns. Besides possible *external* physical perturbations, like a non stationary total mass flux or an unsteady gravitational field (including shocks, vibrations, and so on), the system could be *intrinsically* unstable, despite anything else. Within the well known instabilities, the Kelvin-Helmholtz, the Rayleigh-Taylor and the Plateau-Rayleigh instabilities are the ones related to the presence of two separate phases (i.e. liquid and vapor). The Kelvin-Helmholtz instability can occur when velocity shear is present within a continuous fluid, or when there is sufficient velocity difference across the interface between two fluids. The Rayleigh-Taylor instability is an instability of an interface between two fluids of different densities, which occurs when the lighter fluid is pushing the heavier fluid. Finally, the Plateau-Rayleigh instability explains why and how a falling stream of fluid breaks up into smaller packets with the same volume but less surface area: this type of instability is induced by the surface tension but the characteristic unstable wavelength depends only on the radius of the falling stream. One way of triggering the instability in the condensing flow is simply by reducing the mass flux while keeping constant the heat flux (or, equivalently, the wall temperature): in this way the condensation process is favored, the total vapor quality variation increases and at a certain point the combined effect of the surface tension forces, the gravitational forces and the inertia forces lead to a flow pattern transition. Although the model has been developed only for annular flows, it is however possible to analyze the beginning of this instability, up to nearly the end of the annular flow condition. In order to do so, the complete set of unsteady equations has to be solved, accounting for all the terms related to the inertia.

In the following presentation of the simulation results, these parameters have been set constant:

- the channel cross sectional shape is circular and the length to diameter ratio is 30;
- the wall thickness is equal to $100\ \mu\text{m}$ and the wall material is copper ($k_w = 400\ \text{W}/(\text{mK})$);
- the simulated fluid is R-134a at 30°C saturation temperature;
- a constant heat flux equal to $25\ \text{kW}/\text{m}^2$ is imposed along the channel between $Z = 3$ and $Z = 27$, while it linearly goes to zero at the two extremes of the channel;
- the initial condensate film thickness is set equal to $5\ \mu\text{m}$ everywhere.

In the first instants of the simulation, the film rapidly increases, due to the fast condensation rate imposed by the heat flux. As the film grows, it also accelerates towards the exit of the channel and the deposition rate gradually slows down. If the mass flux is sufficiently large, the solution may manifest either a monotonic evolution (the liquid-vapor interface gradually reaches

its steady state condition) or some periodic oscillations appear before they are gradually damped out and the steady state condition is reached. By reducing the mass flux below a certain value, these oscillations do not extinguish rather they tend to grow. Fig. (6.35) shows the evolution of the liquid-vapor interface in the instants where these perturbations grow indefinitely, until the end of the annular flow. This simulation has been obtained for a total mass flux equal to $25 \text{ kg}/(\text{m}^2\text{s})$ and in the absence of gravity. It is interesting to note how fast, under these circumstances, the perturbation forms ($t \simeq 600 \text{ ms}$), grows and eventually leads to a new flow pattern formation ($t \simeq 690 \text{ ms}$), most likely a slug type of flow. The capillary forces are the most responsible for the appearance of this instability: when a small wave appears, it tends to accelerate towards the exit of the channel; nevertheless the regions of low pressure generated by the surface tension forces tend to attract liquid thus increasing the wave size. Fig. (6.36) shows the evolution with time of the film thickness along the axis: the colored scale shows the peaks and valleys that form, accelerate and expand. The characteristic wavelength of the instability, although it is not constant along the channel, is about 8 times the local radius of the vapor core, a value which is very close to the 9.01 ratio which is the value corresponding to the fastest growing unstable wavelength in the Plateau-Rayleigh instability [67]. The waves do not travel at the same speed and they are not equally spaced; the formation of each wave is unique as their dynamics tend to be reciprocally influenced. For the same conditions, increasing the mass flux retards the formation of the instability: Fig. (6.37) shows an example obtained for a total mass flux equal to $30 \text{ kg}/(\text{m}^2\text{s})$. The development of this phenomenon is slowed down and it occurs slightly more downstream. The apparent pattern formation is also different compared to the previous case and it is now characterized by four main wave crests instead of three. This is more evident by analyzing Fig. (6.38). The presence of a stationary gravitational field tends to favor the stratification therefore the solution loses its axial symmetry (but it maintains a planar symmetry): this tends to anticipate the onset of the instability as a low pressure region is established earlier in correspondence of the stratification. Fig. (6.39) shows the evolution of the liquid-vapor interface for a mass flux equal to $35 \text{ kg}/(\text{m}^2\text{s})$ and a normal gravity field oriented perpendicularly to the channel. A single wave of low pressure forms approximately after half a second and it is convected downstream while it grows; in correspondence to the last frame represented in figure, it is possible to note that the liquid is rapidly pulled by the surface tension into the meniscus region. Similar simulations have been run with an internal diameter of $500 \mu\text{m}$: differently from what has been noticed for the 1 mm case, the stratification process, although still present, is drastically reduced in presence of gravity. In Fig. (6.40) the liquid-vapor interface time evolution near the onset of the instability is shown at different instants: compared to the 1 mm case, the instability occurs much earlier and more upstream.

The heat transfer coefficient is also strongly affected by the flow conditions: in Fig. (6.41) a comparison between the average heat transfer coefficients (based on the mean wall temperature) calculated for three different mass fluxes, $G = 25, 30$ and $35 \text{ kg}/(\text{m}^2\text{s})$ and in micro-gravity conditions, are reported for the 1 mm diameter channel. In the first instant, as the condensation process develops, in all three cases the heat transfer coefficient gradually reduces; as the instability

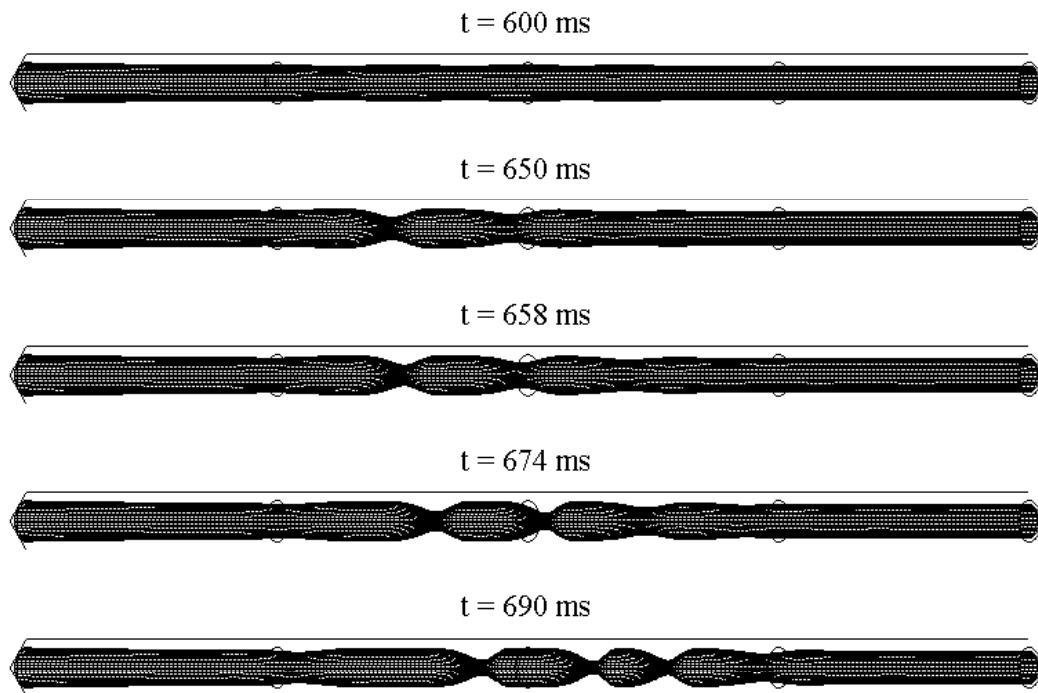


Figure 6.35: Time evolution of the liquid-vapor interface obtained for a mass flux of $25 \text{ kg}/(\text{m}^2\text{s})$; the flow is directed from left to right

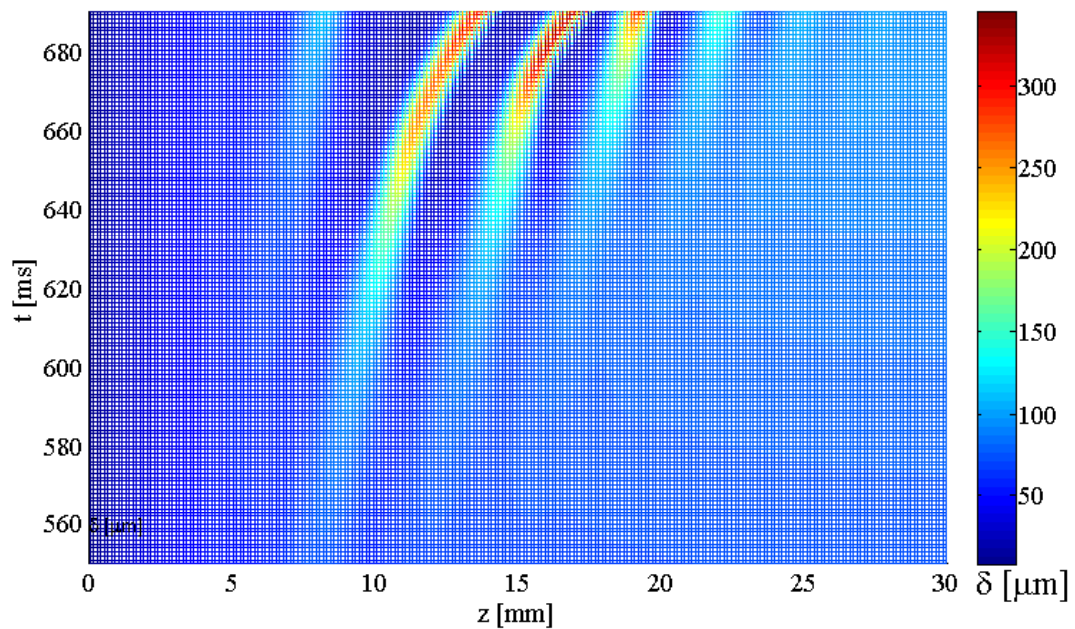


Figure 6.36: Film thickness distribution plotted in a colored scale as a function of time and space, obtained for a mass flux of $25 \text{ kg}/(\text{m}^2\text{s})$ (see Fig. (6.35))

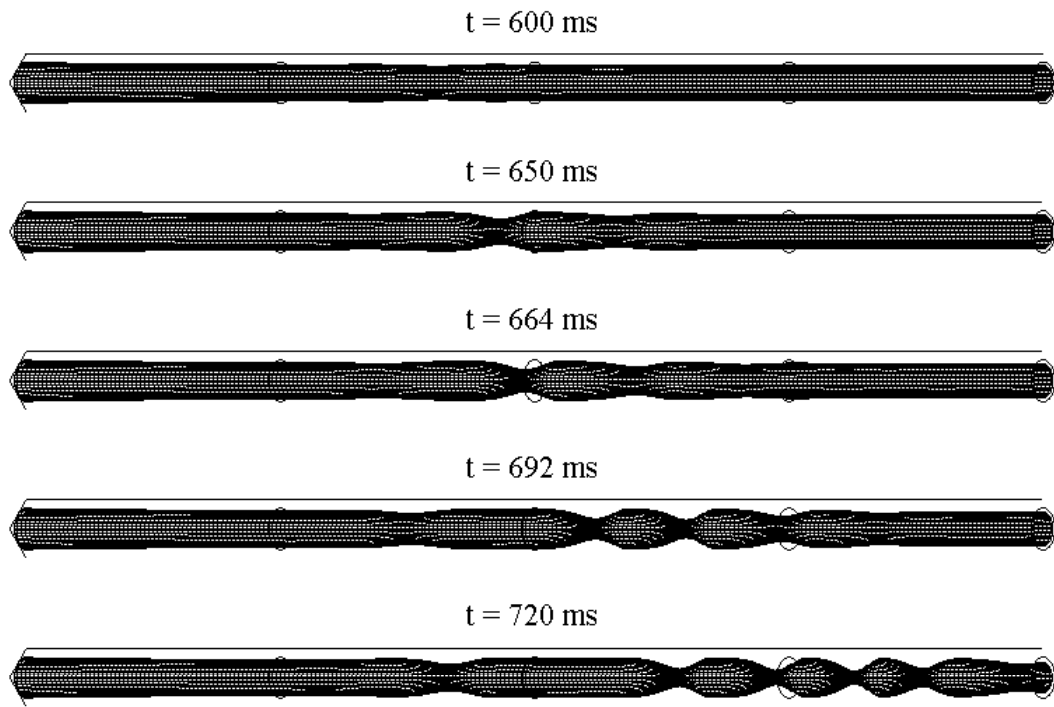


Figure 6.37: Time evolution of the liquid-vapor interface obtained for a mass flux of $30 \text{ kg}/(\text{m}^2\text{s})$; the flow is directed from left to right

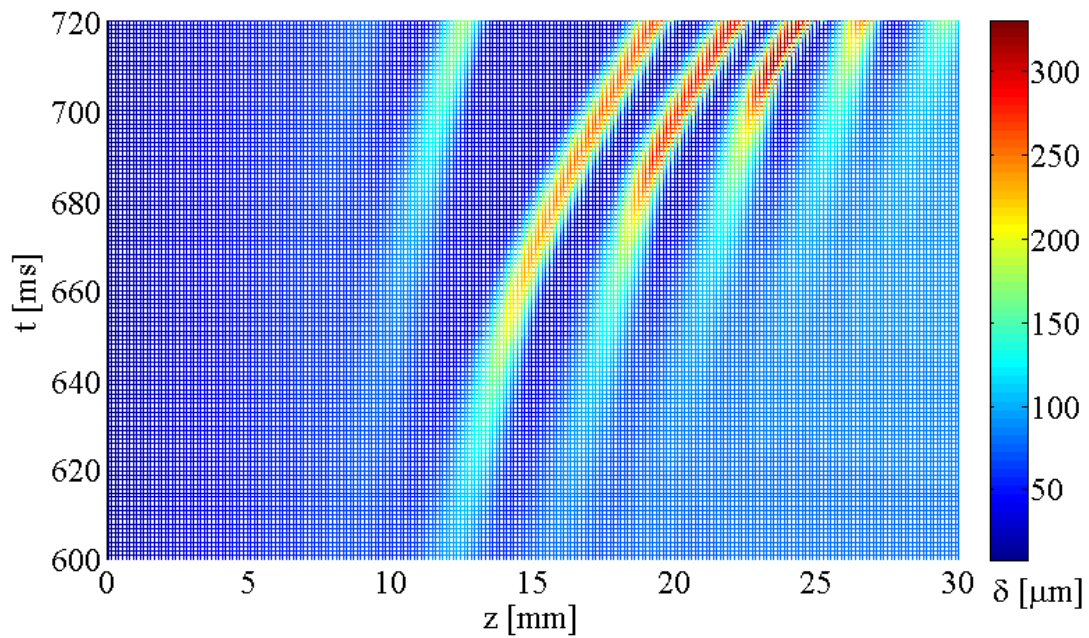


Figure 6.38: Time evolution of the liquid-vapor interface obtained for a mass flux of $30 \text{ kg}/(\text{m}^2\text{s})$; the flow is directed from left to right

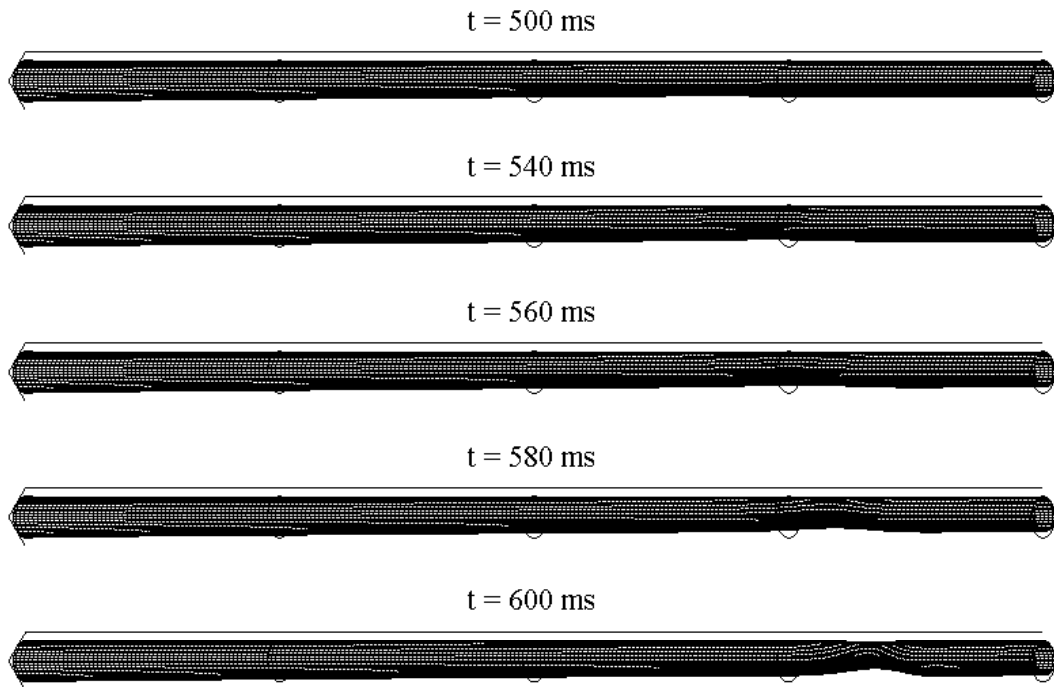


Figure 6.39: Time evolution of the liquid-vapor interface obtained for a mass flux of $35 \text{ kg}/(\text{m}^2\text{s})$ in normal gravity conditions ($g = 9.81 \text{ m}/\text{s}^2$) for a channel having an internal diameter equal to 1 mm; the flow is directed from left to right

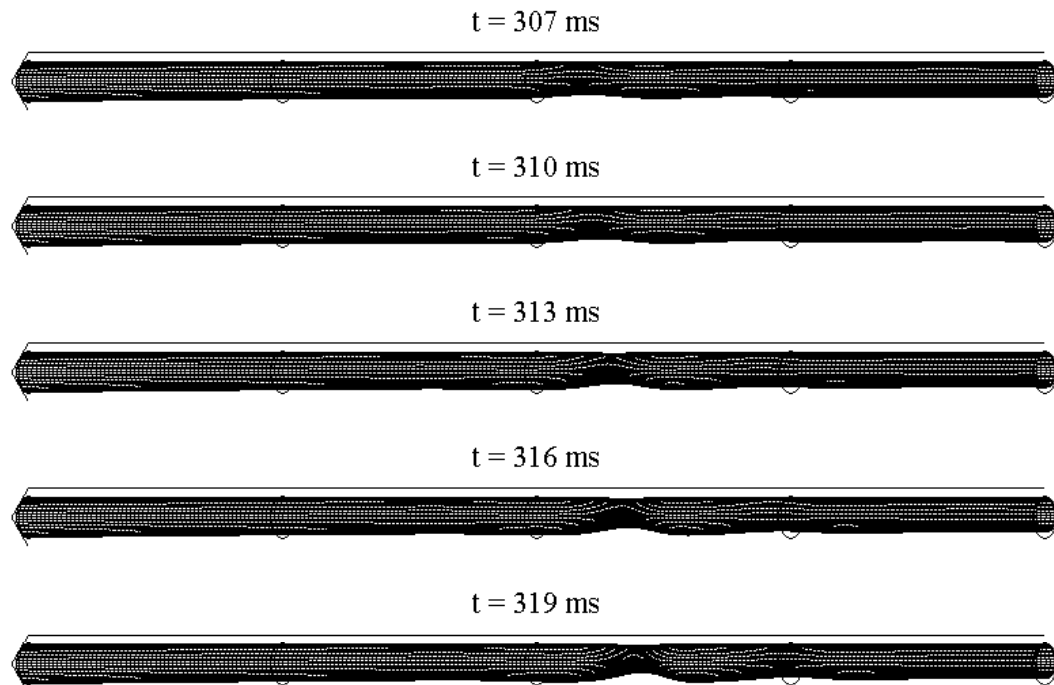


Figure 6.40: Time evolution of the liquid-vapor interface obtained for a mass flux of $35 \text{ kg}/(\text{m}^2\text{s})$ in normal gravity conditions ($g = 9.81 \text{ m}/\text{s}^2$) for a channel having an internal diameter equal to $500 \mu\text{m}$; the flow is directed from left to right

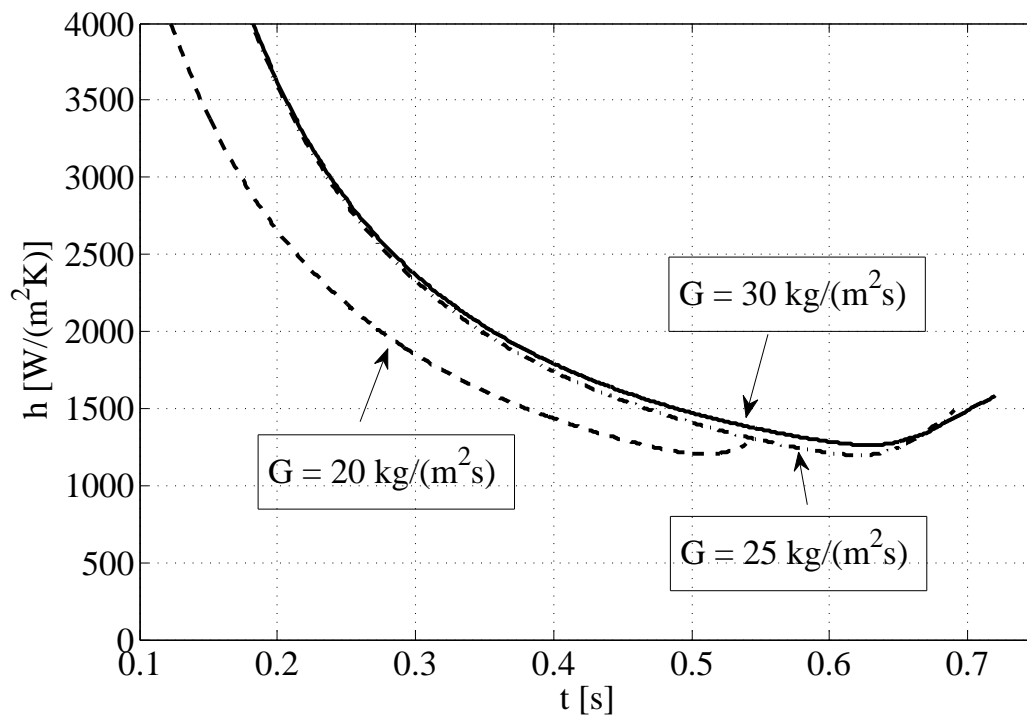


Figure 6.41: Evolution in time of the average heat transfer coefficients obtained for three different mass fluxes and an internal diameter equal to 1 mm

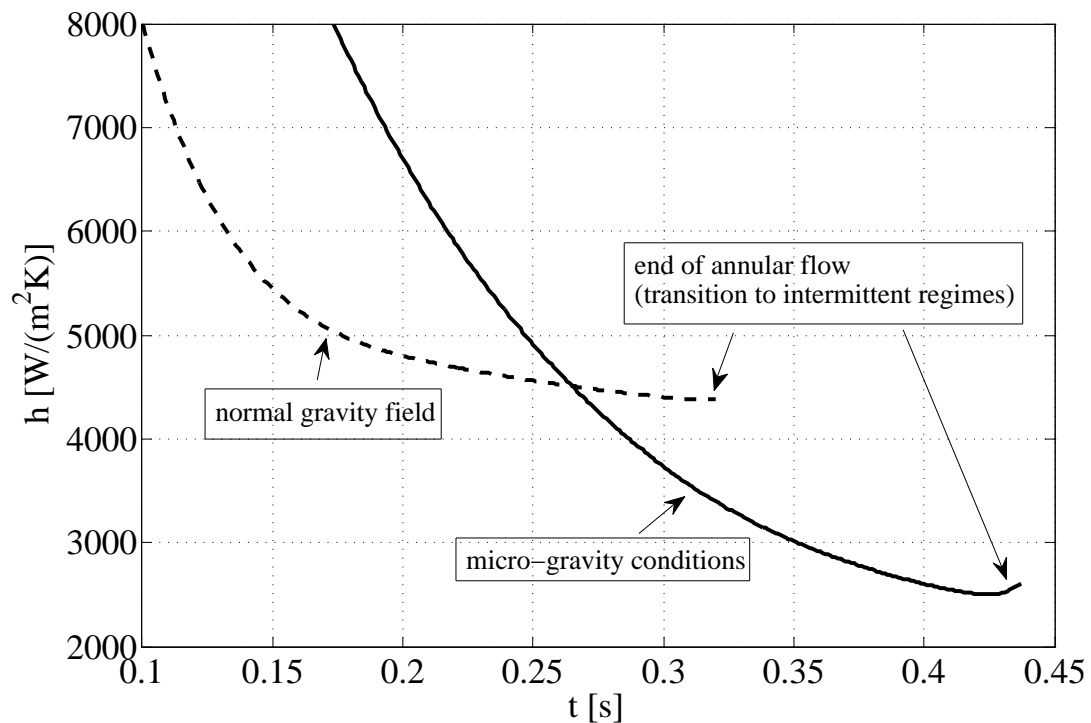


Figure 6.42: Comparison between the global heat transfer coefficient time evolutions obtained for a 500 μm internal diameter channel with and without a gravitational field

starts to grow, the heat transfer coefficient starts increasing again, primarily due to the fact that thin film regions also appear downstream. The results obtained for $G = 30 \text{ kg}/(\text{m}^2\text{s})$ are very close to the ones obtained for $G = 25 \text{ kg}/(\text{m}^2\text{s})$, while a further reduction to $G = 20 \text{ kg}/(\text{m}^2\text{s})$ dramatically influences the heat transfer process. The gravitational field plays an important role even for the smallest channel diameter ($D_h = 500 \mu\text{m}$): in Fig. (6.42) the average calculated heat transfer coefficients based on the saturation to mean wall temperature difference are plotted as a function of time for two gravity levels, normal and micro-gravity conditions. The presence of the gravity accelerates the development process of the condensate flow and this penalizes the heat transfer performance at the beginning; as the flow is established, consistently with what has been found for the steady state solutions, the heat transfer coefficient of the gravity-driven system becomes almost twice as high as in the case of micro-gravity, until the point at which the simulation is interrupted by the onset of the instability.

As a concluding remark it is important to say that this mathematical model allows the onset of the instabilities to be predicted, therefore only a qualitative analysis is possible as, under these conditions, the simulation is pushed towards the limits of the model.

6.5 Parabolic Flights Simulations

The condensation process can be affected in a significative way by the presence of time dependent gravity: this might cause oscillations (with low, medium or high frequency), forced motions or non inertial effects. The presence of non-constant (and non-uniform) gravity typically induces secondary flows that, under certain conditions, become extremely important in the development of the physical process. Centrifugal forces, transport accelerations, angular velocities and Coriolis accelerations, which are included in the developed model, can have an important impact on the global performance of condensers operating in a unsteady gravitational field, as onboard spacecrafts, satellites or airplanes.

As it has been shown in Chapter 3, the body source term can be written as:

$$\vec{f}_b = (\vec{g} - \vec{a}_t) - \vec{\Omega} \times (\vec{\Omega} \times \vec{x}) - \frac{d\vec{\Omega}}{dt} \times (\vec{x} - \vec{x}_0) - 2\vec{\Omega} \times \vec{v} \quad (6.3)$$

where \vec{g} is the gravity field and all the other terms include the non-inertial contributions. In this paragraph, the effects of non-inertial reference systems on the performance of a single tube condenser will be simulated using the "gravitational trace" during an operational flight of the 0-g airplane of the European Space Agency (Fig. (6.43)). This particular airplane is utilized as a test platform for evaluating the effects of micro-gravity conditions on different engineering, biological, chemical, medical and environmental applications. Onboard this aircraft, a micro-gravity environment can be generated while it is manoeuvred in a parabolic trajectory. Within the objectives of these parabolic flight campaigns, the study of single and two-phase heat transfer and fluid flow has become recently very important as newer and better performing heat



Figure 6.43: Picture of the 0-g airplane of the European Space Agency

exchangers are expected to be developed in the next future for space application. One of the main goals is to establish the importance of the so called *residuals* in the measured gravitational field: although the manoeuvre is performed with tight requirements, the resulting gravitational field which is measured onboard can not be as close to the micro-gravity conditions as it would be in deep space. The presence of residual components of the gravity may alter the results of experiments onboard, and thus their reliability. On the other hand, as these *disturbances* are always present, it is much more convenient to rely on a model that includes their effects, and account for this in the data processing phase. This way of proceeding, which at first demands a big effort to develop the simulator of the complete physical system, allows in a second place several different conditions to be studied with less effort. For instance, a real satellite can be subjected to a certain angular velocity (*spin*), thus the effects of centrifugal and Coriolis (if there is a fluid flow) forces should be known for predicting the thermal subsystem behavior accurately.

In the simulations presented below it will be assumed that no condensate from the annular film breaks off and becomes entrained in the vapor core. Fig. (6.44) shows the evolution of the three components of the gravitational field measured onboard the airplane during approximately 20 s of micro-gravity conditions. Referring to Fig. (6.43), the x-axis is directed from left to right while the y-axis is perpendicular to the fuselage. This evolution in time of the gravitational field has been set as an input to the simulator, thus allowing the evolution of the heat transfer coefficient (local and global) to be obtained as a function of the time. For this particular simulation, the fluid HFE7100 has been selected, with a saturation temperature of 70°C (this is a typical test fluid in such flight experiments). Two circular channels have been simulated, with hydraulic diameters of 1 and 2 mm respectively. The total channel length is 10 cm, the mass

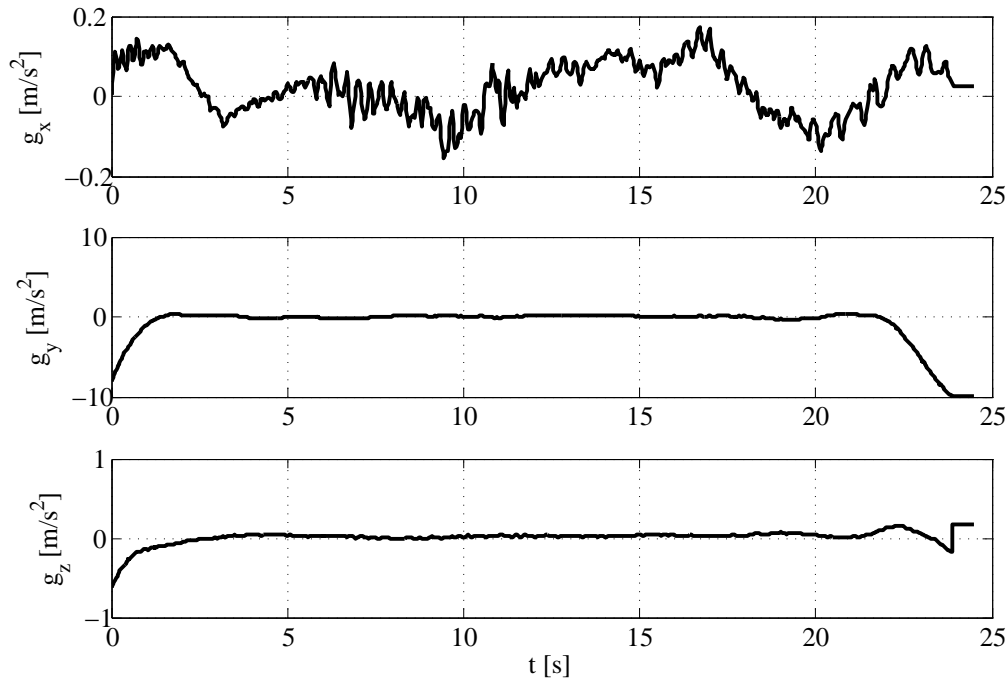


Figure 6.44: Evolution of the three components of the gravitational field measured onboard the airplane during the parabolic flight

flux is $100 \text{ kg}/(\text{m}^2\text{s})$ and the inlet vapor quality is 0.99; an imposed uniform wall temperature $T_w = 69.5 \text{ }^\circ\text{C}$ has been assumed as the wall boundary condition. The evolution of the calculated global heat transfer coefficients (integrated over the entire inner channel surface) is shown in Fig. (6.45), and the evolution in time of the instantaneous exit vapor qualities is depicted in Fig. (6.46). As expected, a smaller hydraulic diameter leads to a higher global performance; as a consequence, as the wall temperature is fixed, higher total vapor qualities variations are obtained.

The evolution of all the flow parameters (pressure, velocity, etc.) are highly fluctuating, mainly as a direct consequence of the residual contributions of the variable gravitational field (in these simulations, only the contributions due to the fluctuations in the gravity field are considered, while no effects of angular rotations and angular accelerations are considered). It is possible to note that, although with different amplitudes, the heat transfer coefficients for the two channels respond in time to the vibrations in a similar way. A more detailed analysis shows that the dynamics of the smaller channels respond faster than the bigger one, and consequently the *response time* is shorter for the 1 mm channel than for 2 mm. The mean heat transfer coefficient calculated over the entire micro-gravity phase results in more than a 15% increase relative to an equivalent steady state 0-g simulation. This is due primarily to the fact that the residuals which are present in the gravitational field still allow the stratification process to give an important contribution on the distribution of the two phases within the section, enhancing the heat transfer process (a thinner film tends to form in opposition to the direction of the instantaneous gravity vector). The sensitivity of the results to the characteristics in amplitude

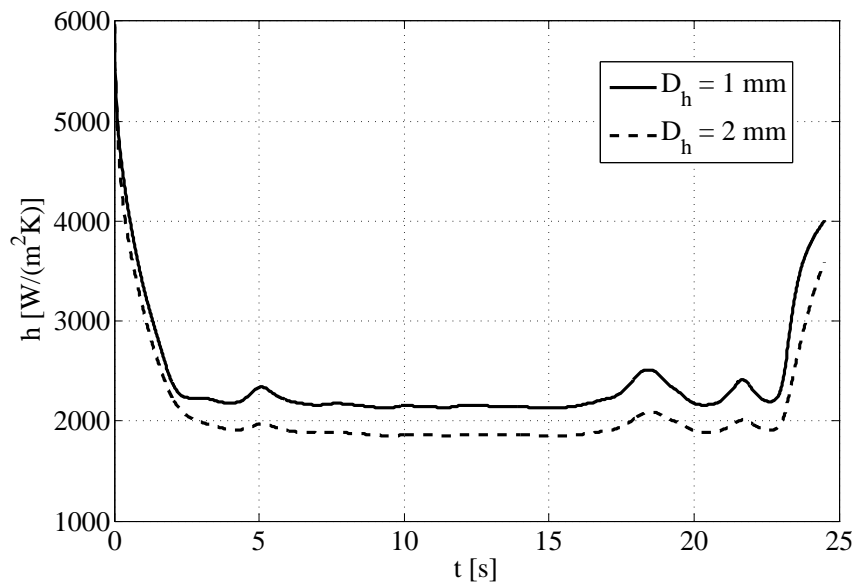


Figure 6.45: Evolution in time of the global heat transfer coefficients calculated for two different channels with $D_h = 1$ mm and $D_h = 2$ mm respectively, during the parabolic flight characterized by the gravitational field depicted in Fig. (6.44). The following operative conditions and parameters are specified: the refrigerant is HFE7100 at $T_s = 70$ °C, $T_w = 69.5$ °C, $G = 100$ kg/(m²s); the channels have a circular cross sectional shape and their total length is 10 cm

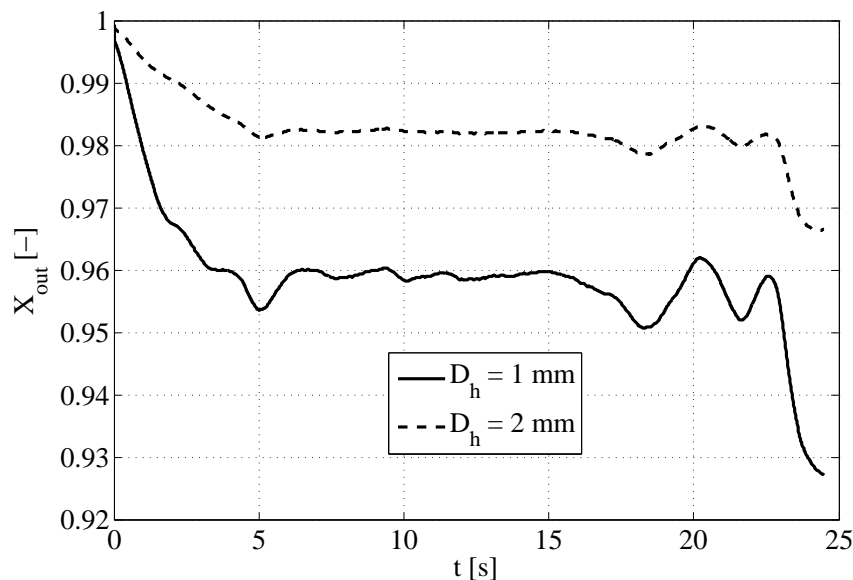


Figure 6.46: Evolution in time of the exit vapor qualities calculated for two different channels with $D_h = 1$ mm and $D_h = 2$ mm respectively, during the parabolic flight characterized by the gravitational field depicted in Fig. (6.44). The following operative conditions and parameters are specified: the refrigerant is HFE7100 at $T_s = 70$ °C, $T_w = 69.5$ °C, $G = 100$ kg/(m²s); the channels have a circular cross sectional shape and their total length is 10 cm

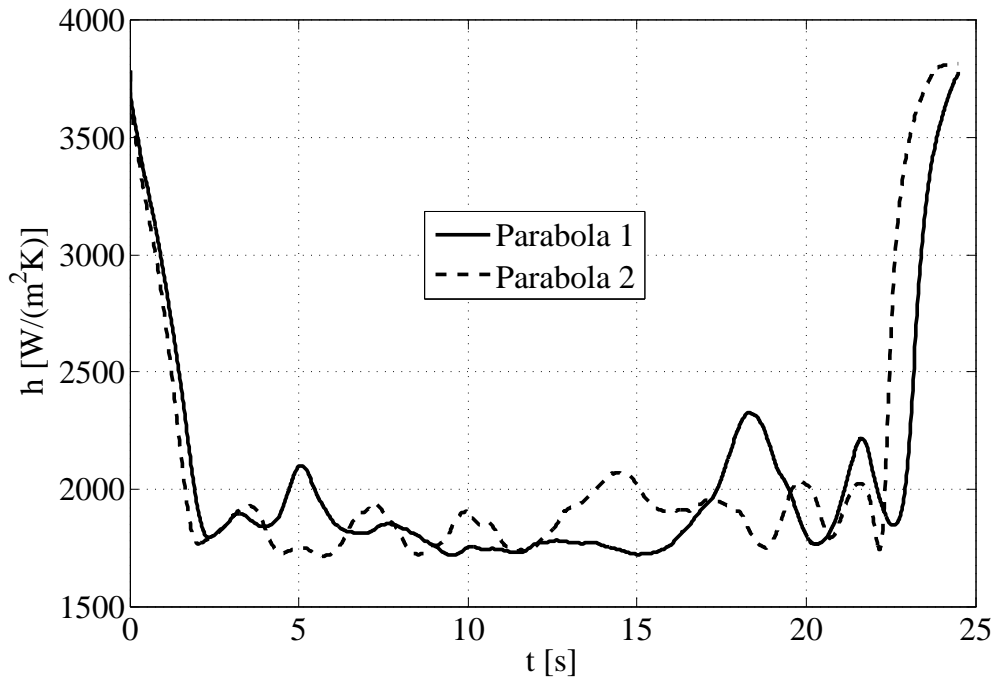


Figure 6.47: Comparison between the calculated mean heat transfer coefficients evaluated during two different simulated parabolic flights. In both cases the following operative conditions and parameters are specified: the refrigerant is HFE7100 at $T_s = 70^\circ\text{C}$, $T_w = 69.5^\circ\text{C}$, $G = 50\text{kg}/(\text{m}^2\text{s})$; the channel has a circular cross sectional shape, the hydraulic diameter is 1 mm and the total length is 10 cm

and frequency of the evolution of the gravitational field is significative and slightly different gravitational profiles may lead to substantial differences in the heat transfer performances: this particular behavior is peculiar of complex non-linear systems, as the one being considered here. In Fig. (6.47) two different plots of the calculated mean heat transfer coefficient are shown as a result of two different simulations that have been obtained for the same fluid, same operative and initial conditions but for two different onboard recorded parabolas. Fig. (6.48) shows the corresponding evolutions of the instantaneous exit vapor qualities. During the micro-gravity phase, the heat transfer coefficients evolves between the values of $1700\text{ W}/(\text{m}^2\text{K})$ and $2350\text{ W}/(\text{m}^2\text{K})$ and, in spite of the fact that the time-averaged heat transfer coefficients are very close, the instantaneous results are highly dependent on the intensity of the gravitational field. The amount of liquid that deposits inside the channel is a function of the integral effect of the heat transfer coefficient and the output vapor quality. Its evolution, in terms of mean volumetric void fraction, is reported in Fig. (6.49) for the two cases, showing that, after one period where the heat transfer coefficient tends to be higher than its mean value, the amount of liquid inside the channel tends to increase, thus reducing the mean void fraction and, consequently reducing the heat transfer coefficient, in a sort of self-adjusting mechanism which naturally prevents these oscillations to diverge.

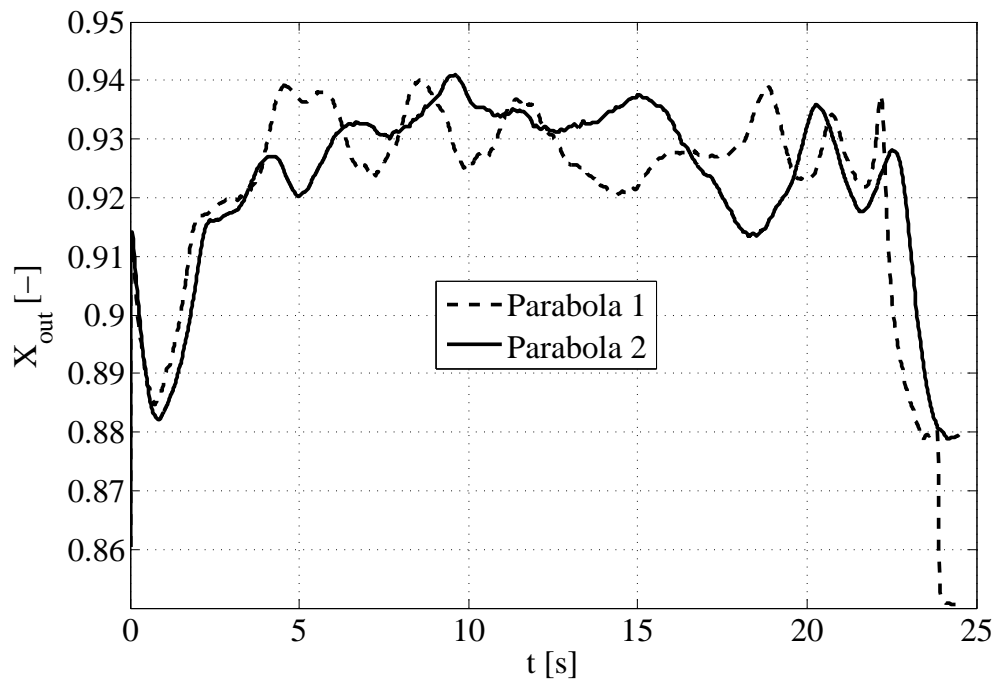


Figure 6.48: Comparison between the calculated exit vapor qualities evaluated during two different simulated parabolic flights. In both cases the following operative conditions and parameters are specified: the refrigerant is HFE7100 at $T_s = 70^\circ\text{C}$, $T_w = 69.5^\circ\text{C}$, $G = 50\text{kg}/(\text{m}^2\text{s})$; the channel has a circular cross sectional shape, the hydraulic diameter is 1 mm and the total length is 10 cm

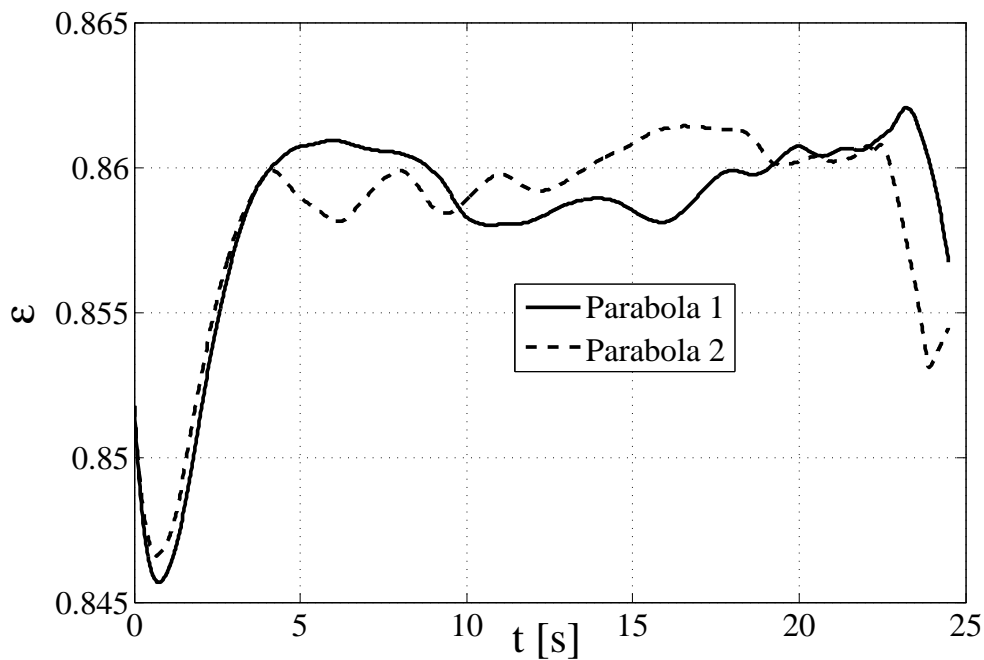


Figure 6.49: Evolution in time of the instantaneous volumetric void fractions during two parabolic flights

Chapter 7

Conclusions

A theoretical and numerical model to predict unsteady annular laminar film condensation heat transfer of pure fluids in mini and micro-channels of different internal shapes has been developed. The model includes the effects of surface tension forces, gravitational forces, shear stresses at the liquid-vapor interface, unsteady terms and, notably, the interphase mass transfer and near-to-the wall effects (*disjoining pressure*). The thermal conduction in the channel wall coupled with the inner heat condensation process may or may not be activated, thus allowing its effects to be investigated. The model has been validated versus different benchmark tests and it has been compared versus published experimental results from different laboratories, predicting micro-channel heat transfer data with an average error of 20% or less.

A theoretical analysis based on the Order of Magnitude Analysis has been developed, thus allowing a better comprehension of the capillary and gravity dominated phenomena to be reached and the set of complete and independent dimensionless groups which control the process to be identified. The development of this numerical tool allows several channel geometries to be simulated and the prediction of the condenser performance can be obtained for different fluids, saturation temperatures, mass fluxes, heat fluxes or wall subcoolings. Unsteady simulations can also be run, thus allowing the effects of time dependent gravitational fields and boundary conditions to be studied and analyzed. Examples of steady and unsteady simulations, including ultra-micro channels condensation heat transfer coefficients, are presented and discussed.

Based on the presented results, the following considerations and conclusions can be highlighted:

1. The existing empirical methods for predicting in-tube condensation heat transfer coefficients are primarily based on turbulent flow regime data. Many experimental conditions for mini and micro-channel fall into the regime where the liquid film is laminar, while the vapor core is turbulent or laminar. Under these circumstances, and even more by progressively reducing the mass flux or the channel size, the capillary forces have been found to play an important role in mini and micro-channel condensation. The importance of the capillary forces has been found to increase nearly linearly as the hydraulic diameter

of channel is progressively reduced.

2. In laminar annular film condensation, the effects of the inner channel shape on the heat transfer coefficient is very strong and significant differences in terms of mean, local or perimeter averaged heat transfer coefficients have been found when comparing heat transfer results of circular, elliptical or flattened tube, under the same operative conditions. The sensitivity on the heat transfer performance to the geometry has been found to be not only a function of the fluid properties, the operating conditions (mass flux, gravitational forces, wall temperature or wall heat flux) but also on the particular features of the geometry itself.
3. The effects of the external wall boundary condition have been analyzed and investigated. Three different cases have been considered: uniform wall temperature, non uniform wall heat flux and single-phase convective cooling. It has been found that the thermal axial and peripheral conduction occurring in the wall of the channel can affect the behavior of the condensate film, not only because the heat is redistributed over the channel wall, but also because the annular laminar film condensation process is dependent on the local saturation to wall temperature difference. As a direct consequence, each particular type of boundary condition can lead to significant differences in the spatial distributions of the heat load and heat transfer coefficient.
4. The coupling between the condensation process and the thermal conduction in the wall, a physical phenomenon which is usually neglected by assuming either a uniform wall temperature or heat flux as a boundary condition at the inner perimeter of the channel, has been found to have a significant impact when moving to microscale: the possibility of investigating this particular range is permitted by including in the model the effects of ultra-thin liquid layers, namely the effects of the temperature and pressure jump occurring at the liquid-vapor interface. As the size of the channel decreases, in the regions where the film is very thin and becomes absorbed in the channel wall, the local interfacial resistance compromises and reduces the local heat transfer coefficient and the heat flux is consequently redistributed; when these regions tend to interest larger portions of the inner channel surface then the global heat transfer coefficient is penalized and the evaluated performance is much lower than expected (if neglecting the coupling mechanism).

The numerical model has been compared to independent experimental results and it predicts experimental data to within $\pm 20\%$. This tool becomes particularly valuable for evaluating the effects of different physical phenomena, and its applicability is especially interesting for development of high thermal performance channel shapes, for the design and optimization of enhanced condensers of future generation and for simulation and performance prediction at low/high gravity and transient gravity applications (i.e. satellite or spacecraft missions) or highly complex experiments.

The following modifications are suggested for further improvements of the model:

- The inertial terms related to the sensible heat of the liquid phase and the wall may also be included in order to investigate their effects on the heat transfer coefficient distribution for steady and unsteady solutions;
- The model as it is can be applied for simulating both film condensation and evaporation as well, provided that in the evaporating regions the shear stress calculation at the liquid-vapor interface is modified in order to suppress the *suction* contribution (which is characteristic of the condensation process only);
- A further suggestion for future work is the possibility of extending the model applicability to turbulent liquid film conditions as well (introducing a smooth transition from the laminar to the turbulent flow), thus allowing the model to be applied for predicting condensation and evaporation heat transfer from micro to macro scale channels.

Appendix A

Lubrication Model

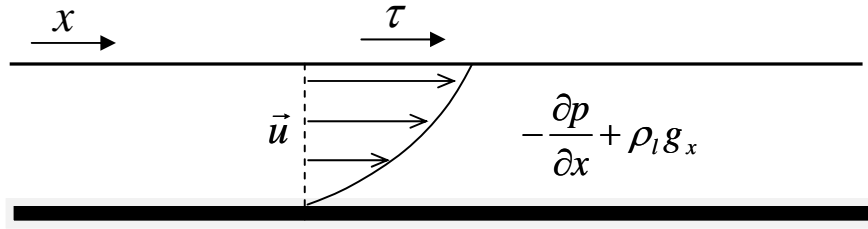


Figure A.1: Schematic of the thin film model: the steady velocity profile \vec{u} induced by the interfacial shear stress, the pressure gradient and the body forces is represented

The objective of this section is to analyze the two-dimensional velocity profile in a thin film subjected to an interfacial shear, an external pressure gradient and constant body force field. The schematic of the film is represented in Fig. (A.1). The model is based on the lubrication theory which is extensively explained and analyzed by A. Oron et al. [68], and extensively applied in literature, for instance by [59, 60, 62]. This theory is used to describe the flow of fluids (liquids or gases) in a geometry in which one dimension is significantly smaller than the others. Mathematically, the lubrication theory can be seen as exploiting the disparity between two length scales being the first one the characteristic film thickness and the second one the characteristic substrate length scale (x direction in Fig. (A.1)). The key requirement for the lubrication theory to be applied is that the ratio between the two length scales is much smaller than unity. For a constant property fluid, the momentum equation corresponding to the x -direction is the following:

$$\mu_l \frac{\partial^2 u}{\partial y^2} = \frac{\partial p}{\partial x} - \rho_l g \quad (\text{A.1})$$

The general solution for the film velocity u is:

$$u(y) = \frac{\tau y}{\mu_l} - \frac{1}{2\mu_l} \left(\frac{\partial p}{\partial x} - \rho_l g \right) \delta^2 \left[2\frac{y}{\delta} - \left(\frac{y}{\delta} \right)^2 \right] \quad (\text{A.2})$$

The average bulk velocity is then:

$$u_{av} = \int_0^{\delta} u(y) dy = \frac{\tau\delta}{2\mu_l} - \frac{1}{3\mu_l} \left(\frac{\partial p}{\partial x} - \rho_l g \right) \delta^2 \quad (\text{A.3})$$

In order to express the wall shear as a function of the average bulk velocity, the parameter α is introduced so that:

$$\tau_w = \mu_l \alpha \frac{u_{av}}{\delta} = \mu_l \left. \frac{\partial u}{\partial y} \right|_{y=0} \quad (\text{A.4})$$

This equations leads to the following expression:

$$\alpha \left[\frac{\tau}{2} - \frac{1}{3\delta} \left(\frac{\partial p}{\partial x} - \rho_l g \right) \delta^2 \right] = \tau - \left(\frac{\partial p}{\partial x} - \rho_l g \right) \delta \quad (\text{A.5})$$

Defining r the dimensionless ratio between pressure gradient forces and interfacial shear forces:

$$r = - \left| \frac{1}{\tau} \left(\frac{\partial p}{\partial x} - \rho_l g \right) \delta \right| \quad (\text{A.6})$$

The expression for α is finally obtained:

$$\alpha(r) = \frac{6 - 6r}{3 - 2r} \quad (\text{A.7})$$

The previous equation can be solved in order to obtain r knowing α :

$$r(\alpha) = \frac{1 - \frac{\alpha}{2}}{1 - \frac{\alpha}{3}} \quad (\text{A.8})$$

From the definitions it follows that:

$$u_{av} = \frac{\tau\delta}{\mu_l} \left(\frac{1}{2} - \frac{1}{3}r \right) \quad (\text{A.9})$$

Substituting the previous equation in Eq. (A.2), the profile can be obtained as a function of y :

$$u(y) = \frac{\tau}{\mu_l} \left[y - \frac{1}{2} \frac{1}{\tau} \left(\frac{\partial p}{\partial x} - \rho_l g \right) \delta^2 \left[2 \frac{y}{\delta} - \left(\frac{y}{\delta} \right)^2 \right] \right] \quad (\text{A.10})$$

From the previous equation it also possible to obtain the expression of the velocity as a function of the bulk velocity, r and the dimensionless coordinate y/δ :

$$u(y) = u_{av} \left(\frac{1}{2} - \frac{1}{3}r \right)^{-1} \left[\frac{y}{\delta} - \frac{1}{2}r \left[2 \frac{y}{\delta} - \left(\frac{y}{\delta} \right)^2 \right] \right] \quad (\text{A.11})$$

The interfacial velocity is calculated substituting $y = \delta$ in the previous expression:

$$u^i = u(y = \delta) = u_{av} \frac{1 - \frac{1}{2}r}{\frac{1}{2} - \frac{1}{3}r} = u_{av} \left(3 - \frac{\alpha}{2} \right) \quad (\text{A.12})$$

The dimensionless velocity profile U^* defined as the ratio of the local velocity and the interfacial velocity is plotted as a function of the dimensionless film coordinate $\frac{y}{\delta}$ in Fig. (A.2) for different values of the dimensionless parameters r .

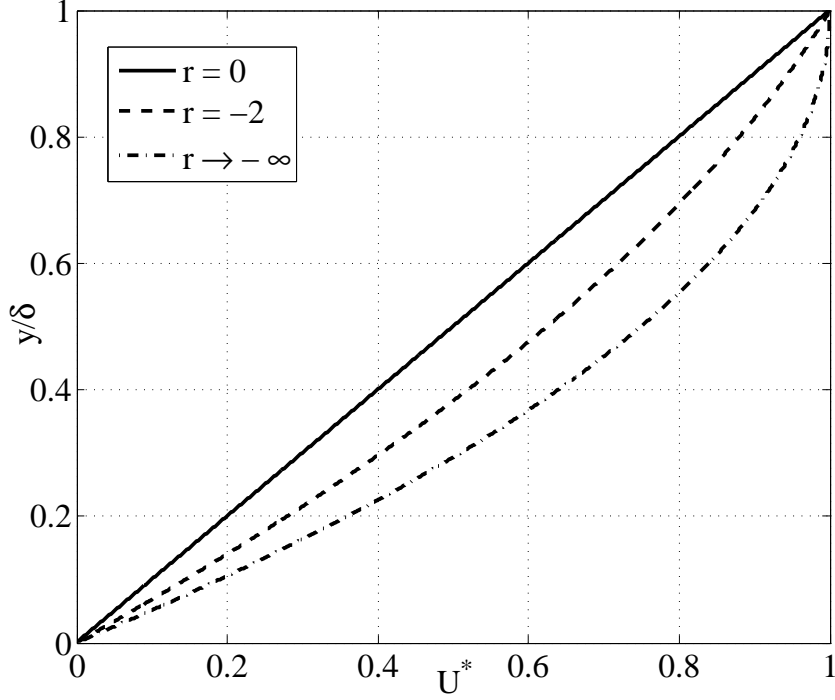


Figure A.2: Dimensionless film velocity profiles as a function of the dimensionless film thickness plotted for different values of the dimensionless parameter r defined in Eq. (A.6)

Given two velocity profiles, $u(y)$ and $v(y)$ characterized by r_u and r_v respectively, following Eq. (A.11), the cross-momentum flux per unit depth can be written as:

$$\int_0^{\delta} \rho_l u(y) v(y) dy = \rho_l \delta u_{av} v_{av} \frac{\int_0^1 (t - \frac{1}{2}r_u (2t - t^2)) (t - \frac{1}{2}r_v (2t - t^2)) dt}{(\frac{1}{2} - \frac{1}{3}r_u) (\frac{1}{2} - \frac{1}{3}r_v)} \quad (\text{A.13})$$

The result of the integral in the second term allows the following expression to be written:

$$\int_0^{\delta} \rho_l u(y) v(y) dy = \rho_l \kappa(r_u, r_v) \delta u_{av} v_{av} \quad (\text{A.14})$$

where:

$$\kappa(r_u, r_v) = \frac{\frac{1}{3} - \frac{5}{24}(r_u + r_v) + \frac{2}{15}r_u r_v}{\frac{1}{4} - \frac{1}{6}(r_u + r_v) + \frac{1}{9}r_u r_v} \quad (\text{A.15})$$

In particular, if the momentum flux has to be calculated, then $r_u = r_v = r$ and:

$$\kappa(r, r) = \frac{\frac{1}{3} - \frac{5}{12}r + \frac{2}{15}r^2}{\frac{1}{4} - \frac{1}{3}r + \frac{1}{9}r^2} \quad (\text{A.16})$$

If the film velocity is dominated by the interfacial shear, then $r \rightarrow 0^-$ and consequently:

$$\begin{aligned} \alpha &\rightarrow 2^+ \\ u^i &\rightarrow 2u_{av}^- \\ \kappa(r, r) &\rightarrow \frac{4}{3}^- \end{aligned} \quad (\text{A.17})$$

If the film velocity is instead dominated by the pressure gradient, then $r \rightarrow -\infty$ and consequently:

$$\begin{aligned} \alpha &\rightarrow 3^- \\ u^i &\rightarrow \frac{3}{2}u_{av}^+ \\ \kappa(r, r) &\rightarrow \frac{6}{5}^+ \end{aligned} \quad (\text{A.18})$$

If $r_v \rightarrow -\infty$ then:

$$\kappa(r_u, r_v \rightarrow -\infty) \rightarrow \frac{\frac{5}{8} - \frac{2}{5}r_u}{\frac{1}{2} - \frac{1}{3}r_u} \quad (\text{A.19})$$

Under the hypothesis of the lubrication theory, i.e. the film thickness is much smaller than the substrate length scale, the local properties of the film are fully described by:

- the mean velocity u_{av}
- the dimensionless ratio r defined in Eq. (A.6), which accounts for the relative importance of the shear stress compared to the pressure gradient and the body forces

The interfacial velocity u^i , the wall shear stress τ_w , the mass and momentum momentum fluxes per unit depth can be calculated through Eq. (A.4), Eq. (A.7), Eq. (A.12) and Eq. (A.16). These expressions have been included in the mathematical model described in Chapter 3 when implementing the Navier-Stokes equations in the thin liquid film.

Appendix B

Buckingham's Π -theorem

This document is based on the notes available online at
<http://www.math.ntnu.no/~hanche/notes/buckingham/>

Theorem

Any physically meaningful relation $\Phi(R_1, R_2, \dots, R_n) = 0$ with $R_j \neq 0$ is equivalent to a relation in the form $\Psi(\Pi_1, \Pi_2, \dots, \Pi_{n-r}) = 0$ involving a maximal set of independent dimensionless combinations.

Definition: units of measures

A physical quantity R_j can be expressed as a dimensional combination in a consistent system of units F_1, F_2, \dots, F_m and a non dimensional number $v(R_j)$:

$$R_j = v(R_j)[R_j] = \rho_j[R_j] \quad (\text{B.1})$$

$$[R_j] = F_1^{a_{1,j}} F_2^{a_{2,j}} \dots F_m^{a_{m,j}} = \prod_{i=1}^m F_i^{a_{ij}} \quad (\text{B.2})$$

Definition: consistent system of units

Given a system of units F_1, F_2, \dots, F_m it is said to be consistent if:

$$\prod_{i=1}^m F_i^{x_i} = 0 \Leftrightarrow x_1 = x_2 = \dots = x_m = 0 \quad (\text{B.3})$$

Definition: scaled system of units

Given a system of units $F_1, F_2, \dots, F_m, T_1, T_2, \dots, T_m$ it is said to be similar to F_j if and only if:

$$T_j = x_j^{-1} F_j \quad \forall j \quad (\text{B.4})$$

Proof

With a scaled similar system of units, the generic physical quantity can be expressed as:

$$\begin{aligned} R_j &= \nu(R_j) F_1^{a_{1j}} F_2^{a_{2j}} \dots F_m^{a_{mj}} = \nu(R_j) x_1^{a_{1j}} x_2^{a_{2j}} \dots x_m^{a_{mj}} T_1^{a_{1j}} T_2^{a_{2j}} \dots T_m^{a_{mj}} = \\ &= \tilde{\nu}(R_j) T_1^{a_{1j}} T_2^{a_{2j}} \dots T_m^{a_{mj}} \end{aligned} \quad (\text{B.5})$$

from which it follows:

$$\tilde{\nu}(R_j) = \nu(R_j) \prod_{i=1}^m x_i^{a_{ij}} \quad (\text{B.6})$$

A combination of the variables R_j is a product of powers: $R_1^{\lambda_1} R_2^{\lambda_2} \dots R_n^{\lambda_n}$. Computing the units of this combination, we obtain:

$$\left[R_1^{\lambda_1} R_2^{\lambda_2} \dots R_n^{\lambda_n} \right] = \left[\prod_{j=1}^n \nu(R_j) \prod_{i=1}^m F_i^{\lambda_1 a_{1i}} \prod_{i=1}^m F_i^{\lambda_2 a_{2i}} \dots \prod_{i=1}^m F_i^{\lambda_n a_{ni}} \right] = \prod_{i=1}^m F_i^{\sum_{j=1}^n a_{ij} \lambda_j} \quad (\text{B.7})$$

This combination is non-dimensional if this unit is 1. From the assumption of a consistent system of units, the only way this is possible is that:

$$\sum_{j=1}^n a_{ij} \lambda_j = 0 \quad \forall i \quad (\text{B.8})$$

or, in a matrix formulation,

$$A \underline{\lambda} = \underline{0} \quad (\text{B.9})$$

where A is a *dimension matrix* and $\underline{\lambda}$ is the vector of exponents. There is a 1-1 correspondence between the null space $N(A)$ and the set of dimensionless combinations of the variables which is independent of the system of units. A basis for $N(A)$ and the corresponding dimensionless combinations $\pi_1, \pi_2, \dots, \pi_{n-r}$, where r is the rank of the matrix A , is defined as a maximal set of dimensionless combinations.

Any physically meaningful relation $\Phi(R_1, R_2, \dots, R_n)$ has to have value and a unit of measure; secondly, it has to be consistent with transformations of system units:

$$[\Phi] = \prod_{i=1}^m F_i^{b_i} \quad (\text{B.10})$$

$$\nu(\Phi(R_1, R_2, \dots, R_n)) = \Phi(\nu(R_1), \nu(R_2), \dots, \nu(R_n)) \quad (\text{B.11})$$

$$\begin{aligned} \Phi(\tilde{\nu}(R_1), \dots, \tilde{\nu}(R_n)) &= \tilde{\nu}(\Phi(R_1, R_2, \dots, R_n)) = \nu(\Phi(R_1, R_2, \dots, R_n)) \prod_{j=1}^m x_j^{b_j} = \\ &= \Phi(\nu(R_1), \nu(R_2), \dots, \nu(R_n)) \prod_{j=1}^m x_j^{b_j} \end{aligned} \quad (\text{B.12})$$

which gives:

$$\Phi \left(\nu(R_1) \prod_{i=1}^m x_i^{a_{i1}}, \nu(R_2) \prod_{i=1}^m x_i^{a_{i2}}, \dots, \nu(R_n) \prod_{i=1}^m x_i^{a_{in}} \right) = \Phi(\nu(R_j), \nu(R_2), \dots, \nu(R_n)) \prod_{j=1}^m x_j^{b_j} \quad (\text{B.13})$$

for all real values. The dimension matrix A , having rank r , has r linearly independent columns. By proper redefinition, we may assume that these are the first r columns, corresponding to the variables R_1, \dots, R_r . The combination $R_1^{\lambda_1} R_2^{\lambda_2} \dots R_r^{\lambda_r}$ is dimensionless if and only if $\lambda_1 = \lambda_2 = \dots = \lambda_r = 0$. This comes out immediately from the assumption that the submatrix $a_{1-r, 1-r}$ has rank r . $\forall k > r$, R_k can be expressed as a function of R_1, R_2, \dots, R_r and $\pi_1, \pi_2, \dots, \pi_{n-r}$. Formally it could be written then:

$$\Phi(R_1, R_2, \dots, R_n) = \Psi(R_1, R_2, \dots, R_r, \pi_1, \pi_2, \dots, \pi_{n-r}) \quad (\text{B.14})$$

Substituting the expression of R_1, R_2, \dots, R_n in the previous expression, assuming $b_j = 0 \forall j$ (otherwise the expression of Φ could be set non-dimensional by simply multiply it with a proper combination of R_j) and assuming the hypothesis of physically meaningful relation:

$$\Psi \left(\nu(R_1) \prod_{i=1}^m x_i^{a_{i1}}, \nu(R_2) \prod_{i=1}^m x_i^{a_{i2}}, \dots, \nu(R_r) \prod_{i=1}^m x_i^{a_{ir}}, \pi_1, \pi_2, \dots, \pi_{n-r} \right) = \Psi(\nu(R_1), \nu(R_2), \dots, \nu(R_r), \pi_1, \pi_2, \dots, \pi_{n-r}) \quad (\text{B.15})$$

Given positive numbers $\nu(R_1), \nu(R_2), \dots, \nu(R_r)$, it is always possible to find x_1, x_2, \dots, x_m so that $\nu(R_j) \prod_{i=1}^m x_i^{a_{ij}} = c_j$, being c_j a constant. This is always possible: taking the logarithm of this last equation:

$$\ln \left(\prod_{i=1}^m x_i^{a_{ij}} \right) = \ln \left(\frac{c_j}{\nu(R_j)} \right) \Rightarrow \sum_{i=1}^m a_{ij} y_i = \varepsilon_j \quad (\text{B.16})$$

having defined $x_i = e^{y_i}$ and $\varepsilon_j = \ln(c_j/\nu(R_j))$. The linear system Eq. (B.16) is solvable (rank $r = m$) therefore it is possible to write for any constant:

$$\Psi(c_1, \dots, c_r, \pi_1, \pi_2, \dots, \pi_{n-r}) = \Psi(\nu(R_1), \nu(R_2), \dots, \nu(R_r), \pi_1, \pi_2, \dots, \pi_{n-r}) \quad \forall c \quad (\text{B.17})$$

This is possible only if Ψ does not depend on R_1, R_2, \dots, R_r , which leads to the proof:

$$\Psi(\pi_1, \pi_2, \dots, \pi_{n-r}) = 0 \quad (\text{B.18})$$

Appendix C

Conjugate Heat Transfer: One Dimensional Model

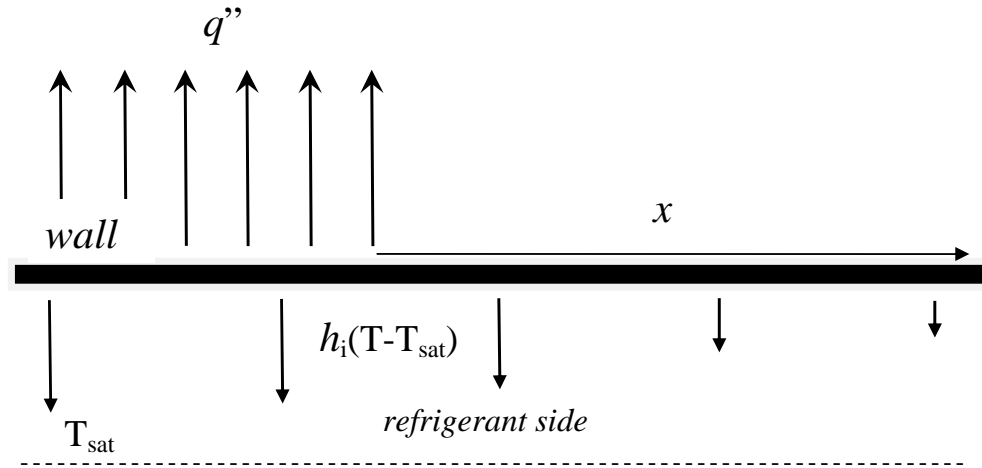


Figure C.1: Schematic of the one-dimensional model of the conjugate heat transfer problem

The objective of this section is to analyze a simple problem involving the coupling between the thermal conduction in the wall and the condensation process occurring on the inner side of the channel. The conjugate heat transfer problem is schematized in Fig. (C.1). The condensing side heat transfer coefficient is assumed to follow a law similar to the one propose in Chapter 4, in particular, following Eq. (D.1). The relationship existing between the condensing side heat transfer coefficient h_i and the local saturation to wall temperature difference ΔT is assumed to be:

$$h_i(\Delta T) = \left(\frac{k_l^4 \sigma \rho_l \Delta h_{l-v} H^4}{\mu_l} \right)^{\frac{1}{5}} H^{\frac{4}{5}} \Delta T^{-\frac{1}{5}} = F_T H^{\frac{4}{5}} \Delta T^{-\frac{1}{5}} \quad (\text{C.1})$$

Referring to Fig. (C.1), we are interested in the region corresponding to $x > 0$ where it is assumed that the external heat flux is zero and the condensing process occurs only through wall thermal conduction. The energy balance equation for this region, indicating with $T(x)$ the wall

temperature, is:

$$k_w \lambda_w \frac{\partial^2 T}{\partial x^2} + h_i (T_s - T) = 0 \quad (\text{C.2})$$

Substituting the expression for the heat transfer coefficient in Eq. (C.1) into this expression leads to:

$$\lambda_w k_w \frac{\partial^2 T}{\partial x^2} - F H^{\frac{4}{5}} (T_s - T)^{\frac{4}{5}} = 0 \quad (\text{C.3})$$

The temperature T is assumed to be $T = T_0 < T_s$ at $x = 0$. The following transformation of variables is applied:

$$\Theta = \frac{T_s - T}{T_s - T_0} \quad (\text{C.4})$$

$$X = \frac{x}{L} \quad (\text{C.5})$$

$$\alpha^2 = \frac{F T}{\lambda_w k_w (T_s - T_0)^{\frac{1}{5}}} H^{\frac{4}{5}} L^2 \quad (\text{C.6})$$

which leads to the following equation:

$$\frac{\partial^2 \Theta}{\partial X^2} - \alpha^2 \Theta^{\frac{4}{5}} = 0 \quad (\text{C.7})$$

The temperature is known at $x = 0$ therefore it has to be:

$$\Theta (X = 0) = 1 \quad (\text{C.8})$$

Since the interest here is focused on how far the heat transfer process proceeds, the following adiabatic condition is assumed at $x = L$:

$$\frac{\partial \Theta}{\partial X} (X = 1) = 0 \quad (\text{C.9})$$

Assuming that $\Theta' \neq 0$ in the considered domain:

$$\frac{\partial \Theta}{\partial X} \frac{\partial^2 \Theta}{\partial X^2} - \alpha^2 \frac{\partial \Theta}{\partial X} \Theta^{\frac{4}{5}} = \frac{\partial}{\partial X} \left[\frac{1}{2} \left(\frac{\partial \Theta}{\partial X} \right)^2 - \frac{5}{9} \alpha^2 \Theta^{\frac{9}{5}} \right] = 0 \quad (\text{C.10})$$

$$\Rightarrow \frac{1}{2} \left(\frac{\partial \Theta}{\partial X} \right)^2 - \frac{5}{9} \alpha^2 \Theta^{\frac{9}{5}} = C \quad (\text{C.11})$$

As the adiabatic boundary condition has been assumed along with the hypothesis that the value of Θ approaches zero for equilibrium conditions (far from the origin the wall temperature will coincide with the saturation temperature), the constant C is equal to zero. This leads to the following formulation:

$$\frac{\partial \Theta}{\partial X} = -\sqrt{\frac{10}{9}} \alpha \Theta^{\frac{9}{10}} \quad (\text{C.12})$$

$$\frac{\partial \Theta}{\partial X} \Theta^{-\frac{9}{10}} = -\sqrt{\frac{10}{9}} \alpha \Rightarrow \frac{\partial}{\partial X} \Theta^{\frac{1}{10}} = -\frac{1}{3} \sqrt{\frac{1}{10}} \alpha \frac{\partial}{\partial X} X \quad (\text{C.13})$$

which leads to the final solution:

$$\Theta^{\frac{1}{10}} - 1 = -\frac{1}{3}\sqrt{\frac{1}{10}}\alpha X \quad (\text{C.14})$$

or:

$$\Theta(X) = \left(1 - \frac{1}{3}\sqrt{\frac{1}{10}}\alpha X\right)^{10} \quad (\text{C.15})$$

The solution found respects the hypothesis done on the derivative $\Theta' \neq 0$ as long as:

$$1 - \frac{1}{3}\sqrt{\frac{1}{10}}\alpha X \geq 0 \quad (\text{C.16})$$

which means:

$$\Theta(X) = \begin{cases} \left(1 - \frac{1}{3}\sqrt{\frac{1}{10}}\alpha X\right)^{10} & X \leq X_C \\ 0 & X > X_C \end{cases} \quad (\text{C.17})$$

where $X_C \equiv \sqrt{10}\frac{3}{\alpha}$. From the definitions it follows that:

$$X_C = \frac{x_C}{L} = \sqrt{10}\frac{3}{\alpha} = 3\sqrt{10}\frac{\lambda_w^{\frac{1}{2}}k_w^{\frac{1}{2}}(T_s - T_0)^{\frac{1}{10}}}{F^{\frac{1}{2}}H^{\frac{2}{5}}L} \quad (\text{C.18})$$

which leads to the total heat transfer length l_t :

$$l_t = 3\sqrt{10}\frac{\lambda_w^{\frac{1}{2}}k_w^{\frac{1}{2}}(T_s - T_0)^{\frac{1}{10}}}{F^{\frac{1}{2}}H^{\frac{2}{5}}} \quad (\text{C.19})$$

The evolution of the dimensionless temperature is then:

$$\Theta(x) = \left(1 - \frac{x}{l_t}\right)^{10} \quad x \leq l_t \quad (\text{C.20})$$

while the evolution of the dimensionless condensing heat flux Q^* is:

$$Q^*(x) = \left(1 - \frac{x}{l_t}\right)^8 \quad x \leq l_t \quad (\text{C.21})$$

These functions are represented in Fig. (C.2) as a function of the dimensionless position x/l_t . From the original expression of the heat transfer coefficient the following relationship is obtained:

$$l_t = 3\sqrt{10}\frac{\lambda_w^{\frac{1}{2}}k_w^{\frac{1}{2}}(T_s - T_0)^{\frac{1}{10}}}{F_T^{\frac{1}{2}}H^{\frac{2}{5}}} = 3\sqrt{10}\frac{\lambda_w^{\frac{1}{2}}k_w^{\frac{1}{2}}(T_s - T_0)^{\frac{1}{10}}\mu_l^{\frac{1}{10}}}{k_l^{\frac{2}{5}}\sigma^{\frac{1}{10}}\rho_l^{\frac{1}{10}}\Delta h_{l-v}^{\frac{1}{10}}H^{\frac{2}{5}}} \quad (\text{C.22})$$

Thus, the total heat transfer length represents how far the condensation process continues occurring supported by the thermal conduction in the wall. Nevertheless, it is clear from Fig. (C.2) that the effectiveness of the thermal conduction expires very fast for small values of X . For instance, if $X = 0.2$, the effective condensing heat flux drops already to 16.8 %. We

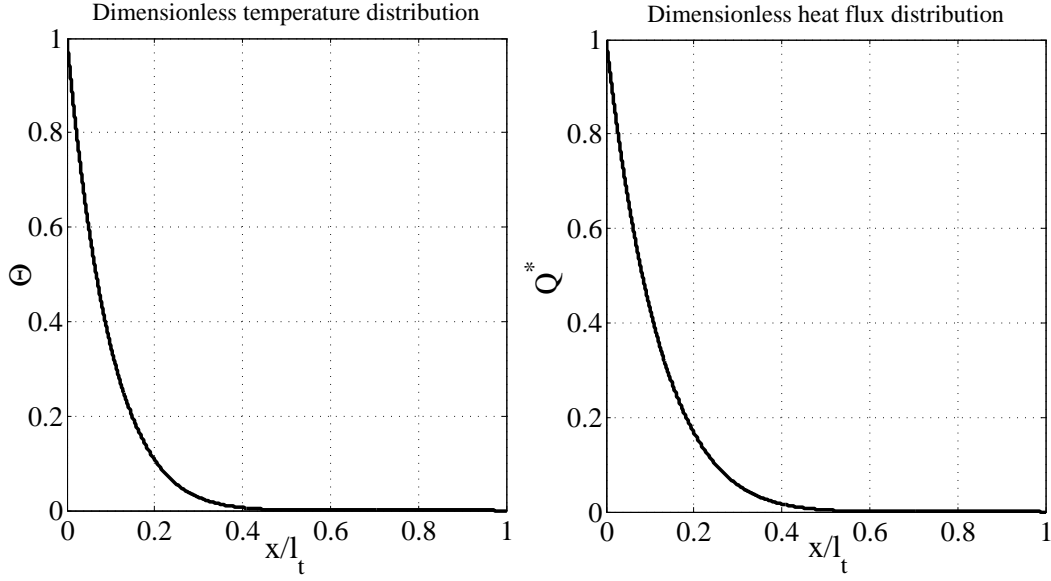


Figure C.2: Solution of the one-dimensional conjugate heat transfer problem: the dimensionless temperature (on the left) and the dimensionless condensing heat flux (on the right) are plotted as a function of the dimensionless position x/l_t

define the 'conjugate' heat transfer length l_{ch} to be the distance at which the local heat flux is reduced to a value of 91.47 % with respect to the nominal one. The expression of l_{ch} is then:

$$l_{ch} \equiv \frac{1}{3\sqrt{10}} l_t = \frac{\lambda_w^{1/2} k_w^{1/2} (T_s - T_0)^{1/10} \mu_l^{1/10}}{k_l^{2/5} \sigma^{1/10} \rho_l^{1/10} \Delta h_{l-v}^{1/10} H^{2/5}} \quad (\text{C.23})$$

Recognizing in the previous equation the expression for the reference condensing side heat transfer coefficient $h_{i,0}$ defined as:

$$h_{i,0} (\Delta T) = \left(\frac{k_l^4 \sigma \rho_l \Delta h_{l-v} H^4}{\mu_l} \right)^{1/5} H^{4/5} (T_s - T_0)^{-1/5} \quad (\text{C.24})$$

the conjugate heat transfer length becomes simply:

$$l_{ch} = \sqrt{\frac{\lambda_w k_w}{h_{i,0}}} \quad (\text{C.25})$$

Appendix D

Dimensional Groups for Different Refrigerants

Based on the theoretical considerations presented in the Chapter 4, it is possible to characterize the order of magnitude of the heat transfer coefficient of different fluids in the capillary dominated regime. In the previous section it has been shown that the (local or global) Nusselt number could be proportional to the characteristic capillary Nusselt number Sn . Under these circumstances, the heat transfer coefficient for imposed wall temperature can be written as:

$$h_T = \frac{k_l}{D_h} Nu \simeq \frac{k_l}{D_h} Sn = \left(\frac{\sigma k_l^4 \rho_l \Delta h_{l-v}}{\mu_l} \right)^{\frac{1}{5}} \Delta T^{-\frac{1}{5}} H^{\frac{4}{5}} = F_T \Delta T^{-\frac{1}{5}} H^{\frac{4}{5}} \quad (D.1)$$

where the dimensional constant F_T is defined as:

$$F_T \equiv \left(\frac{\sigma k_l^4 \rho_l \Delta h_{l-v}}{\mu_l} \right)^{\frac{1}{5}} \quad (D.2)$$

Similarly, the expression of the characteristic heat transfer coefficient h_q in the case of imposed heat flux can be written as:

$$h_q \equiv F_q |\dot{q}|^{-\frac{1}{4}} H \quad (D.3)$$

where:

$$F_q \equiv \left(\frac{\sigma k_l^4 \rho_l \Delta h_{l-v}}{\mu_l} \right)^{\frac{1}{4}} \quad (D.4)$$

F_T and F_q are representative of the fluid properties only, as the scale and the wall subcooling or the heat flux are taken into account separately in the expressions. These dimensional numbers represent a merit parameter for each specific fluid; as the thermodynamic properties of pure fluids are function of the saturation temperature only, these variables are plotted in Fig. (D.1) and Fig. (D.2) for different refrigerants. For instance, water is expected to give extremely high heat transfer coefficients, having a maximum performance (when everything else is set constant) at around 145°C; ammonia allows very high values too, which deteriorate as the

temperature is increased. This characteristic behavior (reduction of heat transfer coefficient with the temperature) is quite common for all the refrigerants. The heat transfer coefficient, following the relationships Eq. (D.1) and Eq. (D.3), increases as the channel characteristic diameter is reduced and if the temperature jump or the heat flux are reduced, although the sensitivities to the ΔT and $|\dot{q}|$ are much more limited, as indicated by the exponents $-\frac{1}{5}$ and $-\frac{1}{4}$.

The heat transfer coefficient which is obtained solving the complete problem depends on all the remaining dimensional groups and the actual heat transfer coefficient will differ by the one predicted by Eq. (D.1) and Eq. (D.3). Nevertheless, as it will be shown in the following paragraph, as long as the capillary dominated regime is considered, the order of magnitude of the result is well predicted.

Another important parameter that affects the interface mass transfer process and therefore the heat transfer performances is the interfacial resistance. This number becomes very important in the micro-scale range as the thin film becomes very thin (in the order of a tenth of a micrometer) and the temperature jump occurring at the interface becomes of the same order of magnitude of the film temperature difference. Following the definitions give by Eq. (4.18) and Eq. (4.32), the interface resistance numbers can be written as:

$$I_{r,T} = R_T H^{\frac{4}{5}} \Delta T^{-\frac{1}{5}} \quad (\text{D.5})$$

$$I_{r,q} = R_q H |\dot{q}|^{-\frac{1}{4}} \quad (\text{D.6})$$

where the dimensional constants R_T and R_q are defined as:

$$R_T = \frac{1}{J_T} \left(\frac{\sigma k_l^4 \rho_l}{\mu_l \Delta h_{l-v}^4} \right)^{\frac{1}{5}} \quad (\text{D.7})$$

$$R_q = \frac{1}{J_T} \left(\frac{\sigma k_l^4 \rho_l}{\mu_l \Delta h_{l-v}^3} \right)^{\frac{1}{4}} \quad (\text{D.8})$$

These dimensional constants are shown in Fig. (D.3) and Fig. (D.4) for different refrigerants as a function of the saturation temperature. Despite the fact that the numerical value is very small, the importance of this number increases progressively moving to small sizes. It is interesting to note that both numbers increases as the temperature difference or the heat flux are reduced.

Similarly, the dimensionless ratios expressing the relative importance of capillary and gravitational forces, Eq. (4.49) and Eq. (4.50), can be written in the following way:

$$\frac{\delta_\sigma}{\delta_g} = \gamma_T H^{-\frac{11}{20}} \Delta T^{-\frac{1}{20}} g^{\frac{1}{4}} \quad (\text{D.9})$$

and

$$\frac{\delta_q}{\delta_{g,q}} = \gamma_q H^{-\frac{2}{3}} |\dot{q}|^{-\frac{1}{12}} g^{\frac{1}{3}} \quad (\text{D.10})$$

where the dimensional constants γ_T and γ_q are defined as follows:

$$\gamma_T \equiv \frac{(\rho_l - \rho_v)^{\frac{1}{4}} \rho_l^{\frac{1}{20}} \Delta h_{l-v}^{\frac{1}{20}}}{\sigma^{\frac{1}{5}} k_l^{\frac{1}{20}} \mu_l^{\frac{1}{20}}} \quad (\text{D.11})$$

and

$$\gamma_q \equiv \frac{(\rho_l - \rho_v)^{\frac{1}{3}} \rho_l^{\frac{1}{12}} \Delta h_{l-v}^{\frac{1}{12}}}{\mu_l^{\frac{1}{12}} \sigma^{\frac{1}{4}}} \quad (\text{D.12})$$

These dimensional groups are represented in Fig. (D.5) and Fig. (D.6). Lower values indicates that the laminar film condensation heat transfer process is dominated by the capillary forces. Furthermore, as suggested by the formal expressions Eq. (4.49) and Eq. (4.50), the transition to the capillary dominated region depends on the characteristic length H^{-1} , with exponents $\frac{11}{20}$ and $\frac{2}{3}$ respectively, and the gravity level, with exponents $\frac{1}{4}$ and $\frac{1}{3}$ respectively.

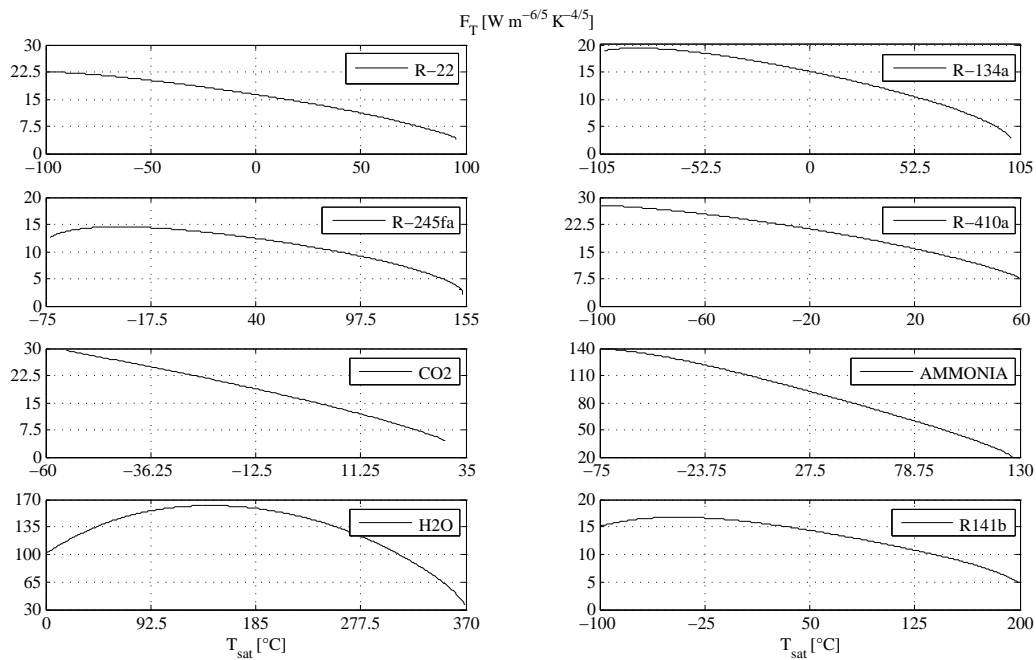


Figure D.1: Evolution of the dimensional variable F_T defined in Eq. (D.2) with the saturation temperature T_{sat} for different refrigerants

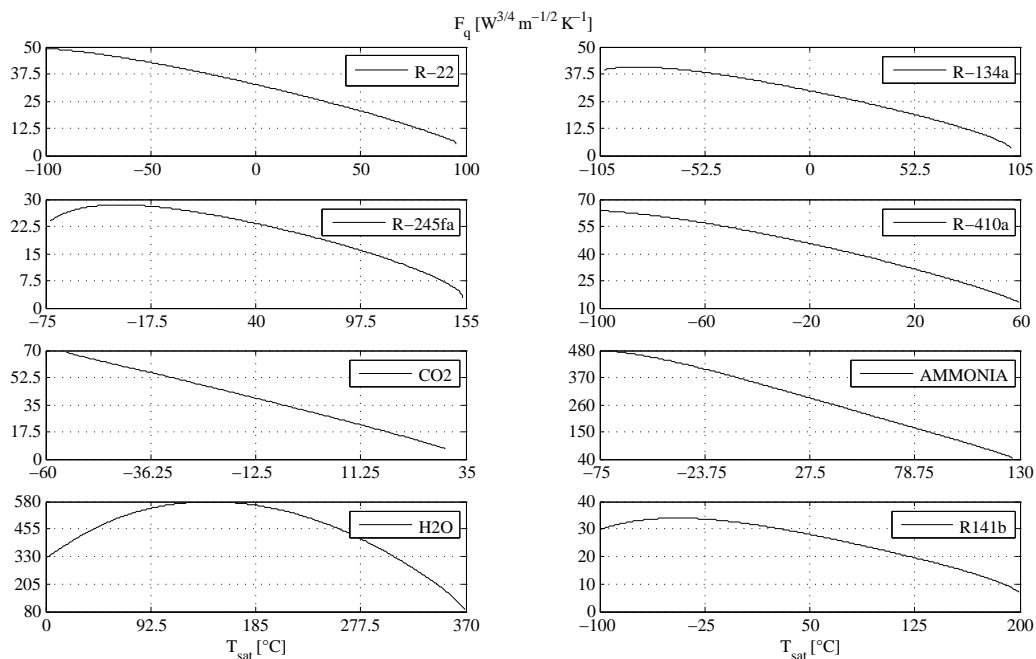


Figure D.2: Evolution of the dimensional variable F_q defined in Eq. (D.4) with the saturation temperature T_{sat} for different refrigerants

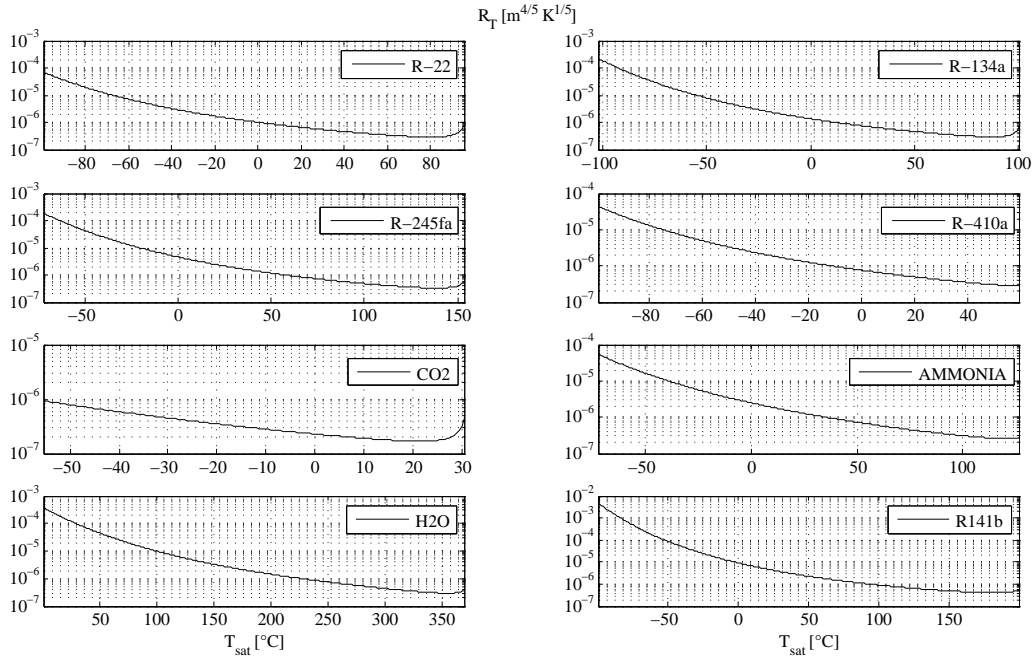


Figure D.3: Evolution of the dimensional variable R_T defined in Eq. (D.7) with the saturation temperature T_{sat} for different refrigerants

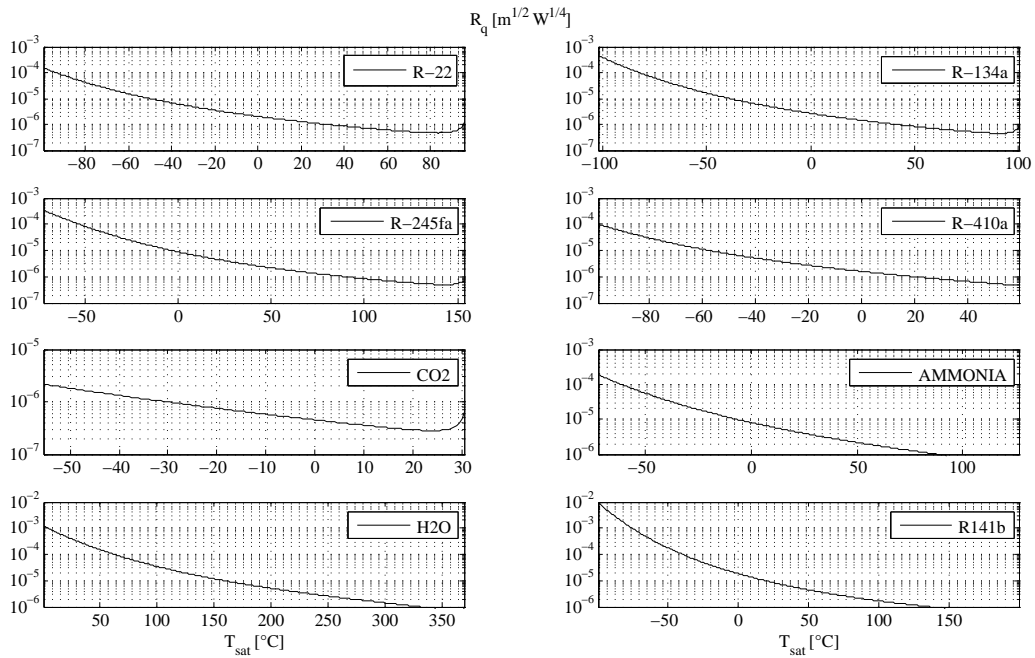


Figure D.4: Evolution of the dimensional variable R_q defined in Eq. (D.8) with the saturation temperature T_{sat} for different refrigerants

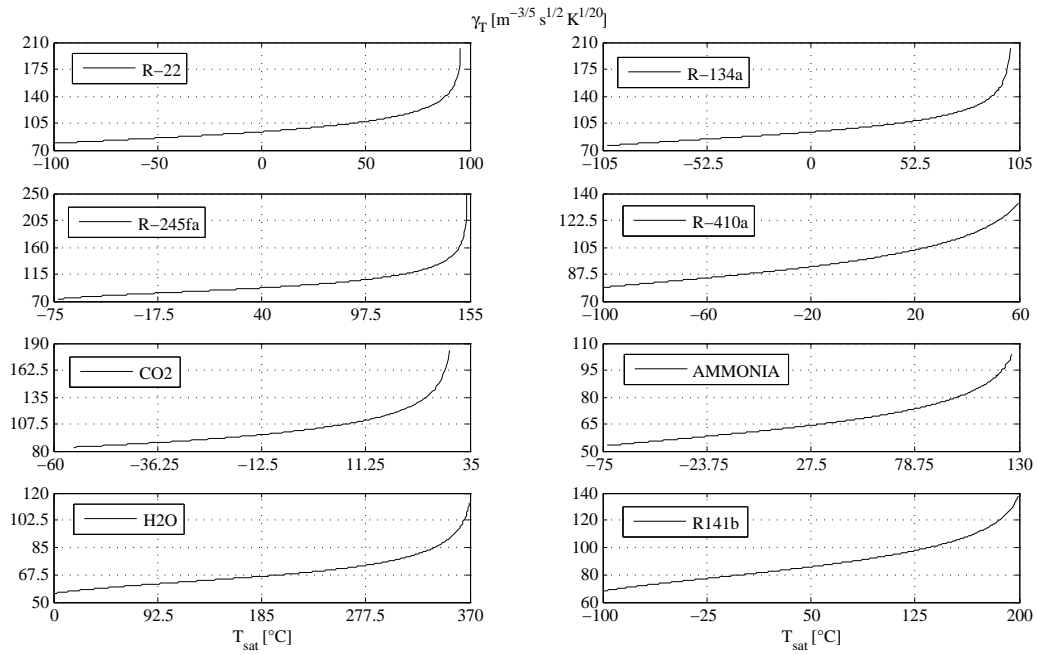


Figure D.5: Evolution of the dimensional variable γ_T defined in Eq. (D.11) with the saturation temperature T_{sat} for different refrigerants

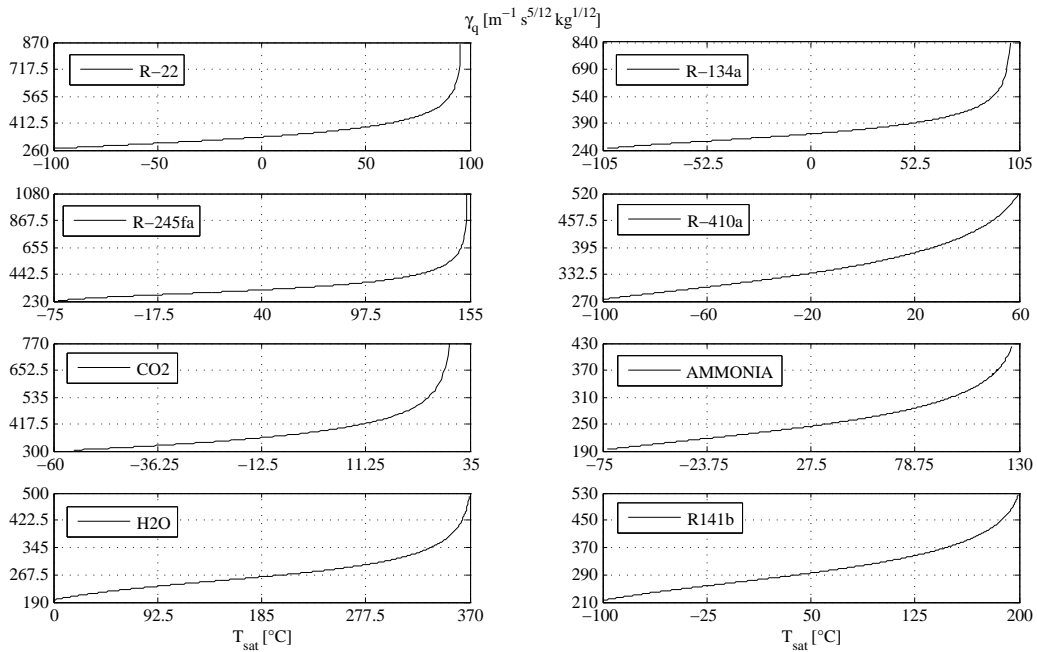


Figure D.6: Evolution of the dimensional variable γ_q defined in Eq. (D.12) with the saturation temperature T_{sat} for different refrigerants

Appendix E

Meshes Examples and Numerical Convergence

In this section, different meshes for different channels shapes are presented. As it has been presented in Chapter 3, the inner geometrical shape is discretized and a set of film thickness vectors is first generated. These film thickness directions $\vec{\delta}$ are fixed and they allow the film thickness to be described as a unique function of the curvilinear coordinate over the inner perimeter of the channel.

An example of a discretized geometry is reported in Fig. (E.1) and in Fig. (E.2) for a flattened shape: the inner perimeter is divided in a set of N points and from these points the film thickness directions are generated. Given a certain liquid-vapor interface, the intersection of the interface with the film thickness directions allows the film thickness function to be obtained, as the one reported in Fig. (E.3). This procedure can be done in both direction, that is from the interface to the film thickness distribution and from the film thickness distribution to the interface reconstruction.

The mesh in the two dimensional domain is then *extruded* along the axis of the channel and with the same mechanism the liquid-vapor interface can be described through two independent coordinates. An example of a mesh generated for an elliptical channel is shown in Fig. (E.4) (in this case, only the boundary of the inner channel surface is represented) and an example of a mesh generated for a flattened shape channel is reported in Fig. (E.5).

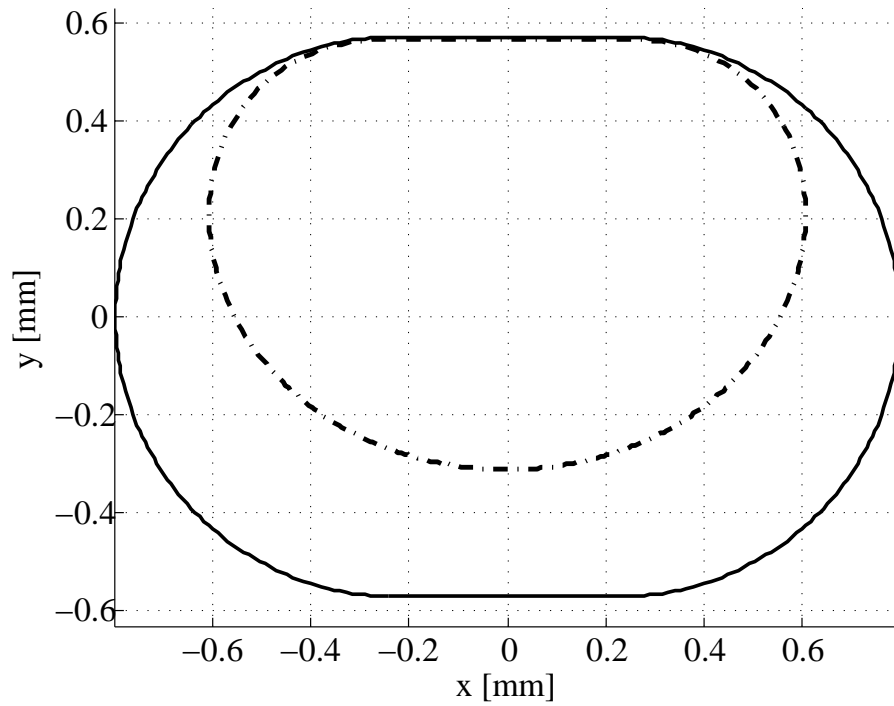


Figure E.1: Example of a liquid-vapor interface (dashed line) in a flattened channel shape

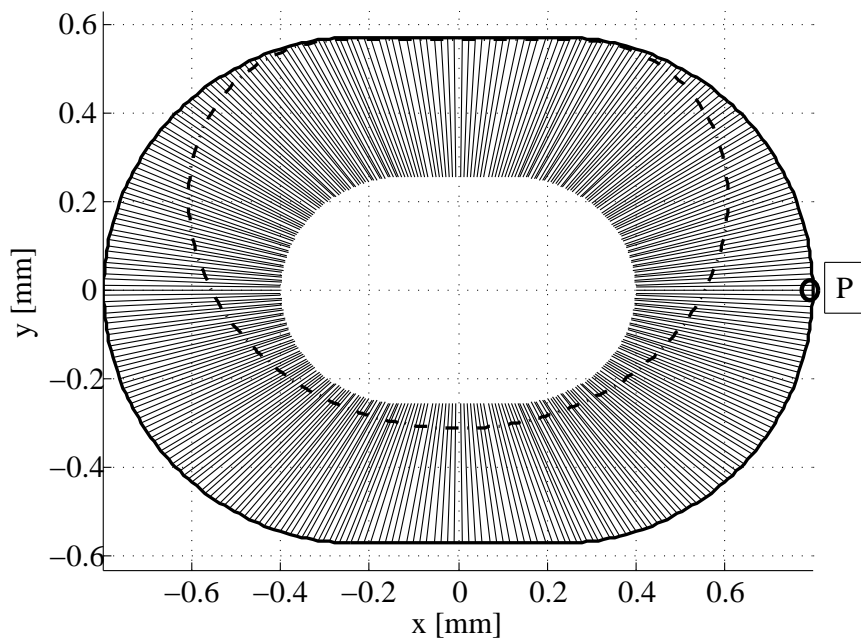


Figure E.2: Liquid-vapor interface (dashed line) and definition of the film thickness directions $\vec{\delta}$ in a discretized geometry

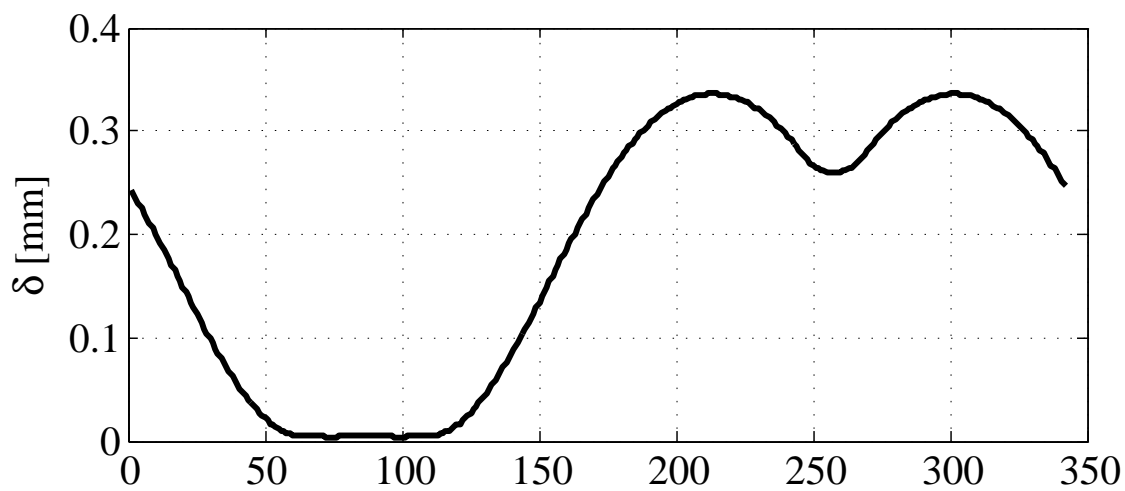


Figure E.3: Distribution of the liquid film thickness corresponding to the interfacial shape represented in Fig. (E.2) as a function of the discretization points. The point having the coordinate 0 in the figure corresponds to the point P indicated in Fig. (E.2)

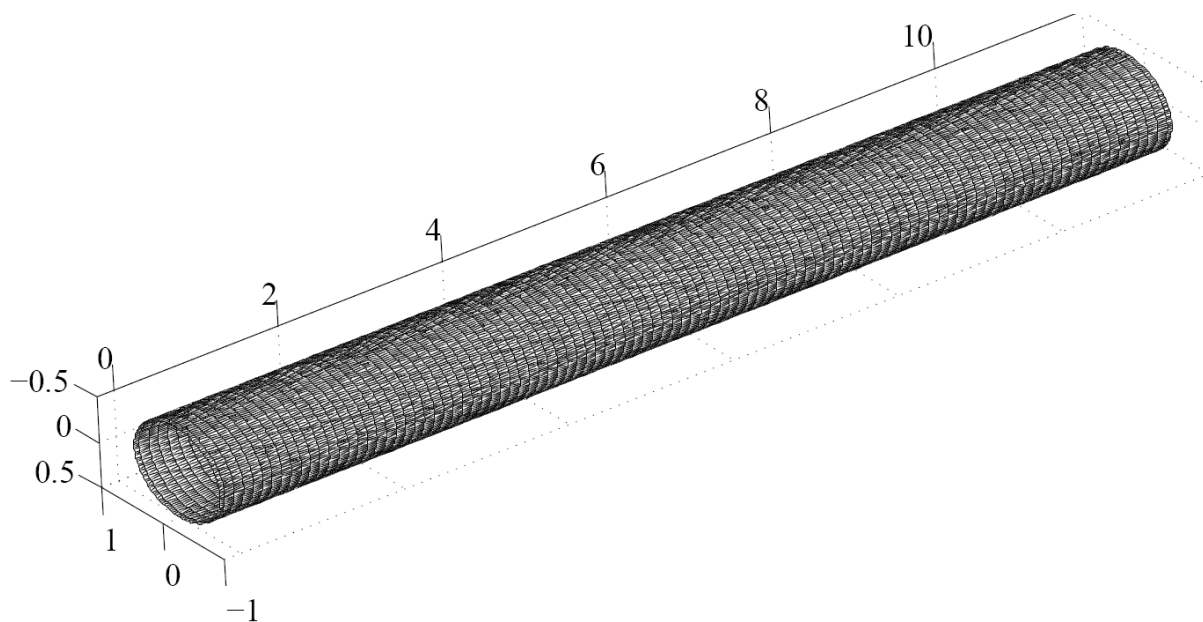


Figure E.4: Example of meshing for an elliptical channel

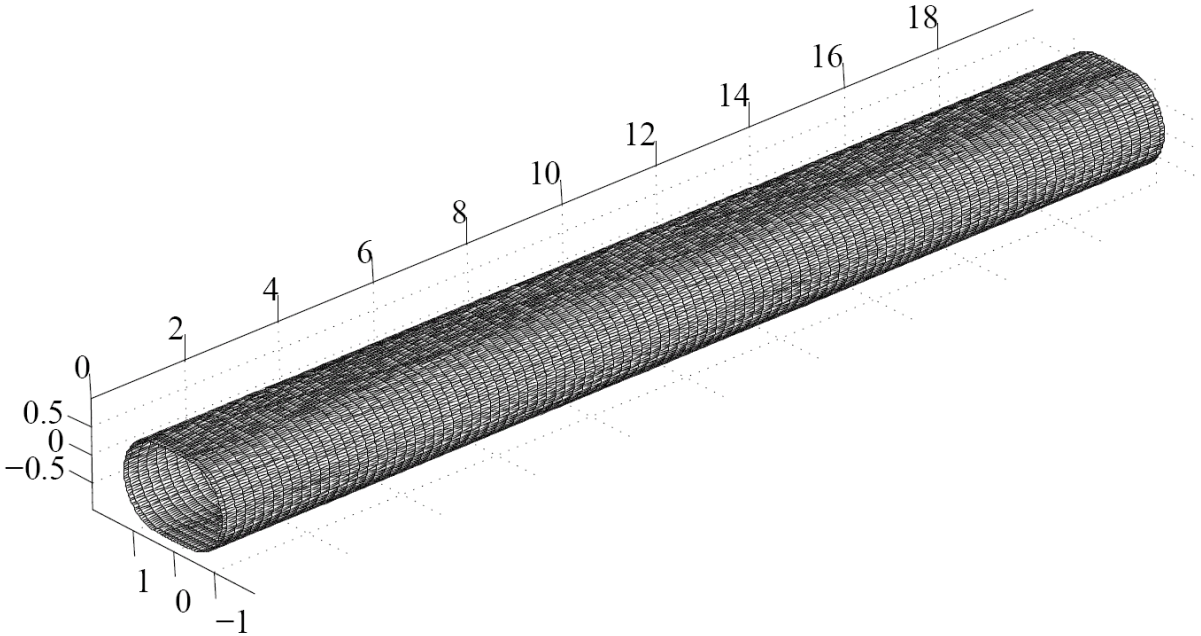


Figure E.5: Example of meshing for a flattened shape channel

E.1 Mesh Size Dependence Test

Using the Richardson extrapolation technique (see [54] for details), it is possible to verify the consistency of the model and the convergence to the solution as a function of the mesh size. In particular two free variables can be modified: the number of discretization points N in the two dimensional domain and the number M of sections along the axis. Fig. (E.6) shows the calculated error as a function of these two numbers for an elliptical shape with an aspect ratio of 1.2 and for the following conditions: $Sn_q = 25$, $Re_q = 0.3$, $\Gamma = 0.05$, $Re_v = 15000$, $We = 3.0$, $Bo_y = -1.5$ and $L_{ht} = 0.05$.

The graphs shows that the model converges to the asymptotic solution as the error tends to reduce as the number of discretization points increases.

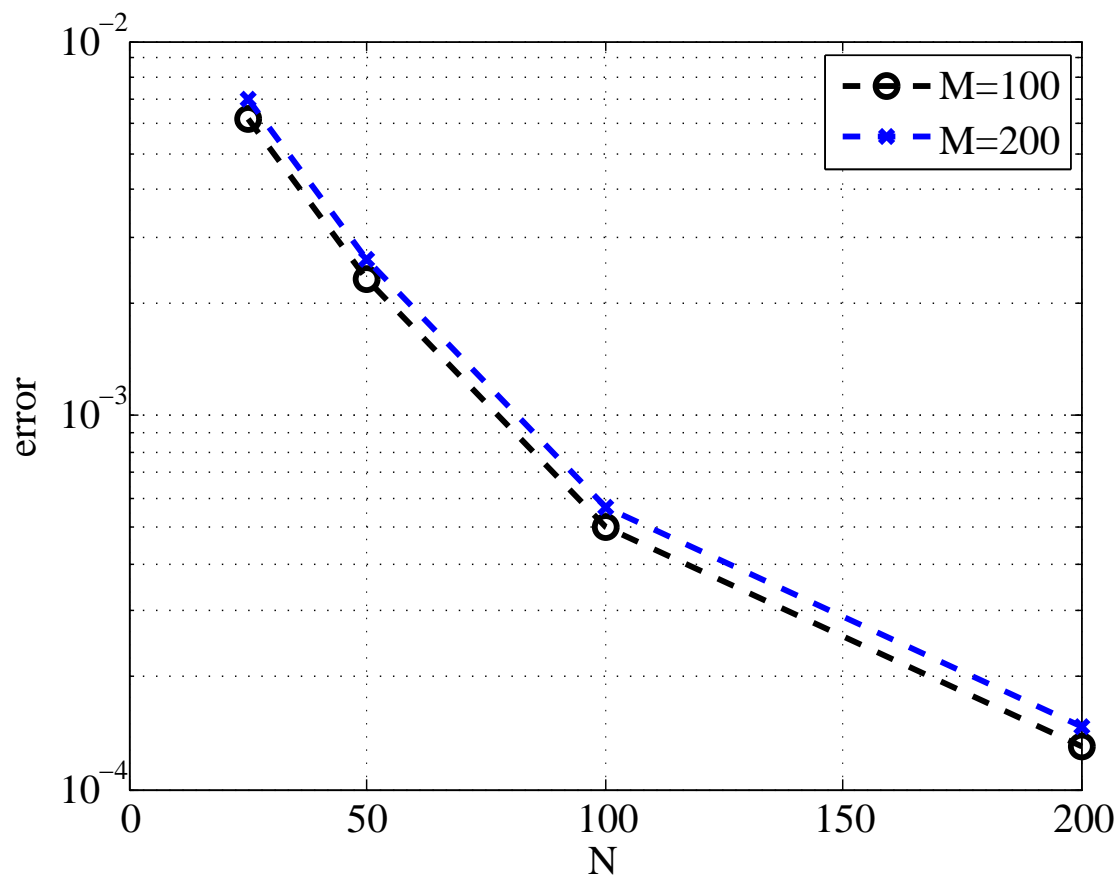


Figure E.6: Evolution of the simulation error evaluated using the Richardson extrapolation technique described in Chapter 5 by varying the mesh size

Appendix F

Publication List from Thesis

S. Nebuloni and J. R. Thome, Film Condensation under Normal and Micro-Gravity: Effect of Channel Shape, *MicroGravity Science and Technology*, International Journal for Microgravity Research and Applications, 19(3-4):125-127, 2007.

S. Nebuloni and J. R. Thome, Film Condensation under Normal and Micro-Gravity: Effect of Channel Shape, Proceedings of the Second International Topical Team Workshop on TWO-PHASE SYSTEMS FOR GROUND AND SPACE APPLICATIONS, Kyoto, Japan, 2007.

S. Nebuloni and J. R. Thome, Numerical Modeling of Laminar Annular Film Condensation for Different Channel Shapes, *International Journal of Heat and Mass Transfer*: paper accepted after review, currently being published.

S. Nebuloni and J. R. Thome, Numerical Modeling of The Conjugate Heat Transfer Problem for Annular Laminar Film Condensation in Microchannels, Proceedings of the 2nd Micro/Nanoscale Heat and Mass Transfer International Conference MNHMT2009, 18–22 December, 2009, Shanghai, China.

S. Nebuloni and J. R. Thome, Conjugate Heat Transfer in Annular Laminar Film Condensation in Microchannels: Comparison of Numerical Model to Experimental Results, abstract accepted for: International Heat Transfer Conference (IHTC-14), 8–13 August, 2010, Washington D.C., USA.

Bibliography

- [1] J. R. Thome. *Engineering Data Book III*. 2008.
<http://www.wlv.com/products/databook/db3/DataBookIII.pdf>.
- [2] S. Garimella. Condensation flow mechanisms in microchannels: Basis for pressure drop and heat transfer models. *Heat Transfer Engineering*, 25:104–116, 2004.
- [3] H. Honda and S. Nozu. A prediction method for heat transfer during film condensation on horizontal low integral-fin tubes. *Journal of Heat Transfer*, 109:218–225, 1987.
- [4] A. Agarwal and S. Garimella. Representative results for condensation measurements at hydraulic diameters 100 microns. *Proceeding of IMECE2007 ASME International Mechanical Engineering Congress and Exposition, Seattle, Washington USA*, IMECE2007-43749, 2007.
- [5] Hua Sheng Wang and John W. Rose. A theory of film condensation in horizontal noncircular section microchannels. *Transactions of the ASME*, 127:1098–1105, 2005.
- [6] M. Miscevic, P. Lavieille, and B. Piaud. Numerical study of convective flow with condensation of a pure fluid in capillary regime. *International Journal of Heat and Mass Transfer*, 52:5130–5140, 2009.
- [7] Qian Su, Guang Xu Yua, Hua Sheng Wang, and John W. Rose. Microchannel condensation: Correlations and theory. *International Journal of Refrigeration*, 32:1149–1152, 2009.
- [8] Y. Y. Yan and T. F. Lin. Condensation heat transfer and pressure drop of refrigerant r-134a in a small pipe. *International Journal of Heat and Mass Transfer*, 42:697–708, 1999.
- [9] J. S. Shin and M. H. Kim. An experimental study of condensation heat transfer inside a mini-channel with a new measurement technique. *International Journal of Multiphase Flow*, 30:311–325, 2004.
- [10] J. S. Shin and M. H. Kim. An experimental study of flow condensation heat transfer inside circular and rectangular mini-channels. *Heat Transfer Engineering*, 26:36–44, 2005.

- [11] A. Agarwal, Todd M. Bandhauer, and D S. Garimella. Heat transfer model for condensation in non-circular microchannels. *Proceedings of the Fifth International Conference on Nanochannels, Microchannels and Minichannels, ICNMM2007, June 18-20, 2007, Puebla, Mexico, ICNMM2007-30223*, 2007.
- [12] T.S. Zhao and Q. Liao. Theoretical analysis of film condensation heat transfer inside vertical mini triangular channels. *International Journal of Heat and Mass Transfer*, 45:2829–2842, 2002.
- [13] H. S. Wang, J. W. Rose, and H. Honda. A theoretical model of film condensation in square section horizontal microchannels. *Institution of Chemical Engineers*, 82:430–434, 2004.
- [14] J. H. Lienhard IV and J. H. Lienhard V. *A Heat Transfer Textbook*. Phlogiston Press, 2006. available online at: <http://web.mit.edu/lienhard/www/ahtt.html>.
- [15] J. El Hajal, J.R. Thome, and A. Cavallini. Condensation in horizontal tubes, part 1: Two-phase flow pattern map. *International Journal of Heat and Mass Transfer*, 46:3349–3363, 2003.
- [16] W. W. Akers, H. A. Deans, and O. K. Crosser. Condensation heat transfer within horizontal tubes. *Chem. Eng. Prog. Symp.*, 55:171–176, 1959.
- [17] M. M. Shah. A general correlation for heat transfer during film condensation inside pipes. *International Journal of Heat and Mass Transfer*, 22:547–556, 1978.
- [18] Frank P. Incropera and David P. DeWitt. *Fundamentals of Heat and Mass Transfer*. Wiley, sixth edition edition, 1996.
- [19] J. R. Thome, J. El Hajal, and A. Cavallini. Condensation in horizontal tubes, part 2: New heat transfer model based on flow regimes. *International Journal of Heat and Mass Transfer*, 46:3365–3387, 2003.
- [20] S. Garimella, J. D. Killon, and J. W. Coleman. An experimentally validated model for two-phase pressure drop in the intermittent flow regime for noncircular microchannels. *Journal of Fluids Engineering*, 125:887–894, 2003.
- [21] S. Garimella, A. Agarwal, and J. D. Killon. Condensation pressure drop in circular microchannels. *Heat Transfer Engineering*, 26:28–35, 2005.
- [22] Beatrice Mederic, Marc Miscevic, Vincent Platel, Pascal Lavieille, and Jean-Louis Joly. Experimental study of flow characteristics during condensation in narrow channels> the influence of the diameter channel on structure patterns. *Superlattices and Microstructures*, 35:573–586, 2004.

- [23] T. M. Bandhauer, A. Agarwal, and S. Garimella. Measurement and modeling of condensation heat transfer coefficients in circular microchannels. *Transactions of the ASME*, 128:1050–1059, 2006.
- [24] S. Garimella and A. Agarwal. Channel size based measurement technique for condensation heat transfer coefficients in mini- and micro-channels. *Proceeding of IMECE2005 ASME International Mechanical Engineering Congress and Exposition, Orlando, Florida USA*, IMECE2005-80242:521–528, 2005.
- [25] A. Agarwal and S. Garimella. Modeling of pressure drop during condensation in circular and non-circular microchannels. *Proceedings of the IMECE 2006*, IMECE2006-14672, 2006.
- [26] Shigeru Koyama, Ken Kuwahara, Kouichi Nakashita, and Ken Yamamoto. An experimental study on condensation of refrigerant r134a in a multi-port extruded tube. *International Journal of Refrigeration*, 24:425–432, 2003.
- [27] K. Mishima and T. Hibiki. Effect of inner diameter on some characteristics of air-water two-phase flows in capillary tubes. *Transactions of JSME*, 61:99–106, 1995.
- [28] H. Haraguchi, S. Koyama, and T. Fujii. Condensation of refrigerants hfc22, hfc134a and hfc123 in a horizontal smooth tube. *Transactions of JSME*, 60:245–252, 1994.
- [29] Alberto Cavallini, Luca Doretto, Marko Matkovic, and Luisa Rossetto. Update on condensation heat transfer and pressure drop inside minichannels. *Heat Transfer Engineering*, 27:74–87, 2006.
- [30] Alberto Cavallini, D. Del Col, L. Doretto, M. Matkovic, and L. Rossetto. Frictional pressure drop during vapour-liquid flow in minichannels: Modelling and experimental evaluation. *International Journal of Heat and Fluid Flow*, 30:131–139, 2009.
- [31] Marko Matkovic, Alberto Cavallini, Davide Del Col, and Luisa Rossetto. Experimental study on condensation heat transfer inside a single circular minichannel. *International Journal of Heat and Mass Transfer*, 52:2311–2323, 2009.
- [32] Knut Arild Marak. *Condensation Heat Transfer and Pressure Drop for Methane and Binary Methane Fluids in Small Channels*. PhD thesis, Norwegian University of Science and Technology, 2009.
- [33] Yeon-Pun Chang, Rueyyih Tsai, and Jiin-Wen Hwang. Condensing heat transfer characteristics of aluminum flat tube. *Applied Thermal Engineering*, 17:1055–1065, 1997.
- [34] Ralph L. Webb and Kelman Elmis. Effect of hydraulic diameter on condensation of r-134a in flat extruded aluminium tubes. *Enhanced Heat Transfer*, 8:77–90, 2001.

- [35] Rin Yun, Jaehyeok Heo, and Yongchang Kim. Film condensation heat transfer characteristics of r134a on horizontal stainless steel integral-fin tubes at low heat transfer rate. *International Journal of Refrigeration*, 32:865–873, 2009.
- [36] Y. Zhang and A. Faghri. Numerical simulation of condensation on a capillary grooved structure. *Numerical Heat Transfer, Part A*, 39:227–243, 2001.
- [37] Yongping Chen, Jiafeng Wu, Mingheng Shi, and G.P. Peterson. Numerical simulation for steady annular condensation flow in triangular microchannels. *International Communications in Heat and Mass Transfer*, 35:805–809, 2008.
- [38] H. S. Wang and J. W. Rose. Film condensation in horizontal microchannels: Effect of channel shape. *International Journal of Thermal Science*, 45:1205–1212, 2006.
- [39] R. Gregorig. Hautkondensation an feingewellten obert&hen bei beriicksichtigung der oberfliichenspannung. *Z. Angew. Math. Phys.*, 5:36–49, 1954.
- [40] H. S. Wang and J. W. Rose. Effect of interphase matter transfer on condensation on low-finned tubes. *International Journal of Heat and Mass Transfer*, 47:179–184, 2004.
- [41] J. Wu, Y. Chen, M. Shi, P. Fu, and G.P. Peterson. Three-dimensional numerical simulation for annular condensation in rectangular microchannels. *Nanoscale and Microscale Thermophysical Engineering*, 13:13–29, 2009.
- [42] T. A. Adamek. Bestimmung der kondensationgrob auf feinewellten oberflächen zur ausle-gun aptimaler wandprofile. *Warme-und Stoffubertragung*, 15:255–270, 1981.
- [43] T. A. Adamek and R. L. Webb. Prediction of film condensation on horizontal integral fin tubes. *International Journal of Heat and Mass Transfer*, 33:1721–1735, 1990.
- [44] O. Kabov, I. Marchuk, and D. Radionova. Condensation on curvilinear fins (effect of groove flooding): Emerald experiment of esa. *Microgravity Science and Technology*, 19:121–124, 2007.
- [45] M. Miscovic, B. Méderic, P. Lavieille, U. Soupremanien V., and Serin. Condensation in capillary-driven two-phase loops. *Microgravity Science and Technology*, 19:116–120, 2007.
- [46] Yongping Chen, Mingheng Shi, Ping Cheng, and G.P. Peterson. Condensation in microchannels. *Nanoscale and Microscale Thermophysical Engineering*, 12:117–143, 2008.
- [47] J. Straub. The role of surface tension for two-phase heat and mass transfer in the absence of gravity. *Experimental Thermal Fluid Science*, 9(ISBN 3-540-42074-6):253–273, 1994.
- [48] A. Faghri and L. C. Chow. Annular condensation heat transfer in a microgravity environment. *Int. Comm. Heat Mass Transfer*, 18:715–729, 1991.

- [49] Yongping Chen, C. B. Sobhan, and G. P. Peterson. Review of condensation heat transfer in microgravity environments. *Journal of Thermophysics and Heat Transfer*, 20:353–360, 2006.
- [50] R. J. Naumann. Optimizing the design of space radiators. *International Journal of Thermophysics*, 25(6):1929–1941, 2004.
- [51] David G. Gilmore. *Satellite Thermal Control Handbook*. The Aerospace Corporation Press, 1994.
- [52] NIST. *REFPROP Thermodynamic and transport properties of refrigerant and refrigerant mixtures*, 2007.
- [53] J. H. Ferziger and M. Peric. *Computational Methods for Fluid Dynamics*. Springer, 2002.
- [54] H. K. Versteeg and W. Malalaskera. *An Introduction to Computational Fluid Dynamics - The Finite Volume Method*. Pearson, 1995.
- [55] C. D. Pagani and S. Salsa. *Analisi Matematica, volume 2*. Zanichelli, 2002.
- [56] J. Madejski. The effect of molecular-kinetic resistances on heat transfer in condensation. *International Journal of Heat and Mass Transfer*, 9:35–39, 1966.
- [57] P. C. Wayner Jr., Y. K. Kao, and L. V. LaCroix. The interline heat transfer coefficient of an evaporating wetting fluid. *International Journal of Heat and Mass Transfer*, 19:487–492, 1976.
- [58] Dalton J. E. Harvie and David F. Fletcher. A simple kinetic theory treatment of volatile liquid-gas interfaces. *Transactions of the ASME*, 123:486–491, 2001.
- [59] V. S. Ajaev and G. M. Homsy. Steady vapor bubbles in rectangular microchannels. *Journal of Colloid and Interfacial Science*, 240:259–271, 2001.
- [60] V. S. Ajaev. Spreading of thin volatile liquid droplets on uniformly heated surfaces. *Journal of Fluid Mechanics*, 528:279–296, 2005.
- [61] H. Wang, S. V. Garimella, and J. Y. Murthy. Characteristics of evaporating thin film in a microchannel. *International Journal of Heat and Mass Transfer*, 50:3933–3942, 2007.
- [62] Y. Hristov, D. Zhao, D. B. R. Kenning, K Sefiane, and T. G. Karayiannis. A study of nucleate boiling and critical heat flux with ehd enhancement. *Heat and Mass Transfer*, page SPECIAL ISSUE, 2007.
- [63] H. Wang, S. V. Garimella, and J. Y. Murthy. An analytical solution for the total heat transfer in the thin-film region of an evaporating meniscus. *International Journal of Heat and Mass Transfer*, 51:6317–6322, 2008.

-
- [64] K. Stephan. Influence of dispersion forces on phase equilibria between thin liquid films and their vapour. *International Journal of Heat and Mass Transfer*, 45:4715–4725, 2002.
- [65] Andrea Cioncolini, John R. Thome, and Carlo Lombardi. Algebraic turbulence modeling in adiabatic gas-liquid annular two-phase flow. *International Journal of Multiphase Flow*, 35:580–596, 2009.
- [66] Alfio Quarteroni, Riccardo Sacco, and Fausto Saleri. *Numerical Mathematics*. Springer, 2004.
- [67] John W. M. Bush. Mit lecture notes on surface tension, lecture 5, 2004.
- [68] Alexander Oron, Stephen H. Davis, and S. George Bankoff. Long-scale evolution of thin liquid films. *Reviews of Modern Physics*, 69:931–980, 1997.

Curriculum Vitae

PERSONAL DATA

| | |
|---------------|-----------------------------|
| Name | Stefano Nebuloni |
| Date of birth | 24 th June, 1980 |
| Birthplace | Cuggiono (MI), Italy |
| Nationality | Italian |

EDUCATION

| | |
|-----------|--|
| 2006–2010 | Doctoral Student and Assistant , Laboratory of Heat and Mass Transfer, Swiss Federal Institute of Technology Lausanne (EPFL), Switzerland |
| 1999–2005 | Master of Science in Aerospace Engineering , Politecnico di Milano, Milano |
| 1994–1999 | High School Certificate , Liceo Scientifico Galileo Galilei, Legnano (IT), Diploma of High School |

WORKING EXPERIENCE

| | |
|-----------|---|
| 2007–2009 | Swiss Federal Institute of Technology (EPFL), Laboratory of Heat and Mass Transfer, Lausanne Doctoral Research Assistant; |
| 2006 | Swiss Federal Institute of Technology (EPFL), Laboratory of Heat and Mass Transfer, Lausanne, StratXX Near Space Technologies AG , Design and Simulation of a Thermal Control System for a high altitude balloon for Telecommunication and Ground Observation; |
| 2005 | European Space Agency ESA-ESTEC, Noordwijk , Traineeship in TEC-MMA section for the preliminary design of a Lunar Mobility System for manned exploration. |

PUBLICATIONS

M. Massari, P. Massioni, S. Nebuloni, G. Sangiovanni, F. Bernelli-Zazzera, Realization and Control of a Prototype of Legged Rover for Planetary Exploration, IEEE/ASME Conference of Advanced Intelligent Mechatronics, Monterey, USA, 2005

S. Nebuloni and J. R. Thome, Film Condensation under Normal and Micro-Gravity: Effect of Channel

Shape, *MicroGravity Science and Technology*, International Journal for Microgravity Research and Applications, 19(3-4):125-127, 2007.

S. Nebuloni and J. R. Thome, Film Condensation under Normal and Micro-Gravity: Effect of Channel Shape, Proceedings of the Second International Topical Team Workshop on TWO-PHASE SYSTEMS FOR GROUND AND SPACE APPLICATIONS, Kyoto, Japan, 2007.

S. Nebuloni and J. R. Thome, Numerical Modeling of Laminar Annular Film Condensation for Different Channel Shapes, *International Journal of Heat and Mass Transfer*: paper accepted after review, currently being published.

S. Nebuloni and J. R. Thome, Numerical Modeling of The Conjugate Heat Transfer Problem for Annular Laminar Film Condensation in Microchannels, Proceedings of the 2nd Micro/Nanoscale Heat and Mass Transfer International Conference MNHMT2009, 18-22 December, 2009, Shanghai, China.

S. Nebuloni and J. R. Thome, Conjugate Heat Transfer in Annular Laminar Film Condensation in Microchannels: Comparison of Numerical Model to Experimental Results, abstract accepted for: International Heat Transfer Conference (IHTC-14), 8-13 August, 2010, Washington D.C., USA.

